CLASS VI PERMIT APPLICATION NARRATIVE
40 CFR 146.82(a)

Kern River Eastridge CCS

Project Background and Contact Information

GSDT Submission - Project Background and Contact Information
GSDT Module: Project Information Tracking ***Tab(s):*** General Information tab; Facility Information and Owner/Operator Information tab Please use the checkbox(es) to verify the following information was submitted to the GSDT: ☒ Required project and facility details ***[40 CFR 146.82(a)(1)]***

Chevron U.S.A. Inc. (Chevron) is submitting this application for the Kern River Eastridge Carbon Capture & Sequestration (CCS) Project ("Project") to the U.S. Environmental Protection Agency (EPA) Region 9 for a Class VI Underground Injection Control (UIC) permit to construct carbon dioxide (CO_2) injection wells. CO_2 will be captured from a variety of emission sources (e.g., direct air capture). The CO_2 will be compressed and transported via pipeline to the injector well locations (**Figure 1**). The CO_2 will be injected into the Vedder Sand for 20 years and then monitored for a period of 50 years after last CO_2 injection.

The Project, which is located in Kern County, California, will inject and sequester between 265,000 and 455,000 metric tonnes of CO_2 per year in the Vedder Sand within the Kern River Oil Field for a period of 20 years. The cumulative amount of sequestered CO_2 is expected to total 6.82 million tonnes over the life of the Project.

Chevron is submitting applications for four (4) Class VI injection wells. Two (2) wells will be drilled upon receipt of Authorization to Construct. The remaining two (2) wells are contingent wells to be drilled in the event that one or both of the initial injection wells requires plugging and abandonment prior to planned cessation of injection. Contingent wells will be placed approximately 200 ft away from the initial wells in the target formation.

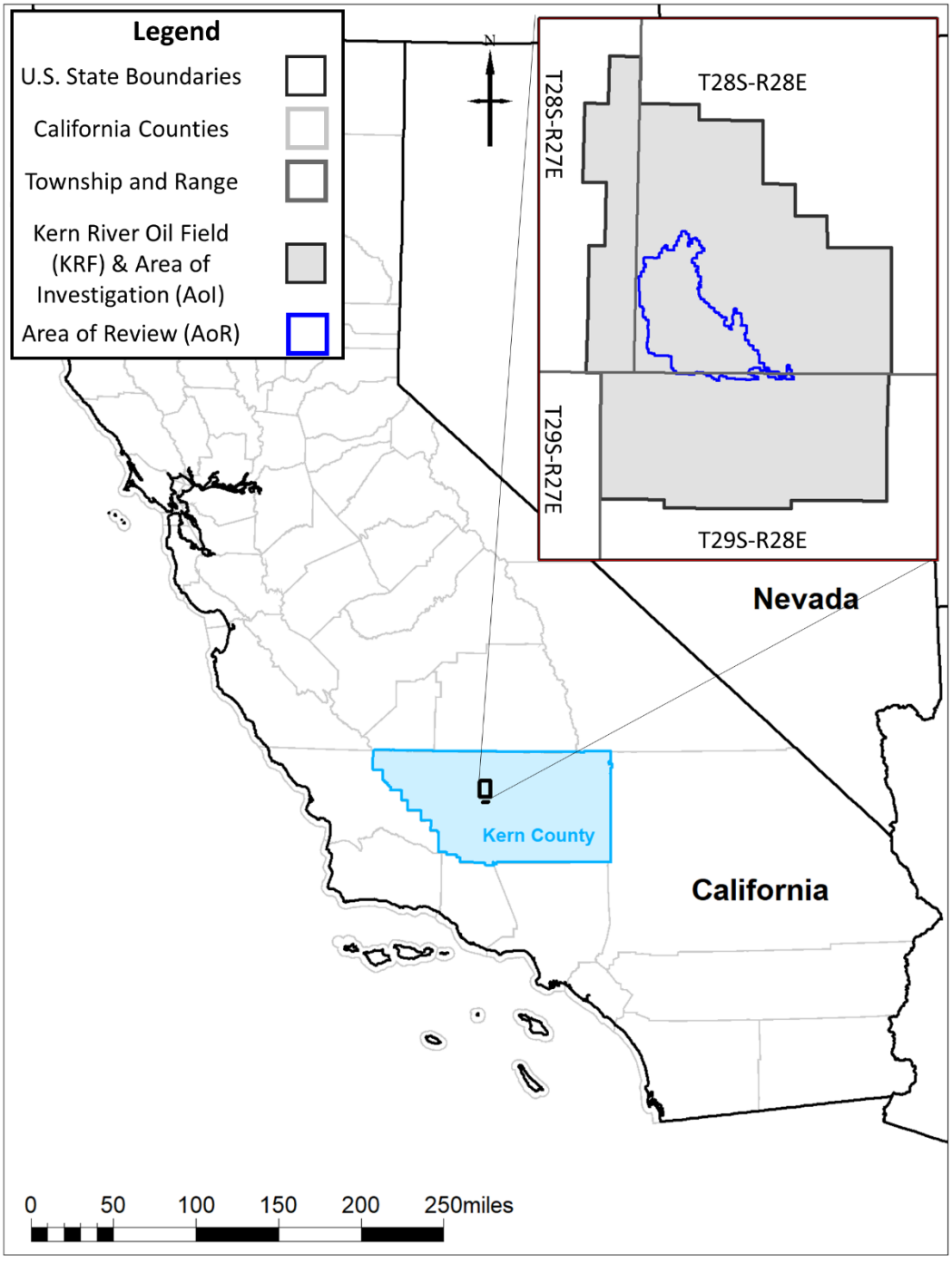

Figure 1. Location of the proposed Project Area of Investigation (AoI) is located approximately 10 miles northeast of the City of Bakersfield in Kern County, California.

The Project will inject CO_2 into the Vedder Sand using two dedicated injector wells in the Kern River Oil Field. Additionally, Chevron plans to have two undrilled permitted contingent injectors to be drilled in the event that one or both of the injectors must be abandoned during the injection phase of the Project. Pressure in the injection zone will be managed using between two and four water-production wells. Chevron has designed a robust monitoring program to track the progression of the CO_2 and pressure front within the target interval, and monitor the dissipation zone and lowermost Underground Source of Drinking Water (USDW). The Project Area of Review (AoR) is shown in **Figure 2** and is delineated based on the migration of injected CO_2 and resultant pressure increase through the 20-year injection period and 50-year Post-Injection Site Care (PISC).

The Project injection zone is in the Vedder Sand, which is located more than 3,000 feet below the base of the Kern River Reservoir, which is the main producing zone of the Kern River Oil Field. The Kern River Oil Field, as defined by the California Geologic Energy Management Division ((CalGEM); State of California, 2010), contains more than 3.5 billion barrels original oil in place (OOIP) of heavy oil (Ginger et al., 1995). Steamflooding and gravity assisted drainage is the current method of thermal Enhanced Oil Recovery (EOR) to produce oil from gently dipping fluvial deposits of the overlying Kern River Formation (Bartow and Pitman, 1983).

The Kern River Oil Field covers nearly 20 square miles of 29 Sections of T28S-29S/R27-28E of the Mountain Diablo Baseline and Meridian, in Kern County, California. The communities of Oildale and Bakersfield are immediately west and south of the Kern River Oil Field, respectively. The Area of Investigation (AoI) for the Project is within the administrative boundary of the Kern River Oil Field (**Figure 2**). The Vedder Sand is in an exempted aquifer within the AoI.

Chevron currently owns approximately 97 percent of the surface and mineral estates of parcels included within the AoR boundary and is pursuing rights and access to the remaining acreage through Carbon Sequestration Easement Agreements. Chevron has contacted the identified property owners for areas not owned by Chevron, received executed Authorizations for Permit Applications, and is pursuing contractual rights to utilize pore space. A portion of the Carbon Sequestration Easement Agreements have been completed and returned to Chevron and negotiations with property owners are ongoing.

Chevron has submitted a Conditional Use Permit (CUP) application for this project to Kern County Planning and Natural Resources Department.

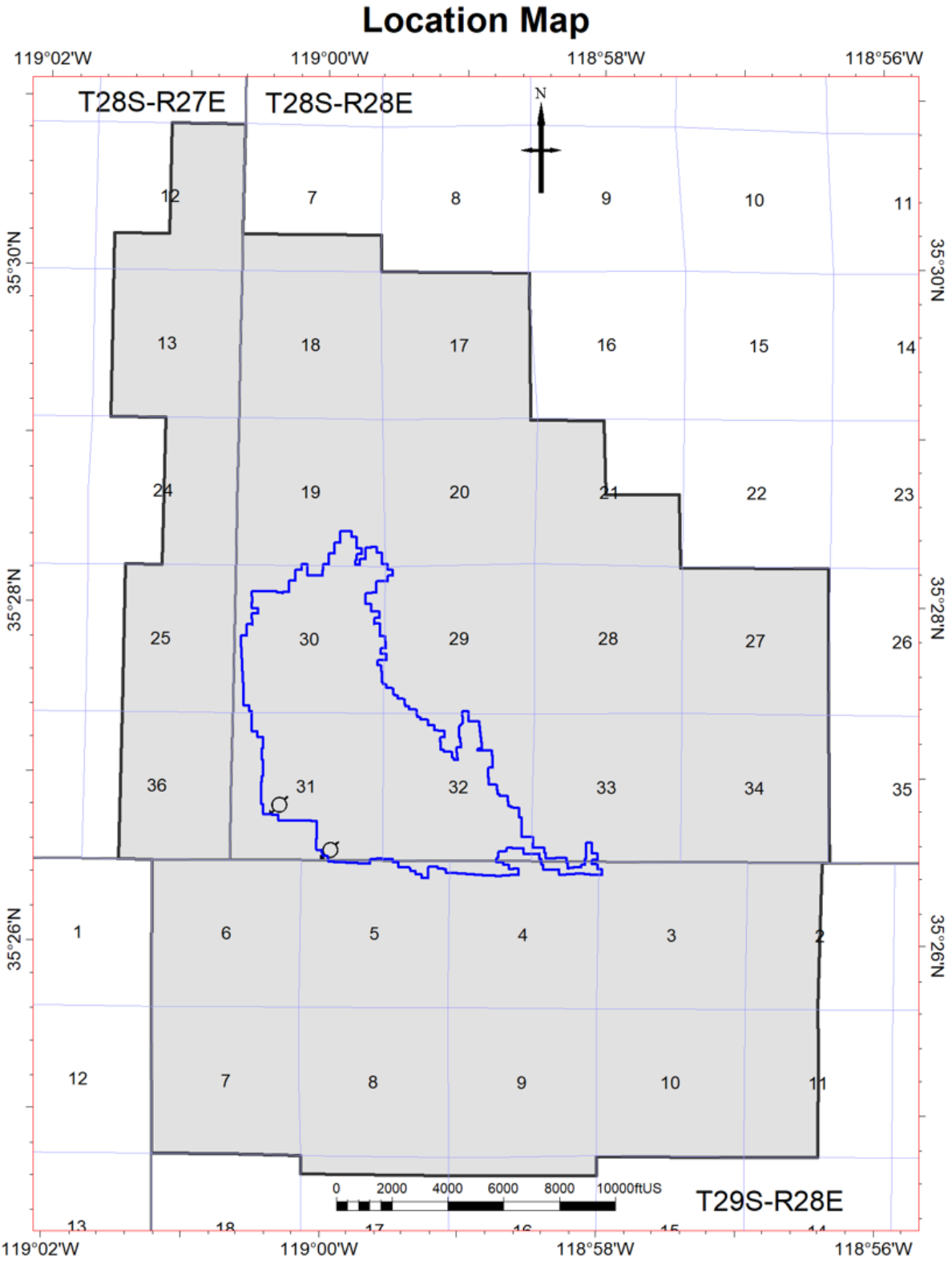

Figure 2. Location of Project AoI & AoR.

Due to permitting requirements, the Project is subject to the California Environmental Quality Act (CEQA) with Kern County as the lead agency. As part of this effort, Chevron contacted the Native American Heritage Commission to obtain a listing of tribal contacts. There are no tribal lands within the AoR. The following Federally recognized tribes were identified for Kern County (**Table 1**).

Table 1. Native American contact list (Native American Heritage Commission, accessed July 23, 2023).

Name	Contact	Address	Phone	Email	County
Santa Rosa Rancheria Tachi Yokut Tribe	Leo Sisco, Chair-person	P.O. Box 8 Lemoore, CA, 93245	(559) 924-1278		Fresno, Kern, Kings, Merced, Monterey, San Benito, San Luis Obispo, & Tulare
Tejon Indian Tribe	Candice Garza, CRM Scheduler	4941 David Rd. Bakersfield, CA, 93307	(661) 345-0632	cgarza@tejonindiantribe-nsn.gov	Kern
Tule River Indian Tribe	Neil Peyron, Chair-person	P.O. Box 589 Porterville, CA, 93258	(559) 781-4271	neil.peyron@tulerivertribe-nsn.gov	Alameda, Amador, Calaveras, Contra Costa, Fresno, Inyo, Kern, Kings, Madera, Mariposa, Merced, Monterey, Sacramento, San Benito, San Joaquin, San Luis Obispo, Stanislaus, Tulare, & Tuolumne

In addition, Chevron has engaged or expects to engage with the various federal, state and local agencies identified in **Table 2** as part of it's permitting efforts**.** In the event that additional agency involvement is required as the project progresses the EPA will be provided with updated contact information.

Table 2. Federal, State and Local Permits and Programs

Permit or Program	**Agency**	**Status**	**Contact Information if available**
Hazardous Management under RCRA	EPA	Large Quantity Generator ID – CAT080011943	
UIC Program under SDWA	EPA	Class VI application in progress (this application)	
NPDES Program under CWA	Central Valley Regional Water Quality Control Board	Construction Storm Water General Permit - required	Fresno Office (559) 445-5116
PSD program under CAA	San Joaquin Valley Air Pollution Control District	Not required	Erin Scott 661 392-5500 Erin.Scott@valleyair.org
Nonattainment Program under CAA	San Joaquin Valley Air Pollution Control District	Title V permit revision or new permit	Erin Scott 661 392-5500 Erin.Scott@valleyair.org
NESHAPS preconstruction approval under CAA	San Joaquin Valley Air Pollution Control District	Asbestos Demolition Notification – not yet submitted	Erin Scott 661 392-5500 Erin.Scott@valleyair.org
Ocean dumping permit under MPRSA	EPA	Not required	
Dredge and fill permit under 404 of CWA	U.S. Army Corps of Engineers	Not anticipated – evaluation in progress	
Section 7 of the Endangered Species Act	U.S. Fish and Wildlife Service	Consultation required Incidental take permit not anticipated	Sacramento Office (916) 414-6621
Water Quality Certification under Section 401 of the CWA	Central Valley Regional Water Quality Control Board	Not anticipated – evaluation in progress	Fresno Office (559) 445-5116
Lake or Streambed Alteration Agreement	California Department of Fish and Wildlife (CDFW)	Not anticipated – evaluation in progress	Jaime Marquez Jaime.Marquez@Wildlife.ca.gov

Permit or Program	Agency	Status	Contact Information if available
California Endangered Species Act	California Department of Fish and Wildlife (CDFW)	Consultation required Incidental take permit not anticipated	Fresno Office (559) 445-5116
Authority to Construct/ Operate	San Joaquin Valley Air Pollution Control District	Title V permit revision or new permit	Erin Scott 661 392-5500 Erin.Scott@valleyair.org
Low Carbon Fuel Standard Certification	California Air Resources Board	Project and Pathway Certification – to be completed	Carbon Capture and Sequestration Protocol (916) 322-2280
Well Abandonment Permit	California Geologic Energy Management Division	Oil well abandonment permit – to be completed	Central District (661) 322-4031
General Plan Amendment, Zone Change, Conditional Use Permit	Kern County Planning and Natural Resources Department	Applied	Lorelei Oviatt - Director 661-862-8866
Local Ministerial Permits (Building, Grading)	Kern County Public Works	Required - to be completed	Building Inspection (661) 862-8650
Water Well Permits	Kern County Public Health Department	Water production and monitoring well permits – to be completed	Public Health (661) 321-3000

This narrative permit application is one of many separate documents submitted to the EPA using their Geologic Sequestration Data Tool (GSDT), and includes information concerning facilities, injector-well design, geology, hydrogeology, reservoir modeling, simulation, pre-operational logging and testing, subsurface monitoring, post-injection site care, emergency and remedial response. Chevron believes the data and analysis presented throughout this permit demonstrate the Vedder to be a safe and secure reservoir for geologic carbon sequestration within the Project AoI.

Site Characterization

The Vedder Sand has been a historic target for oil and gas development in the eastern San Joaquin Basin, where it has produced approximately 1.8 million barrels of light oil (32-40° American Petroleum Institute (API)) from fault-bounded oil pools in the Kern River Oil Field (Condon, 1986; California Geological Survey, 2006; and Wagoner, 2009). The Vedder Sand has produced more than 600 million barrels of oil (MMBO) and 200 billion cubic feet of gas (BCFG) in the southeastern San Joaquin Basin (Tye et al., 1993). The presence of oil pools in the Vedder Sand demonstrates containment over geological time scales, indicating that the Vedder Sand reservoir and Freeman–Jewett Silt upper confining zone are well-suited for the secure and long-term storage of CO_2 in the subsurface.

Lawrence Livermore National Laboratory identified the Vedder Sand as a saline aquifer that can serve as a key sequestration zone in the State of California with 0.9-3.6 billion tons of CO_2 storage capacity (Baker et. al, 2020). Chevron has evaluated injection and long-term sequestration of supercritical carbon-dioxide (CO_2) in the Vedder using geological, geophysical, and petrophysical data sourced from within the AoI and surrounding region including, but not limited to, legacy well-log data, core, and a 3D seismic survey.

The temperature and pressure conditions of the Vedder Sand are favorable for maintaining injected CO_2 in a supercritical state (**Figure 3**).

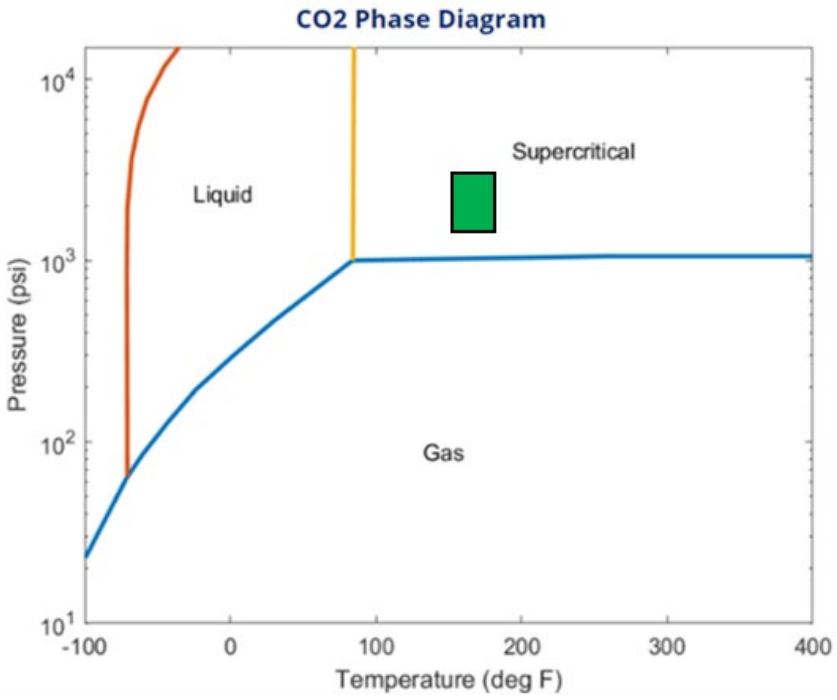

Figure 3. Phase diagram for CO_2 indicating pressure and temperature conditions of the Vedder Sand within the Project AoR (green box) are favorable for maintaining supercritical conditions.

Geologic and hydrogeologic data described in the site characterization sections below were used to develop a conceptual model of the proposed carbon-dioxide storage complex within the Project AoI and AoR. **Figure 4** illustrates the conceptual model for the Project with the Vedder Sand target reservoir (yellow) and associated primary (black) and secondary (brown) sealing units.

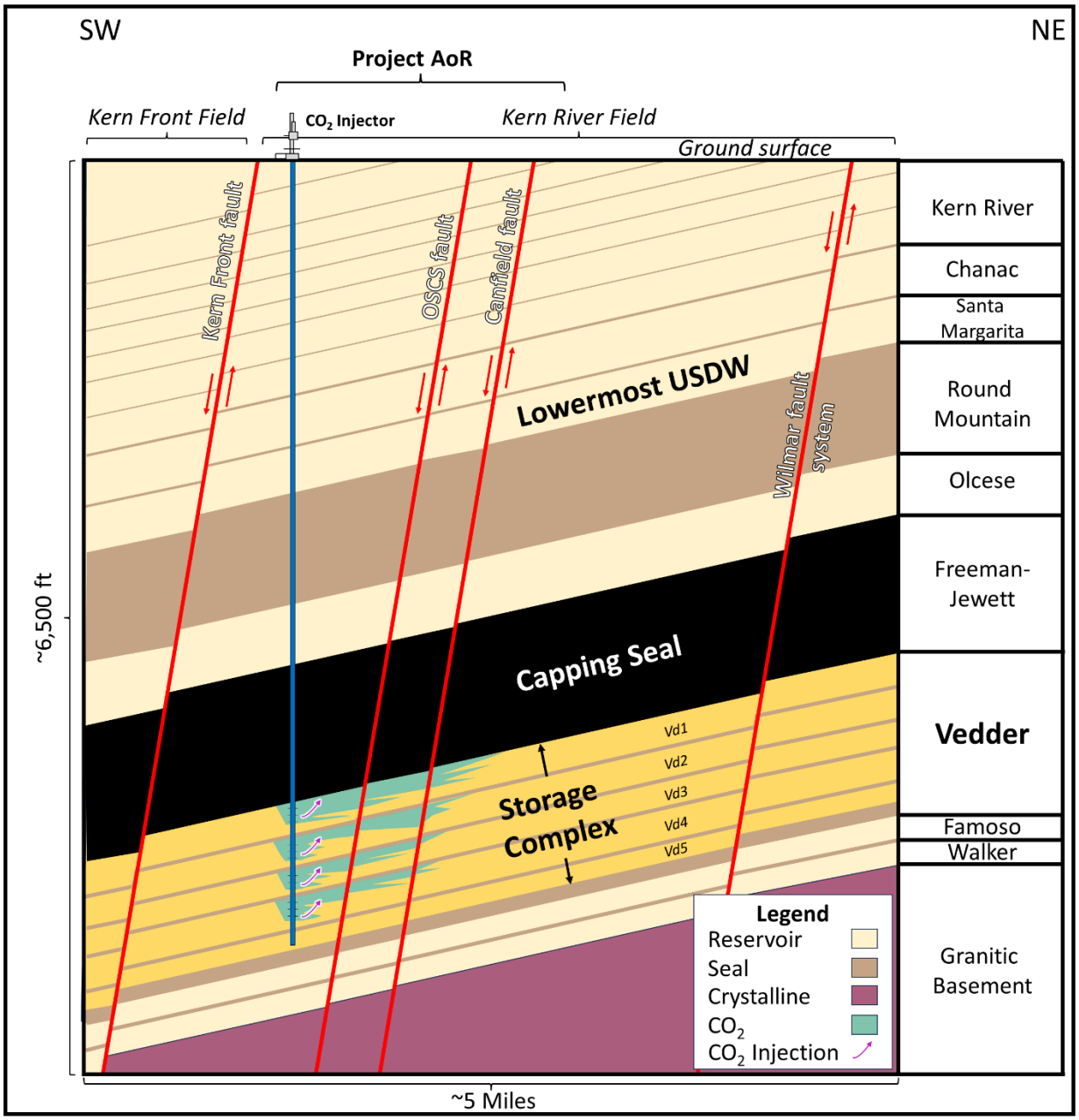

Figure 4. Conceptual model highlighting known geologic conditions for injection and long-term confinement of supercritical CO_2 within the Project AoI.

Data Sources

The regional geology of the San Joaquin Basin of California is documented using legacy wells and seismic surveys obtained for hydrocarbon exploration and development, groundwater resource studies, and water disposal. Chevron has collected and analyzed oil-field operational and proprietary data over the past 120 years. Regional geologic data is available through the California Geological Survey (CGS), United States Geological Survey (USGS), and the California Geologic Energy Management Division (CalGEM) of the California Department of Conservation (DOC). Additional information comes from the U.S. Department of Energy (DOE) and State of California sponsored studies to evaluate the subsurface potential for CO_2 sequestration (e.g., California Geological Survey, 2006; Wagoner, 2009; and Baker et al., 2020).

Legacy wells provide information to define pore space, permeability, reservoir heterogeneity and connectivity, seal presence, and seal character of the entire Cenozoic sedimentary succession in the Project AoI (**Figure 5**). Seventy (70) wells penetrating the Vedder Sand, their associated well-logs and core records, and a propriety 3D seismic survey within the AoI (**Figure 5**) were used to characterize the site and develop the reservoir model comprising the entire Project AoI. A list of wells used to develop the reservoir model are in **Appendix A**. This reservoir model was used to simulate CO_2 plume migration and reservoir pressure response to define the Project AoR.

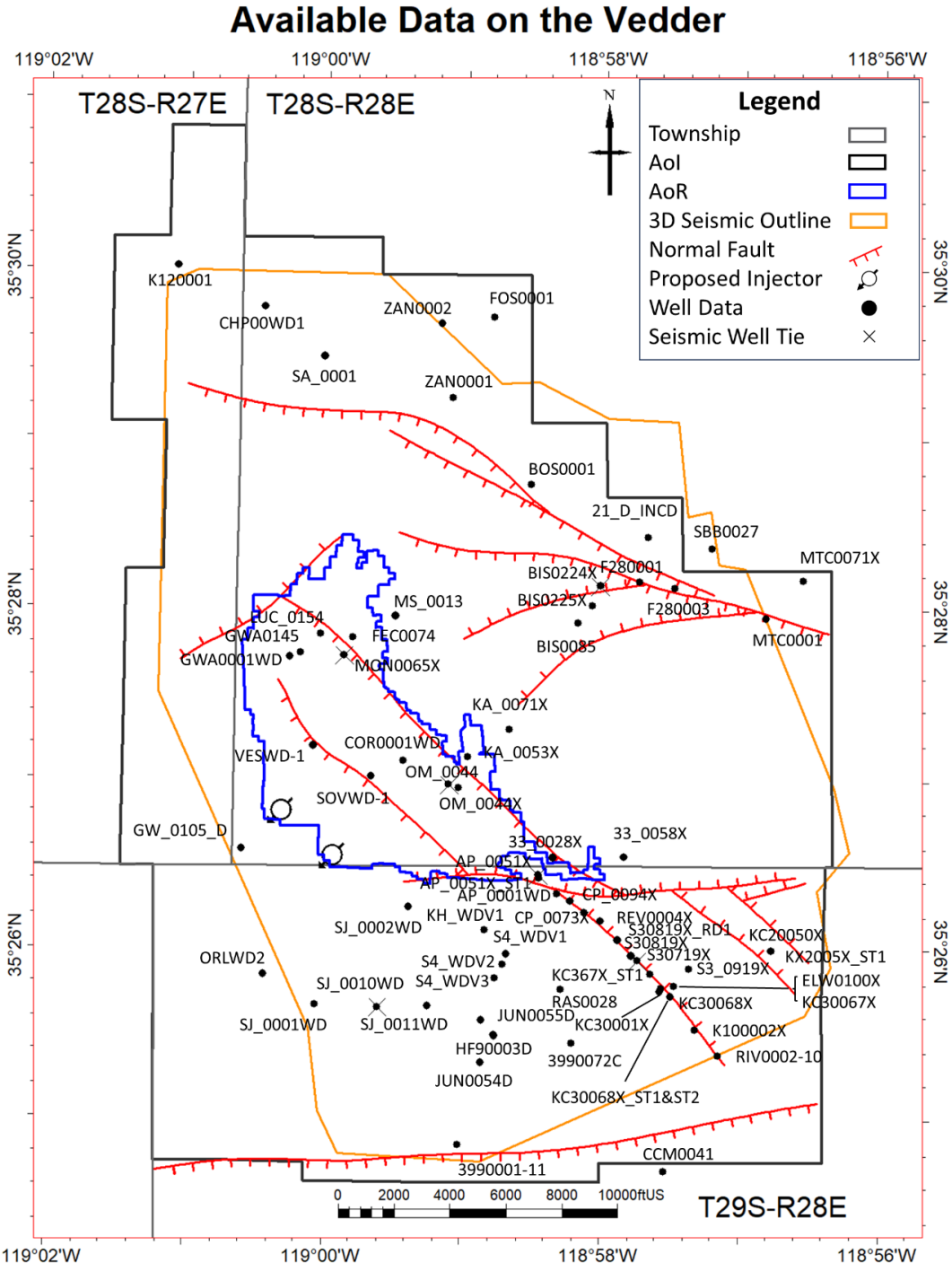

Figure 5. Location of wells within the Project AoI that penetrate the Vedder Sand and the footprint of the 3D seismic survey. Faults displayed at their intersection with the top of the Vedder Sand.

A three-dimensional (3D) seismic survey, acquired by Global Geophysical Services in 2007, covers 20.23 square miles, which comprises 100 percent of the AoR and nearly 90 percent of the AoI. This seismic survey was optimized for imaging the Vedder Sand. The survey utilized 29,922 receivers and 10,046 sources covering distances of 311.7 and 104.6 linear miles, respectively. The survey layout consisted of a shot-and-receiver spacing of 55 ft, with inline and cross line spacings of 330 ft and 990 ft, respectively. The resulting fold of the data is 100 to 115. Seismic processing was completed by WesternGeco and included Post-Stack Kirchoff Time Migration, Pre-Stack Kirchoff Time Migration with Tau-p filtering and spectral whitening, and Pre-Stack dip moveout (DMO) Stolt Time Migration with Tau-p filtering and spectral whitening. This seismic volume was converted from time (TWTT in seconds) to depth (in feet) to allow for the interpretation of seismic features, including major stratigraphic horizons and faults in the depth domain. To do this, synthetic well ties were generated for 6 wells across the survey area:

1. AP_0051X (API #040296721700),
2. BIS0224X (API #040297107500),
3. OM_0044 (API #040296655800),
4. MON0065X (API #040296758700),
5. S3_0719X (API #040297135800), and
6. SJ_0010WD (API #040301418200).

These wells (**Figure 5**) were used to generate time-depth relationships where they had correlation coefficients ranging from 0.6 to greater than 0.7 and reasonably good vertical and spatial coverage across the AoI. In areas of closely clustered wells, the well tie having the highest correlation coefficient was used. An extended statistical wavelet was extracted from the log data with a peak frequency of 15-20 Hz (i.e., medium to low frequency). Assuming a 20 Hz frequency and an average velocity for the top of the Vedder Sand of 7750 ft/s, the resolvability (vertical resolution) of the seismic volume is approximately 100 ft. The seismic survey was not zero-phased and the phase ranges from 20-60 degrees. No phase rotation was applied to the seismic volume because of inconsistencies among phases in the extractions; however, well control is sufficient to compare log correlations with the seismic interpretations.

A velocity model framework for the seismic survey was divided into stratigraphic zones to establish time-depth relationships approximating structural surfaces for the tops of the Santa Margarita, Olcese, Vedder, and basement. The model framework was populated using well velocities and infilled using a kriging algorithm. Seismic mis-ties were determined for fifty-seven (57) wells at the top of the Vedder Sand, yielding an average mis-tie of 1.5 ft and a maximum mis-tie of 14 ft.

Reservoir Framework

The stratigraphic and structural framework for the Project AoI was informed by subsurface mapping and interpretations of depth-converted 3D seismic data and well data (**Figure 6** and **Figure 7**). Stratigraphic horizons were mapped using seismic reflectors and/or well-log correlations to characterize the structural geology of the AoI through examinations of reservoir geometries, offset stratigraphic sections, and hydrocarbon occurrence, distribution, and fluid contacts. The stratigraphic framework was validated through mapping of stratigraphic markers identified in the legacy wells in and around the AoI. Faults were mapped and extrapolated into areas outside of seismic coverage using established throw to length ratios. Wells within and surrounding the AoI provide additional stratigraphic controls on the reservoir framework.

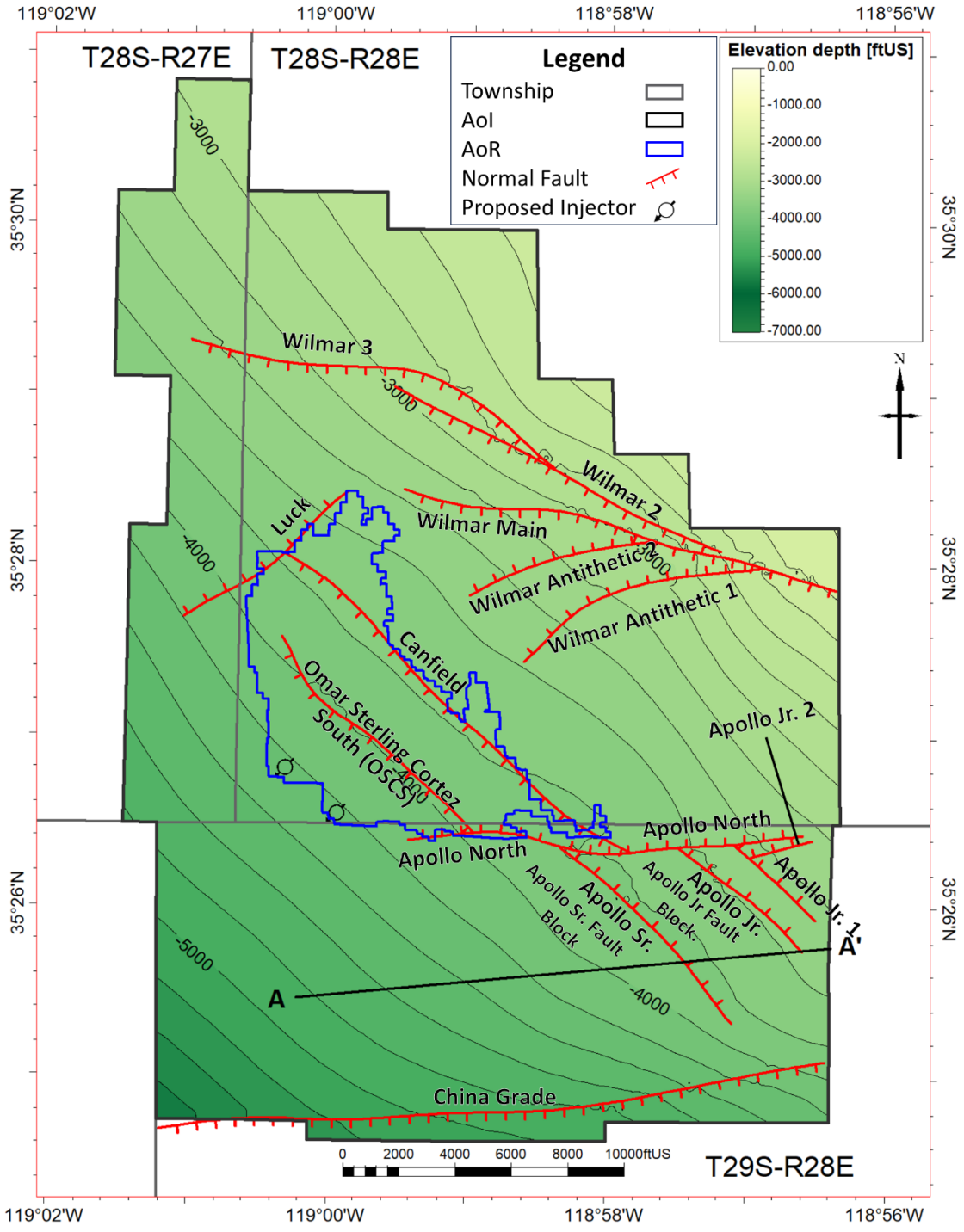

Figure 6. Structural contour map (contour interval 100 ft.) of the 1st Vedder depicting mapped faults within the AoI. Hachures mark the downthrown side of apparent-normal faults.

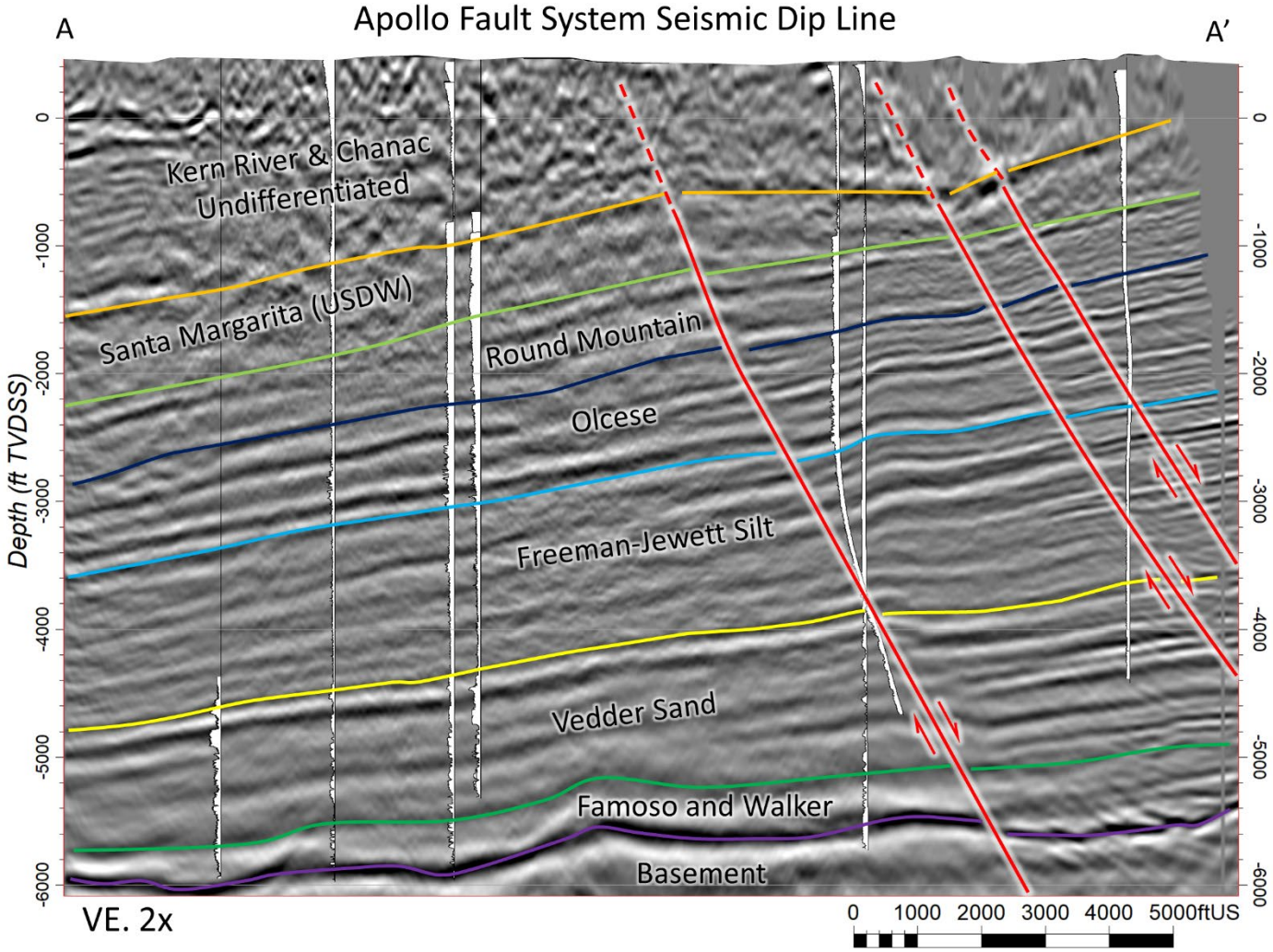

Figure 7. Structural cross section A-A' transecting the southeastern portion of the AoI, showing depth-converted seismic (in ft TVDSS) from ground surface to basement, interpreted stratigraphic horizons, faults, and projections of nearby wells with normalized spontaneous potential (SP) logs (white) that penetrate the Vedder Sand. Cross section line location is shown on **Figure 6.** Cross section is vertically exaggerated by a factor of two (VE:2x).

Structural, geologic, and stratigraphic information was used to develop a full-field reservoir framework for the Vedder Sand in the following manner:

- Stratigraphic and structural architecture established from mappable well-log markers and 3D seismic.
- Continuous reservoir-framework surfaces generated using minimum-curvature interpolators with discrete structural discontinuities (i.e., faults) modeled using structural framework modeling and pillar gridding algorithms.
- Reservoir properties were determined from standard logging suites and calibrated to core data.
- Reservoir heterogeneity calculated from porosity logs and modeled permeability.

Geophysical and borehole datasets and structural-framework models were analyzed and built using Petrel™ (SLB, 2023), a software platform that is widely used in the energy industry to enable visualization and interpretation of seismic and well-log datasets, well-log correlation, and to build and validate three-dimensional reservoir models.

Reservoir properties were determined from standard logging suites (**Geomechanical and Petrophysical Information Section**). The stratigraphic architecture of the Vedder Sand was delineated using multiple cross sections to illustrate lateral and vertical variations in well-log responses. Reservoir heterogeneity was interpreted using the Rock Quality Index (RQI), a petrophysical property calculated from porosity and modeled permeability logs (Amaefule et al., 1993).

Regional Geology, Hydrogeology, and Local Structural Geology [40 CFR 146.82(a)(3)(vi)]

Regional Geologic Setting

The San Joaquin Basin is located within the southern part of the Great Valley Province (Central Valley), a northwest-trending asymmetrical trough that is approximately 450 miles in length and 50-70 miles wide. The Stockton arch, near the City of Stockton, divides the Great Valley province into the Sacramento Basin to the north, and the San Joaquin Basin to the south.

The San Joaquin Basin extends about 220 miles from the Stockton arch to the northern flank of the San Emigdio-Tehachapi Mountains and Transverse Ranges (**Figure 8**). The San Joaquin Basin is bounded on the west by the central Coast Ranges and San Andreas fault zone and on the east by the Sierra Nevada Mountain range.

Because of its importance in energy and groundwater resources, the San Joaquin Basin has a long history of geological studies, many of which have been summarized in a U.S. Geological Survey report on the San Joaquin Basin petroleum system (Hosford Scheirer, 2007). Unless otherwise specified in the section below, geological descriptions are summarized from Dibblee and Chesterman (1953), Addicott (1970), Bartow (1984 and 1991), Bartow and McDougall (1984), Olson et al. (1986), Loomis (1990), Tye et al. (1993), Hewlett et al. (2015), Hewlett and Tye (2015), Hosford Scheirer and Magoon (2007), and Johnson and Graham (2007).

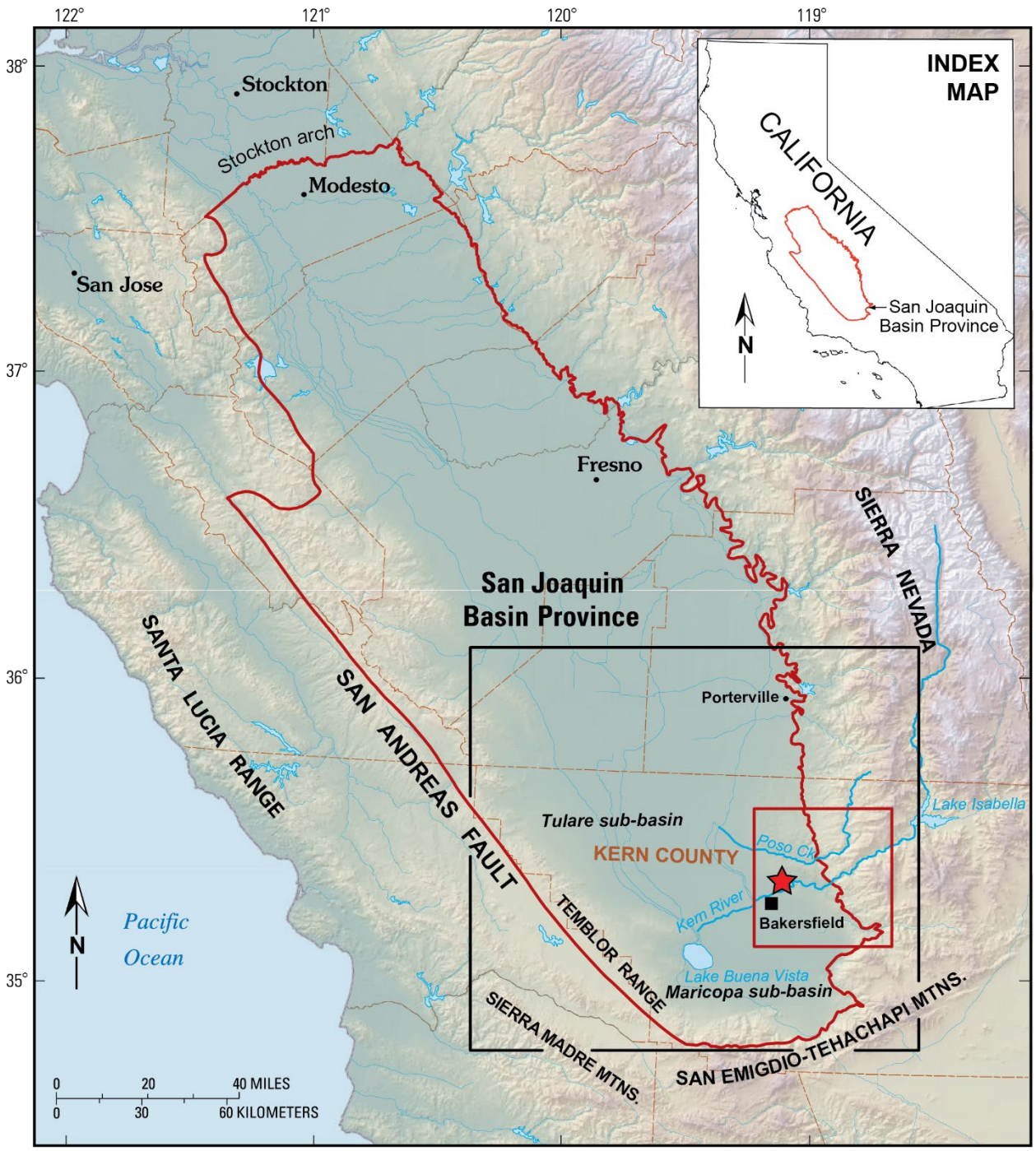

Figure 8. Location of the San Joaquin Basin as defined by the USGS Petroleum Assessment Model (from Lillis and Magoon, 2007). The large black square denotes the approximate location of the regional geologic map on **Figure 9**. The smaller red square denotes the approximate location of the geologic map on **Figure 10**. The red star denotes the location of the Project area.

The Project AoI is along the southeastern flank of the San Joaquin Basin, a northwest-trending synclinorium that evolved from a Mesozoic fore-arc basin into a Cenozoic transpressional successor basin that recorded the tectonic evolution of the region from a Cretaceous-Paleogene forearc basin, Miocene migration of the Mendocino triple junction, and Plio-Pleistocene oblique convergence (e.g., Bartow, 1984; and Hosford Scheirer and Magoon, 2007).

The sedimentary fill of the San Joaquin Basin contains more than 25,000 ft of Mesozoic and Cenozoic siliciclastic and bioclastic detritus (**Figure 9**; Hosford Scheirer and Magoon, 2007). The Bakersfield arch is a west-plunging structural culmination that segments the southern San Joaquin Basin into the northern Tulare sub-basin and southern Maricopa sub-basin.

Cenozoic sedimentation in the San Joaquin Basin records a shift from predominantly forearc-basin sedimentation to a complicated array of transpressional and transtensional basins associated with the development of the San Andreas fault system during Neogene time (Bartow and Nilsen, 1990; Miller and Graham, 2018). During Paleogene time, erosion along the western flank of the ancestral Sierra Nevada delivered clastic detritus to the eastern flank of the southern San Joaquin Basin, forming deltaic depositional systems, such as the Vedder Sand. By late Miocene time, the southern San Joaquin Basin underwent rapid structural changes, with flanking uplifts shedding clastic detritus into the basin as deep-marine turbidite channel-and-lobe systems interfingered with siliceous (diatomaceous) shale of the Monterey Formation and correlative units. During this time, sediments eroded from the Sierra Nevada were laid down as marine deposits of the Santa Margarita Sandstone, marginal-marine and fluvial deposits of the Chanac Formation, and fluvial deposits of the Kern River Formation.

Emergence of the Bakersfield arch exposed much of the Cenozoic stratigraphic section along the eastern edge of the San Joaquin Basin (**Figure 10**). The overall southwest-plunge of the Bakersfield arch forms a 3-6 degree southwest-dipping homocline that has been cut by high-angle normal faults. Outcrops of the Vedder Sand are limited to a narrow band of light-gray, fine-to medium-grained sandstone along the eastern flank of the San Joaquin Basin, where the Vedder Sand has thinned due to erosional truncation by the overlying Jewett Sand of the Freeman–Jewett Silt (Bartow, 1984).

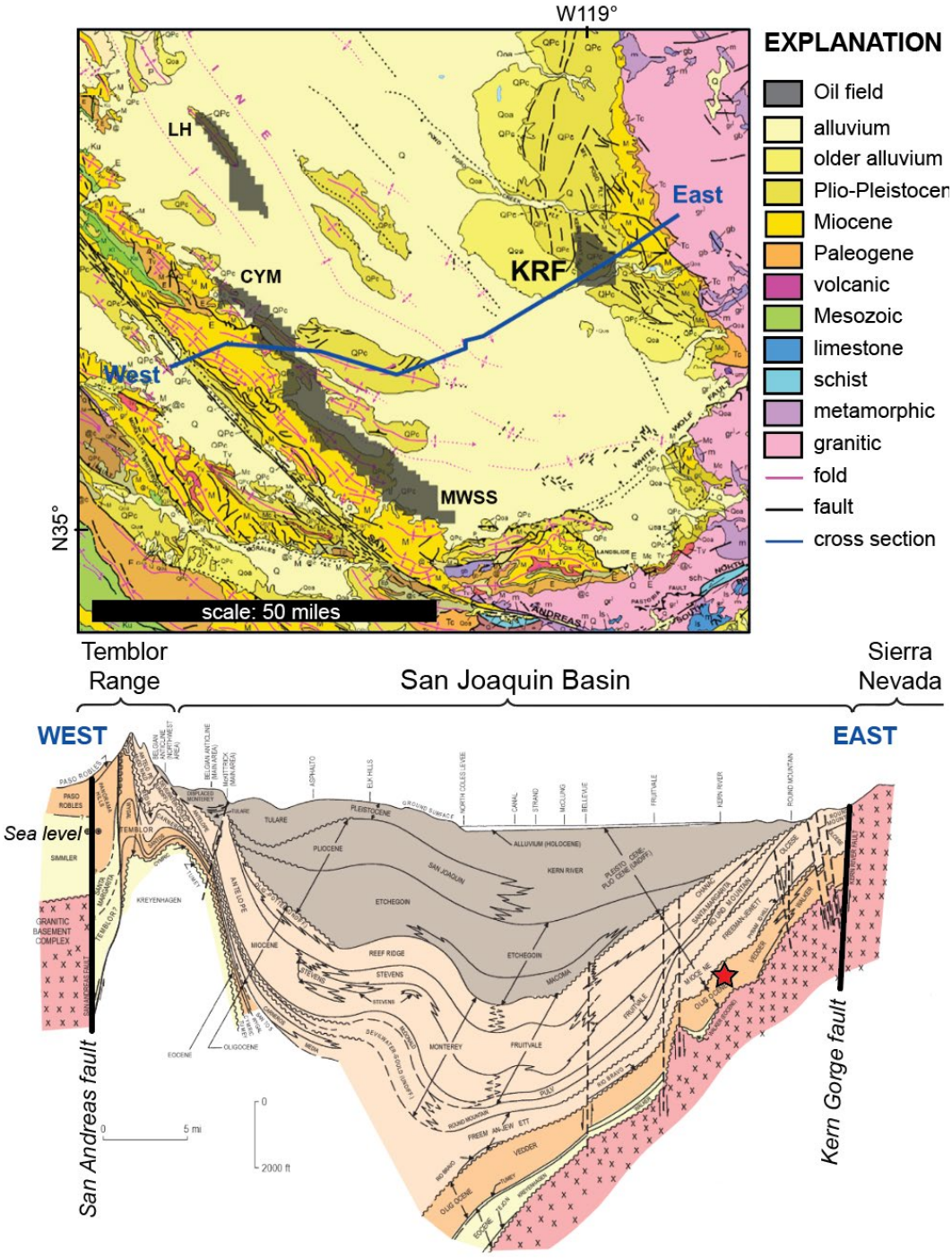

Figure 9. Regional surface geologic map of the southern San Joaquin Basin (*top;* Jennings et al., 2010) and locations major oil fields with Chevron operations, including the Project AoI at Kern River Oil Field. Generalized structural cross section (*bottom,* after DOGGR, 1998) marking location and depth of the Vedder Sand in the Project area (red star).

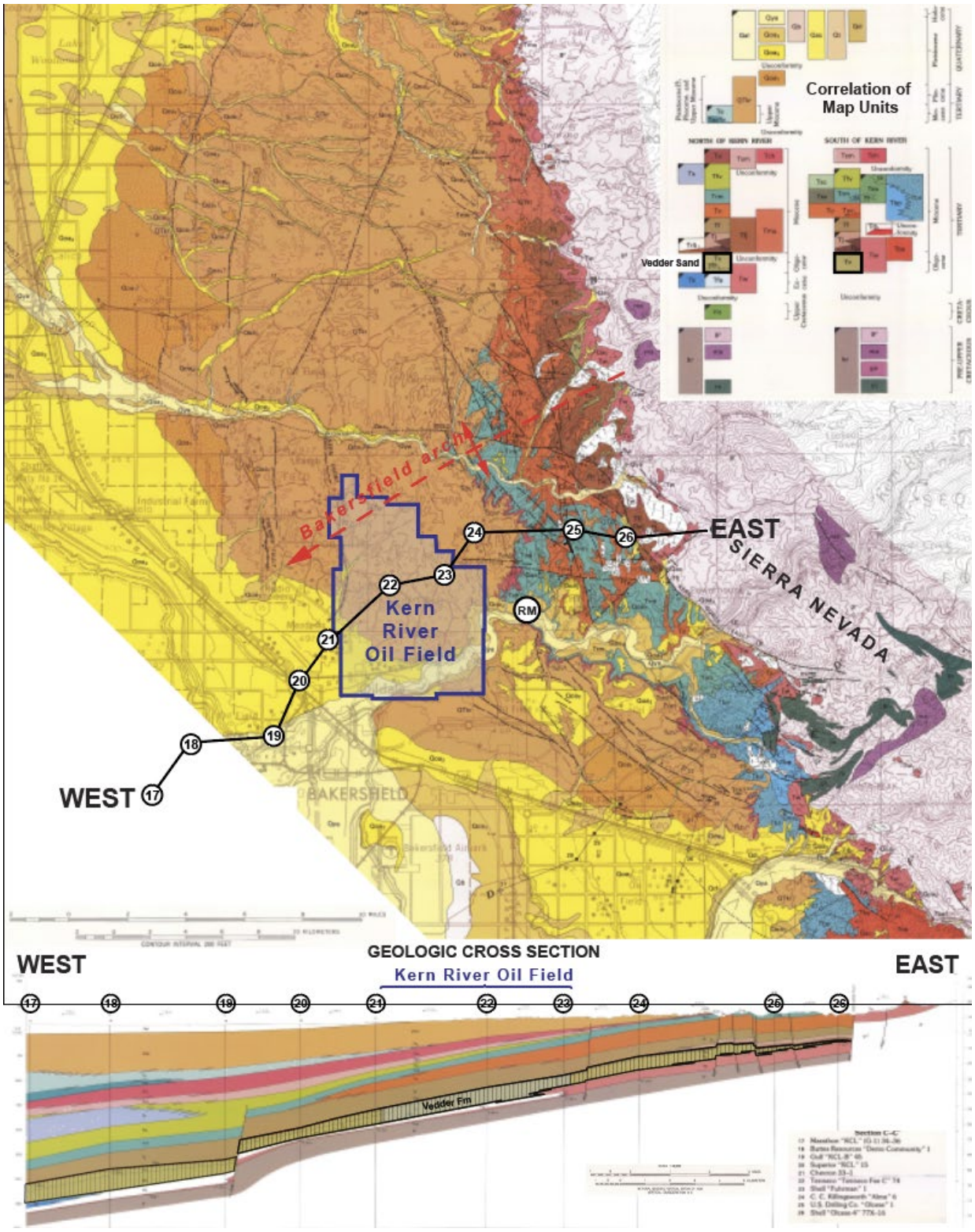

Figure 10. Geologic map and map-unit correlations along the southeastern San Joaquin Basin, including the Bakersfield arch (red dashed line), updip outcrops of the Vedder Sand (Tv), and geologic cross-section line (modified from Bartow, 1984). Numbers denote wells used in cross section. RM marks the location of the ARCO Round Mountain #1 well on the map.

Figure 11 portrays major stratigraphic relationships in the southeastern San Joaquin Basin and a reference stratigraphic column for the Kern River Oil Field, highlighting the stratigraphic units within the Project AoI (Hosford Scheirer and Magoon, 2007; and California Division of Conservation, 1998). This stratigraphic reference section is a composite log that shows resistivity (right) and spontaneous potential (left) logs for key stratigraphic units, primary and secondary confining zones (stratigraphic seals), and key markers denoting the base of USDW and Vedder Sand subunits within the Vedder exempted aquifer. For the purposes of the Project, the China Grade sands, Fruitvale shale, and McVan sand units were not delineated for the Project framework and model.

North of the crest of the Bakersfield arch, the Vedder Sand is part of the 36-23 Ma "Vedder/Temblor Megasequence", which is informally subdivided into third-order sequences of shelf and slope sandstone that include highstand and lowstand systems tracts (see Johnson and Graham, 2007). The "lower Vedder/Vaqueros equivalent" sequence was deposited between 36 Ma and 28-29 Ma, and the "upper Vaqueros/lower Temblor equivalent" sequence was deposited 28-29 Ma to 23 Ma.

The Vedder Sand is over 1,000-ft thick in the Project AoI (**Figure 11**), where it is subdivided into five reservoir intervals that are informally referred to, in descending stratigraphic order, as the 1st Vedder (Vd1), 2nd Vedder (Vd2), 3rd Vedder (Vd3), 4th Vedder (Vd4), and 5th Vedder (Vd5). More than 3,000 ft of stratigraphic section is between the floor of existing Class II Enhanced Oil Recovery (EOR) operations in the Kern River Formation, and the top of the Vedder Sand. Laterally extensive, fine-grained (siltstone, mudstone, and shale) zones within and above the Vedder Sand form multiple stratigraphic seals within the proposed zone of injection and in overlying units. **Figure 12** is a cross section near the crest of the Bakersfield arch and through the Project AoI that highlights the stratigraphic relationships between the Vedder Sand and overlying and underlying units.

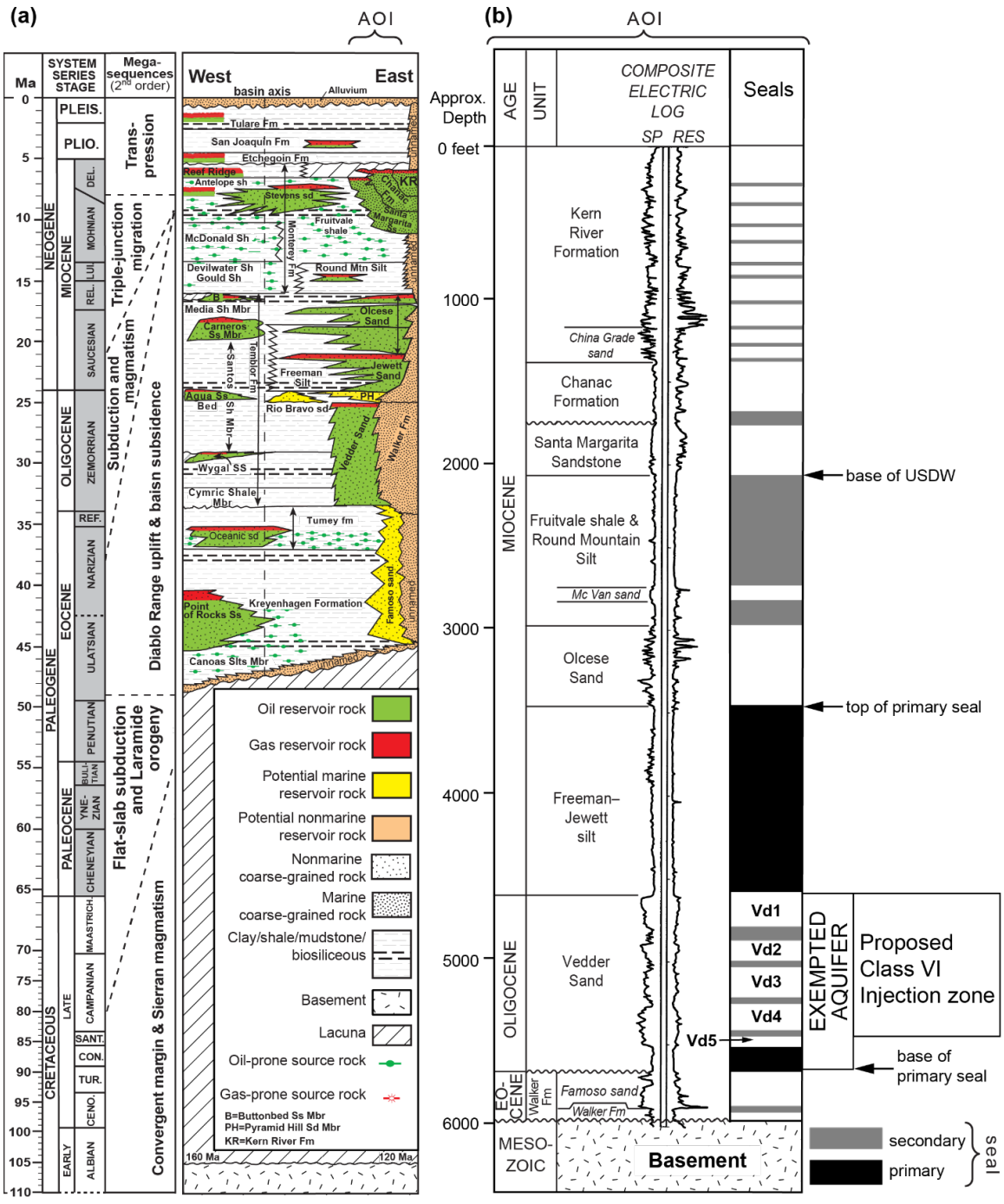

Figure 11. Regional chronostratigraphic column for the southeastern San Joaquin Basin (**a**; Hosford Scheirer and Magoon, 2007) and composite reference log for the Project AoI (**b**; modified from California Division of Conservation, 1998), illustrating the base of USDW, Vedder Sand subunits (Vd1-Vd5), Vedder Sand Exempted Aquifer zone, proposed Class VI injection zone, and primary (dark gray) and secondary (light gray) confining zones (i.e., stratigraphic seals).

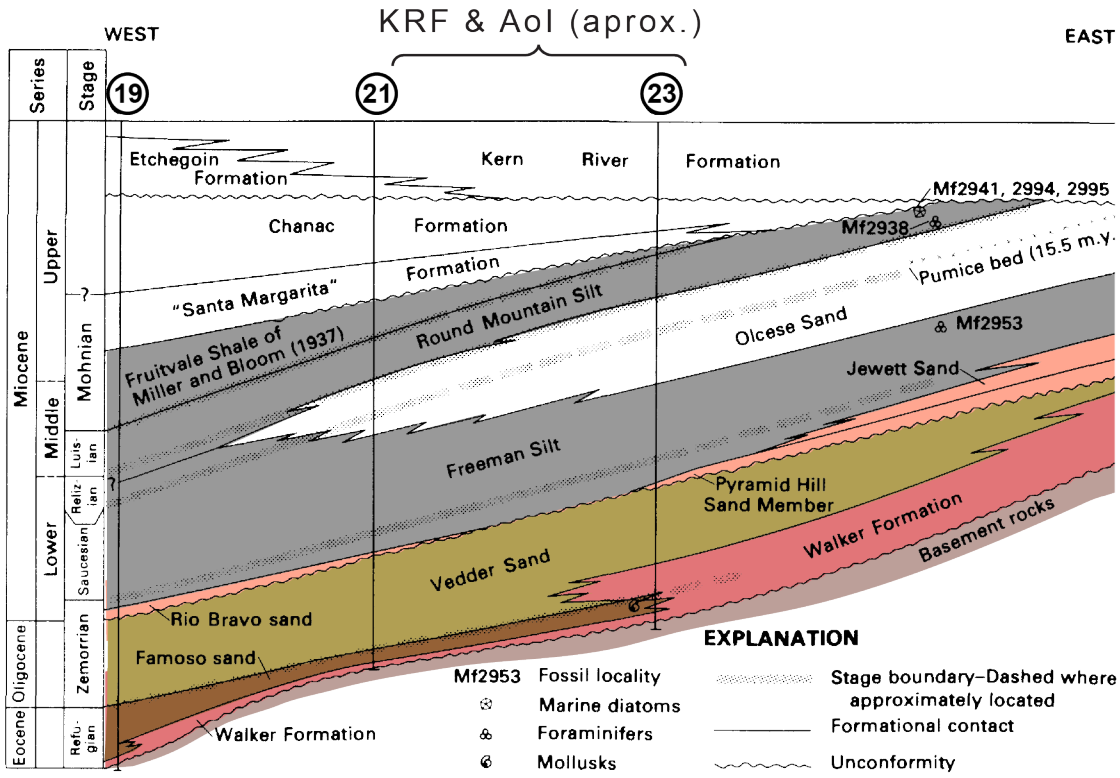

Figure 12. Stratigraphic cross section through the Kern River Oil Field and vicinity, highlighting stratigraphic relationships among the major Cenozoic lithostratigraphic units across the Project AoI (modified from Bartow and McDougall, 1984). Numbers indicate wells shown on **Figure 10.**

The stratigraphic framework of Cenozoic sediments beneath and surrounding the Project AoI are summarized below in ascending stratigraphic order. Although the focus of this report is on the Vedder Sand injection zone and the Freeman–Jewett Silt confining zone, the following summary provides stratigraphic geological context for lithostratigraphic units in or near the Project AoI.

Basement (Mesozoic)

Basement rocks consists of undivided Jurassic metasedimentary rocks and intrusive rocks of the Sierra Nevada (mostly quartz diorite).

Walker Formation and Famoso sand (Eocene to Oligocene)

The Eocene and lower Miocene Walker Formation is a nonmarine succession of arkosic sandstone and shale that nonconformably overlies granitic basement. Both the Walker Formation and Vedder Sand were defined in the Shell Oil Company #1 (API#040291284300) Vedder well (Addicott, 1970; and Olson et al., 1986; and Evans, 2012), where the Walker Formation interfingers with the Vedder Sand. Basinward, the Walker Formation grades into the Famoso sand and is thus, the Famoso sand is considered a member of the Walker Formation. The age of

deposition of the Walker is estimated to be 34-25 Ma based on regional stratigraphic relationships; however, the Walker Formation may be as young as 21 Ma south of the Bakersfield arch (Hosford Scheirer and Magoon, 2007). In outcrops north of the Kern River, the Walker Formation forms a narrow outcrop belt that is unconformably overlain by the Vedder Sand and Freeman–Jewett Silt (Bartow, 1984).

The Eocene (49-33.5 Ma) Famoso sand is locally defined in wells along the eastern side of the southern San Joaquin Basin. The upper part of the Famoso sand grades into, and interfingers with, the lower part of the Walker Formation. North of the Bakersfield arch, the Famoso sand is the marine equivalent of the Walker Formation and part of the Vedder Sand. South of the Bakersfield arch, the upper part of the Walker Formation is equivalent in age to Freeman–Jewett Silt.

Vedder Sand (Oligocene)

The Oligocene Vedder Sand is a seismically defined wedge of fluvial and deltaic deposits along the southeastern margin of the San Joaquin Basin (**Figure 13** and **Figure 14**; Tye et al., 1993). The Vedder Sand was deposited along an east-sloping ramp on the southeastern margin of the San Joaquin Basin, which formed a large marine embayment at the time. The Vedder Sand is interpreted as marine slope, shelf, and deltaic sands that grade basinward into age-equivalent fluvial deposits of the Walker Formation (Bartow and McDougall, 1984). Seismic data shows large-scale stratified bundles in the Vedder. Sequence boundaries and flooding surfaces define parasequence-set stacking patterns and abrupt shifts in depositional environments that permit interwell correlations across the AoI.

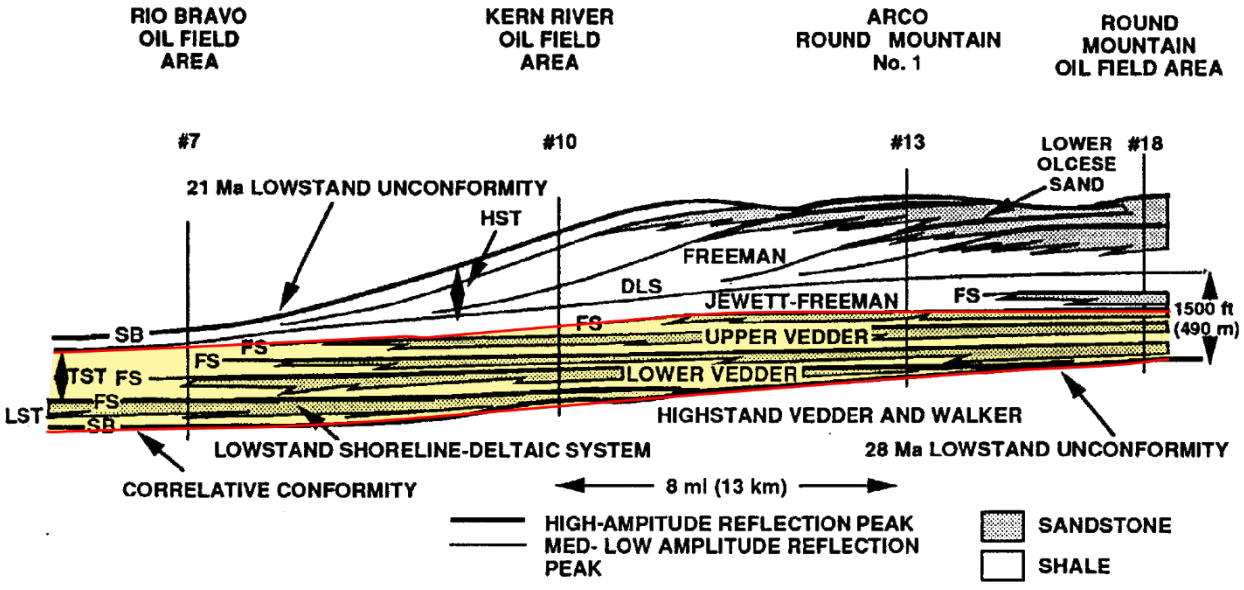

Figure 13. Sequence-stratigraphic framework of Vedder Sand (Tye et al., 1993). Vedder subunits are capped by laterally extensive mudstone and shale zones associated with flooding surfaces that provide excellent chronostratigraphic control for reservoir framework correlation and provide additional intraformational seal potential.

Sparse paleontological data indicate deposition of the Vedder Sand occurred between 33 and 23 Ma, during the Zemorrian micro-faunal stage (Bartow and McDougall, 1984; Hosford Scheirer and Magoon, 2007; and Johnson and Graham, 2007).

The Vedder Sand was named for the Shell Oil Co. #1 Vedder exploration well that encountered 751 ft of quartzose sandstone (Addicott, 1970, in Olson et al., 1986). The Vedder Sand produced oil in numerous fields on the Bakersfield arch and in the southern and northeastern portions of the San Joaquin Basin. Oil trapping mechanisms are predominantly structural (Richardson, 1966; and Condon, 1986).

The thickness of the Vedder Sand ranges from 0-260 ft in outcrop to more than 1246 ft in thickness towards the basin center (Bartow and McDougall, 1984). In outcrop, the Vedder unconformably overlies the Walker Formation, whereas, in the subsurface, the Vedder Sand is the lateral equivalent to the upper part of the Walker Formation (Bartow and McDougall, 1984). The Vedder Sand is unconformably overlain by the Freeman–Jewett Silt north of the Bakersfield arch. South of the Bakersfield arch and west into the basin, the Vedder Sand is partly equivalent to the Freeman–Jewett Silt and Walker Formation (Bartow and McDougall, 1984). In the subsurface, the Famoso sand is recognized between the base of the Vedder Sand and the Walker Formation (**Figure 12**).

Previous studies of the regional sequence-stratigraphic framework of the southern San Joaquin Basin included reports on the stratigraphic and seismic-stratigraphic character of the Vedder Sand (**Figure 14**), which are summarized in Tye et al. (1993), Hewlett et al. (2015), and Hewlett and Tye (2015). Sequence boundaries and flooding surfaces are based on stratal stacking patterns and abrupt shifts in depositional environments (EODs) that define primary and secondary seals within and overlying the Vedder Sand. Incised valley deposits have been reported in the upper part of the Vedder Sand, indicating regression, followed by transgression by the Pyramid Hill Sand Member at around 23 Ma (Tye et al., 1993).

Regionally, the Vedder Sand can be defined by backstepping and onlapping reflections that mark stratigraphic discontinuities identified on wireline logs (**Figure 14**). The Vedder and Jewett sands represent seismically defined parasequence sets that record transgression across a west-sloping ramp on the eastern flank of the San Joaquin Basin (Tye et al., 1993). Based on well-log correlations and seismic interpretations, the Vedder Sand has been subdivided into at least five distinct parasequences that represent progradational episodes of a fluvially dominated delta, each of which are bounded by laterally continuous shaley zones that define marine transgressions.

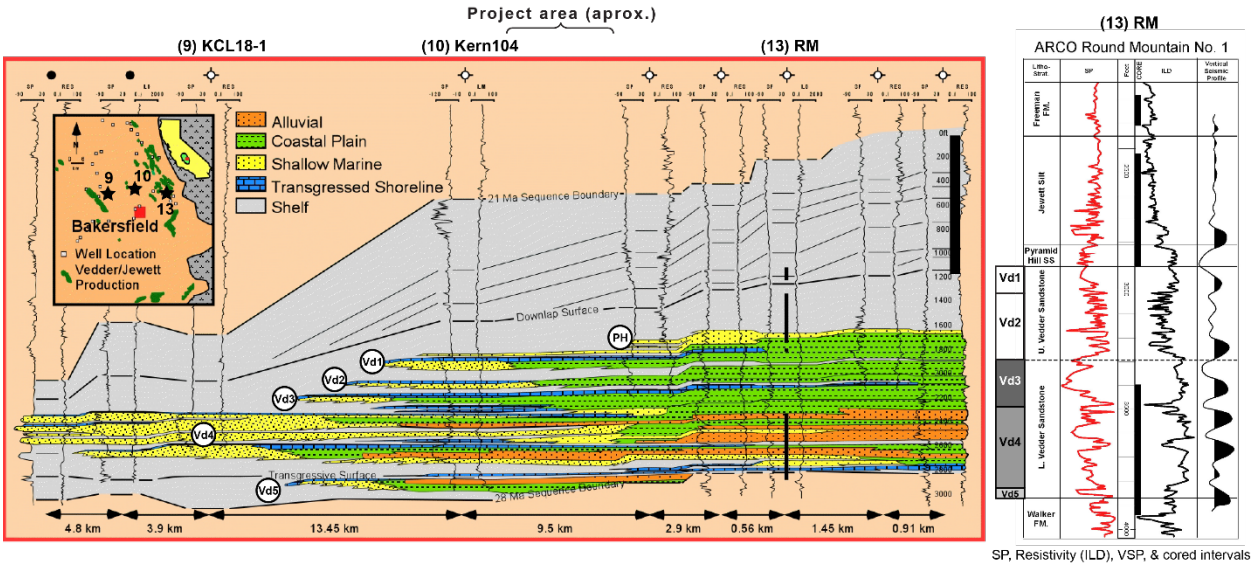

Figure 14. Correlation of the Vedder Sand and Freeman–Jewett Silt based on integration of well-log, core, seismic information, and interpreted environments of deposition (Tye et al., 1993; Hewlett et al., 2015; and Hewlett and Tye, 2015). The ARCO Round Mountain 1 well log illustrates SP, Resistivity (ILD), and vertical seismic profile (VSP) logs, and cored intervals described in Tye et al. (1993) and Hewlett et al. (2015). The thick, vertical black lines on the well log indicates cored intervals in the Round Mountain 1 well.

Tye et al. (1993) integrated well-logs and seismic using the ARCO Round Mountain #1 core, approximately 5 miles east and updip of the Project AoI (**Figure 10**). **Figure 15** illustrates interpreted core in the Vedder Sand and Walker Formation (from Hewlett and Tye, 2015). In this cored interval, Tye and colleagues described five facies associations that correspond with deposition on a marine shelf, shallow-marine (deltaic), estuarine, alluvial/coastal plain, and fluvial settings. A paleosol marks the boundary between the Famoso and Walker units and the overlying Vedder Sand (e.g., Tye et al., 1993).

Available plane-light and ultraviolet light images of Vedder Sand whole core from two (2) wells within the AoI are shown on **Figure 16, Figure 17, Figure 18** and **Figure 19**. These images show that the intraformational seals consist of fine-grained, massive to mottled mudstone that contains a low diversity ichnofauna and scattered shell beds that indicate deposition in a brackish to marine environment (**Figure 16** and **Figure 17)**.

Whole-core images of sandstone show mottling at the top of the 2nd Vedder interval, indicating brackish to marine conditions during deposition (**Figure 18** and **Figure 19**). The core contains oyster shell fragments and scattered black detritus that suggests the presence of carbonaceous sediment associated with deltaic depositional environments. The downward decrease in bioturbation and presence of faint cross bedding suggests the presence of channels associated with distributary drainage.

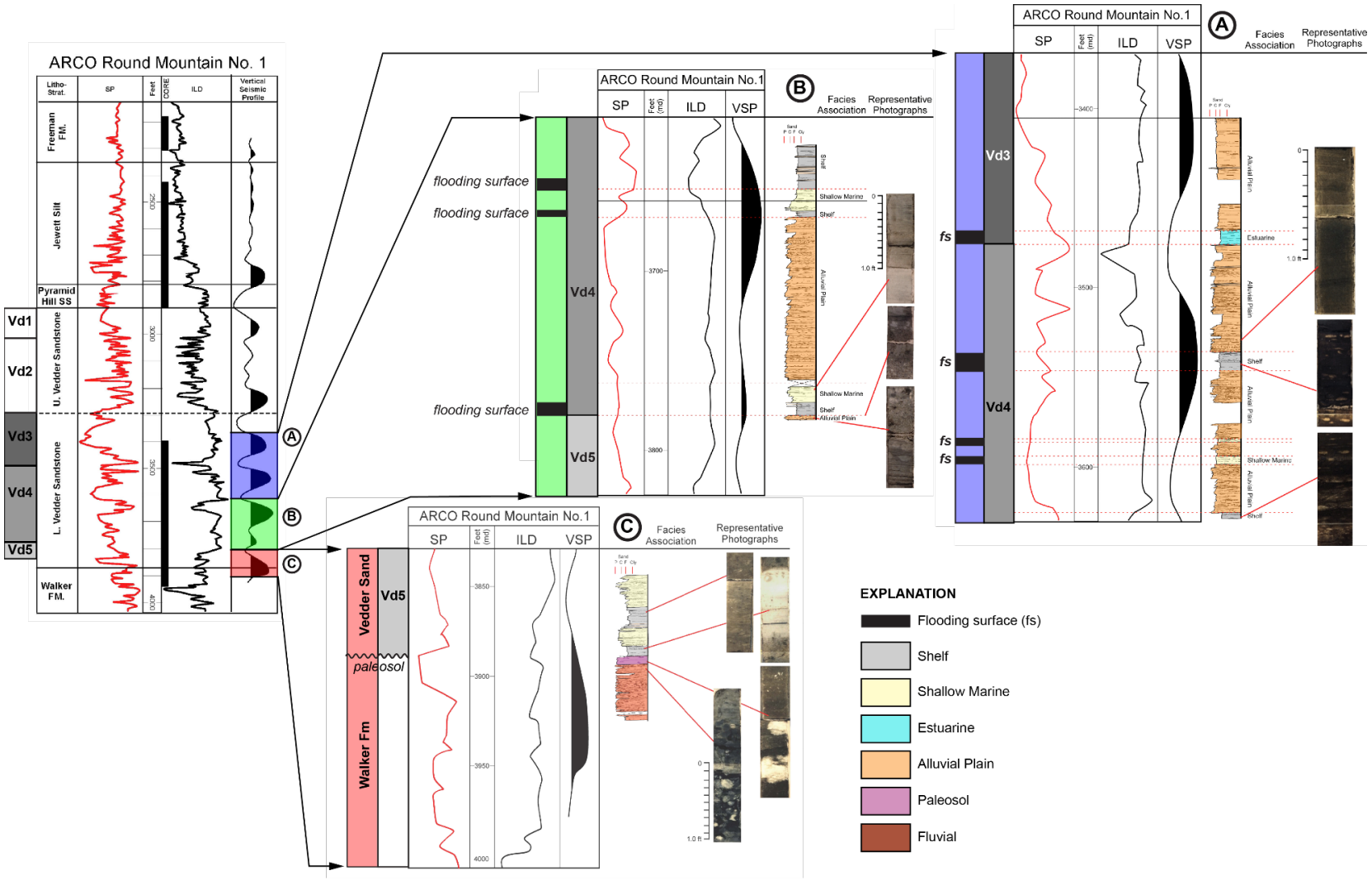

Figure 15. ARCO Round Mountain #1 logs of SP, Resistivity (ILD), and Vertical Seismic Profile (VSP), core interpretations and facies associations, and core photographs (Hewlett and Tye, 2015).

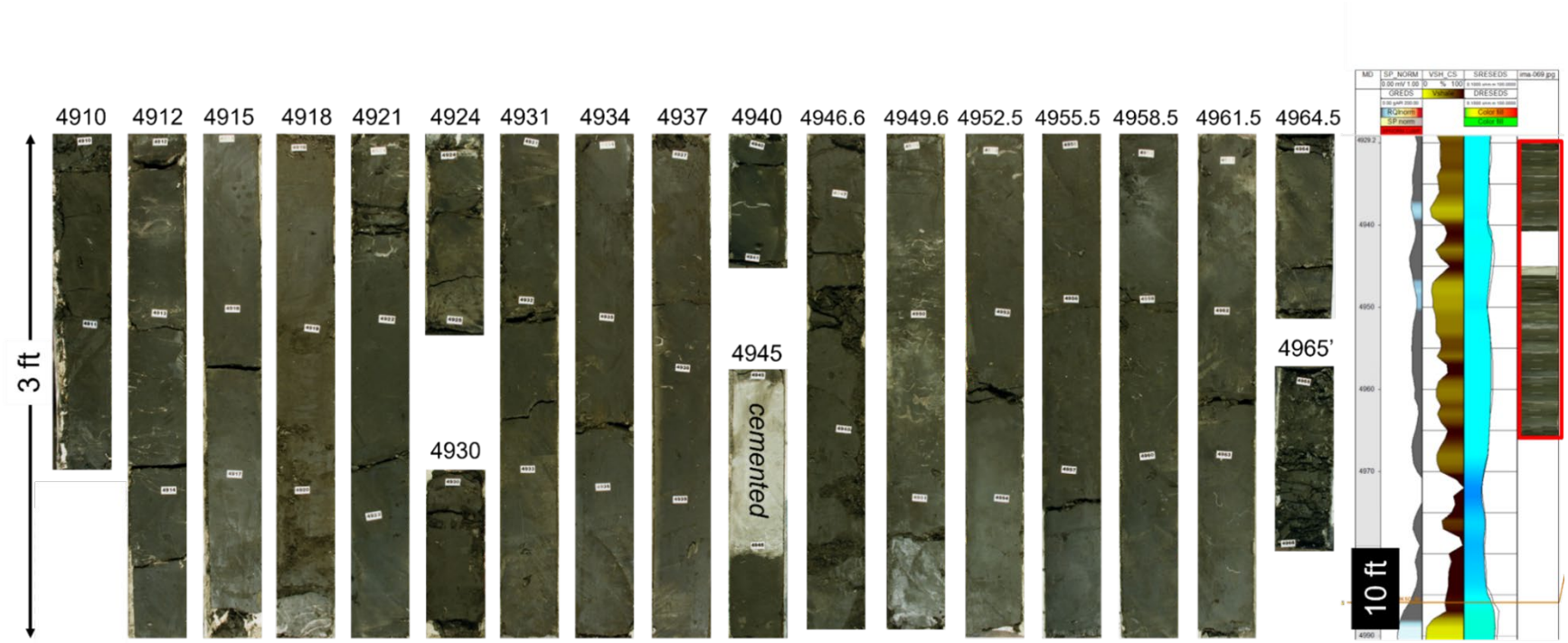

Figure 16. Whole-core (plane-light) photographs of a secondary confining zone capping Vd2 in the SOVWD-1 well (API 040297837600) (see **Figure 5** and **Figure 60** for well location). Numbers at the top of each image denote the measured depth (in ft) for the top of each 3-ft long core segment. Well-log (*right*) shows well-log responses of SP, GR, Vshale, and Resistivity and core images (from left to right).

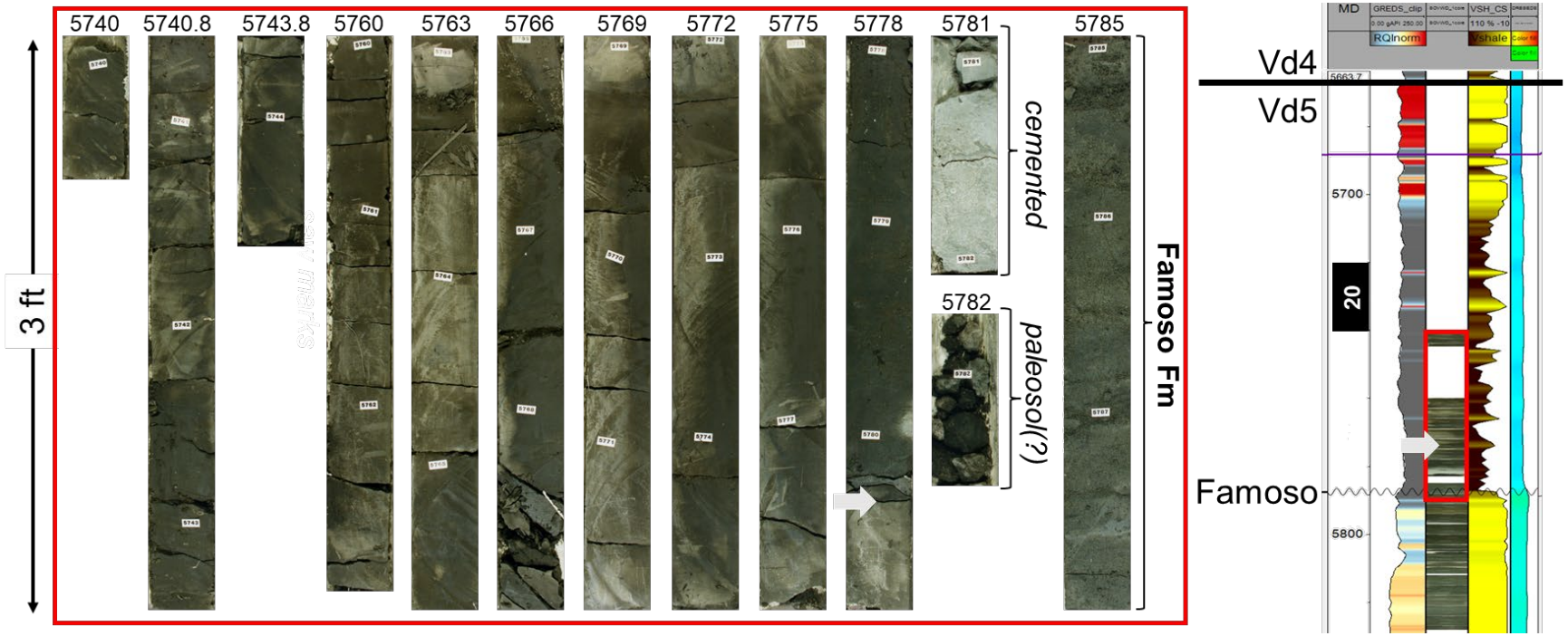

Figure 17. Whole-core (plane-light) photographs of a lower confining zone and top of Famoso sand in the SOVWD-1 well (API 040297837600) (see **Figure 5** and **Figure 60** for well location). Numbers at the top of each image denote the measured depth (in ft) for the top of each 3-ft long core segment. Well-log (*right*) shows well-log responses of GR, core images, Vshale, and Resistivity (from left to right).

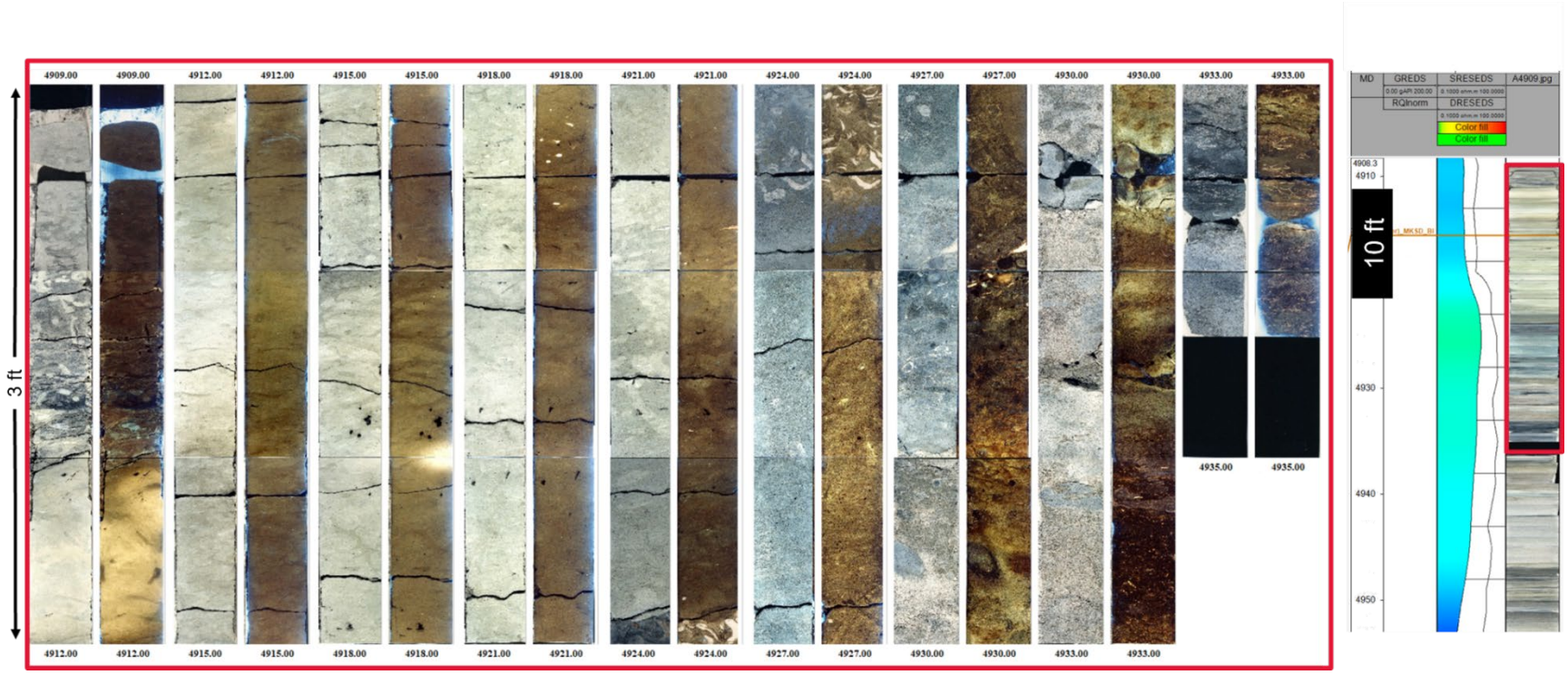

Figure 18. Whole-core photographic pairs, in plane (*left*) and ultraviolet (*right*) light, illustrating reservoir-quality sandstone in parts of the 1st and 2nd Vedder Sand (Vd1 and Vd2) from well S4_WDV2 (API 040298201900) (see **Figure 5** and **Figure 60** for well location). Numbers at the top of each image denote the measured depth (in ft) for the top of each 3-ft long core segment. Well-logs show resistivity responses in the cored interval.

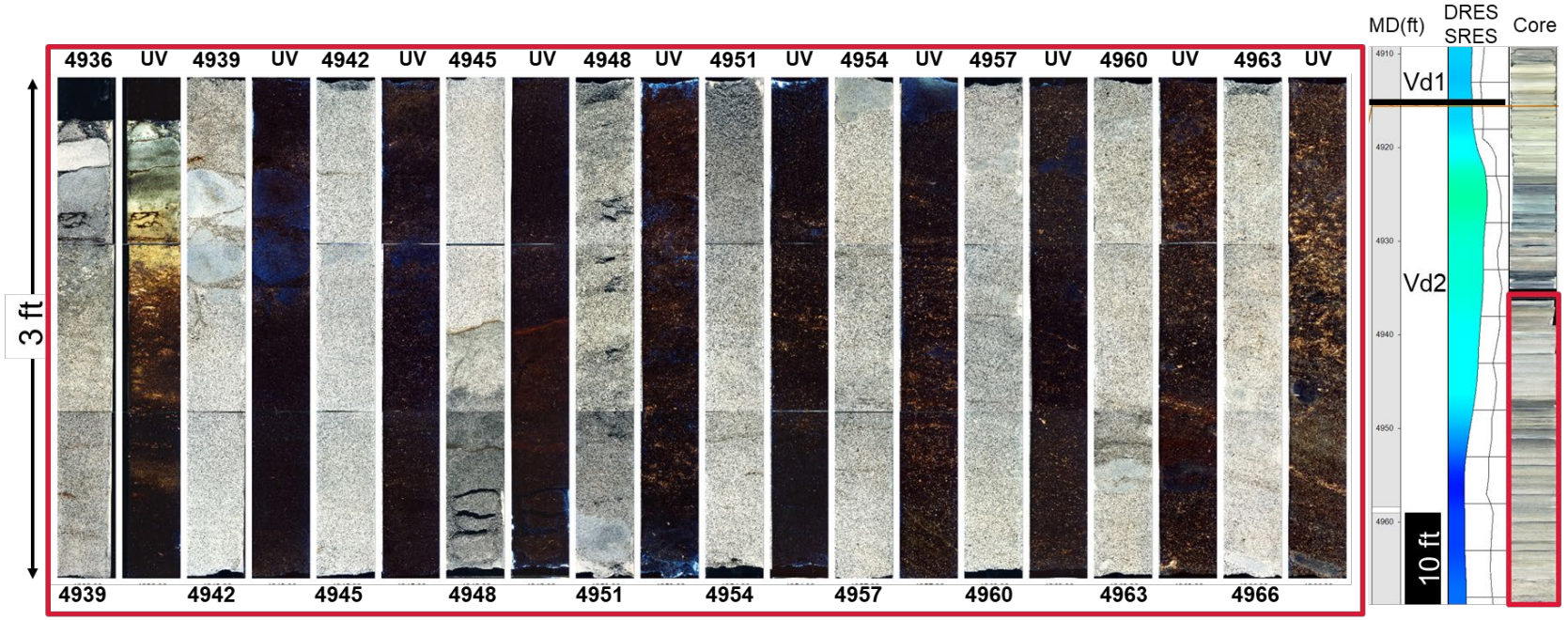

Figure 19. Downhole continuation of whole-core photographic pairs, in plane (*left*) and ultraviolet (*right*) light, illustrating reservoir-quality sandstone in parts of the 2nd Vedder Sand (Vd2) from well S4_WDV2 (API 040298201900). Numbers at the top of each image denote the measured depth (in ft) for the top of each 3-ft long core segment. Well-logs show resistivity responses in the cored interval. (see **Figure 5** and **Figure 60** for well location).

Pyramid Hill Sand and Freeman–Jewett Silt (upper Oligocene to lower Miocene)

The 25-19 Ma Freeman–Jewett Silt is a group of Oligo-Miocene units that are considered an eastern equivalent of the Temblor Formation (e.g., Hosford Scheirer and Magoon, 2007). In ascending stratigraphic order, the Freeman–Jewett Silt consists of the basal Pyramid Hill Sand Member, Jewett Sand, and Freeman Silt. Regionally, the Pyramid Hill and Freeman–Jewett Silt (FJ) units have an aggregate thickness of more than 1,000 ft. Within the AoI, the Freeman-Jewett Silt is dominantly fine-grained, with the dominant lithofacies being marine silt and shale (**Figure 10, Figure 11, Figure 12, and Figure 13**).

The Oligocene (25-24 Ma) Pyramid Hill Sand is a member of the Oligo-Miocene Jewett Sand, which is part of the Freeman–Jewett Silt. The Pyramid Hill Sand member is interpreted to be a basal transgressive sandstone associated with the base of the Freeman–Jewett Silt (Tye et al., 1993). Regionally, the Pyramid Hill Sand consists of grayish-brown, fossiliferous, poorly sorted, coarse-grained sandstone containing subangular quartz grains and black chert pebbles with local bentonitic and thin calcareous sandstone beds that unconformably overlies mudstone of the Vedder Sand (Addicott, 1970).

The Oligocene Rio Bravo sand is an informal unit that is either a local equivalent to, or slightly older than, shelfal deposits of the Pyramid Hill Sand. The Rio Bravo sand is not identified in well logs in the AoI, where it would occupy a similar stratigraphic position as the Pyramid Hill Sand. Thus, for the purposes of this study, the Rio Bravo sand has not been differentiated from the Freeman–Jewett Silt.

The Jewett Sand is nearly 260 ft thick at a measured section northeast of Project AoI (Olson et al., 1986), where it is a massive, buff white-green, silty sandstone with reddish-brown spherical concretions. The Jewett Sand thins and pinches out towards the Project AoI, and the sand-prone facies described in more easterly sections is not present in the AoR (see **Figure 10** and **Figure 12**). Time equivalent silts and shales comprise the Jewett Sands in the AoI and are not distinguished here from the overlying Freeman Silt.

The Freeman Silt conformably overlies and is interbedded with the Jewett sandstone (Bartow and McDougall, 1984). The Freeman Silt is nearly 240 ft thick in a nearby measured outcrop section northeast of the AoI, where it consists of white-gray, friable siltstone, sandy siltstone, and clayey shale (Olson et al., 1986). The Freeman Silt thickness westward in the subsurface, where it is more fine-grained in composition. Benthic foraminifera in the Freeman Silt have been interpreted to represent deposition in shallow to bathyal water depths of 500 ft to more than 1,500 ft near the Project area (Bartow and McDougall, 1984).

Within the project AoI, the undifferentiated “Freeman Silt” is a laterally continuous, seal-prone, sand-poor geobody with an average gross thickness of 1,140’, forming a continuous upper confining zone across the Project AoI and AoR (**Figure 12** and **Figure 34**).

Olcese Sand (lower Miocene)

The mostly marine conditions of many Miocene lithostratigraphic units along the southeastern flank of the San Joaquin Basin was punctuated by an episode of fluvial deposition in the Olcese Sand that was followed by a resumption of marine deposition. The Miocene (21-16.5 Ma) Olcese Sand is restricted to the southeastern flank of the basin where it is dominantly medium- to coarse-grained sandstone that reaches a thickness of about 1,180 ft in the nearby Round Mountain Field (Bartow and McDougall, 1984). Regionally, the Olcese Sand ranges in depth from 2,300 ft to 8,900 ft. The Olcese Sand grades basinward into the upper part of the Freeman Silt and the overlying Round Mountain Silt.

The upper and lower members of the Olcese Sand record deposition in a tidally influenced nearshore environment (Olson et al., 1986). The central unit is nonmarine (fluvial). The lower part of the Olcese Sand consists of thinly bedded to blocky, white, siltstone and sandstone with sandstone and pumice pebbles (Bent, 1985). Facies associations indicate mid-shelf depositional environments and a tidally influenced inner shelf area, nearshore environment. The middle part of the Olcese Sand consists of cobble conglomerate, sandstone and siltstone associated with deposition of a braided river system (Olson et al., 1986). The middle nonmarine part of the Olcese Sand transitions upwards into the overlying shallow-marine upper Olcese Sand, which contains conglomeratic beds, sandstone, and siltstone associated with lower to upper shoreface deposition.

Round Mountain Silt and Fruitvale shale (middle Miocene)

The Miocene (16-13.5 Ma) Round Mountain Silt conformably overlies the Olcese Sand, which forms a laterally extensive stratigraphic seal (**Figure 11** and **Figure 12**). The Round Mountain Silt recorded deposition in an inner shelf environment and has been subdivided into a lower siltstone unit, a middle diatomite unit, and an upper siltstone unit. Paleowater depths of the Round Mountain Silt are interpreted to have been between 400 ft and near sea level in the intertidal zone. The presence of diatomite indicates deposition in anoxic open-marine conditions. The upper siltstone disconformably overlies a middle diatomite-bearing unit that recorded deposition in a marine middle to outer shelf environment.

The McVan sand is an informal unit that has been described within the Round Mountain Silt north of Kern River Oil Field (Addicott, 1970). The McVan sand has locally been delineated within the AoI. The McVan sand is completely encased within the Round Mountain Silt and is included within the Round Mountain Silt (**Figure 11**).

The Fruitvale shale of Miller and Bloom (1937) is an informal member of the deep-marine Monterey Formation. The Fruitvale shale conformably overlies the Round Mountain Silt and is unconformably overlain by the Santa Margarita Sandstone (Bartow and McDougall, 1984; and Hosford Scheirer and Magoon, 2007). The Fruitvale shale has not been subdivided within the Kern River Oil Field and for the purposes of this report, the Fruitvale has been grouped with the Round Mountain Silt and McVan sand.

Santa Margarita Sandstone (upper Miocene)

The Miocene (11-6.5 Ma) Santa Margarita Sandstone unconformably overlies the Fruitvale shale and Round Mountain Silt (**Figure 11**). The Santa Margarita Sandstone consists of gray to white, coarse-grained sandstone and silty shale interbeds that onlap older units toward the eastern flank of the basin (Kodl et al., 1990; **Figure 12**). The Santa Margarita Sandstone mostly consists of coarsening-upward successions of sandstone that is interspersed with silt and shale that thins to the east across the Project AoI.

Chanac Formation (upper Miocene)

The 9-6 Ma Chanac Formation unconformably overlies the Santa Margarita Sandstone and is unconformably overlain by the Kern River Formation (**Figure 11** and **Figure 12**). The Chanac Formation is mostly a nonmarine fine- to coarse-grained sandstone with interbedded mudstone that grades basinward into marine sandstone and siliceous shale. The Chanac Formation has hydrocarbon accumulations in various locations in the Kern River Oil Field and is a hydrocarbon producer in the adjacent Kern Front Field, located west of Kern River Oil Field.

Kern River Formation (upper Miocene to Pliocene)

The Miocene Kern River Formation is a fluvial deposit that interfingers with marine deposits of the Etchegoin Formation to the west (**Figure 11**). The Kern River Formation contains interbedded sandstone, conglomerate, and mudstone (Olson et al., 1986). The Kern River Formation was originally considered a Plio-Pleistocene unit (Graham et al., 1988). Radioisotopic dating of a volcanic ash within the Kern River Formation indicates a late Miocene age (Baron et al., 2008), which indicates that the lower part of the Etchegoin Formation is Miocene in age.

The Kern River Formation is the youngest oil-producing reservoir along the eastern flank of the San Joaquin Basin. China Grade sands on **Figure 11** refers to zones assigned to R-series reservoirs (Kodl et al., 1990).

Pliocene and Quaternary deposits

Regionally, the Pliocene Etchegoin Formation overlies the Chanac Formation and Santa Margarita Sandstone, and the San Joaquin Formation overlies the Etchegoin Formation (**Figure 11 and Figure 12**). These Plio-Pleistocene formations represent a transition from dominantly deep-marine, nearshore, and brackish-water environments to prevailing nonmarine conditions that are represented by the Tulare Formation. The San Joaquin and Tulare formations are not recognized in the Project AoI. The Etchegoin interfingers with the Kern Formation in the Kern Front Oil Field, located west of the Project AoI (Edwards, 1941) and pinches out along the western side of Kern River Oil Field.

The modern Kern River enters the San Joaquin Basin through a deeply incised canyon at the western end of the Kern River Gorge, where the namesake river incised a broad valley (e.g., Davis et al., 1959). The Kern River valley contains river terraces underlain by coarse-grained pebble to boulder alluvium associated with former courses of the Kern River (Bartow, 1984; and Bedrossian et al., 2014).

Except for deposits associated with the modern Kern River Valley, the Project area is partly covered by thin, discontinuous veneers of locally derived poorly consolidated deposits of conglomerate, alluvial and fluvial sand, silt, and clay, overlain by Holocene alluvium.

Vedder Sand Environments of Deposition

Conceptual depositional models provide a way to integrate well-log and seismic data into a three-dimensional framework that can be used to estimate spatial relationships, reservoir architectures, connectivity, and heterogeneity trends in the Vedder Sand. Conceptual models of the major EODs can be used to populate petrophysical properties and define lithological trends in reservoir models.

Paleogeographic reconstructions indicate that deposition of the Vedder Sand was associated with deltaic deposition along a relatively narrow shelf within a marine embayment that widened over 9-10 million years (m.y.) (**Figure 20**). The presence of a relatively narrow shelf and somewhat restricted embayment that likely had limited tidal influence on Vedder deposition.

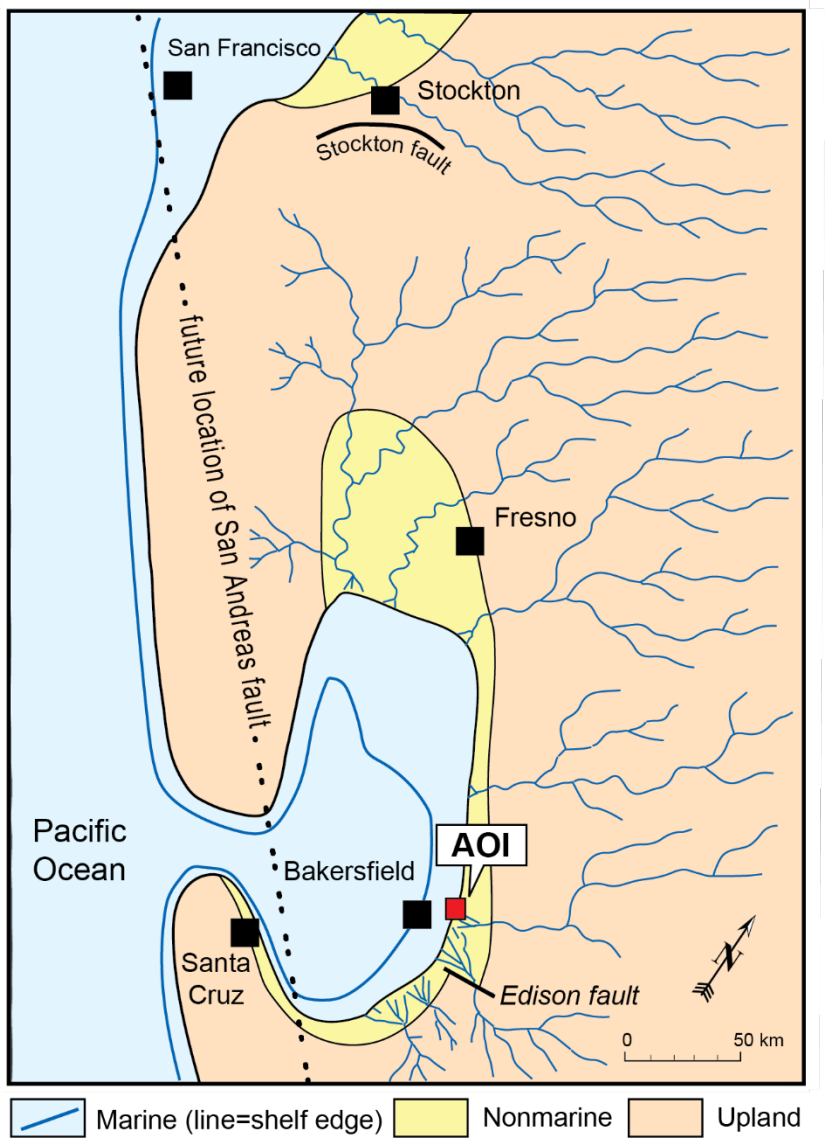

Figure 20. Paleogeographic map of California during Oligocene time (*ca.* 30 Ma), illustrating the distribution of nonmarine sediments, including the Vedder Sand, along the periphery of the San Joaquin Basin (modified from Bartow, 1991). The approximate location of the AoI is denoted by the red square.

The Vedder Sand has been interpreted as shelfal mudstones and shoreface sandstone (**Figure 21;** Tye et al., 1993). Multiple facies associations are interpreted in the Vedder Sand, ranging from deposition in shallow-marine, deltaic/coastal plain, and fluvial settings that include incised valleys, amalgamated fluvial channel-belts associated with braided river systems, tidally influenced distributary channels and distributary mouthbars, and shoreface and marine sediments.

Vertical seismic resolution within the project area is about 100 ft; however, interpretation of legacy well data and previously published paleogeographic reconstructions identified facies associations of parasequence-sets that were defined by widespread horizons that have been interpreted to represent flooding surfaces that separate the Vedder Sand into subunits that can be further subdivided into depositional facies, which are summarized on **Table 3** and **Figure 22.**

Fluvial deposits were identified in wells as sand-rich packages defined by sharp bases and sharp to gradational tops with low GR and low SP responses Vertical log trends are commonly blocky to upward fining, that grade vertically into floodplain siltstone or are unconformably overlain by other fluvial channel belts. Fluvial channel-belts can be locally subdivided into a lower sand-dominated package of cross-stratified sandstone and pebbly sandstone that grades upward into finer-grained, massive to laminated sandstone. Locally thin upward coarsening sandbodies are interpreted as crevasse splays. Fluvial deposits are recognized in Vd4 and Vd5.

Distributary channels were identified in wells as sand-rich packages defined by sharp bases and sharp tops with low GR and SP log responses. Vertical log trends within these packages are commonly blocky to upward fining. These deposits typically overly or are or updip of mouth-bar and proximal delta-front facies associations and are found in Vd2 and Vd3.

Mouth-bars were identified as low GR and low SP log responses and contain sand-packages with an upwards-coarsening profile and sharp top. Well-log character is dominantly homogeneous, with minimal log serration. Sharp tops associated with these packages are commonly associated with overlying distributary channels and are interpreted to reflect subsequent incision of the mouth-bar in Vd2 and Vd3.

Proximal delta-front deposits are identified as exhibiting strongly upward-coarsening packages with upwards-decreasing serrated well-log character. Bases typically have moderate-to-high sand content that are commonly expressed as moderate GR and SP log responses but exhibiting clear serration in the log signature. Well-log serration decreases upwards and becomes increasingly blocky and sand rich. This upwards decrease in serration is interpreted to reflect progradation of a delta-front deposit dominated by waning sediment gravity flows. These deposits are commonly directly overlying and up-dip of associated distal delta front deposits. These features are recognized in Vd2 and Vd5.

Distal delta-front deposits typically exhibit strongly upward-coarsening log responses with a highly serrated well-log character. Packages are typically sand-poor (moderate GR and SP) at the base and increase upwards to moderate sand content (moderate to low GR and SP). Well-log serration is high and consistent from base to top, reflecting high vertical heterogeneity. These deposits are interpreted to reflect the distal component of a basinward-prograding delta front, where deposition is dominated by interbedded sandstones and siltstones deposited by waning sediment gravity flows. These features are recognized in Vd2, Vd4, and Vd5.

Sand-prone delta/coastal plain and incised valley deposits exhibit thick, blocky, sand-rich packages of low GR and low SP with sharp bases and tops. Thicknesses of blocky packages are thicker than distributary channel packages and commonly occur in sets that are amalgamated and locally separated by high GR and high SP shale-rich interbeds. Amalgamated sandstone packages have variable thickness. Incised valley deposits are associated with river incision into the coastal plain leaving a generally thicker accumulation of coarse-grained fluvial sediment. A likely incised valley deposit has been identified in Vd1. The local occurrence of siltstone and mudstone is interpreted to reflect channelization within a sand-rich coastal plain in Vd1 and Vd3.

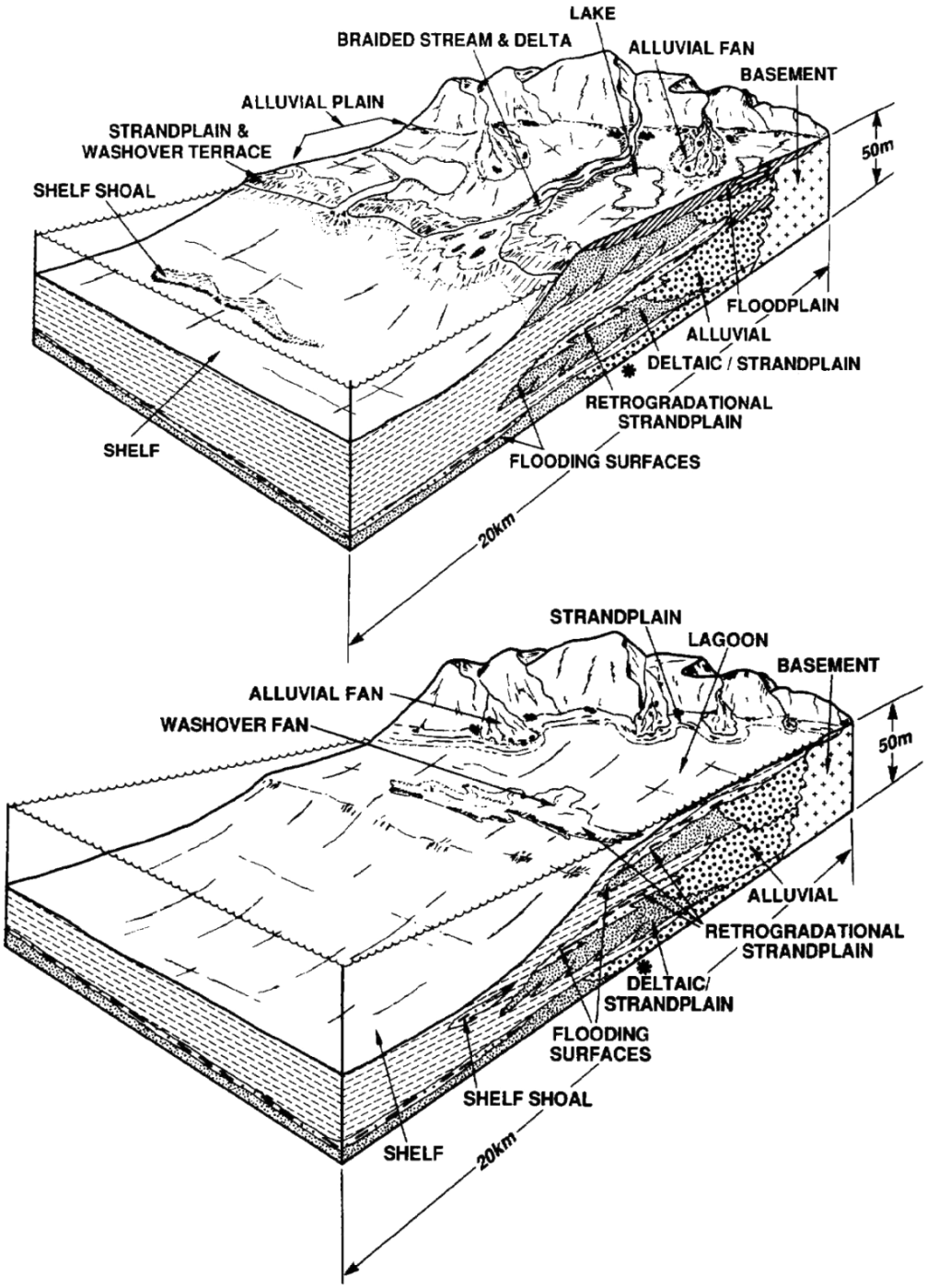

Figure 21. Environments of deposition interpreted for the Vedder Sand during progradational (*top*) and retrogradational (*bottom*) phases (Tye et al., 1993).

Table 3. Dominant facies associations in the Vedder Sand.

Facies association	Log character	Internal facies	Reservoir quality	Connectivity / Heterogeneity
Fluvial channel-belt	Sharp base & top	Dominantly clean sand	High	High connectivity Low heterogeneity
Distributary channel	Blocky & sharp base	Dominantly clean sand	High	High connectivity Low heterogeneity
Proximal delta front	Strong upward-coarsening; slightly serrated	Higher proportion of clean sand; interbedded think shaly sand & shale	Moderate to variable	Moderate connectivity High-to-moderate heterogeneity
Distal delta front	Strong upward-coarsening; highly serrated	Interbedded shaley sand & local clean sand	Low to variable	Low connectivity High heterogeneity
Delta/Coastal plain	Blocky; upward-fining; discontinuous	Clean sand & silty interbeds	High	Moderate connectivity High heterogeneity
Incised Valley	Blocky amalgamated sand	Dominantly clean sand	High	High connectivity Low heterogeneity
Marine mudstone	High GR & Low Resistivity	Massive	None	Confining zone

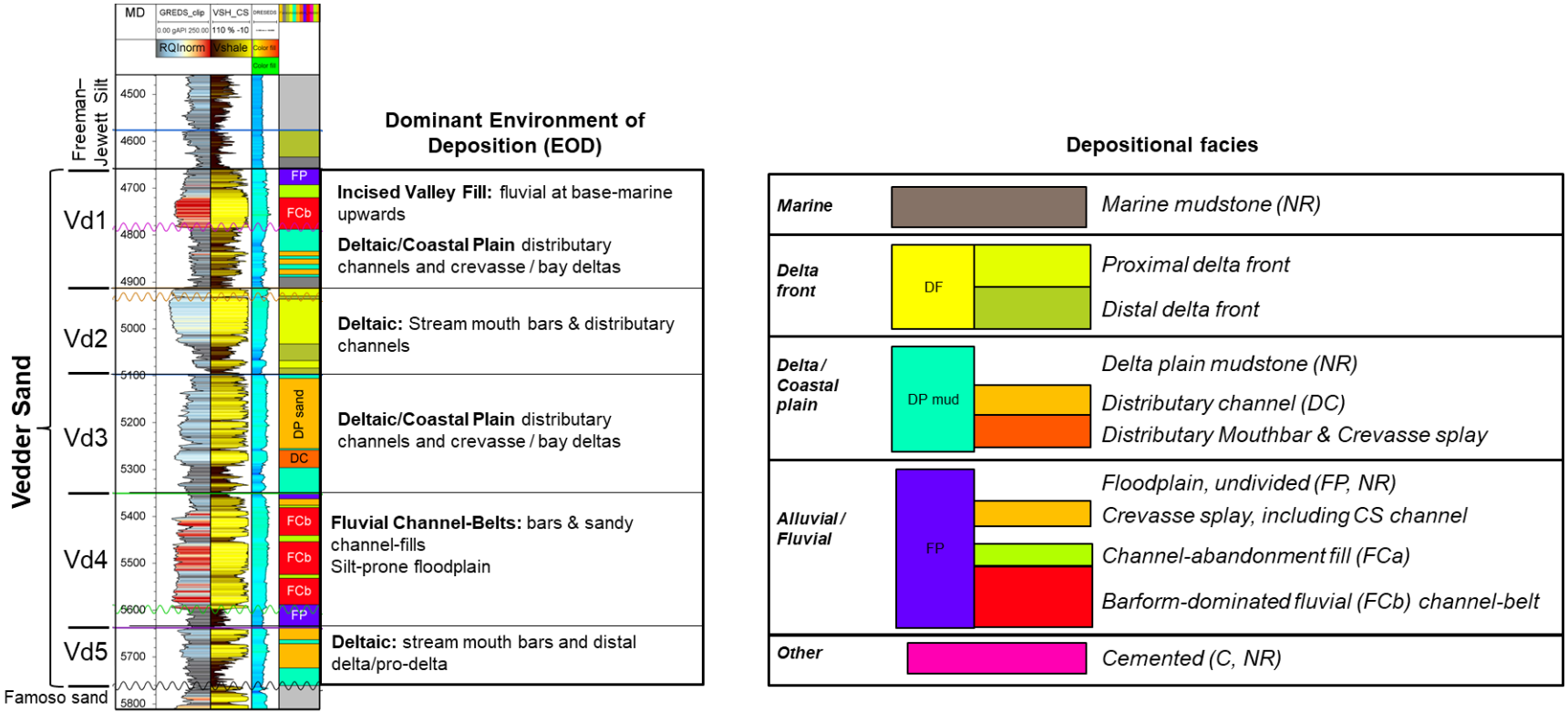

Figure 22. Depositional facies and dominant EODs of the Vedder Sand.

Regional Hydrogeologic Setting

The Project AoI is within the Kern County part of the Tulare Lake Hydrologic Region of the San Joaquin Valley Groundwater Basin (California Department of Water Resources, 2020). The Tulare Lake Hydrologic region encompasses approximately 17,000 square miles of the southern San Joaquin Valley, a structurally complicated endorheic groundwater basin where much of the water resources are consumed by agricultural activities. Groundwater recharge is limited to streams that drain the flanking ranges and terminate into ephemeral lakes in the southern San Joaquin Valley. The Kings River and Kern River originate in glaciated headwaters of the Sierra Nevada, whereas the southern and western ranges are more arid. The region is arid to semi-arid, with a mean annual temperature of 65.4° F and annual rainfall of less than 6 inches on the valley floor to more than 10-15 inches on the foothills of the Sierra Nevada (NRCS, 2007).

Within the Kern County Sub-Basin of the San Joaquin Groundwater Basin, sediments that comprise the shallow to intermediate depth water-bearing deposits in the groundwater subbasin are primarily continental deposits of Tertiary and Quaternary age. In descending stratigraphic order, youngest to oldest, include the younger alluvium and coeval flood basin deposits, older alluvium/stream deposits, the Kern River formation, and the Santa Margarita and Olcese Sands (California Department of Water Resources, 2003). The Olcese and Santa Margarita Formations are current or potential sources of drinking water only in the northeastern portion of the subbasin where they occur as confined aquifers (California Department of Water Resources, 2003). Importantly, in the AoI, the Santa Margarita represents the base of USDW (see "Hydrologic and Hydrogeologic Information [40 CFR 146.82(a)(3)(vi),146.82(a)(5)]").

Local Structural Geology

Cenozoic sedimentation in the San Joaquin Basin records a shift from predominantly forearc-basin sedimentation to a complicated array of transpressional and transtensional basins associated with the development of the San Andreas fault system during Neogene time (Bartow and Nilsen, 1990; Miller and Graham, 2018). During Paleogene time, erosion along the western flank of the ancestral Sierra Nevada delivered clastic detritus to the eastern flank of the southern San Joaquin Basin, forming deltaic depositional systems within the region and the AoI, such as the Vedder Sand. By late Miocene time, the southern San Joaquin Basin underwent rapid structural changes, with flanking uplifts shedding clastic detritus into the basin as deep-marine turbidite channel-and-lobe systems interfingered with siliceous (diatomaceous) shale of the Monterey Formation and correlative units. During this time, sediments eroded from the Sierra Nevada were laid down as marine deposits of the Santa Margarita Sandstone, marginal-marine and fluvial deposits of the Chanac Formation, and fluvial deposits of the Kern River Formation within the AOI.

The Project AoI is near the crest of the Bakersfield arch, a broad southwest-plunging anticlinal feature on the eastern side of the southern San Joaquin Basin (e.g., Sheehan, 1986). The maximum extent of this structural arch extends approximately 55 miles from around the City of Porterville towards the northwestern flank of the Tehachapi Mountains. The Bakersfield arch plunges about 20 miles to the west, where it separates the southern San Joaquin Basin into a northern Tulare sub-basin and a southern Maricopa sub-basin (e.g., Saleeby and Saleeby, 2019). Although the location of the Bakersfield arch approximately coincides with the locations of pinchouts of early Cenozoic lithostratigraphic units, such as the Eocene Kreyenhagen Formation (not described in this report), the main structural expression of this archhas been interpreted to have formed during Quaternary uplift and deformation (Saleeby and Saleeby, 2019).

Emergence of the Bakersfield arch exposed much of the Cenozoic stratigraphic section along the eastern edge of the San Joaquin Basin (**Figure 10**) (Bartow, 1984). Outcrops of the Vedder Sand are limited to a narrow band of light-gray, fine-to medium-grained sandstone along the eastern flank of the San Joaquin Basin northeast of the AoI, where the Vedder Sand has thinned due to erosional truncation by the overlying Jewett Sand of the Freeman–Jewett Silt (Bartow, 1984). The southwest-plunge of the Bakersfield arch forms a 3-6 degree southwest-dipping homocline, interrupted by high-angle normal faults which have been the primary trapping mechanism for Vedder oil accumulations in the eastern San Joaquin basin and in the AoI.

Deposits on the Bakersfield arch are cut by high-angle normal faults that are interpreted to have been active since Miocene time (Saleeby et al., 2013a and 2013b). Faults in this region of the San Joaquin Basin exhibit dominantly normal separation, although some faults likely have normal-oblique displacement. Regional studies indicate that faulting largely occurred after middle Miocene time (Saleeby et al., 2013a & b). Within the AoI, apparent-normal faults with both easterly and westerly dip are well-documented. Faults have been the primary trapping mechanism for light oil accumulations within the AoI.

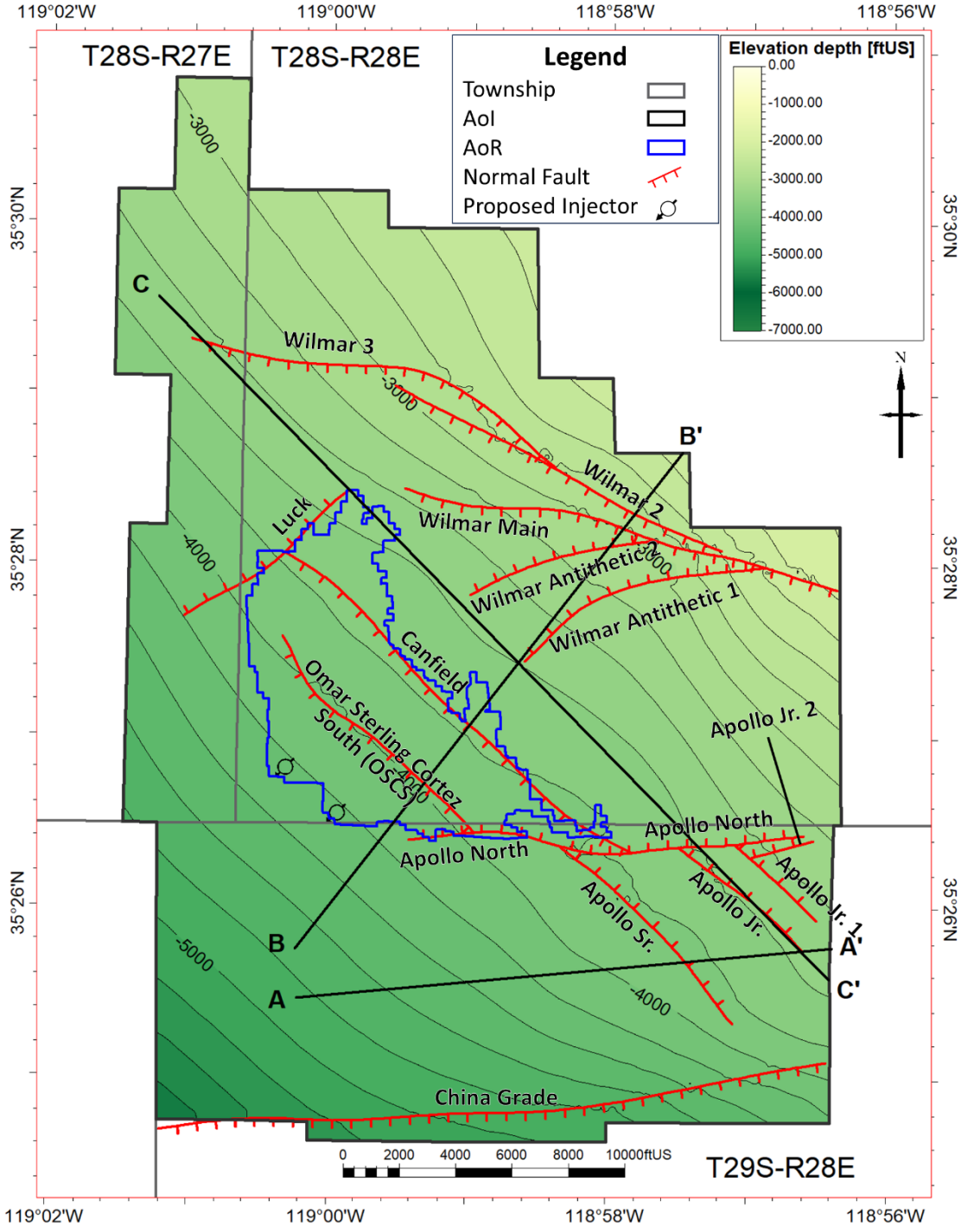

Figure 23. Structural contour map at top Vedder Sand depicting mapped faults. The contour interval is 200 ft, and hachures mark the downthrown side of fault traces.

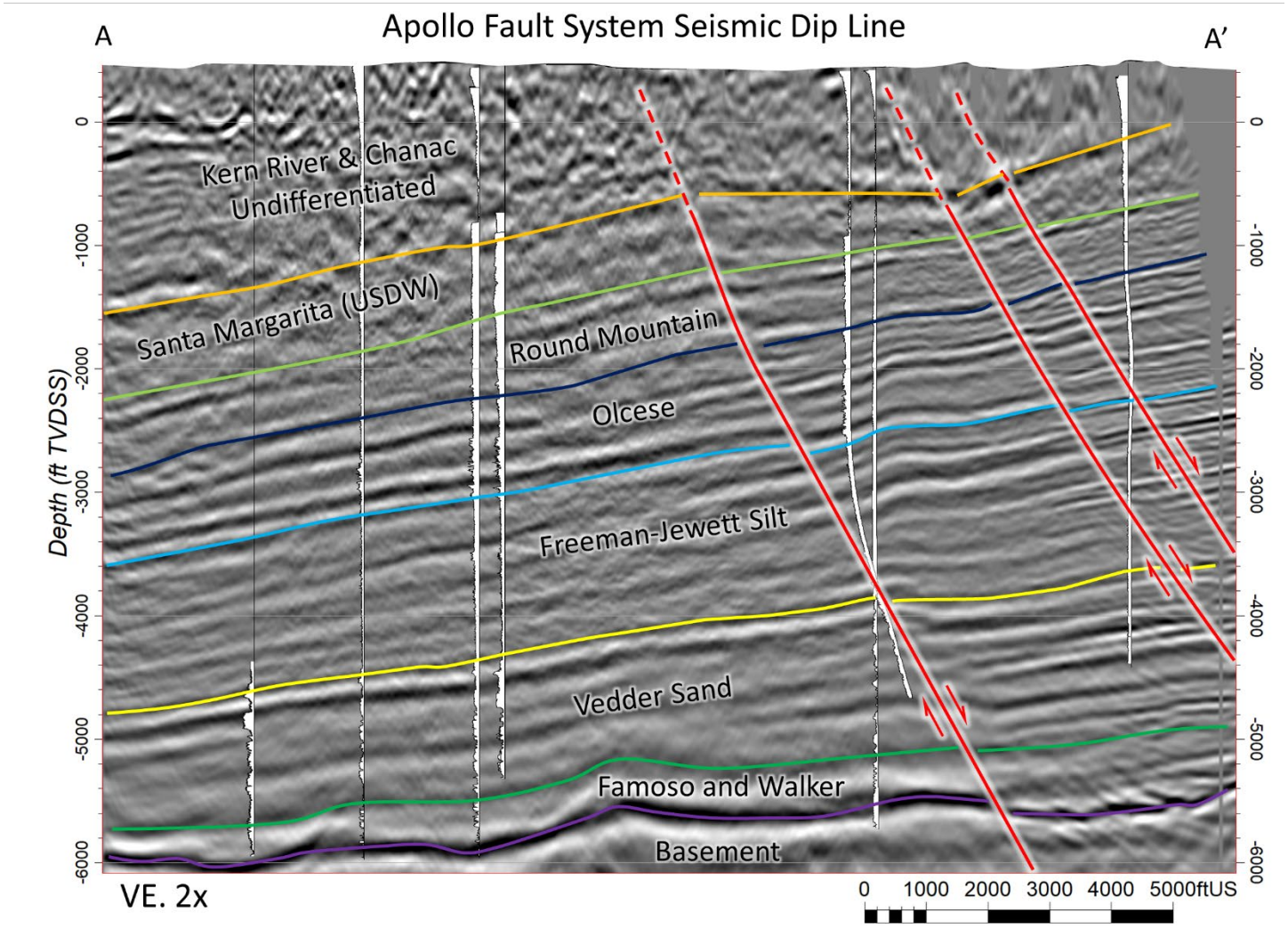

Figure 24. Cross section A-A'. Geologic cross section shows depth-converted seismic (in ft TVDSS), interpreted horizons and faults, as well as projections of nearby wells with normalized SP logs. Cross section is vertically exaggerated by a factor of two (VE:2x). See **Figure 23** for location.

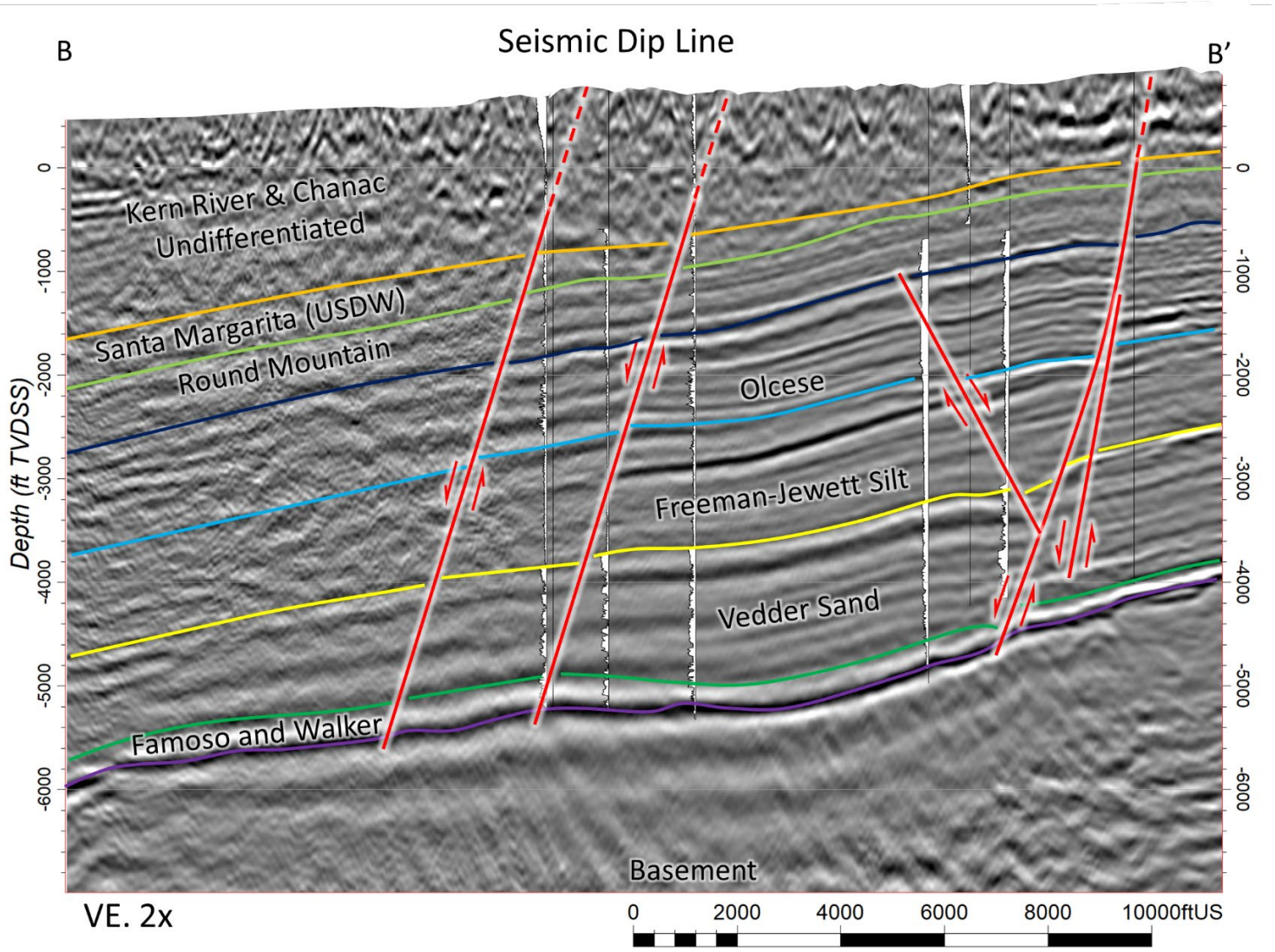

Figure 25. Cross section B-B'. Geologic cross section shows depth-converted seismic (in ft TVDSS), interpreted horizons and faults, as well as projections of nearby wells with normalized SP logs. Cross section is vertically exaggerated by a factor of two (VE:2x). See **Figure 23** for location.

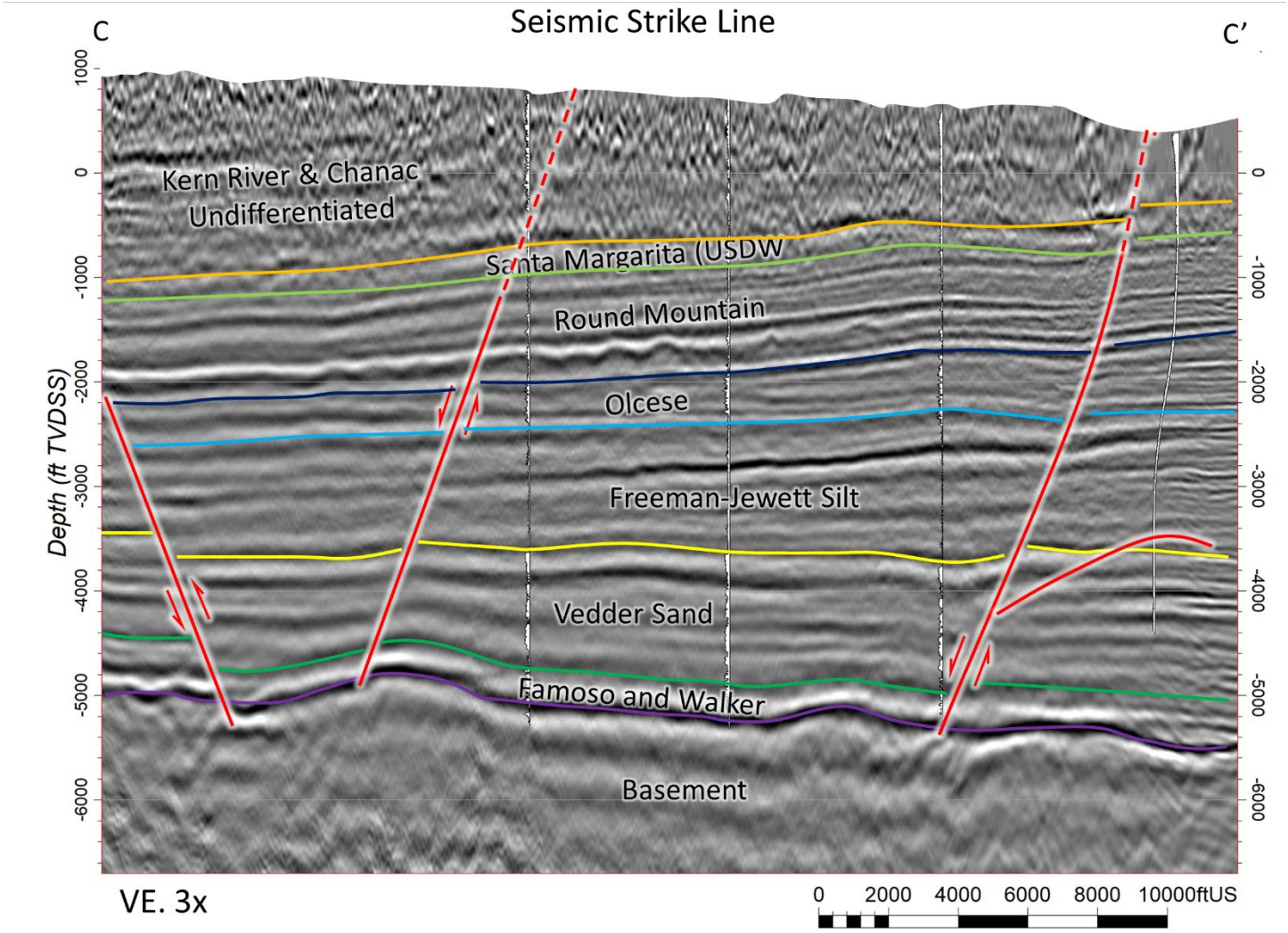

Figure 26. Cross section C-C'. Geologic cross section shows depth-converted seismic (in ft TVDSS), interpreted horizons and faults, as well as projections of nearby wells with normalized SP logs. Cross section is vertically exaggerated by a factor of two (VE:2x). See **Figure 23** for location.

The upper and lower boundaries of the proposed injection zone are defined by laterally extensive fine-grained confining zones that have been delineated on well logs. The Freeman–Jewett Silt is recognized on well logs across the southeastern San Joaquin Basin (**Figure 11** and **Figure 12**) and represents the upper confining zone for the Vedder Sand.

Structural cross sections and the associated location map are shown on **Figure 23, Figure 24, Figure 25,** and **Figure 26**. Structural surfaces for the Freeman–Jewett Silt, Vedder Sand, and Famoso sand are shown on **Figure 27, Figure 28, Figure 29, Figure 30, Figure 31, Figure 32,** and **Figure 33**. These structural surfaces are used to define isochore thickness for the upper confining zone, injection zone, and subunits of the Vedder Sand that are shown on **Figure 34, Figure 35, Figure 36, Figure 37, Figure 38, Figure 39,** and **Figure 40**. Slight thickness variations near mapped faults are largely due to juxtaposition of the stratigraphy across moderately dipping normal faults, yielding apparent "missing section".

The Freeman–Jewett Silt is laterally continuous across the region and has mean thickness of ~1,140 ft within the AoI with a mean thickness of ~1,180 ft in the AoR (**Figure 34**). Thickness variations along fault trends are due to structural juxtapositions that locally decrease apparent thickness across normal faults.

Figure 41, Figure 42, Figure 43, and **Figure 44** are cross-sections and the associated location map showing interwell correlations of these structural surfaces.

Mapped faults have maximum throws of 380 ft, which are approximately one-third of the average thickness of the Freeman–Jewett Silt caprock seal; therefore, the Freeman–Jewett Silt is considered a continuous sealing element for the injection zone within the Project AoI. In addition to the presence of a thick and continuous caprock seal provided by the Freeman–Jewett Silt, numerous secondary seals occur within, above, and below the Vedder Sand; these improve overall containment and enable subdivision of the Vedder Sand (**Figure 28** through **Figure 32**) and internal thickness measurements (**Figure 36** through **Figure 40**). The base of the 5th Vedder Sand (Vd5) is defined by a fine-grained unit that serves as the bottom seal for the Vedder Sand.

The Round Mountain Silt contains thick (600 ft), laterally continuous, fine-grained siltstone and shale intervals that also function as vertical seals. Intraformational seals have been interpreted as marine flooding surfaces (e.g., Tye et al., 1993), which support additional secondary sealing capabilities within the injection zone.

The distribution of sand porosity and permeability are shown by average property maps on **Figure 45, Figure 46, Figure 47,** and **Figure 48**. These maps show an overall westerly trend in porosity and permeability that generally corresponds to paleogeographic reconstructions and original depositional trends in the Vedder Sand.

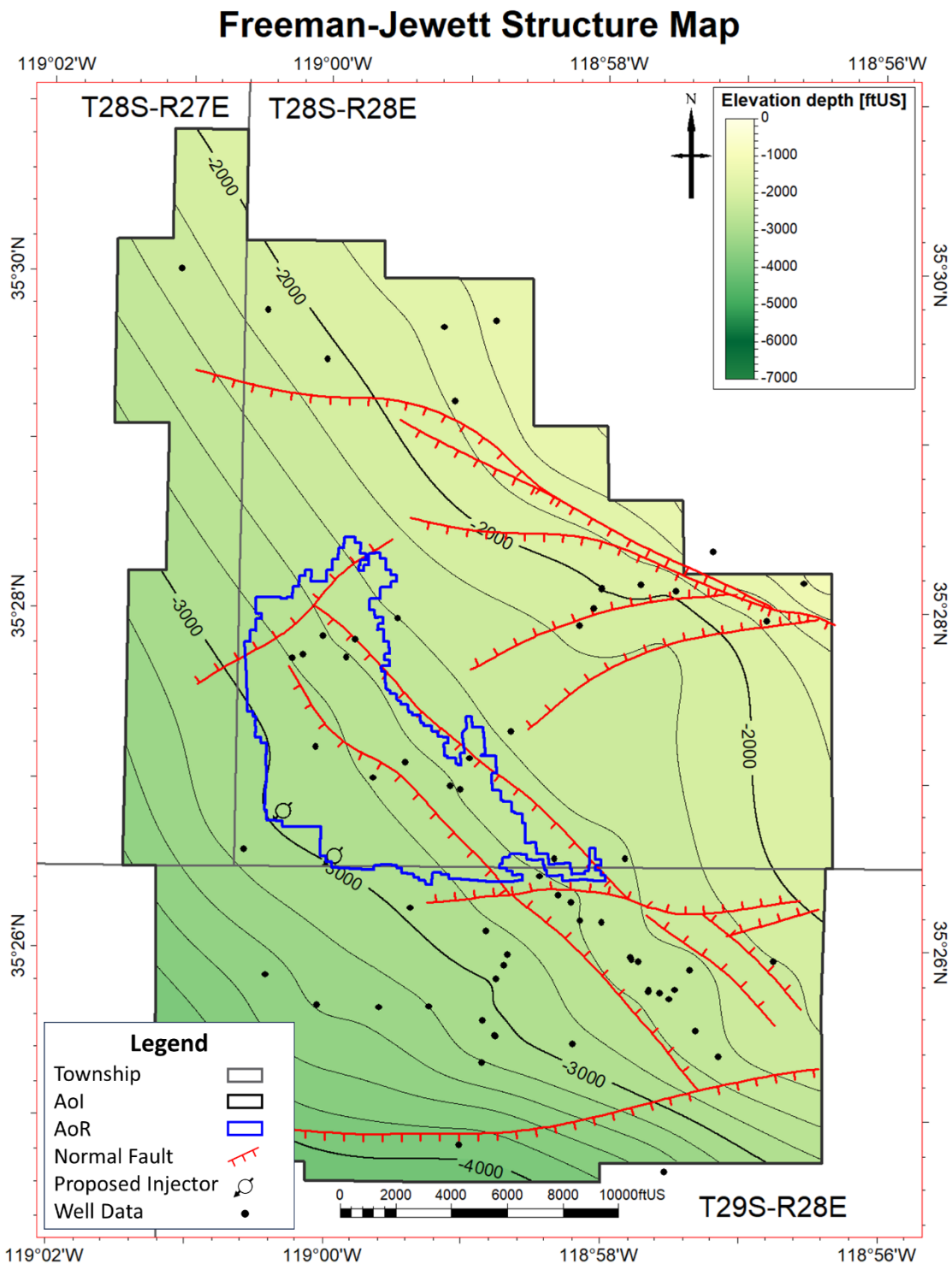

Figure 27. Structural surface map of the upper confining zone defined by the top of the Freeman–Jewett Silt. Red hachured lines denote mapped faults. Contour interval is 200 ft.

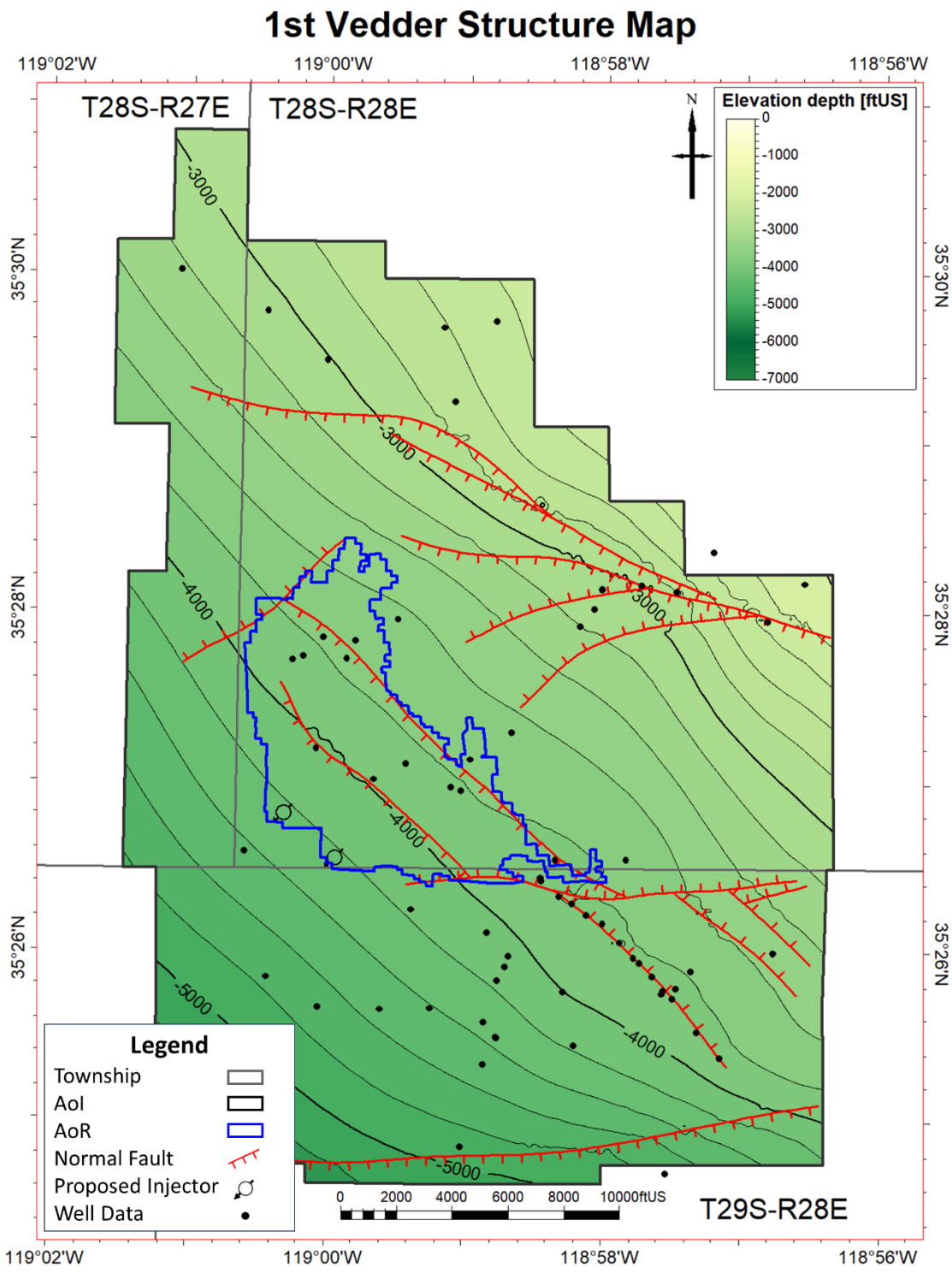

Figure 28. Structural surface map of the top injection zone defined by the top of the Vedder Sand (top of Vd1). Red hachured lines denote mapped faults. Contour interval is 200 ft.

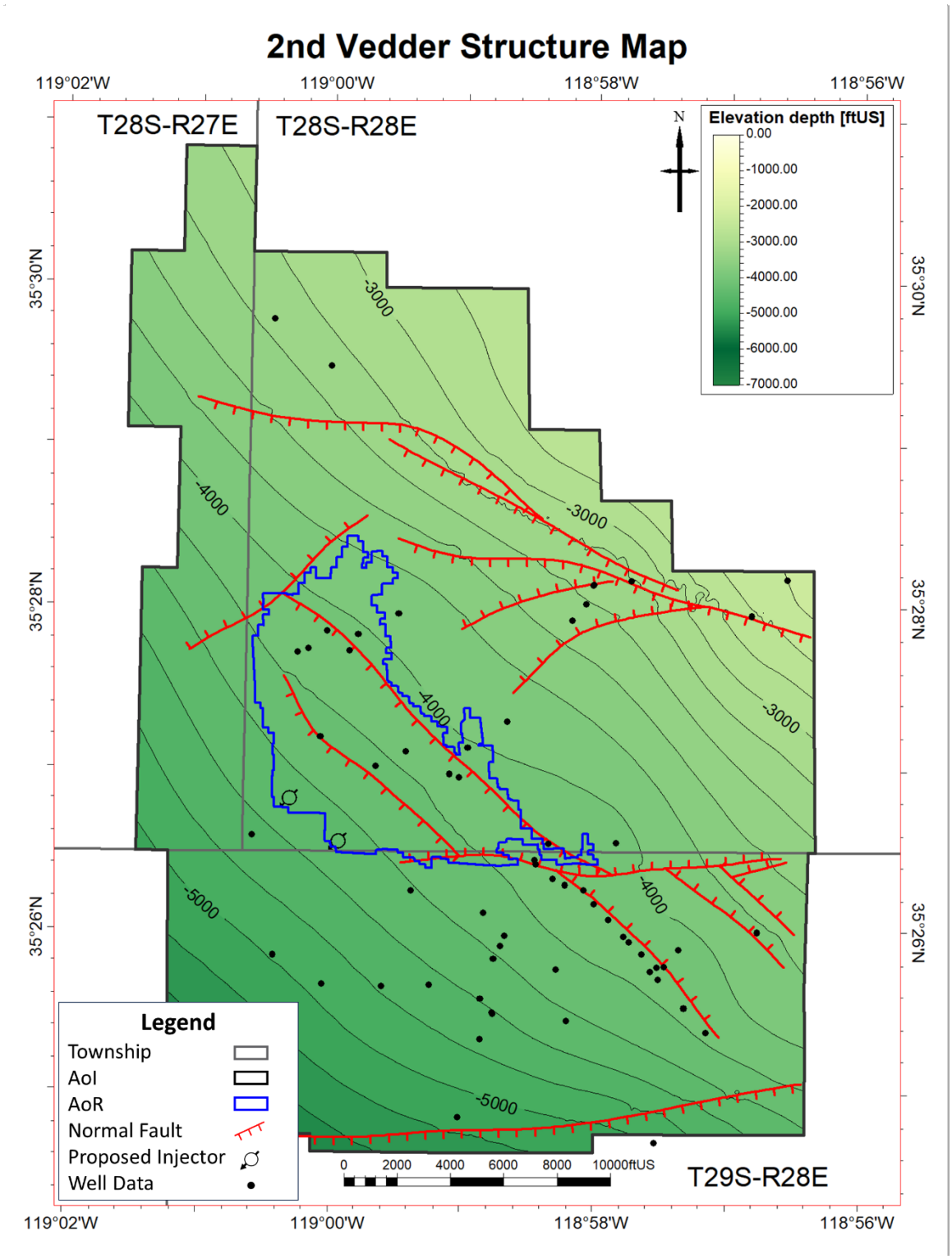

Figure 29. Structural surface of the top of the 2nd Vedder Sand (Vd2). Red hachured lines denote mapped faults. Contour interval is 200 ft.

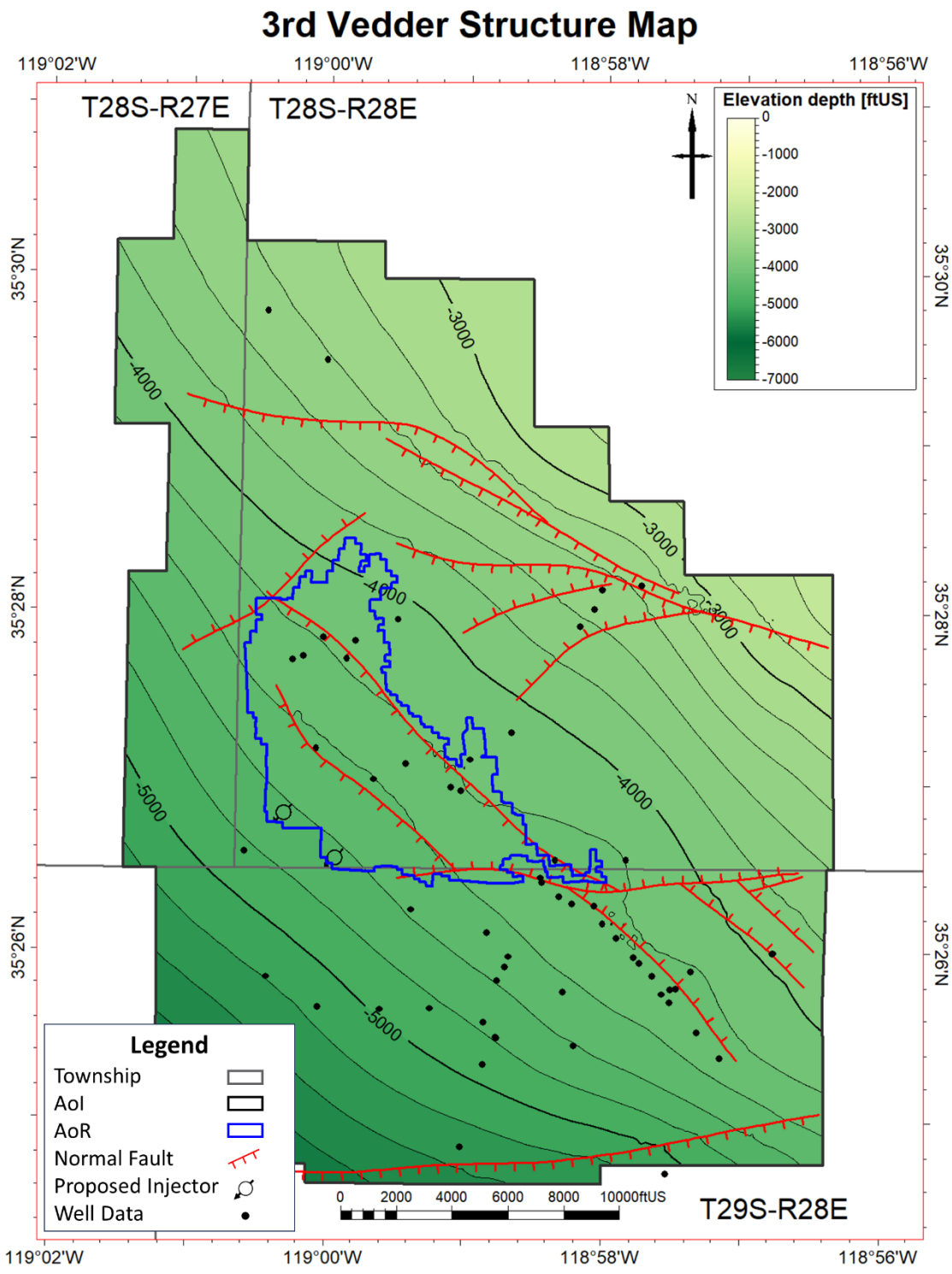

Figure 30. Structural surface of the top of 3rd Vedder Sand (Vd3). Red hachured lines denote mapped faults. Contour interval is 200 ft.

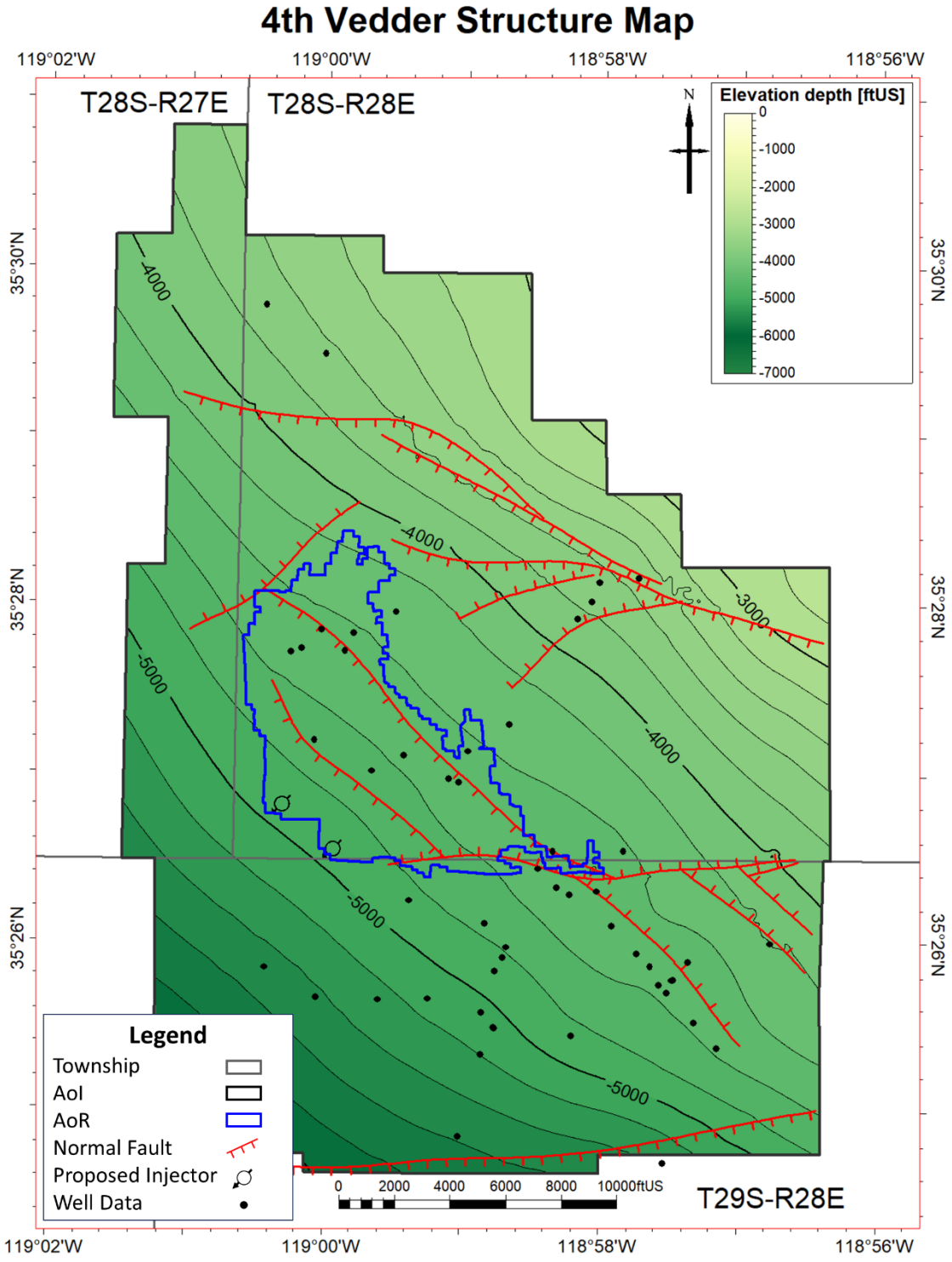

Figure 31. Structural surface of the top of 4th Vedder Sand (Vd4). Red hachured lines denote mapped faults. Contour interval is 200 ft.

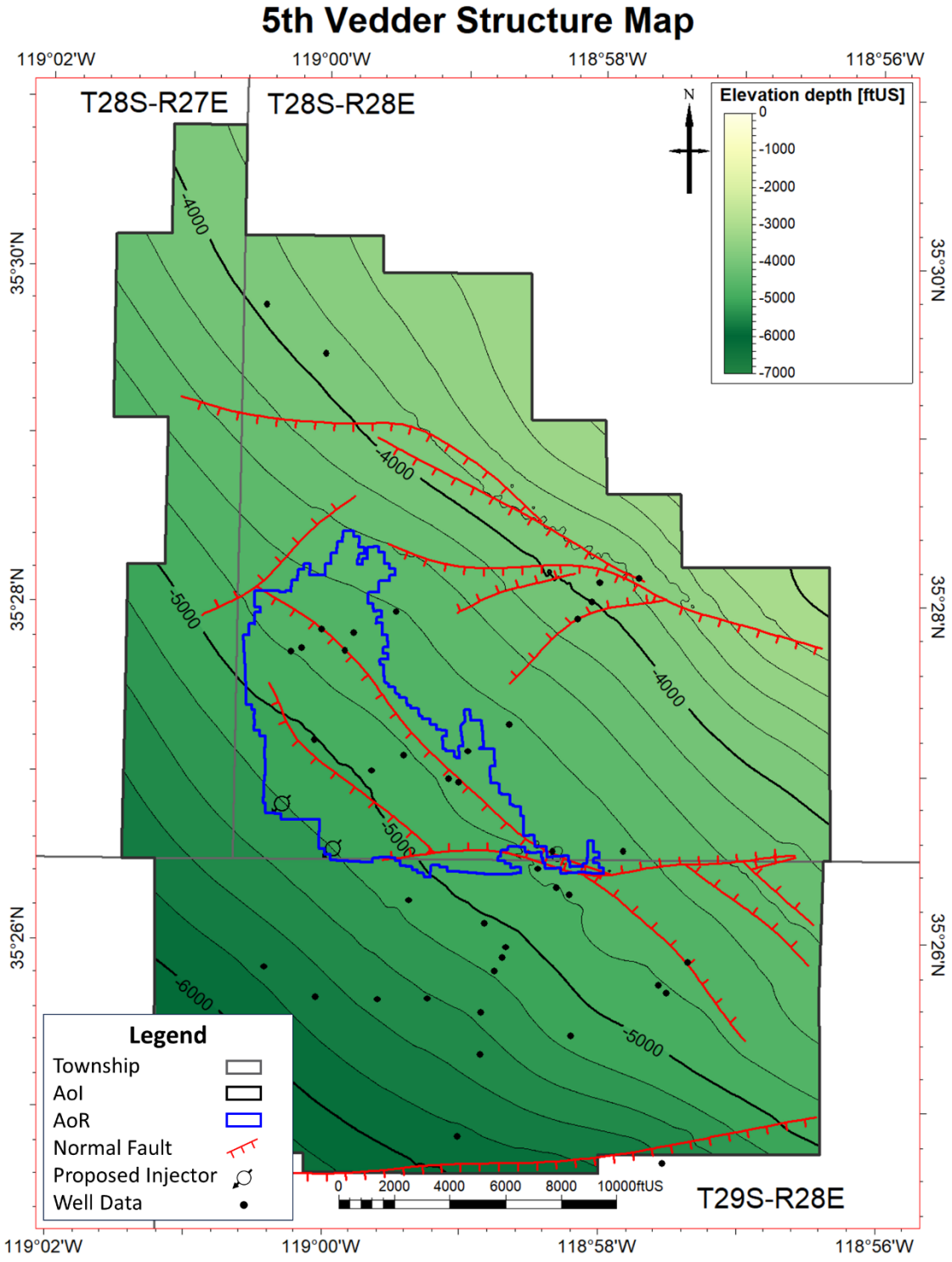

Figure 32. Structural surface of the top of 5th Vedder sand (Vd5). Red hachured lines denote mapped faults. Contour interval is 200 ft.

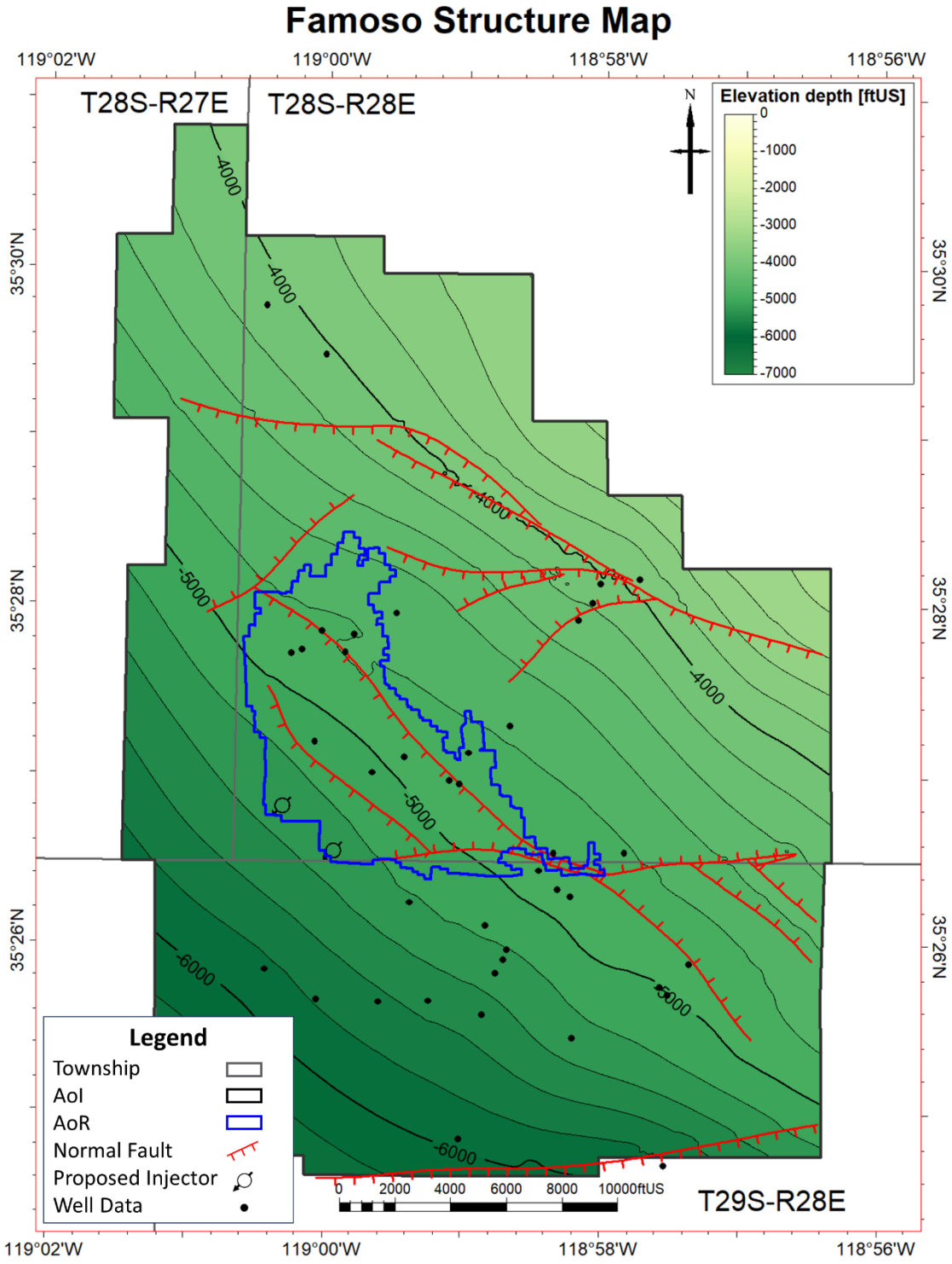

Figure 33. Structural surface of the top of the Famoso sand. Red hachured lines denote mapped faults. Contour interval is 200 ft.

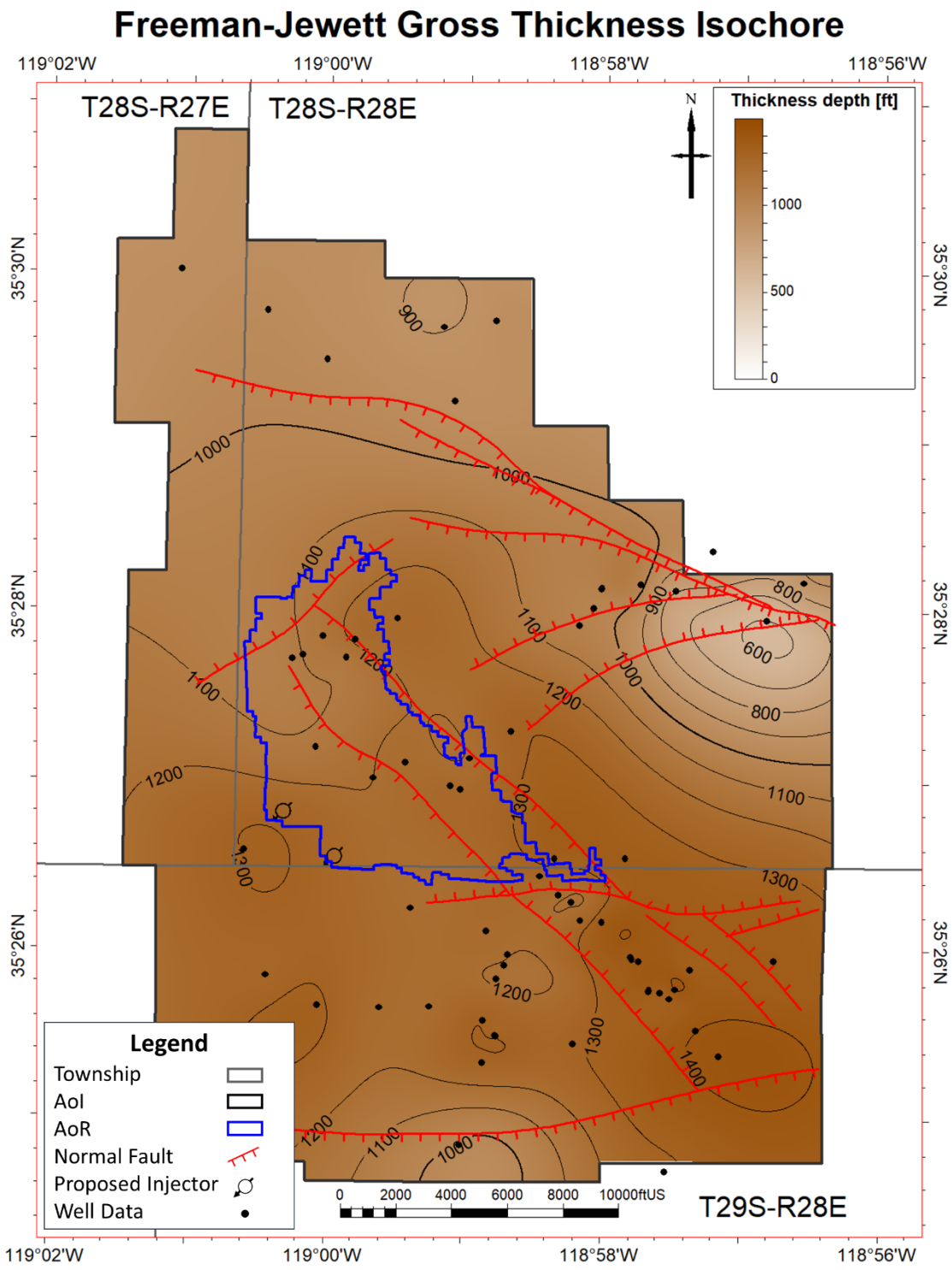

Figure 34. Isochore map of the Freeman–Jewett Silt upper confining zone. Red hachured lines denote mapped faults. Contour interval is 100 ft.

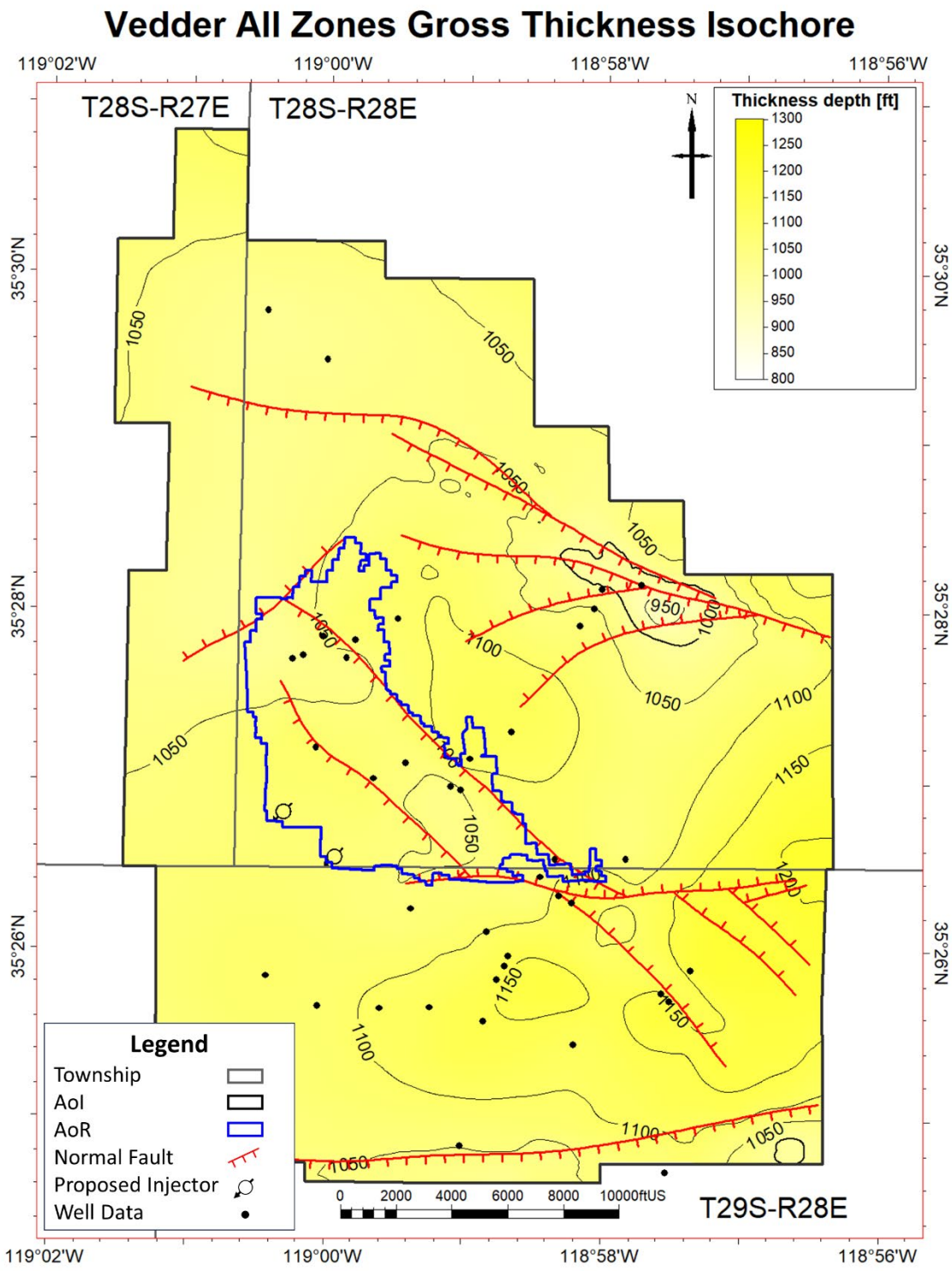

Figure 35. Isochore map of the Vedder Sand (including subunits Vd1-5). Red hachured lines denote mapped faults. Contour interval is 100 ft.

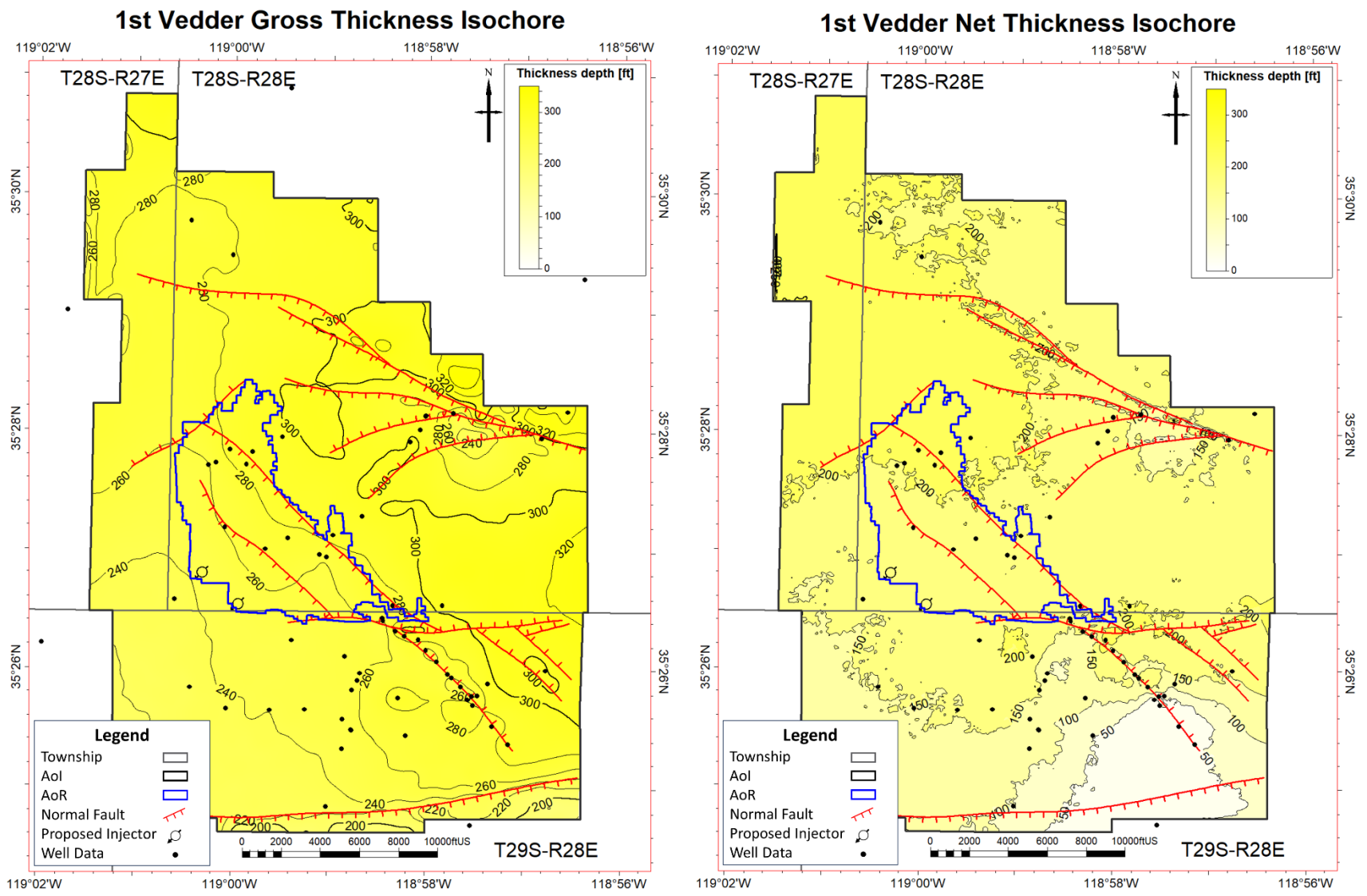

Figure 36. Gross thickness and net thickness isochore maps of the 1st Vedder subunit (Vd1). Red hachured lines denote mapped faults. Contour intervals are 20 and 50 ft respectively.

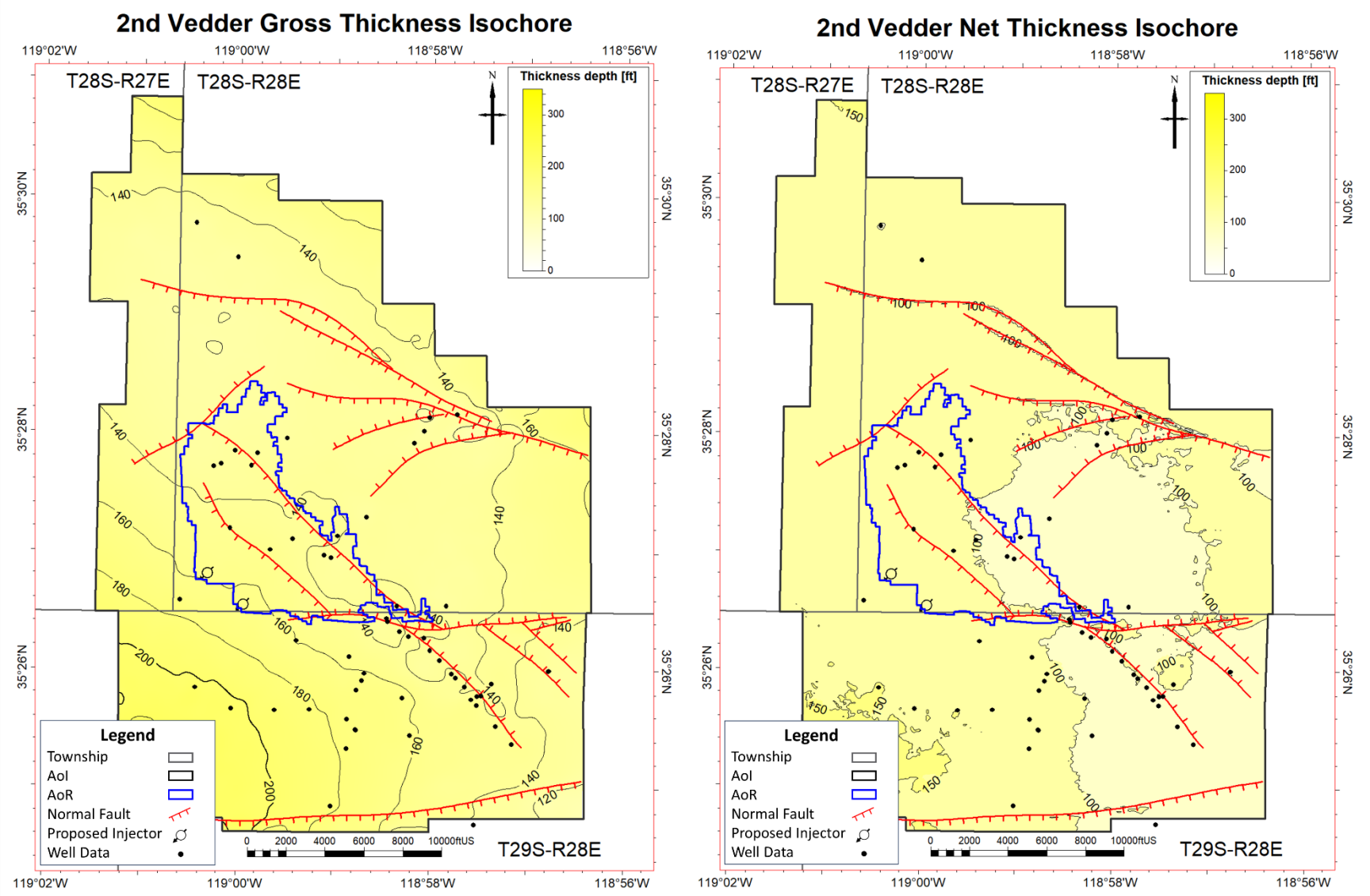

Figure 37. Gross thickness and net thickness isochore maps of the 2nd Vedder subunit (Vd2). Red hachured lines denote mapped faults. Contour intervals are 20 and 50 ft respectively.

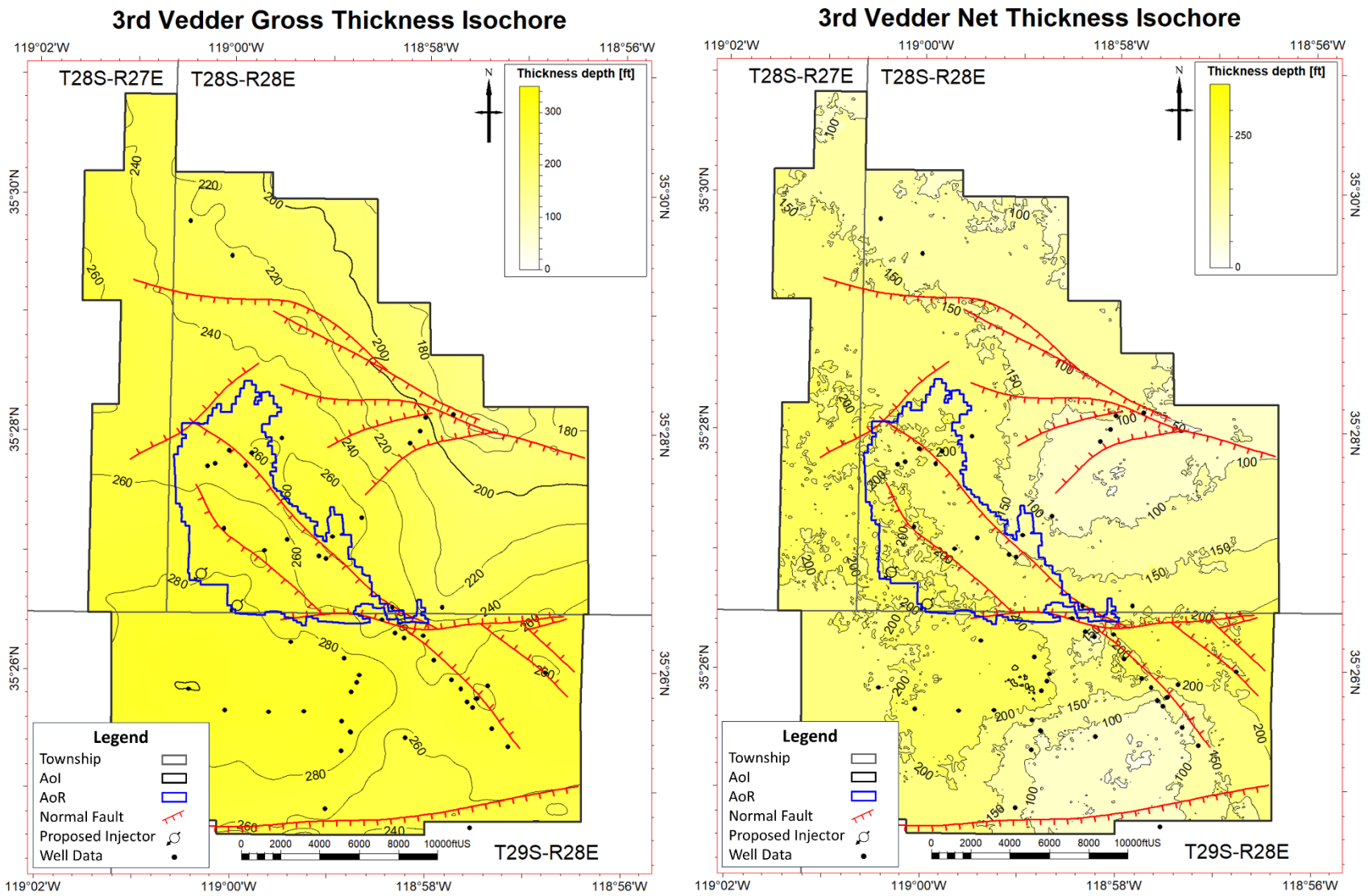

Figure 38. Gross thickness and net thickness isochore maps of the 3rd Vedder subunit (Vd3). Red hachured lines denote mapped faults. Contour intervals are 20 and 50 ft respectively.

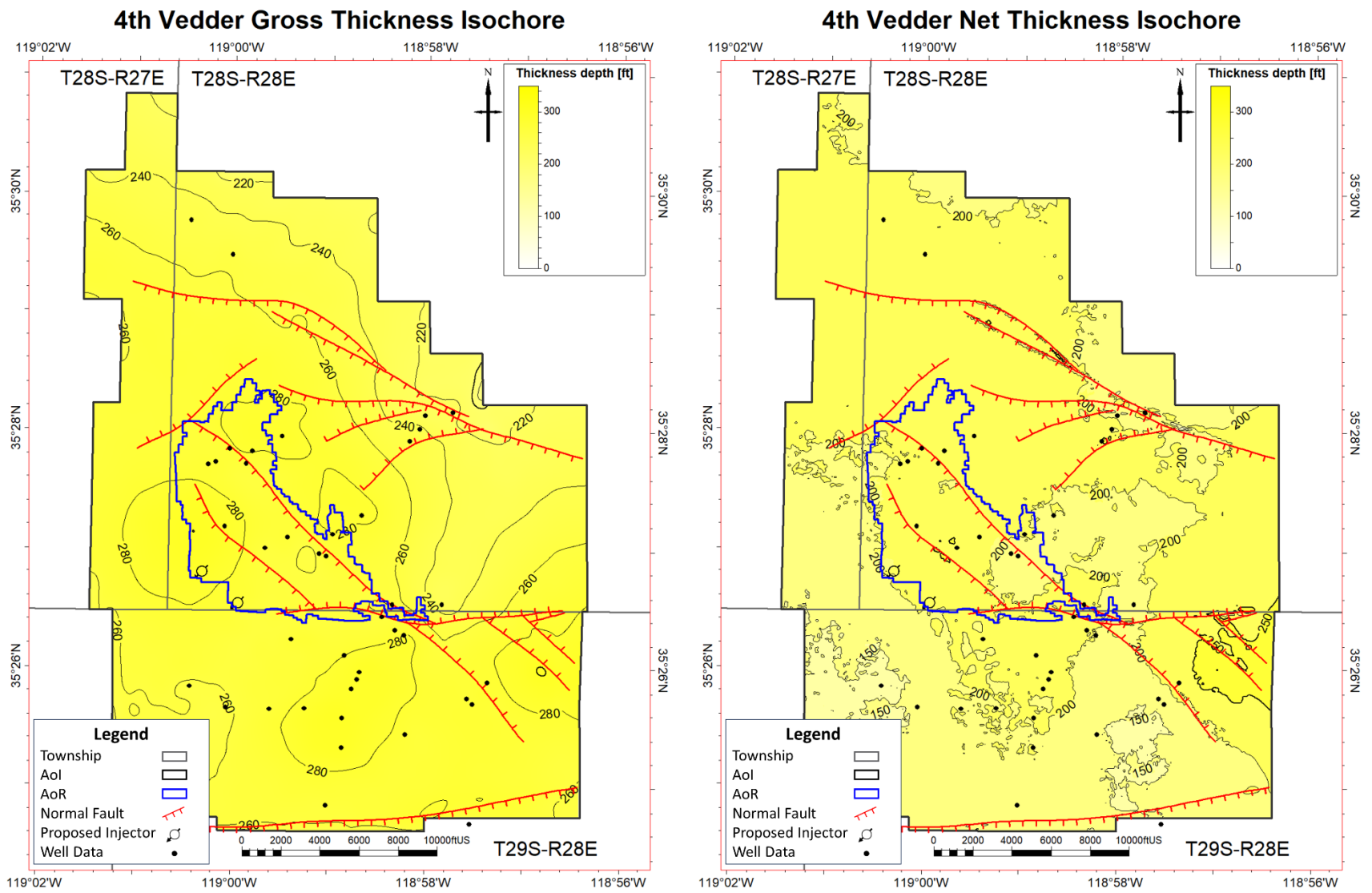

Figure 39. Gross thickness and net thickness isochore maps of the 4th Vedder subunit (Vd4). Red hachured lines denote mapped faults. Contour intervals are 20 and 50 ft respectively.

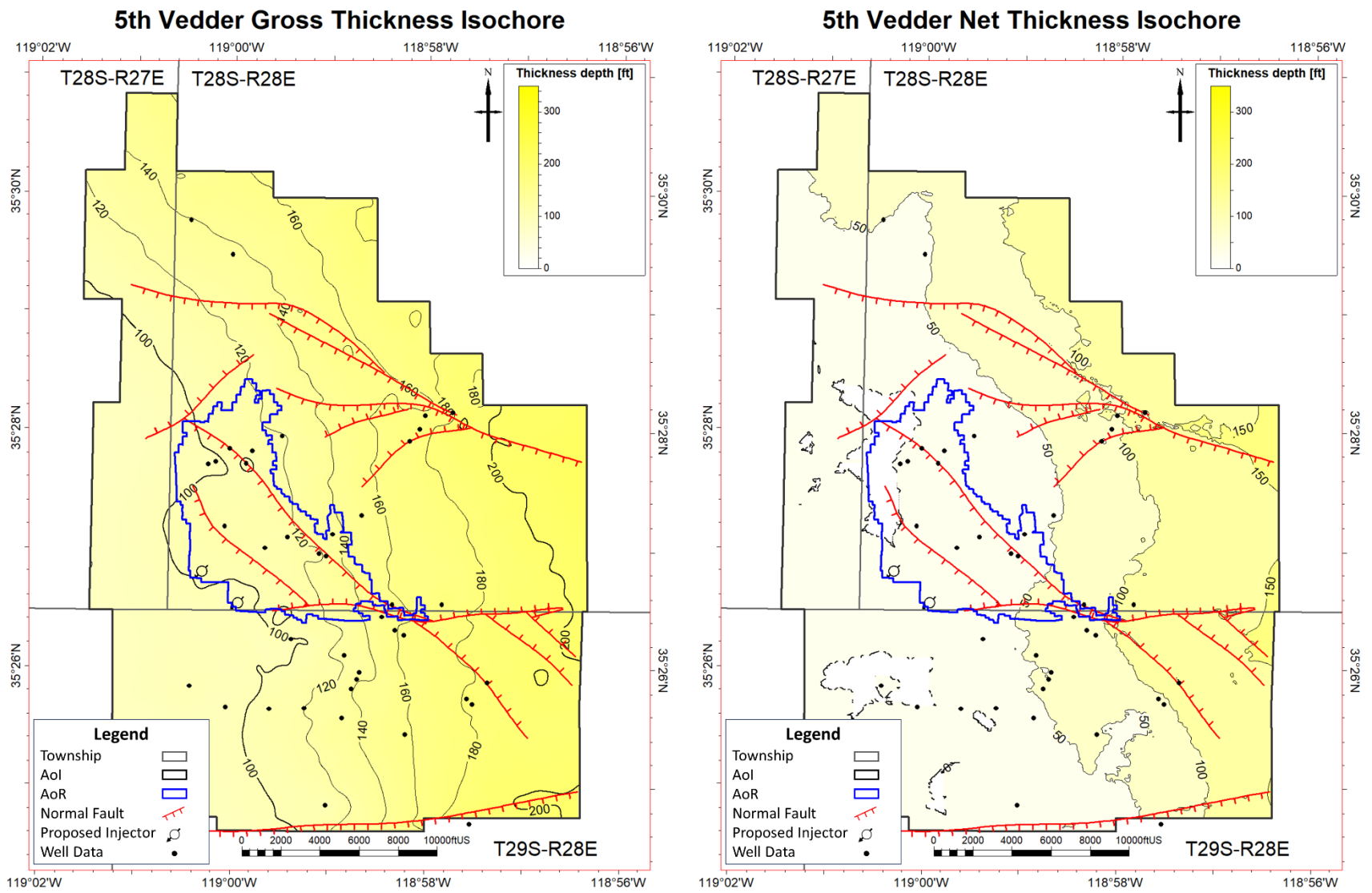

Figure 40. Gross thickness and net thickness isochore maps of the 5th Vedder subunit (Vd5). Red hachured lines denote mapped faults. Contour interval are 20 and 50 ft respectively.

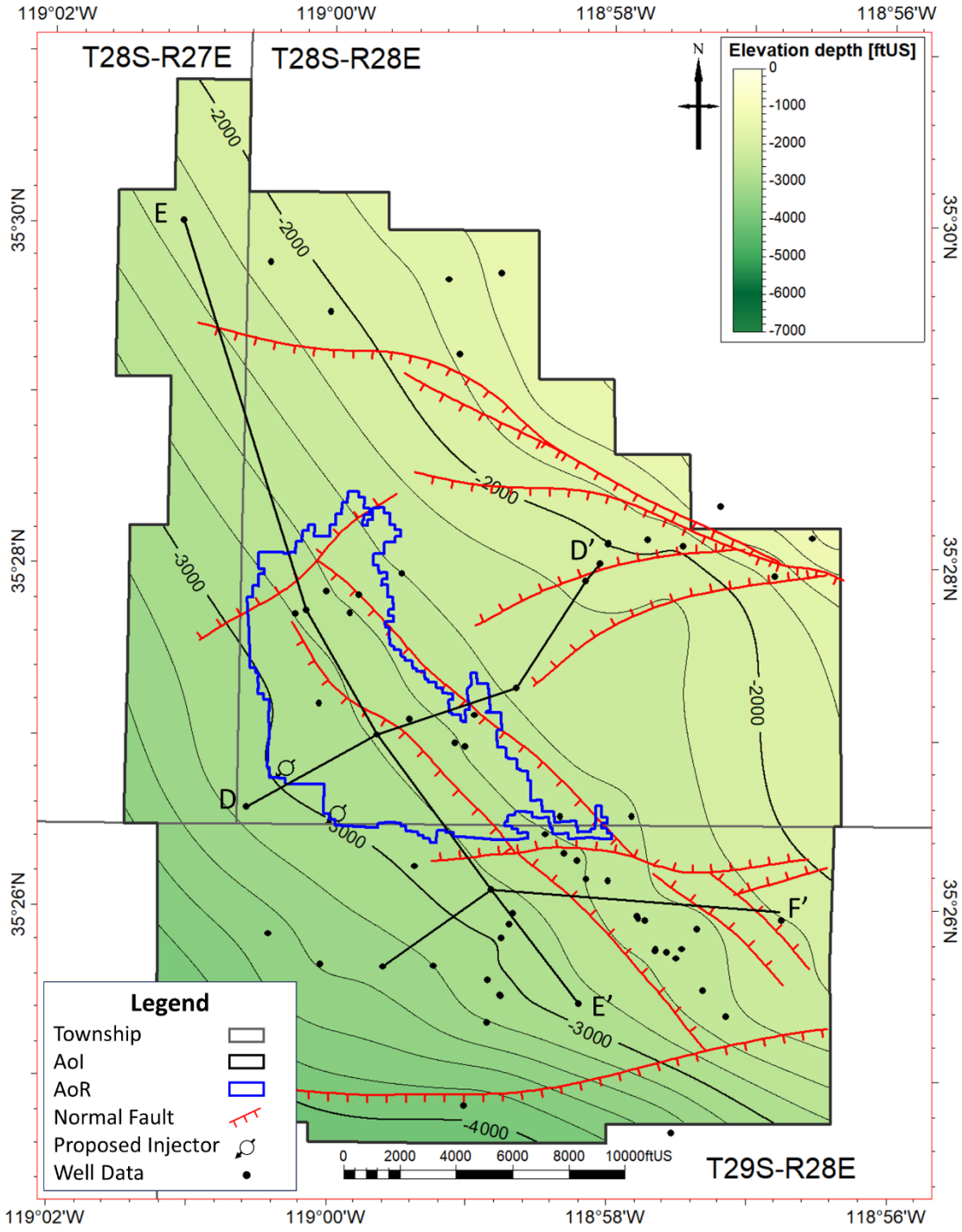

Figure 41. Location map for Freeman-Jewett Silt well section in **Figure 42** through **Figure 43**

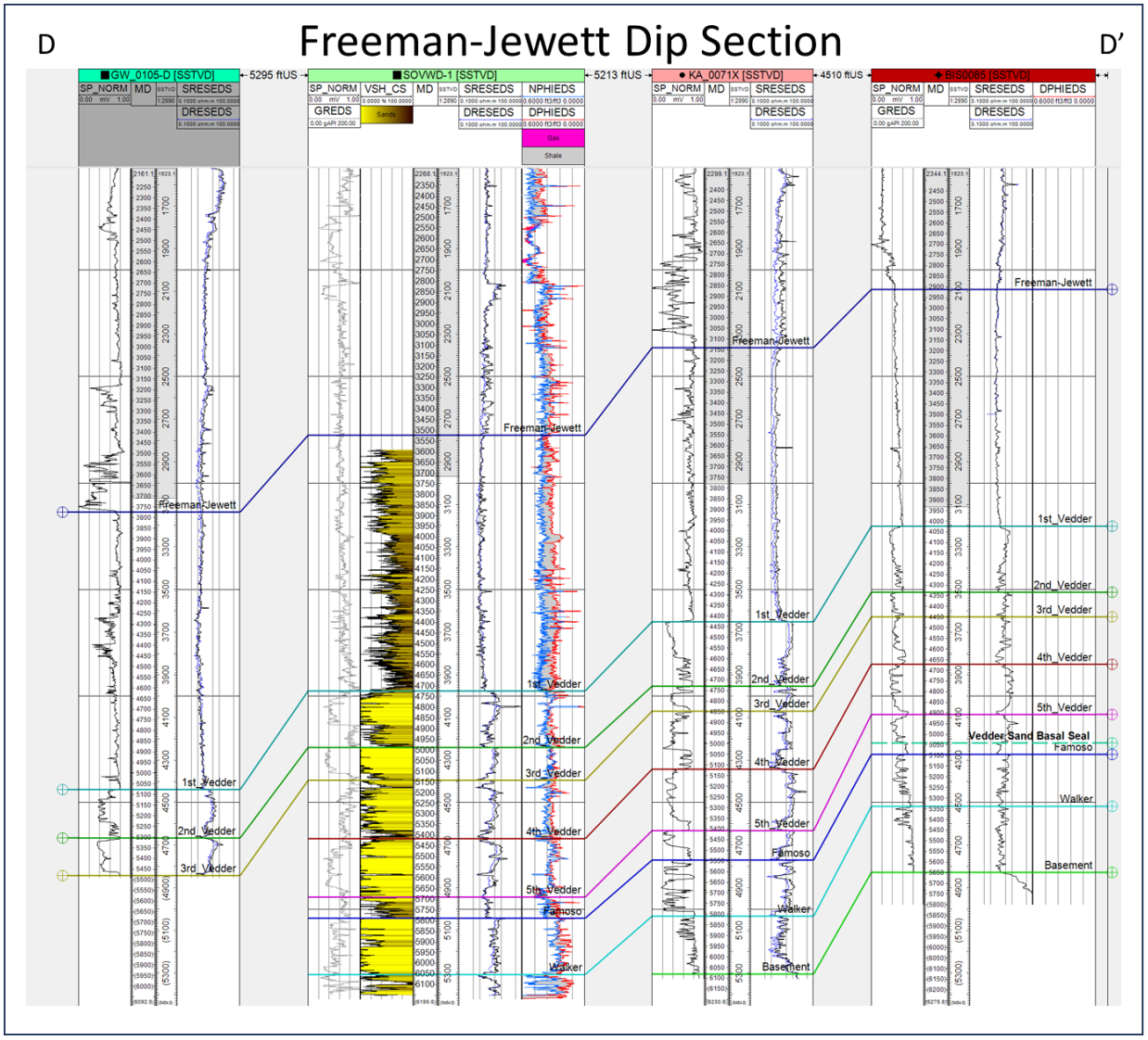

Figure 42. Well section D-D' showing correlation of confining and injection zones along depositional dip. Refer to **Table 10** for well-log names. See previous figure, **Figure 41** for the location of this section.

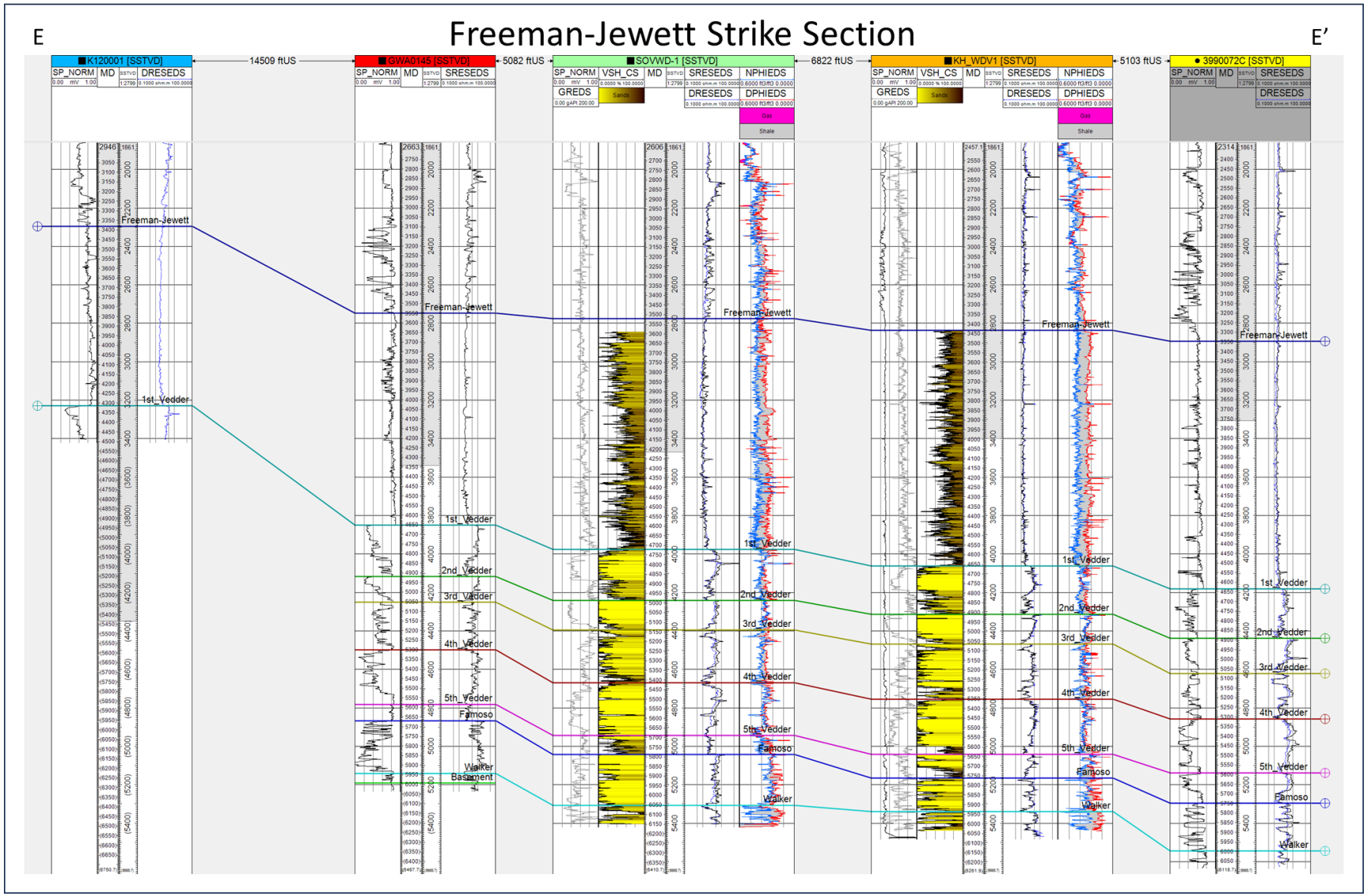

Figure 43. Well section E-E‘ showing correlation of confining and injection zones along depositional strike. Refer to **Table 10** for well-log names. See **Figure 41** for the location of this section.

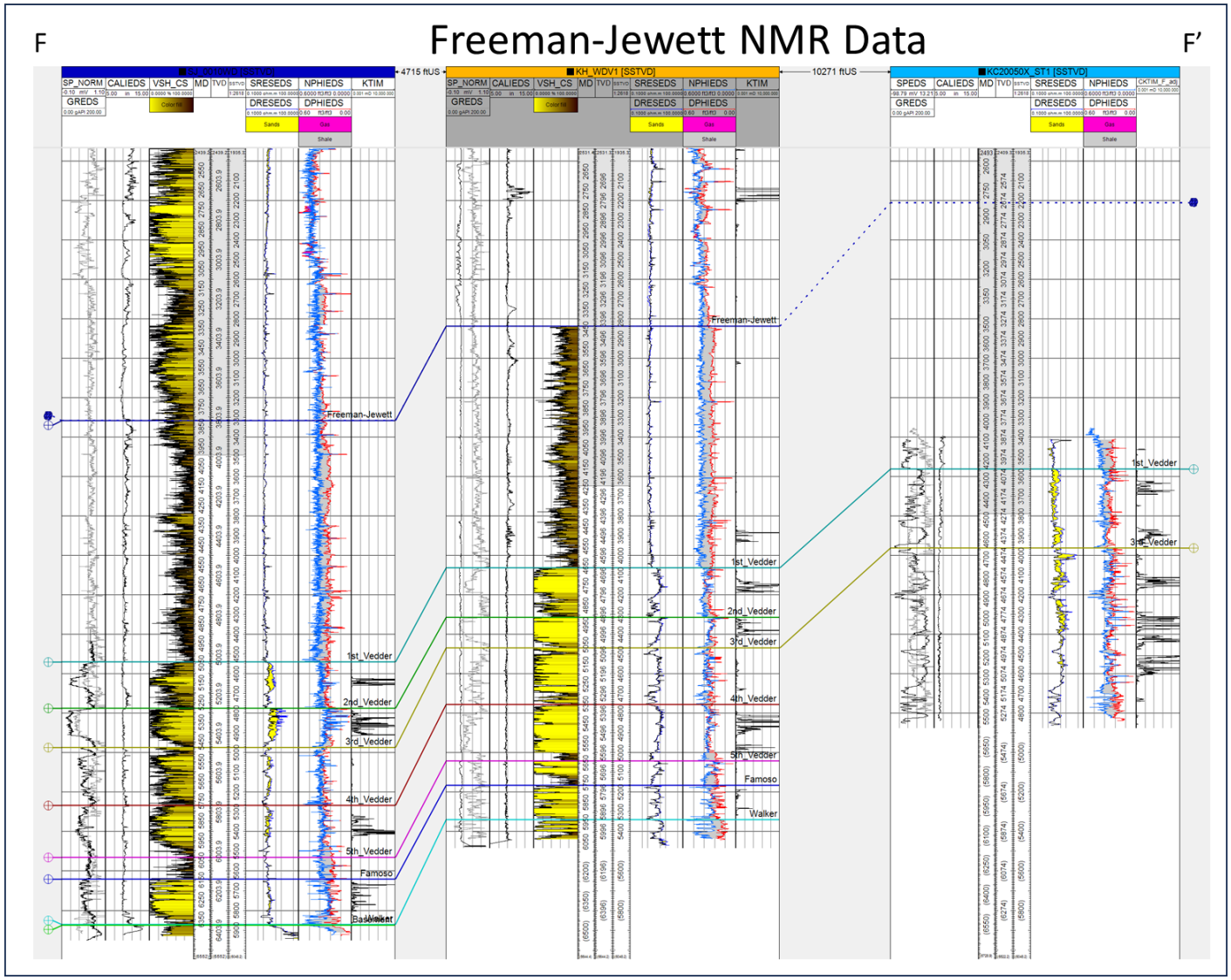

Figure 44. Well section F-F' showing correlation with Nuclear Magnetic Resonance (NMR) logs (KTIM & CKTIM_F). Refer to **Table 10** for well-log names. See **Figure 41** for the location of this section.

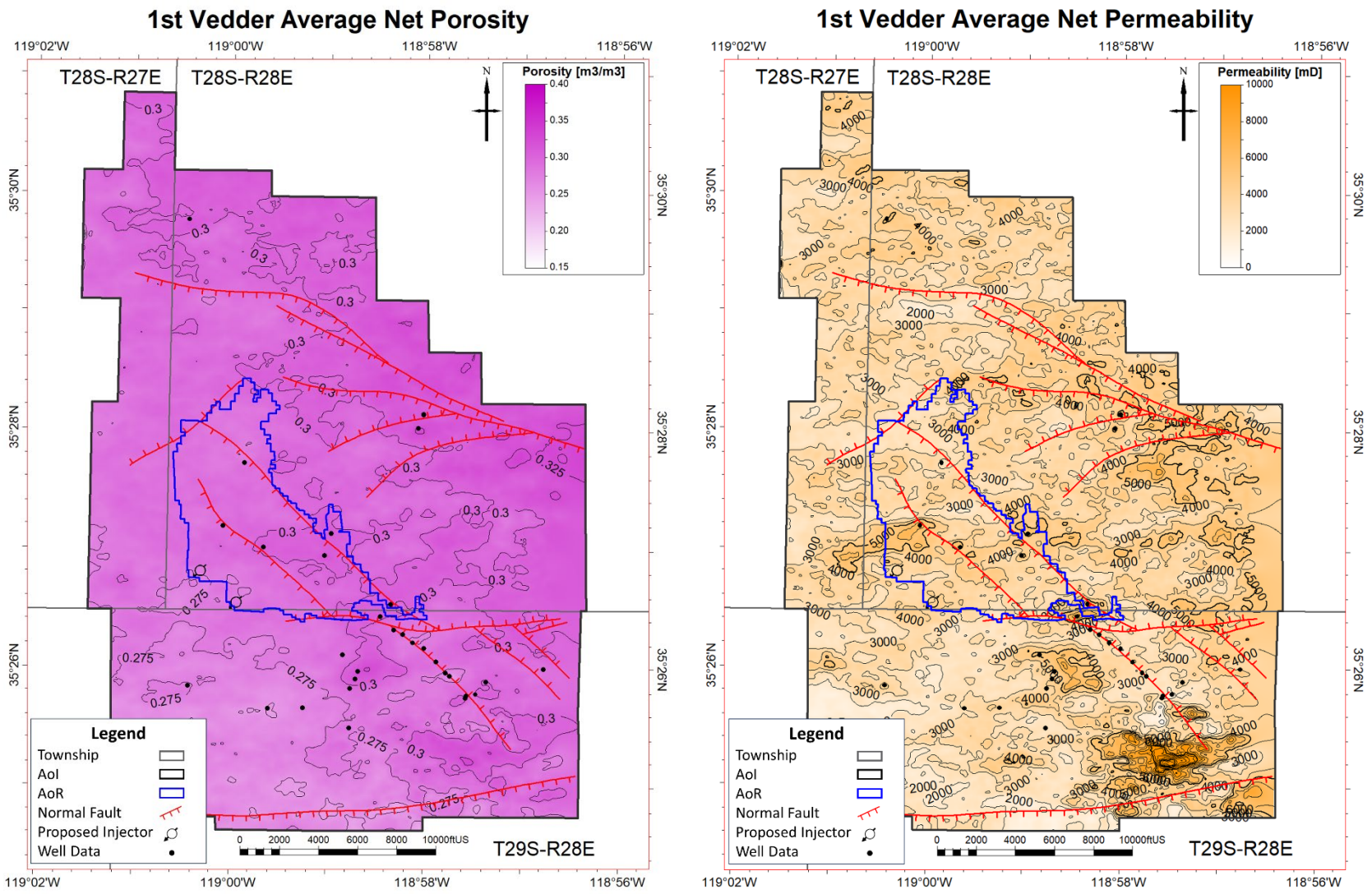

Figure 45. Maps of average sand porosity (left) and sand permeability (right) for the 1st Vedder Sand (Vd1). Red hachured lines denote faults.

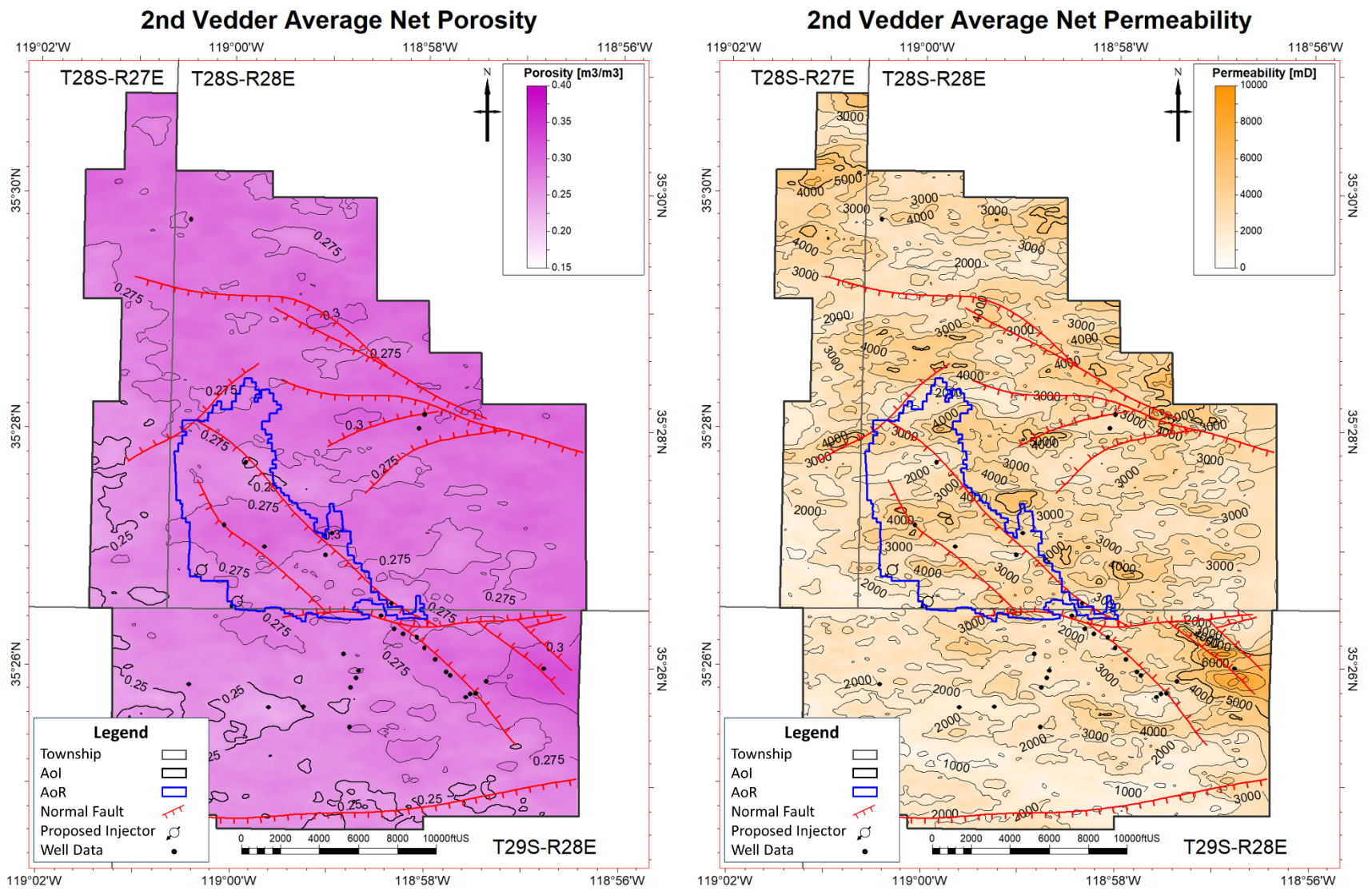

Figure 46 Maps of average sand porosity (left) and sand permeability (right) for the 2nd Vedder Sand (Vd2). Red hachured lines denote faults.

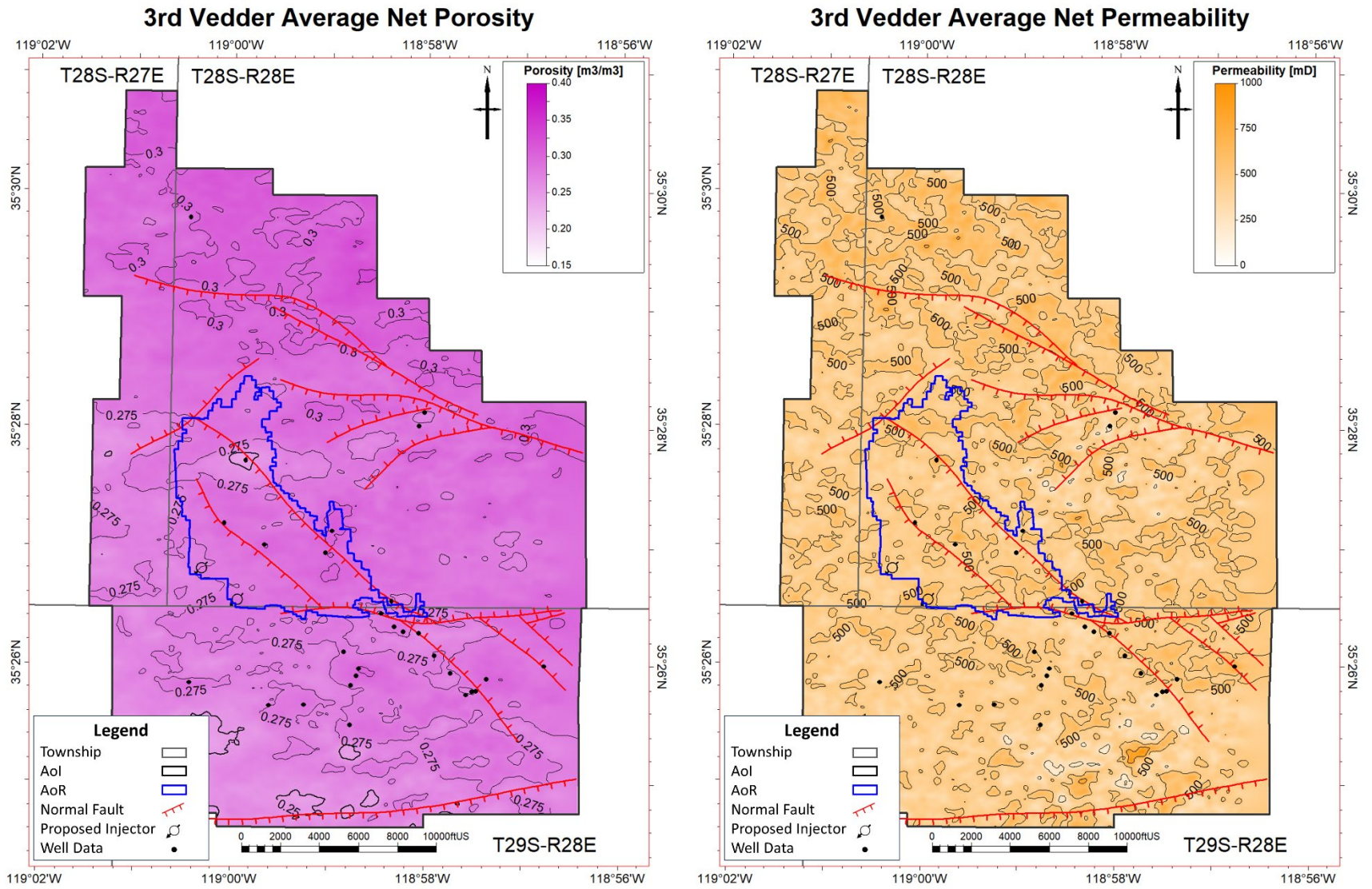

Figure 47. Maps of average sand porosity (left) and sand permeability (right) for the 3rd Vedder Sand (Vd3). Red hachured lines denote faults.

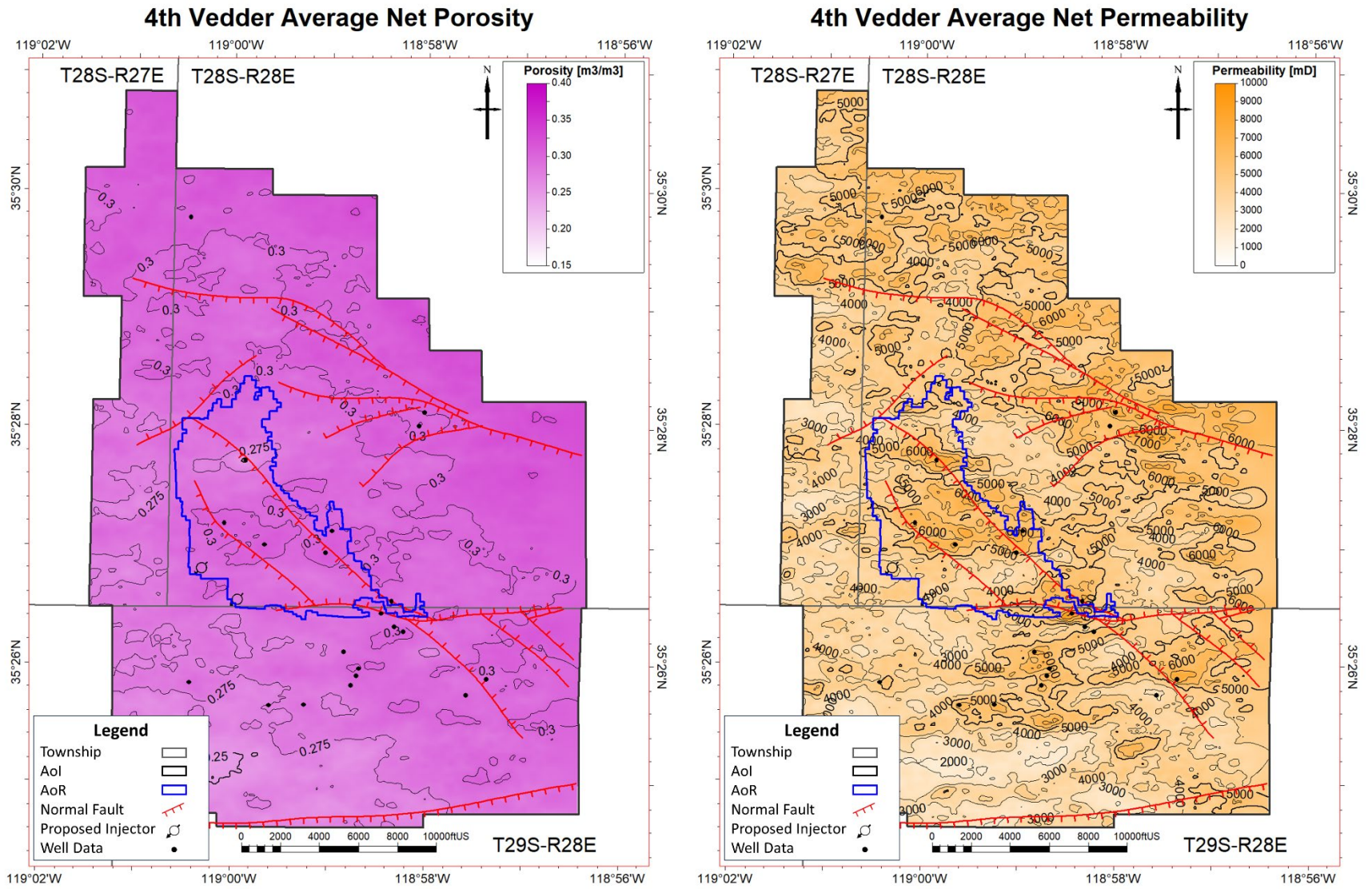

Figure 48. Maps of average sand porosity (left) and sand permeability (right) for the 4th Vedder Sand (Vd4). Red hachured lines denote faults.

Faults and Fractures [40 CFR 146.82(a)(3)(ii)]

Fault Framework

Faults were mapped using seismic and well data. The structural framework (**Figure 49)** delineates two major hard-linked, northwest-striking, normal-oblique fault systems and northeast-striking normal faults that cut a homoclinal stratigraphic succession that dips 3-6 degrees to the southwest. Image logs confirm the dips measured from structure maps. Near faults, bedding observed on image logs have variable dips, mostly due to local deformation near faults where the steepest bedding planes approach dips of the mapped faults. Faults typically branch into *en echelon* splays that display both northward and southward dips ranging from 60-70 degrees. Fault splays are interpreted to be hard linked based on seismic observations and are corroborated by pressure transient analysis (PTA) data for the Apollo Jr fault block shown in **Figure 56**.

No fractures, apart from faults zones, are observed in the Vedder Sand. Chevron's pre-operational testing plan includes collecting image logs to further confirm the lack of fractures.

Primary fault systems within the AoI include the Wilmar, Apollo, Omar-Sterling-Cortez South (OSCS), and Canfield fault systems (**Figure 49**) and normal faults that strike approximately orthogonal to the southwestern flank of the Bakersfield arch. The China Grade fault zone is a system of east-striking normal faults located near the southern boundary of the AoI. The Kern Front fault is a south-striking normal fault, whose surface trace is located near the western boundary of the AoI.

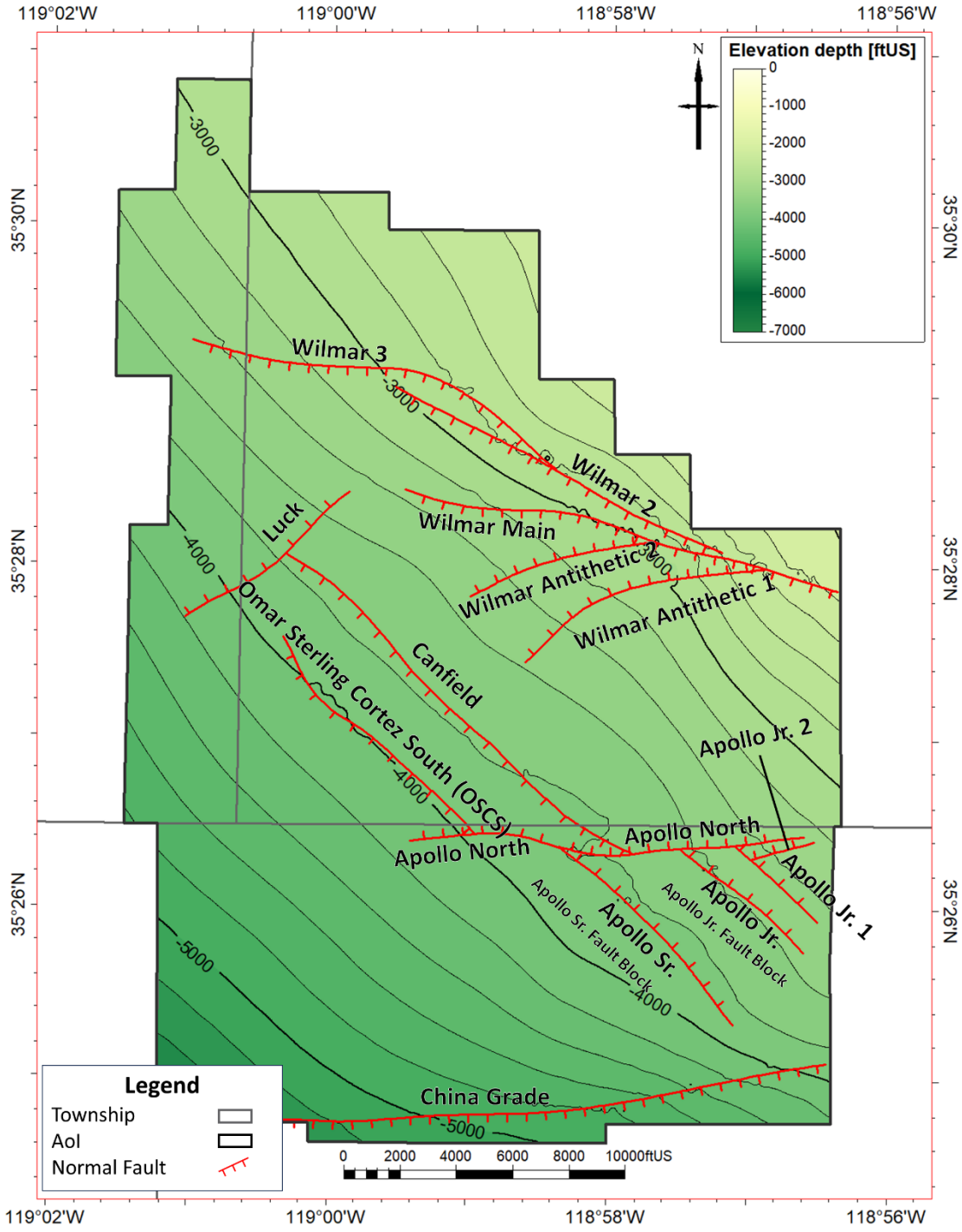

Figure 49. Structural Framework. A structure map of the top Vedder Sand illustrating the intersection with mapped faults. Fault names are indicated on the map. The contour interval is 200 ft.

Mapped faults were characterized based on throw-to-length (D/L) relationships, fault-throw gradients, fault-throw profiles, and fault ellipticity. Stratigraphic horizons and faults were integrated into a structural framework in Petrel. Structural surfaces were used to construct horizon-fault intersections enabling 3D analyses of the fault planes as described by Allan (1989).

Maximum fault throws range from 50-380 ft within the AoI, with greater throw recognized along the northern part of the Wilmar fault system. Mapped faults have D/L ratios typical for normal faults (1-8%), and display regular, parabolic throw profiles and D/L gradient ratios of less than 0.3 (**Figure 50**). Throw profiles and D/L relationships were used to extrapolate faults beyond the resolution of the 3D seismic survey data.

The Wilmar fault system consists of a northwest striking composite fault comprised of branching, hard-linked, normal faults dipping to the southwest (Wilmar 2 & Wilmar 3) and two east to northeast striking secondary splays (Wilmar Antithetic 1 & Wilmar Antithetic 2) south of the composite master fault that dip to the northwest.

Segments of the composite Wilmar master fault dip to the southwest and have maximum throws ranging from 220 ft to 380 ft, whereas secondary splays have maximum throws of approximately 100 ft. The Wilmar fault system extends into basement and is at least 4.7 miles (7.6 km) in length within the area of 3D seismic coverage. Based on D/L ratios and throw profiles, the Wilmar fault system likely continues to the northwest and southeast by an additional 1-6 miles.

In the central portion of the AoI, the northwest- to west-striking Apollo, southeast-striking Omar-Sterling-Cortez South (OSCS) and southeast-striking Canfield fault systems are a network of normal faults that are over 4.7 miles in length.

The north- to northeast-dipping Apollo faults (i.e., Apollo Sr., Apollo Jr., Apollo Jr. 1, and Apollo North) have maximum throws ranging from 80 to 125 ft. Based on D/L relationships, the Apollo Sr., Apollo Jr., and Apollo Jr. 1 faults extend southeast beyond seismic coverage.

The Omar-Sterling-Cortez South and Canfield faults dip to the southwest and have smaller maximum throws of 60-80 ft. Parts of the Canfield and Omar faults are not directly observable across the seismic survey and are substantiated based on well data (i.e., missing section resulting in structural thinning) and the downward projection of faults mapped in shallower intervals where well-based stratigraphic juxtapositions have been determined. The projection of faults into areas of limited seismic quality is supported by vertical-throw gradients observed elsewhere in the AoI.

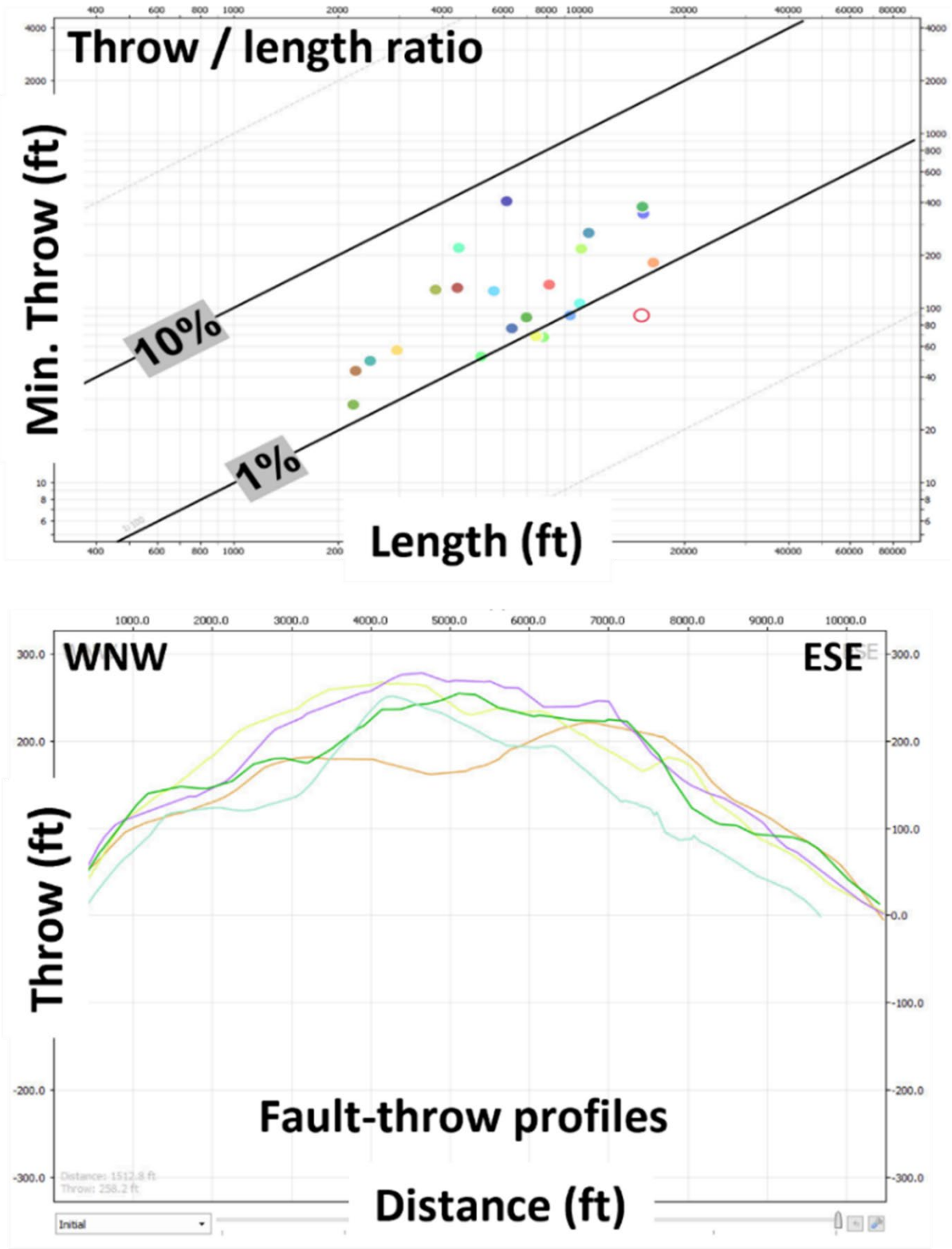

Figure 50. Examples of quantitative analysis of faults that cut the Vedder Sand, showing orientation, throw-length relationships and throw profiles.

Fault Seal Capacity

Fault seal capacity can be described using several different mechanisms. Juxtaposition seal of reservoir sand against sealing units (shale) is the simplest to describe, tied to the throw and stratigraphy of a system (**Figure 51**). Juxtaposition of reservoir sand against another sand is more complex and can be interpreted with multiple different mechanisms where the faults impede or prevent flow due to their fault-rock composition (Knipe, 1993). One such mechanism is shale gouge and fault smear along the fault plane (Yielding et al., 1997; and Doughty, 2003) creating a fault membrane seal due to capillary entry pressure. Permeability alteration through cataclasis and diagenesis in the damage zones of poorly consolidated rocks (Knipe, 1993; Rawling and Goodwin, 2003) is another process used to characterize the flow potential and sealing capacity across faults.

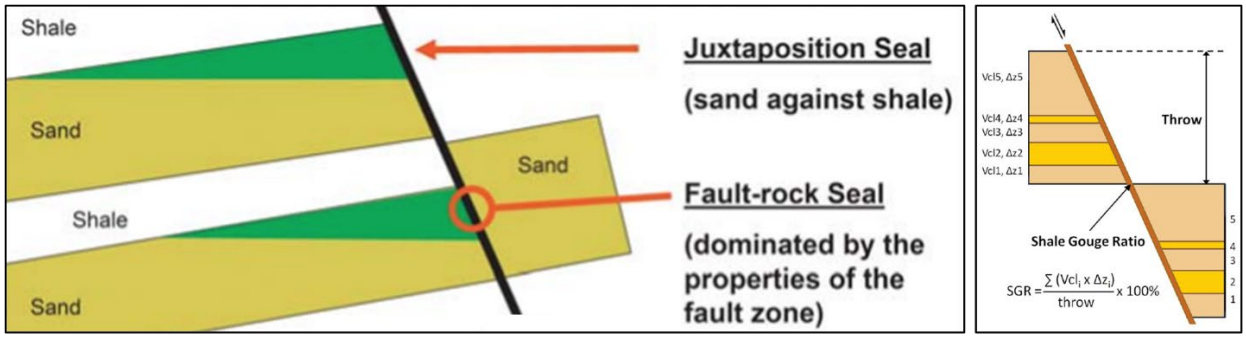

Figure 51. Fault zone sealing mechanisms and a theoretical mixing algorithm for computing Shale Gouge Ratio (SGR; from Yielding et al., 1997).

The fault seal membrane is the first portion of the fault characterization described. A fault seal membrane occurs when the buoyant force of the non-wetting phase is insufficient to penetrate the pores of the finer grained material (Watts, 1987). Shale-gouge ratio (SGR) is a methodology used to predict fault rock membrane seal presence based on grain size distributions (Yielding et al., 1997; and Freeman et al., 1998). Shale-gouge ratio (SGR) has been used in CO_2 storage studies to explain or predict subsurface fault rock seal from fault zones (e.g., Bretan et al., 2003; and Karolytė et al., 2020). The volume of clay (Vcl) is used in conjunction with fault displacement to calculate the SGR of the fault (**Figure 51**). SGR is then used to calculate the threshold capillary entry pressure (Bretan et al., 2003). Threshold capillary entry pressure is also referred to as the across-fault pressure difference (Yielding et al., 1997) and is defined as the buoyant force needed to overcome the pressure required for the non-wetting phase to enter and pass through the largest interconnected pore throat to establish flow across the fault.

The structural interpretation was used as input for fault displacement along with a characterization of the Vcl from well logs to calculate the SGR along faults. Using the equation below, the threshold capillary entry pressure was calculated in psi, where the constant C is 0.5 for formations < 9850 ft deep (Bretan et al. 2003).

Equation 1.

$$Threshold\ Pressure = 14.5 * 10^{(\frac{SGR}{27} - C)}$$

The resultant pressure assumes the interfacial tension and contact wetting angle of a brine-hydrocarbon system and was adjusted for a brine-CO_2 system using interfacial tensions (IFT) and the cosine of the wetting angles, theta (IFT*Cos-Theta). For the brine-hydrocarbon system, a wetting angle of 30 degrees and an interfacial tension of 30 dynes/cm were used. For the brine-CO_2 system, a wetting angle of 40 degrees and an interfacial tension of 30.2 dynes/cm were used (core tests on the Vedder Sand showed an IFT of 30.2 mN/m and contact angle ranges from 35 – 44 degrees for the CO_2-Vedder Brine at 2100 psi and 159 F). This results in a 11% reduction of threshold pressure.

The average threshold pressure of each fault was calculated by filtering on the lower 50th percentile of sand-sand connections. This eliminates high values of threshold pressure associated with shale connections, captures the effective threshold pressure of the connections that control the fault seal along the entire fault, and results in a more conservative (lower) average value to implement within the reservoir simulation model. **Figure 52** below shows the raw threshold pressure and average compared to the filtered threshold pressure and average for the Omar Sterling Cortez South (OSCS) fault.

Faults were characterized in the same manner and generally show that larger amounts of displacement result in larger threshold pressures.

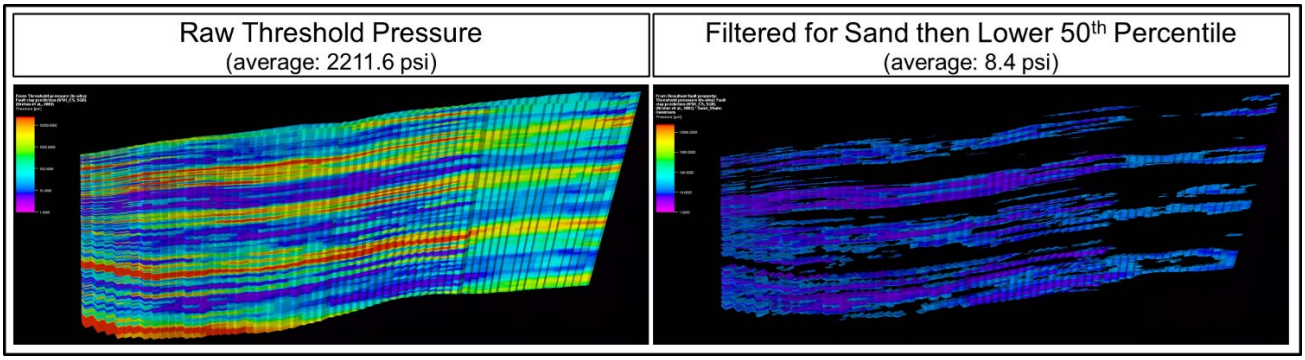

Figure 52. Raw and filtered threshold capillary entry pressure for the Omar Sterling Cortez South fault. Unfiltered, the average threshold pressure is too high to be representative of the sand-on-sand connections across the fault. After filtering for sands and the lower 50th percentile, the average threshold pressure is lower and more conservative.

The Apollo Sr. and Apollo Jr. faults hold oil columns up to ~90 ft within their respective footwall blocks (**Figure 53**) in the 1st, 2nd, and 3rd Vedder. These accumulations indicate active seal across faults in the Vedder Sand and are referenced in the model validation section of the AoR and Corrective Action portion of this permit.

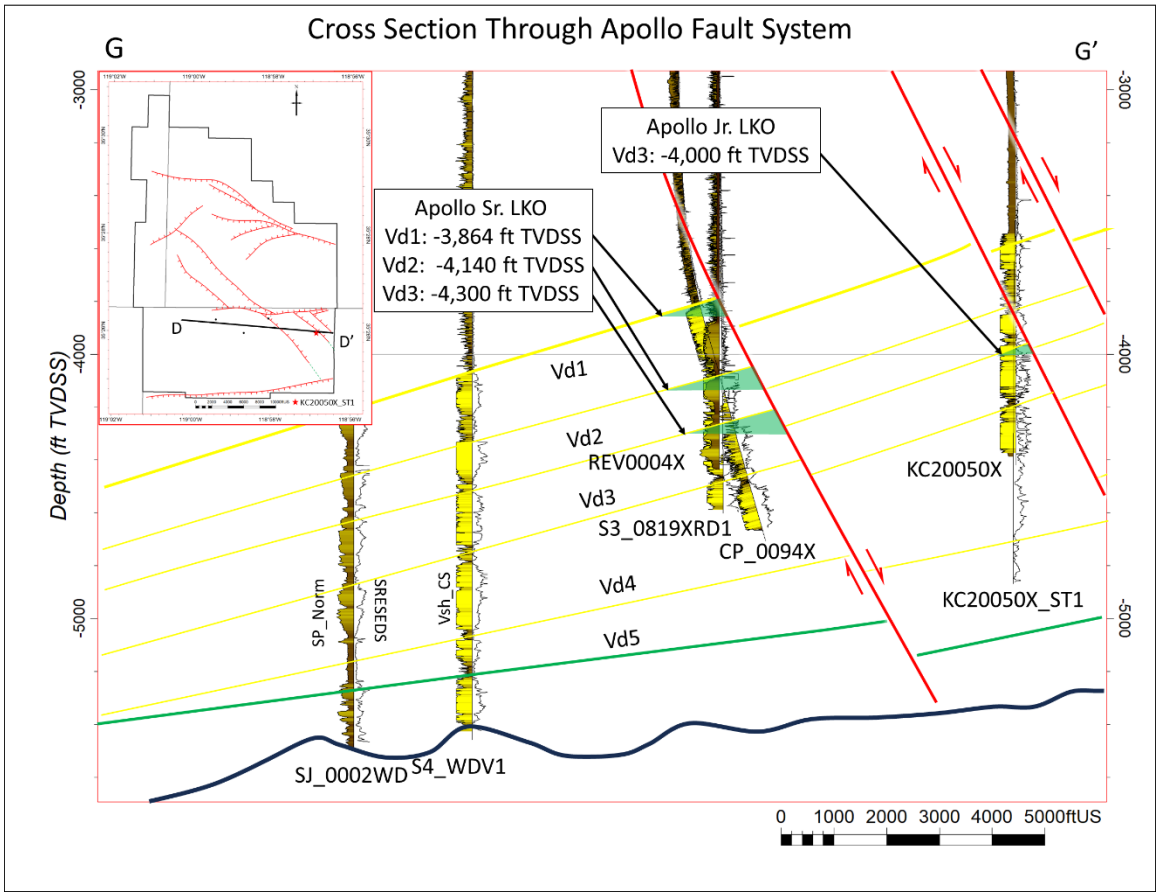

Figure 53. Cross Section G-G' focused on the Apollo fault system, illustrating multiple oil columns and the extent of "lowest known oil" (LKO) identified in the Apollo fault blocks. Location map shows fault intersections at the top of the 3rd Vedder Sand.

In addition to the fault seal described above (fault threshold capillary entry pressure), fault zone damage and cataclasis can result in the alteration of the permeability within the fault zone. The alteration of fault zone permeability and the impact on flow is characterized by defining the thickness and the permeability of the fault zone. The thickness and the permeability of the fault zone relative to the surrounding host rock is used to calculate the fault-transmissibility in the reservoir simulation model (Manzocchi et al. 1999).

Fault zone thickness was estimated using a 1:100 thickness-to-displacement ratio (Childs et al., 2009). This relationship is conservative (resulting in more transmissive faults) when compared to compilations of fault datasets built over multiple decades (Nubian Sandstone, Moab Faults, Westphalian sandstone, etc.). These datasets show an average thickness-to-displacement ratio of 1:66 (Manzocchi et al., 1999). Fault thickness was calculated along the fault surface and averaged over the interval of the Vedder sands.

Fault permeability was estimated using the SGR and the displacement of the faults. Empirical predictions of fault zone permeability are described by the following equation (Manzocchi et al., 1999).

Equation 2.

$$\log k_f = -4 * SGR - 0.25 * \log(D) * (1 - SGR)^5$$

Where k_f is the fault permeability (mD), D is the displacement (meters), and SGR is the shale-gouge-ratio (ranging from 0 to 1). Fault permeability was calculated along the fault surface and averaged over the interval of the Vedder sand.

Each fault in the model is given its own average fault zone thickness and permeability from which continuous transmissibility multipliers are calculated along the fault plane (gridblock by gridblock). This transmissibility multiplier is a function of the fault zone properties (thickness and permeability) and the grid block permeability and geometry on either size of the fault (Manzocchi et al., 1999) as shown in **Figure 54**.

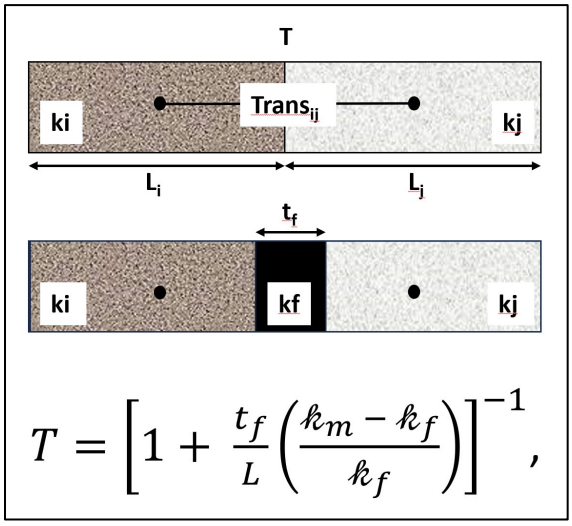

Figure 54. Fault Transmissibility multiplier as a function of fault thickness (t_f), fault permeability (k_f), and the geometry and permeability of gridblocks on either side of the fault (Manzocchi et al., 1999).

The result of using average fault zone thickness and permeability for each fault, combined with the gridblock properties neighboring the faults from the reservoir simulation model, is a range of fault transmissibility applied across the fault as shown in **Figure 55** for the Omar Sterling Cortez South (OSCS) fault.

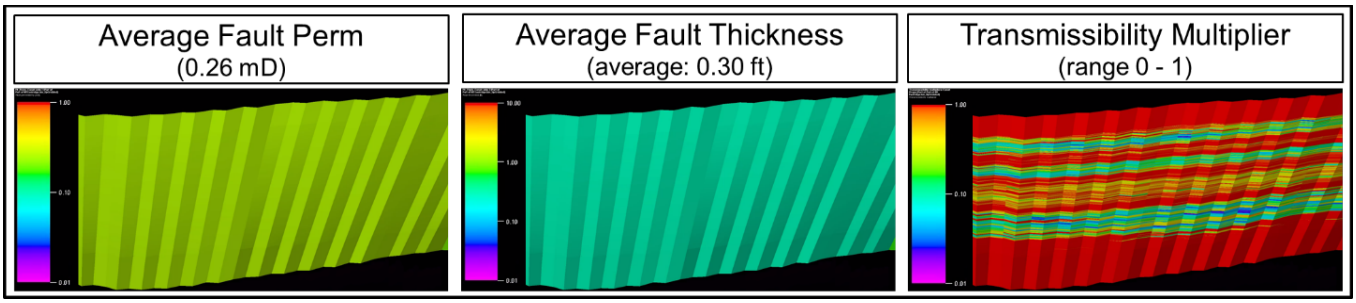

Figure 55. Input average fault permeability and thickness along with the resultant transmissibility multiplier for the Omar Sterline Cortez South (OSCS) fault. Heterogeneity of the transmissibility multiplier is driven by the gridblock properties on either side of the fault in the model and the average permeability and thickness assigned to the fault plane. Red values of 1.0 are associated with shale-on-shale or sand-on-shale connections whereas cooler colors are associated with sand-on-sand connections.

The results of the fault characterization property averages are shown below in **Table 4**. Fault properties for displacement, SGR, thickness, permeability, and threshold pressure are calculated along the fault plane with the structural interpretation and the Vcl characterization. The averages for fault thickness, permeability, and threshold pressure are used in the simulation model. This results in fault transmissibility multipliers that vary as a function of gridblock properties (see **Figure 55**) and an average threshold pressure for the entire fault.

Table 4. Fault names and average values for fault displacement, SGR, thickness, permeability, and threshold pressure.

Fault Name	Fault Displacement Mean (ft)	Shale-Gouge-Ratio (SGR) Mean	Fault Thickness Mean (ft)	Fault Perm Mean (mD)	Threshold Press Mean (psi)
Omar Sterling Cortez South	**30**	**0.250**	**0.300**	**0.260**	**8.4**
Canfield	**38**	**0.280**	**0.380**	**0.160**	**15.7**
Ap North	**66**	**0.260**	**0.660**	**0.200**	**11.7**
Luck	**68**	**0.310**	**0.680**	**0.130**	**23.8**
Ap Sr	**91**	**0.340**	**0.910**	**0.140**	**20.8**
Wilmar 2	**256**	**0.370**	**2.560**	**0.050**	**51.4**
Wilmar Main	**212**	**0.390**	**2.120**	**0.070**	**27.4**
Wilmar 3	**167**	**0.320**	**1.670**	**0.070**	**31.3**
Wilmar_Antithetic_2	**100**	**0.270**	**1.000**	**0.230**	**11.6**
Wilmar_Antithetic_1	**41**	**0.220**	**0.410**	**0.310**	**8.4**
Apollo Jr & Jr 1	**29**	**0.210**	**0.290**	**0.300**	**7.7**

An injection well test followed by a pressure fall-off was conducted on the KC20050X well, which is located within a semi-rhombohedral fault block created by the intersection of the Apollo Jr., Apollo North, Apollo Sr., and China Grade faults. The well test injected fresh water for 110 hours followed by shutting the well in and monitoring the pressure (via a downhole gauge) for another 110 hours.

Analysis of the pressure response during the shut-in period is called a pressure transient analysis (PTA) and indicated an average permeability of 253 mD and the presence of four "no-flow" boundaries located 700 ft, 4000 ft, 5000 ft, and 7000 ft away from KC20050X (**Table 5** and **Figure 56**). These distances correspond to the locations of the four faults that define this fault block. This implies that the four faults that define the Apollo Jr. fault block are hard-linked and exhibit sealing capacity. The PTA is discussed further in the model validation section of the AoR and Corrective Action portion of this permit.

Table 5. Analytical parameters for PTA fall-off test.

Parameter	Value	Boundary	Distance
Permeability * Thickness	49,335 mD*ft	North (no flow)	7,000 ft
Thickness	195 ft	East (no flow)	700 ft
Average Permeability	253 mD	South (no flow)	4,000 ft
		West (no flow)	5,000 ft

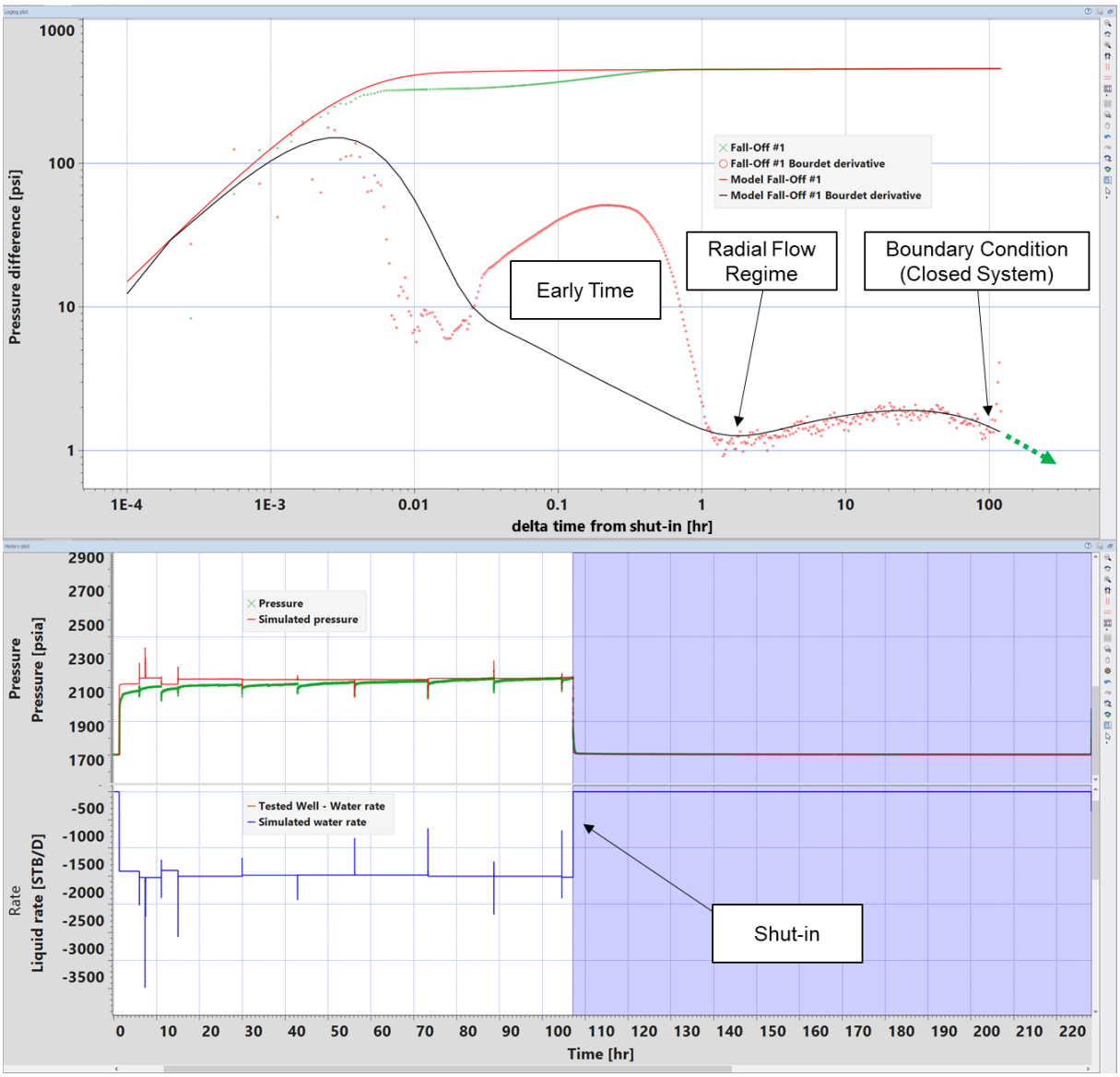

Figure 56. Liquid rate and pressure response of the injection well test (lower image) and the pressure transient analysis (top image). Top image shows the analytical match of the well test pressure response (solid black line) and data (red dots). Identification of the radial flow regime is used to interpret the permeability thickness and the downward slope of the late time (identified by green dotted arrow) is used to characterize the boundary condition (closed outer boundary). The early time data is believed to be a near wellbore phenomena and not impacting the identification of the radial flow regime or the late time boundary condition.

Additional Evidence of Fault Seal Capacity

Over the course of the Kern River Oil field development, wells occasionally targeted the Vedder Sand. Oil accumulations were discovered against the Apollo Sr and Apollo Jr faults as shown in **Figure 53**. These accumulations further demonstrate the sealing potential of faults in the Vedder Sand.

Geochemical gas chromatographic (GC) analysis of oils from the 2nd and 3rd Vedder Sands shows a lack of lateral fluid communication through the faults in the 3rd Vedder Sand and a lack of vertical fluid communication through the faults or intraformational shales between the 2nd and the 3rd Vedder Sand. **Figure 57** is 4 GC samples where the two top samples are from the 3rd Vedder for the Section 3 819X (S3_0819X) and Revenue 4X (REV0004X) wells (from left to right, respectively) and the two bottom samples are from the 2nd Vedder for the same two (2) wells. These two (2) wells are in the same accumulation of oil, as shown in **Figure 53**. The difference between the GC signatures between the 2nd and 3rd Vedder Sand are distinct. In the 2nd Vedder samples, a larger relative presence of the NC19 through NC30 components is clearly visible when compared to the 3rd Vedder samples.

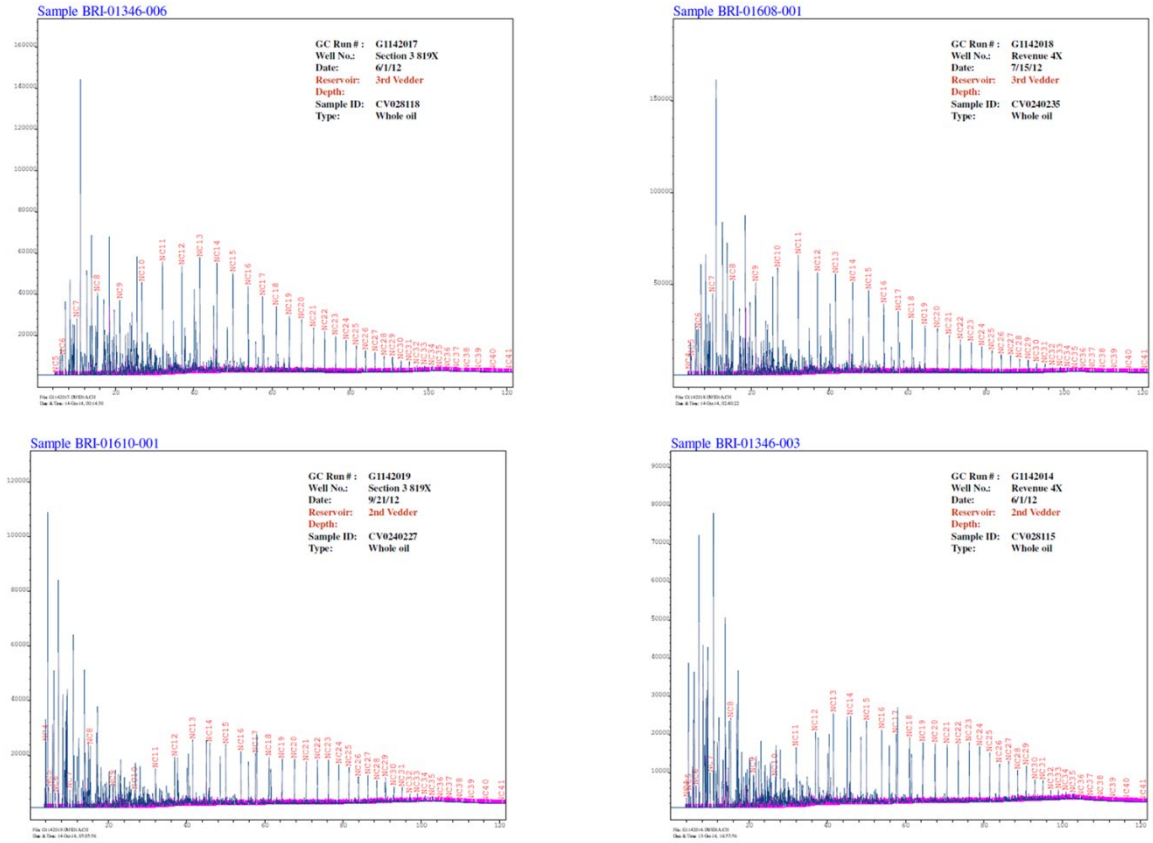

Figure 57. Gas chromatograph (GC) samples from the 3rd Vedder oil samples (top) and 2nd Vedder oil samples (bottom) for wells Section 3 819X (S3_0819X) and Revenue 4X (REV0004X) (left to right, respectively). 2nd Vedder oil samples show more presence of the heavier end components (NC19 to NC30) than the 3rd Vedder samples. This demonstrates a lack of vertical communication between the 2nd and 3rd Vedder Sand.

Below in **Figure 58** are three (3) GC samples from the 3rd Vedder for the Section 3 819X (S3_0819X, top), Revenue 4X (REV0004X, middle), and Kern Co. Lease 2 50X (KC20050X, bottom) wells. Revenue 4X and Section 3 819X are in the same fault block, whereas KC20050X is in a separate fault block, as shown in **Figure 53**. The difference between the GC signatures of the top two (S3_0819X & REV0004X) and the bottom well (KC20050X) is visible in the relative presence of the NC7 through NC11 components when compared to the other components.

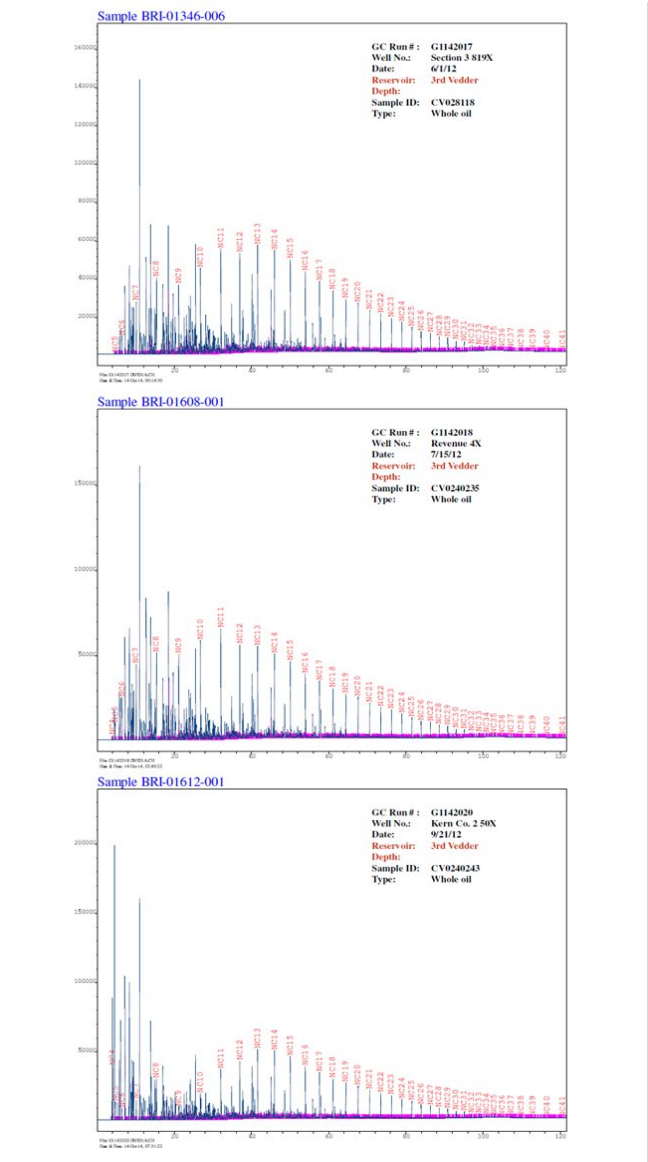

Figure 58. GC oil samples from the 3rd Vedder for the Section 3 819X (S3_0819X), Revenue 4X (REV0004X), and Kern Co. Lease 2 50X (KC20050X) wells. 3rd Vedder oil sample from the Kern Co. Lease 2 50X (KC20050X) well (on the footwall of the Apollo Jr. fault) shows less relative presence of the lighter components (NC7 through NC11) when compared to the other two (2) wells on the footwall of the Apollo Sr fault.

This data demonstrates that the subunits of the Vedder Sand do not communicate vertically or laterally through the faults or vertically through intraformational shale layers.

In summary, evidence suggests faults within the Vedder Sand in the AoI seal. Chevron has designed the Testing and Monitoring Plan to collect the necessary data to verify injected CO_2 migrates as expected through the life of the project and if needed, modify computational models and the AoR.

Injection and Confining Zone Details [40 CFR 146.82(a)(3)(iii)]

Geologic containment within the Vedder Sand is supported by the presence of multiple, laterally extensive marine shales at depths where they have undergone sufficient burial compaction to reduce porosity and increase sealing capabilities. Fine-grained seals are recognized by high Gamma Ray (GR) log responses, negative Spontaneous Potential (SP) log responses, low Resistivity (R) log responses and separation between the density and neuron porosity log responses. Injection and containment zones were delineated in legacy wells across the Project area using these log responses across the AoI. Stratigraphic seals are characterized by their intrinsic lithologic properties (i.e., fine-grained layers with small pore throat sizes), electric log character, as above, and by reservoir pressure data that indicate pressure connection and/or compartmentalization.

Reservoir and seal properties were derived from whole-core and sidewall core analyses of wells in the Project AoI (**Figure 59** and **Figure 60**).

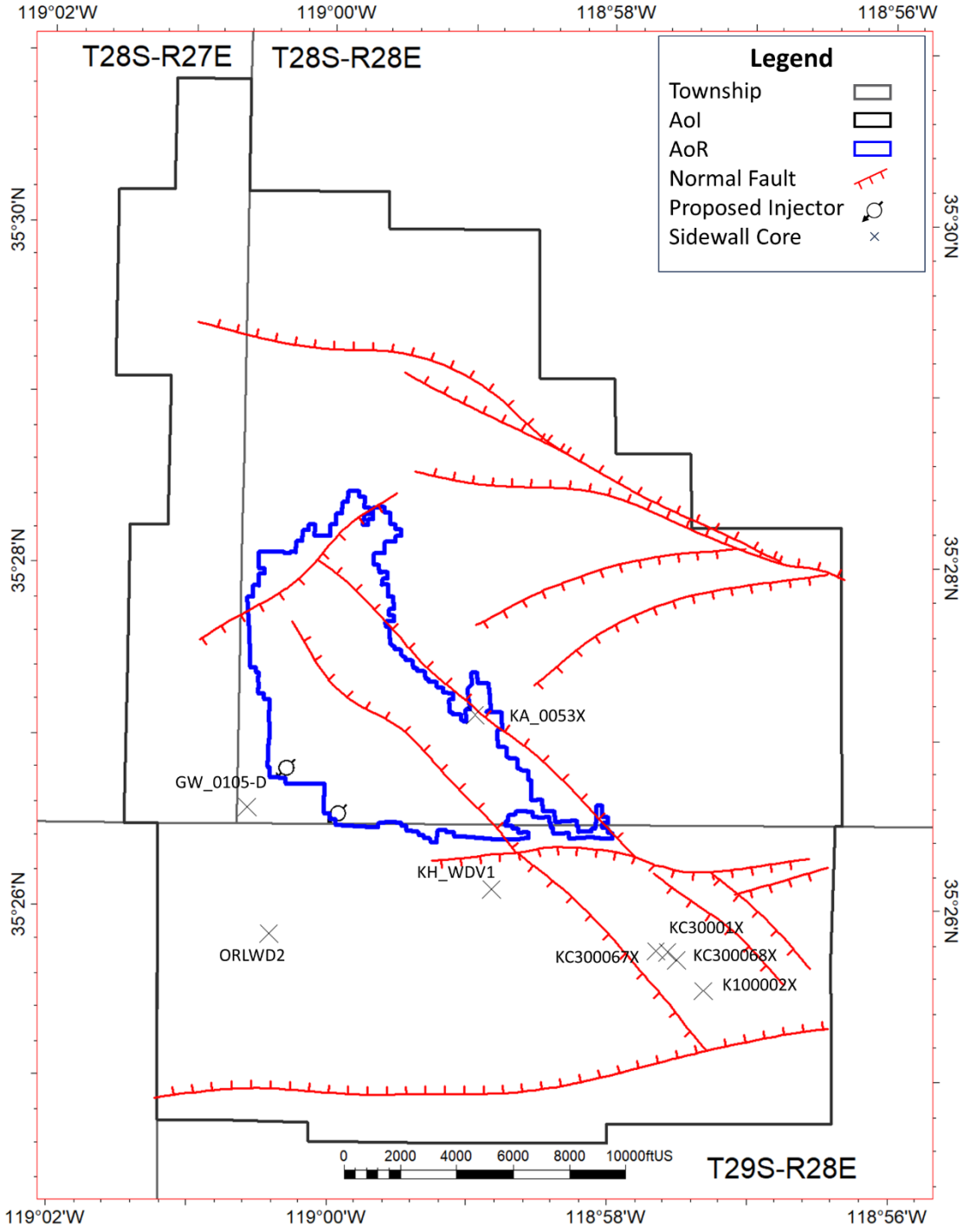

Figure 59. Location of sidewall core data used to characterize the Freeman–Jewett Silt primary seal.

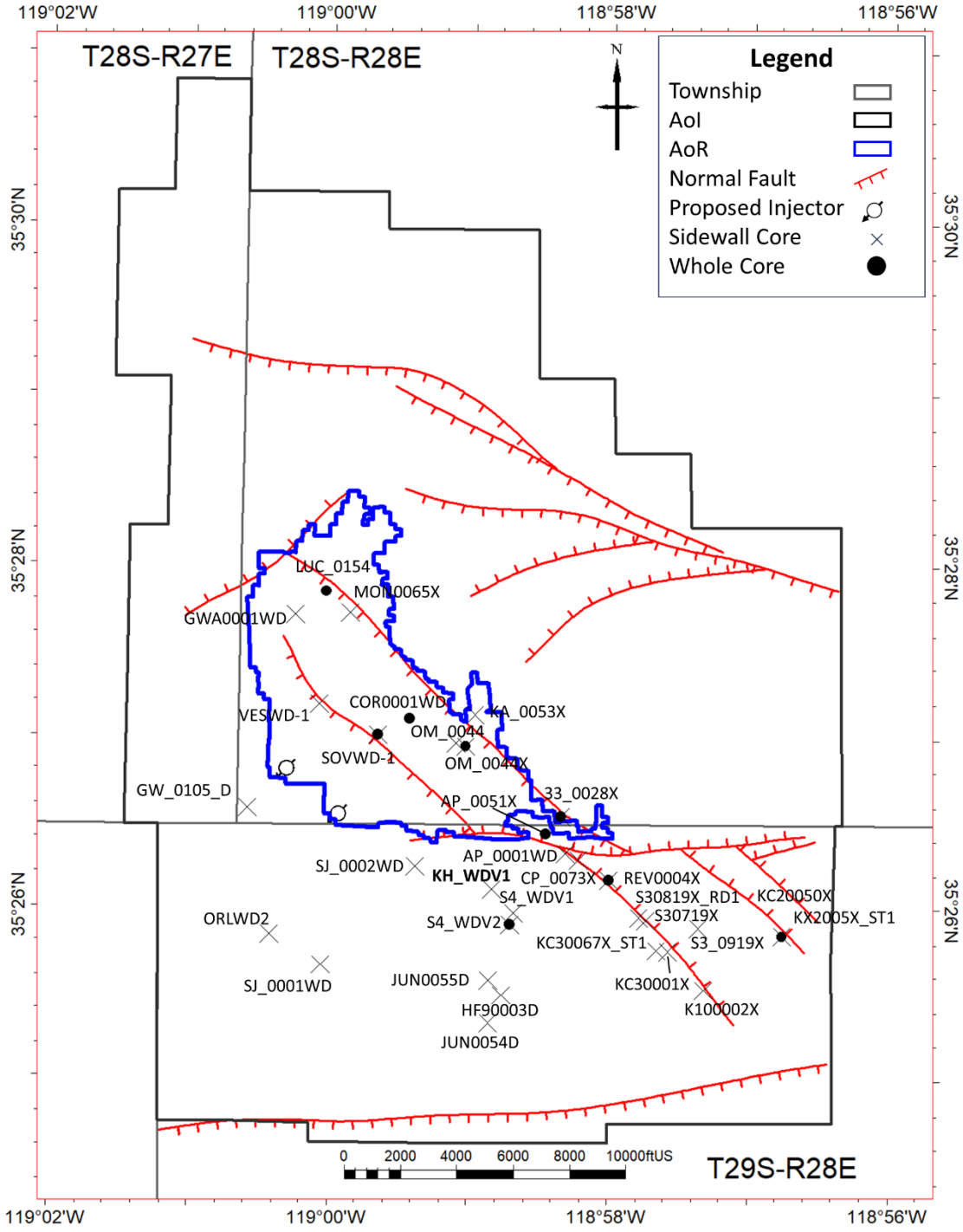

Figure 60. Location of wells with core data for the Vedder Sand.

The KH_WDV1 well is used herein as a reference for Project area stratigraphy because it fully penetrates the Cenozoic section in the Project AoI (**Table 6** and **Figure 61**). **Table 6** is a summary of interpreted stratigraphic markers and interval thickness for this well. Examples of well-log responses are shown for Spontaneous Potential, Gamma Ray, Resistivity, and porosity derived from density and neutron logs (NPHIEDS, DPIEDS). **Table 7** is a summary of depth, thickness, porosity, and permeability ranges for the Freeman–Jewett Silt, Vedder Sand, and Famoso sand.

Table 6. Well markers in KH_WDV1 (API#040306065200). Thickness has not been adjusted for bedding dip.

Unit	Depth (MD ft)	Thickness (ft)	Comment
Kern River Fm	0	1413	
Chanac Fm	1413	175	
Santa Margarita Sand	1588	392	USDW zone (base of fresh water at 1464 ft)
Round Mountain Silt	1980	856	
Olcese Sand	2836	606	
Freeman–Jewett Silt	3442	1212	Top of upper confining zone
Vedder Sand	4654	1116	Top of injection zone
1st Vedder (Vd1)	4654	251	
2nd Vedder (Vd2)	4905	190	
3rd Vedder (Vd3)	5095	285	
4th Vedder (Vd4)	5380	258	
5th Vedder (Vd5)	5638	132	Includes lower confining zone
Famoso sand	5770	171	
Walker Fm	5941	88(?)	
Basement	6029(?)	–	Probable granitic basement at bottom of well
Total depth	6079	6079	

Laterally extensive shale zones within and above the Vedder Sand form multiple vertical seals between proposed injection zones and the base of Underground Sources of Drinking Water (USDW) in stratigraphically higher intervals (**Figure 61**). In the AoI, more than 2,500 ft of overburden exists between the top of the Vedder Sand and the base of the Santa Margarita USDW. The Freeman–Jewett Silt forms a widespread, thick top-seal for the Vedder Sand. The Olcese sand is vertically bounded by thick laterally extensive seals. The Chanac and Santa Margarita Formations are low-salinity aquifers that overly the Round Mountain Silt, which is itself a regional seal. The base of the Santa Margarita Formation marks the base of USDW in the AoI. The overlying Kern River Formation is an exempted aquifer (California Division of Oil and Gas, 1973; see California Department of Conservation, 1981, 1982, and 2015). Additionally, the Vedder Sand is also an exempted aquifer (California Department of Conservation, 1982).

Table 7. Summary of depth, thickness, porosity, and permeability ranges for the Freeman–Jewett Silt, Vedder Sand, and Famoso sand.

Within AoI	Elev. (ft)			Thickness (ft)			PHIE Porosity (%)			Permeability (mD)		
Unit	**Mean**	**Min.**	**Max.**	**Mean**	**Min.**	**Max.**	**Mean**	**Min.**	**Max.**	**Mean**	**Min.**	**Max.**
Freeman–Jewett Silt	-2,610	-4,590	-1,100	1,140	580	1,420	---	---	---	---	---	---
1st Vedder (Vd1)	-3,750	-1,980	-5,760	270	180	360	0.29	0.20	0.34	3,580	510	17,470
2nd Vedder (Vd2)	-4,020	-2,270	-5,980	150	100	220	0.27	0.23	0.32	2,900	660	8,820
3rd Vedder (Vd3)	-4,170	-2,450	-6,200	250	140	300	0.28	0.23	0.33	470	150	940
4th Vedder (Vd4)	-4,420	-2,630	-6,450	260	170	300	0.29	0.23	0.33	4,550	1,480	9,090
5th Vedder (Vd5)	-4,680	-2,850	-6,700	140	80	220	---	---	---	---	---	---
Famoso sand	-4,820	-3,070	-6,760	---	---	---	---	---	---	---	---	---

Within AoR	Elev. (ft)			Thickness (ft)			PHIE Porosity (%)			Permeability (mD)		
Unit	**Mean**	**Min.**	**Max.**	**Mean**	**Min.**	**Max.**	**Mean**	**Min.**	**Max.**	**Mean**	**Min.**	**Max.**
Freeman–Jewett Silt	-2,720	-3,020	-2,310	1,180	1,060	1,340	---	---	---	---	---	---
1st Vedder (Vd1)	-3,910	-3,470	-4,300	270	240	300	0.29	0.27	0.32	3,580	1,810	7,000
2nd Vedder (Vd2)	-4,180	-3,760	-4,540	140	130	160	0.27	0.24	0.31	3,120	1,370	6,380
3rd Vedder (Vd3)	-4,320	-3,880	-4,700	260	230	290	0.28	0.23	0.31	470	260	730
4th Vedder (Vd4)	-4,580	-4,130	-4,980	270	250	300	0.29	0.25	0.31	4,990	2,450	8,540
5th Vedder (Vd5)	-4,860	-4,410	-5,270	110	90	170	---	---	---	---	---	---
Famoso sand	-4,970	-4,530	-5,360	---	---	---	---	---	---	---	---	---

The proposed injection zone includes sand-prone intervals within four of the five mapped Vedder subunits (1st Vedder – 4th Vedder). Laterally extensive fine-grained units provide secondary seals within the Vedder Sand injection zone. The top-seal is defined by a >1000 ft thick succession of marine siltstone and shale in the Freeman–Jewett Silt. The bottom-seal is defined by shale at the base of the Vedder Sand and a paleosol at the top of the Famoso. In addition to the primary top and bottom stratigraphic seals, laterally continuous secondary seals are mapped throughout the Project AoI between the injection interval and the base of USDW (e.g., Base of Santa Margarita Sandstone/Top of Round Mountain Silt).

The Vedder Sand consists of sands and shales that form the basis for sub-divisions of the formation into the 1st Vedder, 2nd Vedder, 3rd Vedder, 4th Vedder and 5th Vedder subunits (**Figure 61**). Intraformational shales between each Vedder sand interval are associated with flooding surfaces and are continuous beneath the AoR (**Figure 62** and **Figure 63**). The thicknesses of Vedder shales are on the order of 10s of feet to 100 feet.

Each Vedder subzone is capped by a laterally extensive shale that indicates multiple vertical stratigraphic seals. No discontinuities in fine-grained layers have been observed in borehole penetrations (e.g., core, image logs, wireline logging) across the AoI, indicating that these shaley zones provide extensive vertical sealing.

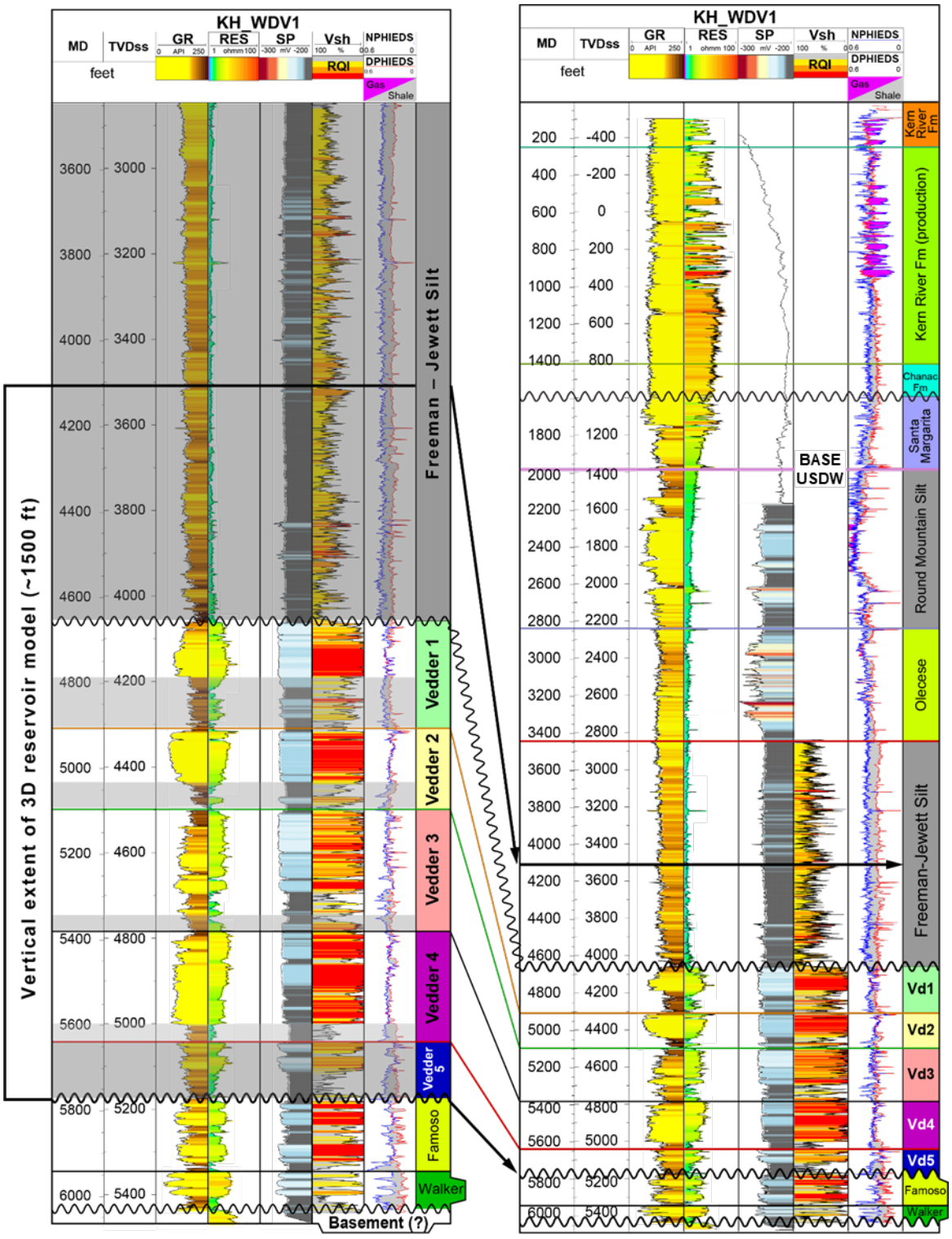

Figure 61. Example of borehole geophysical logs and stratigraphic markers for the KH_WDV1 well, illustrating major the tops of stratigraphic units and the vertical extent of the 3D reservoir model. Shaded areas denote primary (darker) and secondary (lighter) seals. From left to right, the logs shown are Gamma Ray, Resistivity, Spontaneous Potential, Vshale with RQI overlay, and Neutron-Density.

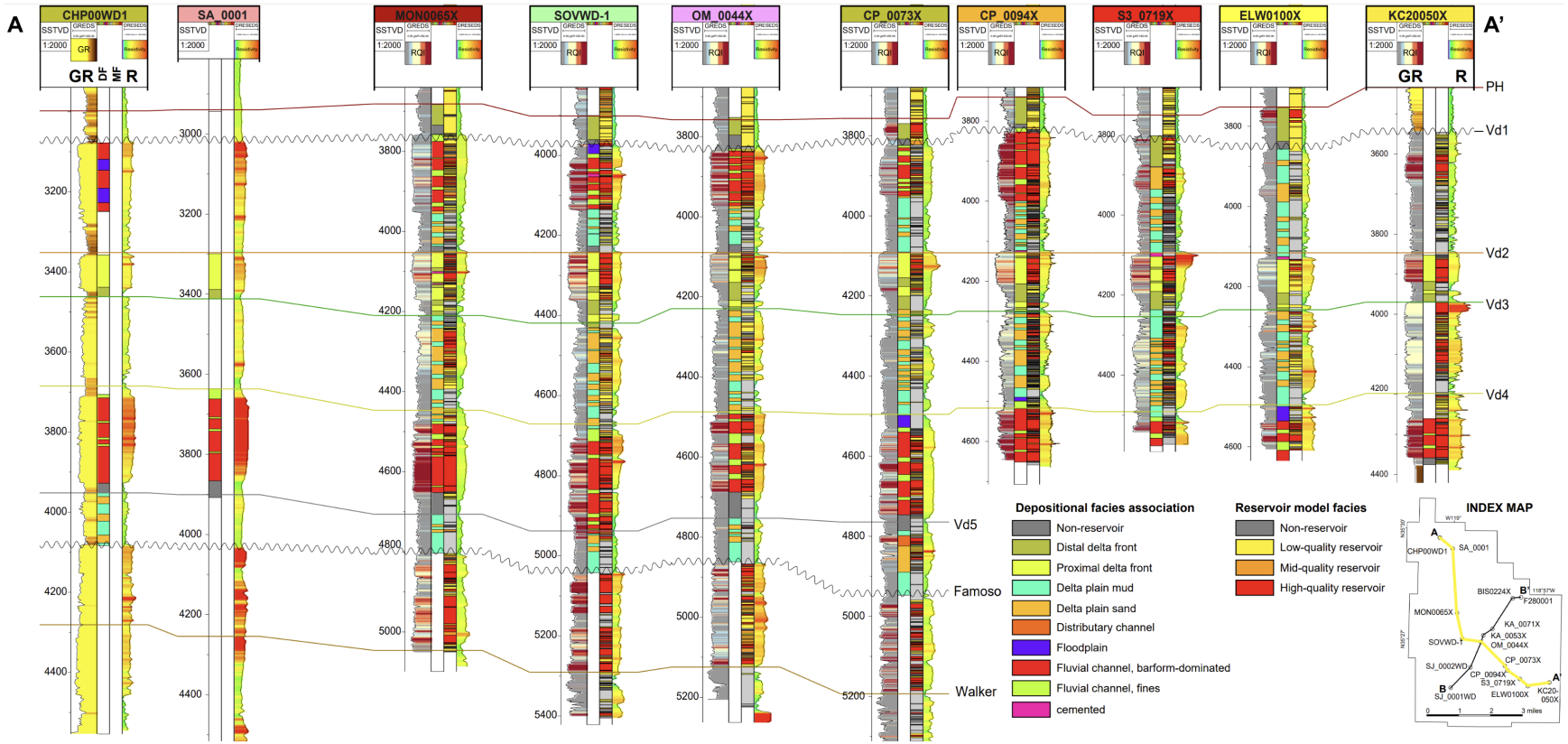

Figure 62. Depositional strike correlation of well logs showing interpreted depositional facies and reservoir-model facies. Stratigraphic datum is top 2nd Vedder.

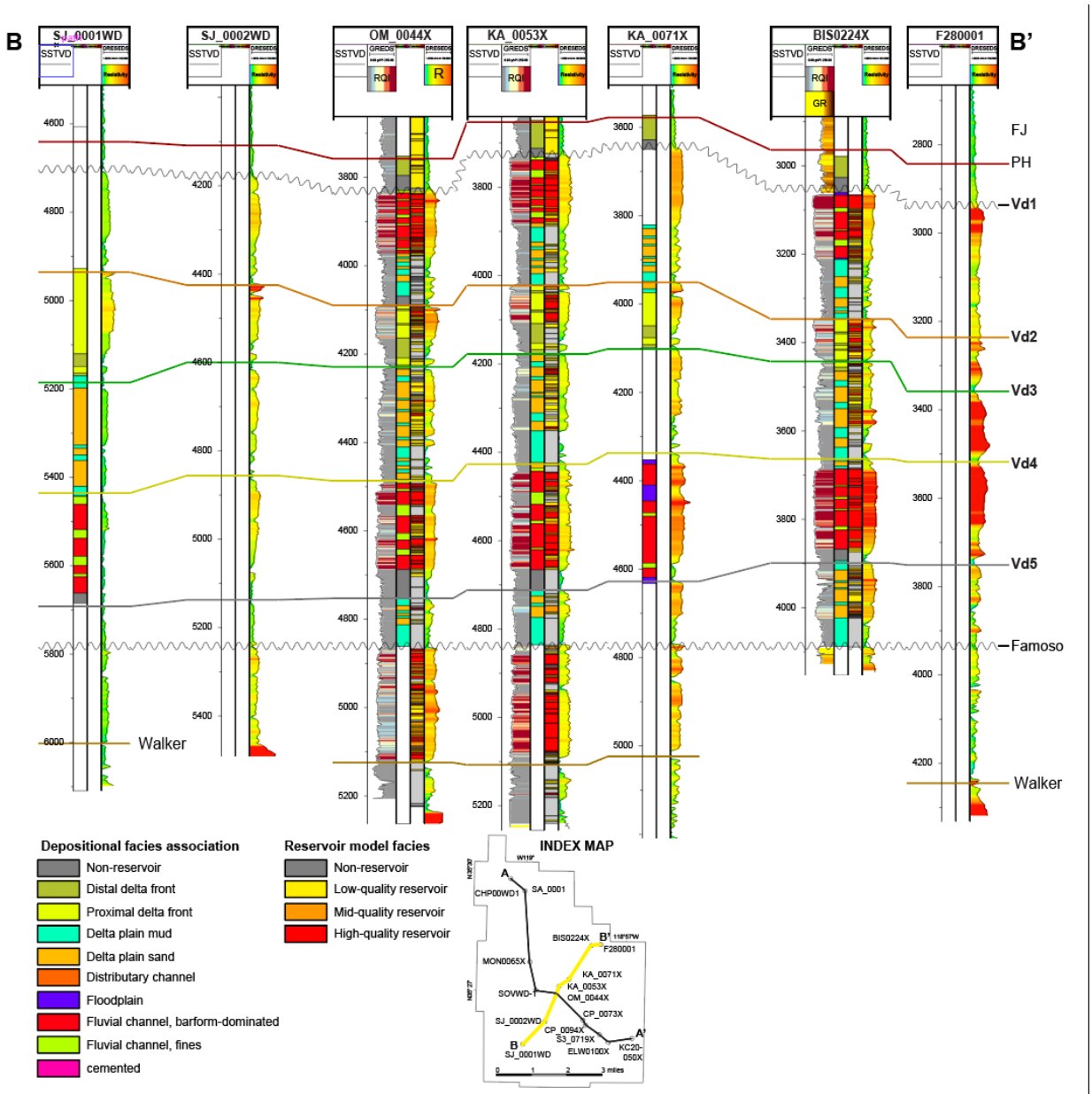

Figure 63. Depositional dip correlation of well logs showing interpreted depositional facies and reservoir-model facies. Stratigraphic datum is base Vedder Sand

Vedder Sand mineralogy data from x-ray diffraction (XRD) measurements two (2) wells within the AoR (AP_0051X, API# 040296721700; 33_0028X, API# 040296641100) and an additional well within the AoI (OM_0044X, API# 040296655800) indicates a mixture of quartz and felspar. Clays occur in distinct layers, as distinct clasts, and in bioturbated intervals, depending on the specific environment of deposition. 19 data points from these three (3) wells indicates clay mineral content ranges of 10-45% and consists of illite, which occurs as authigenic, pore-lining cements and as detrital matrix clay.

Log data from the same wells indicate the presence of occasionally carbonate cements (i.e., calcite and dolomite) that is low (<3% by weight) and is not expected to pose a key concern for mineral dissolution of the top-seal. Well logs indicate that carbonate-rich (~30% by volume) layers occur sporadically through the Vedder Sand.

During construction of the injectors, Chevron plans to collect samples from the Freeman-Jewett Silt and perform similar analysis. Please refer to the Pre-Operational Testing and Logging Plan for additional details on Chevron's future data collection. Currently, sufficient seal quality and capacity for the Freeman-Jewett Silt is supported by geomechanical well data (sourced from well AP_0051X within the AoR and wells MON0065X and KC20050X_ST1 within AoI; discussed in detail in the Geomechanical and Petrophysical Information section of this document), estimates of compaction state from present-day overburden loads (i.e., present-day overburden is essentially the maximum overburden), and observations of light oil and gas trapping in parts of the Kern River Oil Field.

Compaction trends vary by basin and are dependent on mineralogy, grain size, and burial history (sedimentation rate); however, mechanical compaction and porosity reduction in siliciclastic shale tends to diminish with increasing depth below one kilometer (~3,200 ft) of depth (**Figure 64**). Porosity generally decreases with increasing depth and follows typical compaction trends for porosity loss in shale and sand. The minimum overburden depth for the top of the Vedder Sand in the AoR is ~4,400, and therefore deeper than the overburden thickness threshold of approximately 1 km (~3,200 ft).

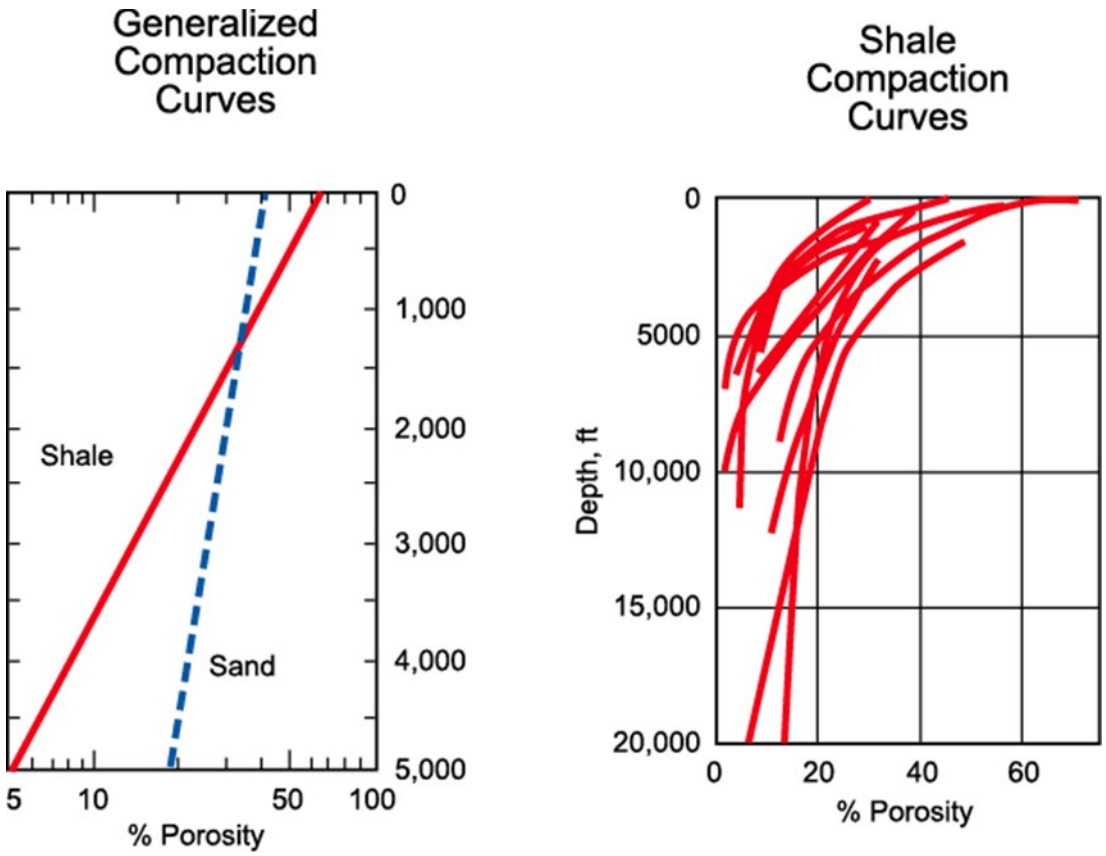

Figure 64. General compaction profiles for porosity loss in shales and sands (modified after Magara, 1986). Note the vertical scale change between plots.

Proposed Upper Confining Zone

The Freeman–Jewett Silt is the primary caprock seal for the Vedder Sand. The Freeman–Jewett Silt is laterally continuous across the region and has a mean gross thickness of 1,140 ft across our AoI. Thickness variations along fault trends are due to structural juxtapositions that locally decrease apparent thickness across normal faults. Faults mapped in the underlying Vedder have maximum throws of 380 ft, which are approximately one third of the average thickness of the caprock seal. Therefore, the Freeman–Jewett Silt is interpreted as a continuously sealing unit in the AoI.

Within the Project AoI, characteristics of the Freeman–Jewett Silt were derived from 70 well penetrations and mapping from 3D seismic data. At the proposed Project injection sites, the Freeman–Jewett Silt is at an elevation of -2,950 and -2,990 ft TVDSS at ANO9002INJ and MC19001INJ respectively. The elevation ranges from -2,610 to -4,590 ft TVDSS across the AoI. The Freeman–Jewett confining zone is laterally continuous across the Project AoI. The thickness of the upper confining zone ranges between approximately 580 and 1,420 ft within the Project AoI. At the proposed injection site, the Freeman–Jewett confining zone is approximately 1,270 ft and 1,260 ft at ANO9002INJ and MC9001INJ respectively.

Permeability data for the Freeman–Jewett Silt comes from NMR measurements taken from the KH_WDV1 well (**Table 8**). The NMR permeability is preferred over sidewall core permeability due to the physical damage that takes place with percussion sidewall core sampling (disaggregation and fracturing during the sampling process (e.g., Bajsarowicz, 1992)) and sampling bias from wells drilled through the Freeman-Jewett Silt (sidewall core was preferentially sampled from thin, discontinuous, sand prone intervals where encountered). Values for horizontal permeability are geometrically averaged over all depths. Vertical permeability is calculated by applying an anisotropy ratio of 0.1 to the horizontal permeability and then harmonically averaging over all depths. Averages for the Freeman-Jewett Silt show a horizontal permeability of 0.784 mD and a vertical permeability of 0.001147 mD. Average porosity over the Freeman-Jewett Silt is 21 percent.

Table 8. Summary of permeability data for the Freeman–Jewett Silt.

Well	Permeability Horizontal (mD)	Permeability Vertical (mD)
KH_WDV1	0.784	0.001147

In addition to the presence of a thick and continuous caprock seal provided by the Freeman–Jewett Silt, numerous secondary seals occur within, below, and above the Vedder Sand, which improves overall seal containment. The Round Mountain Silt, which overlies the Freeman–Jewett Silt, contains relatively thick, laterally continuous, fine-grained siltstone and shale intervals that also function as vertical seals. Intraformational seals within the Vedder sand have been interpreted as marine flooding surfaces (e.g., Tye et al., 1993), which supports additional secondary sealing capabilities.

An important aspect of a vertical confining layer is understanding the variation in fracture pressure between the mechanical top-seal and the injection horizon in such a manner as to limit fracture propagation in either layer. Chevron conducted a leak-off test in 2022 on the Freeman–Jewett Silt in KC20050X, a well within the AoI. Results yielded a Fracture Closure Pressure (FCP) of 2425 psi, equivalent to 0.63 psi/ft. These results are analyzed and discussed in detail in the Geomechanical and Petrophysical Information section of this permit, demonstrating that the Freeman–Jewett Silt can provide sufficient vertical confinement.

Rocks with different effective pore-throat radii have different seal capacities for different fluid types. For a CO_2-water system, interfacial tension varies largely by the subsurface density difference of the two fluids. Wetting contact angle test data indicate that pressure, mineralogy, and water chemistry impart an influence on the contact angle. Core analysis sourced from the Vedder Sand within the AoI (well S4_0002WDV) was analyzed at reservoir temperature and pressure to determine CO_2-brine interfacial tension and contact angles of 30.2 mN/m and 35°-44°, respectively.

Chevron plans to collect whole-rock data and wireline logs across the Freeman–Jewett Silt during the construction phase of the project. Laboratory analysis (e.g., porosity and permeability, MICP, XRD, etc.) and sedimentologic description of the core can validate inputs for seal analyses and reservoir modeling. For more information on Chevron's data collection strategy, see the Pre-Operational Logging and Testing Plan.

Proposed Injection Zone

The Vedder Sand has been mapped across the AoI and in area surrounding our AoI using logs from 210 well penetrations and 3D seismic where available. Reservoir properties were determined from standard and special logging suites, whole-core, and sidewall-core data from 70 partial to full penetrations. Reservoir properties are considered representative of the Vedder Sand within the AoI (**Table 9**). Reservoir porosity was determined through analyses of neutron and density porosity logs, whole-core and sidewall-core data, and application of the Archie equation to well-log parameters. Within the AoR the Vedder Sand has an average thickness of ~1,050 ft with an average porosity of 28% and an average permeability of ~3,000 mD. Within the AoR, the top of the Vedder Sand has an average elevation of -3,910 ft TVDSS and ranges from -3,470 to -4,300 ft TVDSS.

The existing wells and associated logs and core comprise a rich source of petrophysical and routine and special core analysis data (RCA and SCAL) to characterize the Vedder Sand and both overlying and underlying units. The overall quality of borehole geophysical logs varies with vintage and historical development objectives; thus, wells may have distinct types of logs across the AoI. The subsection below summarizes the legacy well evaluation, well logs, and special core analysis that support the geological interpretations and reservoir description of the Vedder Sand in the AoI. A summary of legacy borehole datasets for wells that penetrate the Vedder Sand is provided in the Petrophysical Information section of this document (see **Table 11**).

Table 9. Summary table of average reservoir and fluid properties of Vedder Sand in the AoI. *(Vd1-Vd4)

Average Reservoir Characteristics	Vedder Sand
No. of well penetrations	70
Depth to top (ft TVD)	4440
Top elevation (ft TVDSS)	-3750
Gross thickness (ft)	1070
Net-to-gross (%)	63
Porosity (PHIE, %)*	28
Permeability (mD)*	2900 (range: 470-4550)
Pressure (psi)	1850
Temperature (°F)	160
Water saturation (%)	80-100
Oil gravity (API°)	32-40
Water Quality (TDS, mg/l)	3500-14,000

The storage capacity of the Vedder Sand within the AoR is computationally determined to be 6.82 million tonnes, though it is worth noting that the Vedder Sand has significant additional capacity in other areas of the AoI.

In 2022, Chevron executed a step rate test within the AoI with well KC20050X using fresh water. At the time of execution, the well had just 10ft of perforations open. The results, shown in **Figure 65**, identified an injectivity of 8.1 bbl/d/psi. Though this injectivity is high, the small perforation window artificially limited injectivity. Chevron plans to complete the CO_2 injectors with significantly larger perforation intervals. Additionally, it is worth noting that the injectivity of supercritical CO_2 is expected to be even greater than that of water.

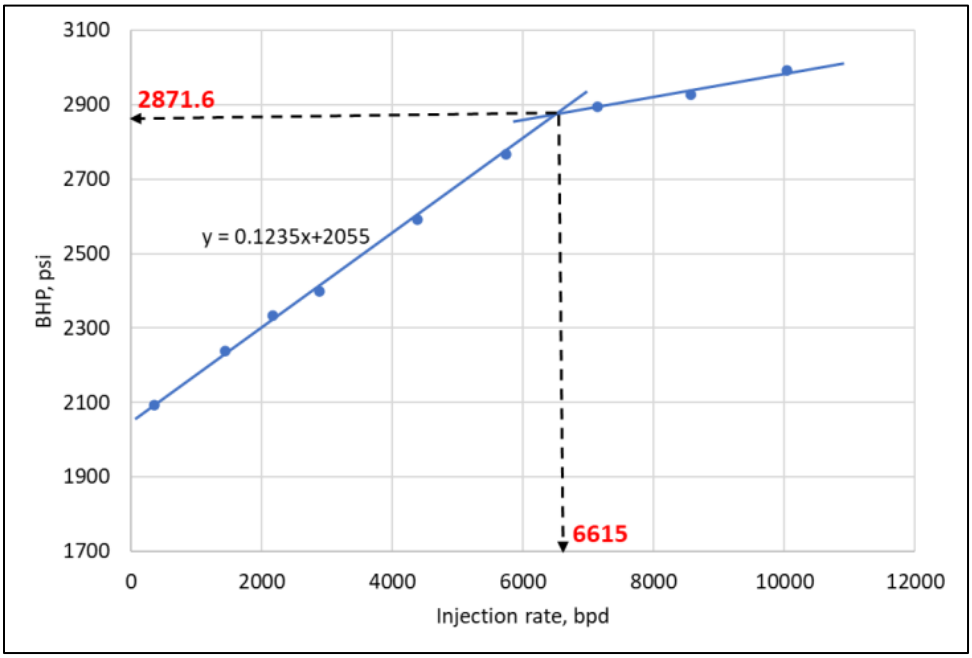

Figure 65. Interpreted Step Rate Test from KC20050X indicating an injectivity of 8.1 bbl/d/psi with fresh water and just 10ft of perforations.

Proposed Lower Confining Zone

The primary lower confining zone for the Vedder Sand is a mudstone at the base of the 5th Vedder (Vd5) subunit and, where present, a paleosol developed in the Famoso sand. Approximately 50 – 60 ft of shale occurs at the base of the Vedder Sand in the AoI and marks the contact with the underlying Famoso Sand.

Mechanical Earth Models

One-dimensional Mechanical Earth Models (MEM) were developed for three (3) wells (KC20050X_ST1, AP_0051X, and MON0065X, **(Figure 66** and **Figure 67**) to examine CO_2 storage potential of the injection zone, to complement fault stability analysis and to support induced seismicity modeling. The well selection for the 1D MEM study was based on CO_2 plume modeling and the relative position of mapped faults to evaluate the variability of potential stress in the Project AoI.

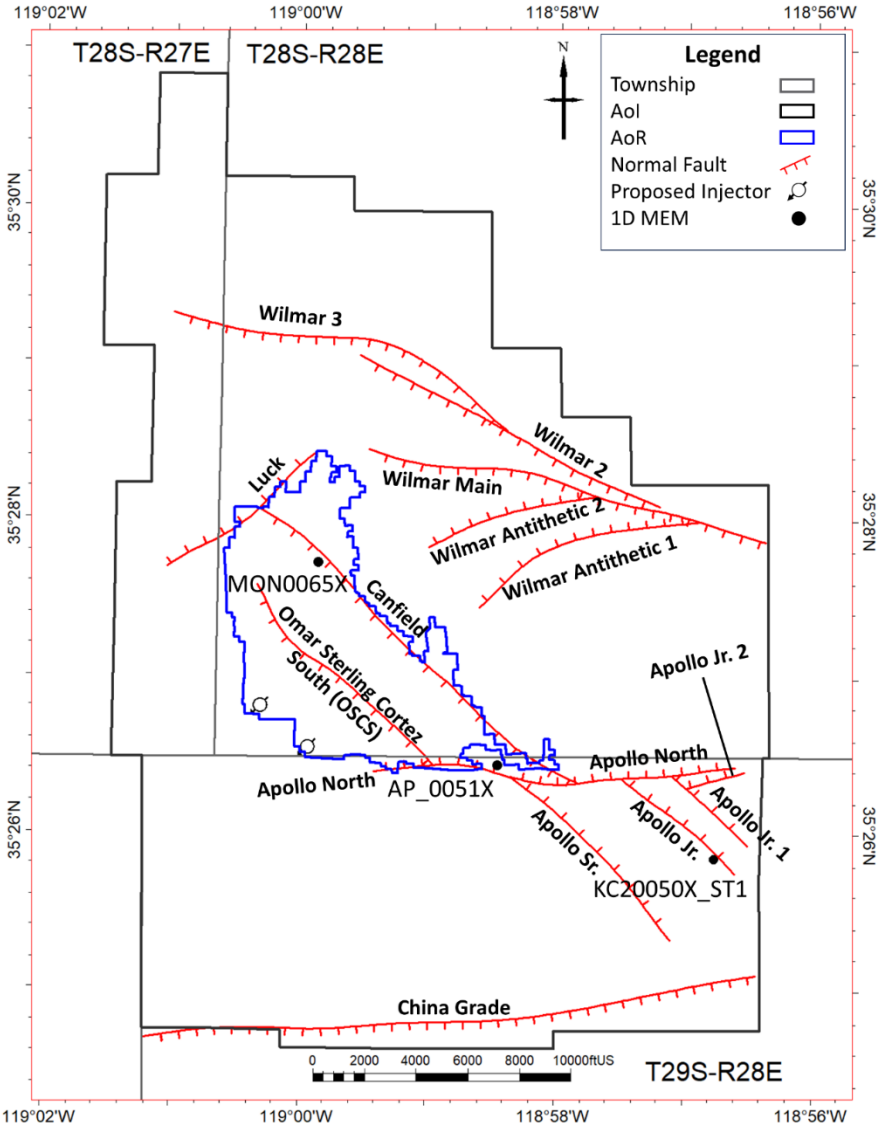

Figure 66. Location of faults intersecting the top of the Vedder Sand and 1D MEMs for wells AP_0051X, MON0065X, and KC20050X_ST1 used for the deterministic fault stability analysis.

A 1D MEM was generated for the KC20050X_ST1 well to evaluate the Vedder Sand and the Apollo Jr. fault, which intersects the wellbores between the 1st and 2nd Vedder subunits. Well-log data collected from KC20050X and KC20050X_ST1 include Gamma Ray, Density, Neutron, Porosity, Compressional Velocity, Shear Velocity, Caliper, and Image Logs. Drilling parameter data includes mud weight (MW), Equivalent Circulating Density (ECD), and Equivalent Static Density (ESD). Pressure measurements and Leak Off Test (LOT) information are used for calibration **(Figure 68**). In addition to the KC20050X_ST1 well, 1D MEMs were constructed for AP_0051X and MON0065X leveraging the same rock properties **(Figure 67).**

A post-drill 1D MEM was generated for the KC20050X_ST1 well (**Figure 67** and **Figure 75**). No losses or kicks were observed while drilling this well and the available borehole log data indicates stable wellbore conditions. Drilling induced tensile fractures or breakouts were not recognized in the Vedder Sand. Pore pressure in the Vedder Sand is constrained by formation pressure measurements that range from 1,628 to 2,117 psia at depths 4,310 to 5,417 ft MD, respectively. These pressures indicate downhole equivalent mud weights of 7.6 and 7.81 ppg between 4,310 and 5,417 ft MD.

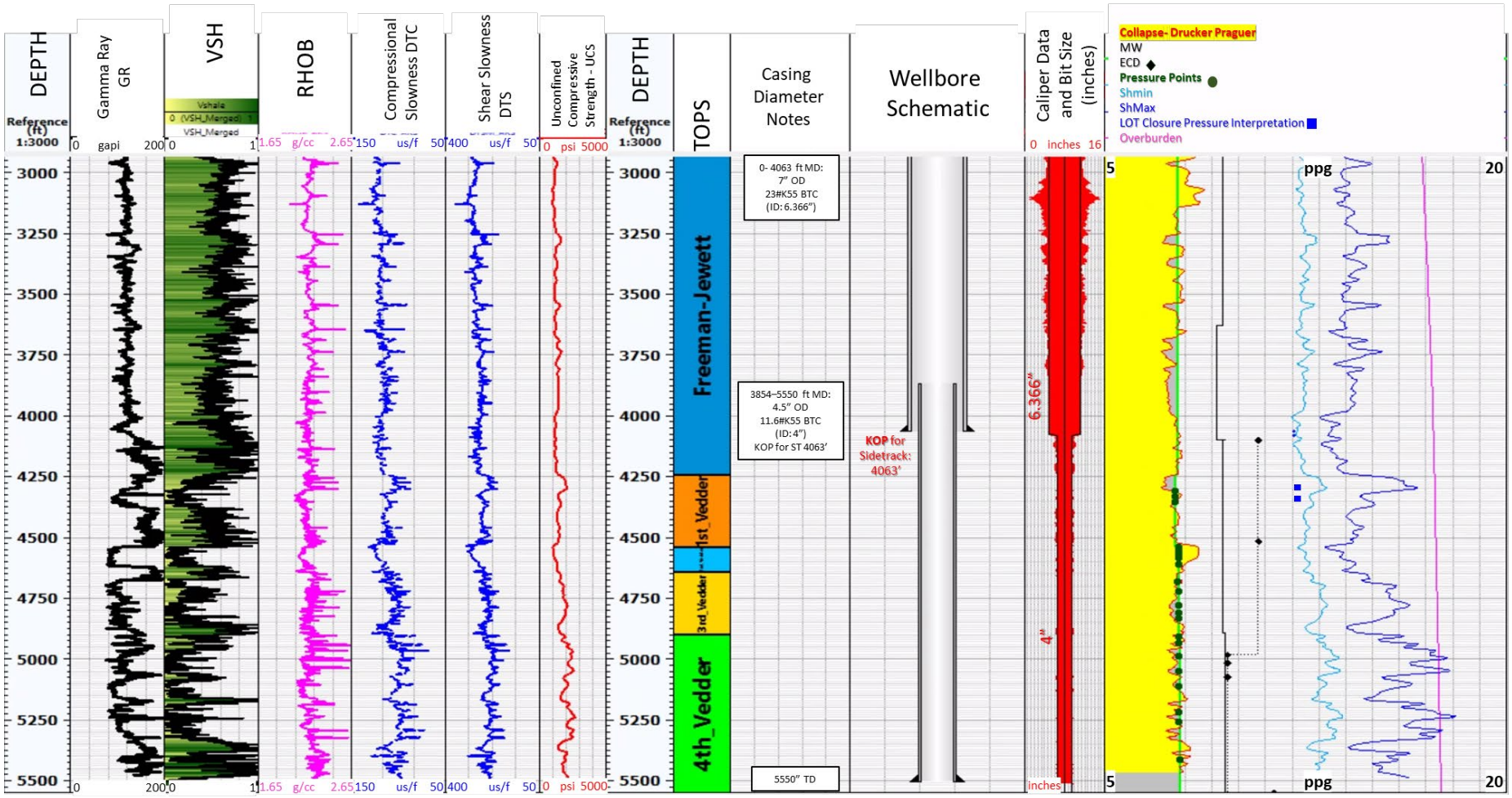

Figure 67. Data display examples of KC20050 and KC20050X_ST1 wells, showing logs used for 1D MEM analysis: Shale Volume, Density, Compressional and Shear sonic, and caliper data.

Figure 68 shows an example of an idealized extended LOT. The minimum horizontal principal stress (SHmin) has been calibrated to the fracture closure pressure (FCP) for the KC20050X_ST1 extended LOT at a depth of 3,858 ft. This LOT was conducted with a mud weight of 9.4 ppg. The first slope change on the LOT data is the Leak-Off Point (LOP) and is typically associated with microfractures or slight borehole volume expansion. As the LOT test continues towards formation breakdown, induced fractures propagate away from the wellbore, resulting in the Formation Breakdown Pressure (FBP). Fracture Propagation Pressure (FPP) is the point on the figure that indicates the pressure required to propagate a fracture away from the wellbore. Fracture Closure Pressure (FCP) is measured after the fracture closes and represents the lower boundary of SHmin. From the data available at KC20050X_ST1, the FBP is 3025 psi, which has a 15.1 ppg mud weight equivalent. The FCP is interpreted to be 2425 psi, or approximately 12.1 ppg mud weight equivalent. These data are used to calibrate SHmin and SHmax in the 1D MEM for KC20050X_ST1 (**Figure 71)**.

Analysis of sonic data collected in the KC20050X well indicates variable orientations of the maximum horizontal stress direction (SHmax) in the Vedder Sand (**Figure 71**). These orientations are derived from the dipole sonic dataset containing fast shear anisotropy information, which has azimuthal data that can be used for SHmax calibration. The 1st and 2nd Vedder have a SHmax that is oriented northeast to southwest, whereas the 3rd and 4th Vedder Sand have a northwest trend in SHmax orientation.

Uncertainties in rock strength and Unconfined Compressive Strength (UCS) parameters are the result of sparse calibration data available in the AoI at the depth of the Vedder target interval. The MEMs presented herein use static rock properties collected in the overlying Kern River Formation within the AoI. Histograms of modeled static Poisson's Ratio (PR), static Young's Modulus (YMOD), and UCS are shown on **Figure 72, Figure 73,** and **Figure 74**. The equation used for UCS is (Chang et al., 2006):

Equation 3.

$$UCS = 0.5\left(\frac{304.8}{\Delta t}\right)^{2.6}$$

where ΔT from the sonic log. Units of UCS are psi.

The 1D MEM results for KC20050X_ST1 suggest a safe mud weight window between pore pressure and SHmin (**Figure 67** and **Figure 75**). The pore pressure model in the Vedder Sands is constrained by formation pressure measurements that range from 1,628 to 2,117 psia at depths 4,310 to 5,417 ft MD. These pressures indicate downhole equivalent mud weights of 7.6 and 7.81 ppg between 4,310 and 5,417 ft MD. SHmin values from depths 4,310 to 5,417 ft range from 2555 psi – 3786 psi, or 12.2 – 13.9 ppg. Resulting stresses from the 1D MEM indicate a predominantly normal to strike-slip stress regime. This interpretation is based on the magnitudes of the minimum horizontal stress and maximum horizontal stress. The overlying formations, 1st through 3rd Vedder Sand subunits (Vd1-3) are in a predominantly normal stress regime, whereas the 4th Vedder Sand (Vd4) is in a marginally strike slip stress regime. In the 1st – 3rd Vedder Sand, the overburden gradient is the largest stress; SHmin and SHMax magnitudes do not exceed

overburden. In the 4th Vedder, the SHMax curve (**Figure 67** and **Figure 75**) begins to exceed overburden stress indicating a strike slip component is present.

An important aspect of a vertical confining layer is understanding the variation in fracture pressure between the mechanical top-seal and the injection horizon in such a manner as to limit fracture propagation in either layer. A LOT conducted in 2022 on the Freeman–Jewett Silt in KC20050X yielded a Fracture Closure Pressure (FCP) of 2425 psi, equivalent to 0.63 psi/ft, as shown in **Figure 69**. A Step Rate Test conducted in 2022 in KC20050X with water obtained a FPP gradient of 0.642 psi/ft in the Vedder Sand (**Figure 70)**. Given a low viscosity injection fluid (water), FPP can act as a proxy for FCP, which provides an opportunity to compare the two fracture gradients. Although the fracture gradient for the Freeman-Jewett Silt is lower, Chevron will operate with automated, fail-safe control systems to ensure bottomhole injection pressures are no more than 90 percent of the observed Propagation Pressure in the Vedder Sand. Taking these tests into account, the equivalent maximum injection pressure will be limited to an equivalent gradient of 0.578 psi/ft, which is lower than the fracture gradient observed in the Freeman–Jewett Silt.

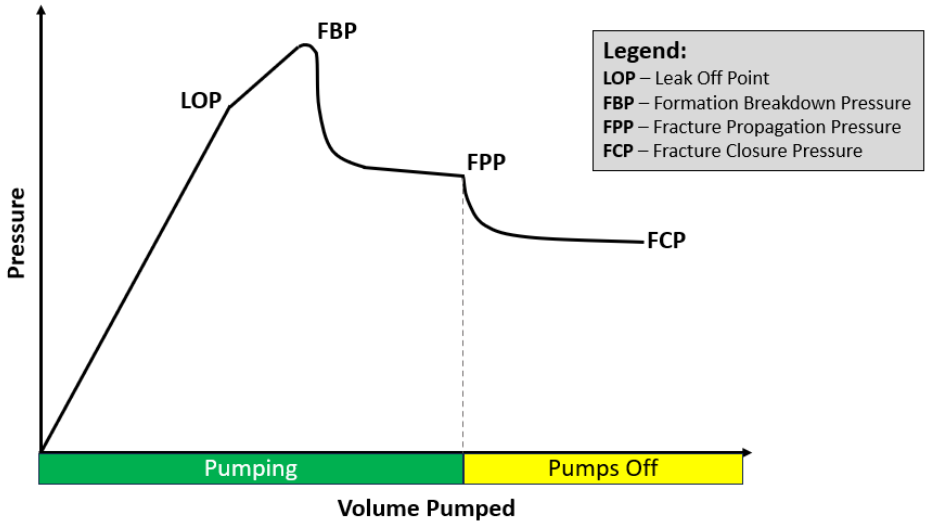

Figure 68. Schematic plot of an idealized leak-off test (LOT), showing formation breakdown pressure (FBP) and fracture closure pressure (FCP). The FBP in KC20050X_ST1 drilling reports has an EMW of 15 ppg, whereas the FCP has an EMW of 12.1 ppg, yielding an equivalent gradient of 0.63 psi/ft.

In addition to the KC20050X_ST1 well, 1D MEMs are generated for the AP_0051X and MON0065X wells (**Figure 76**). Data used in the 1D MEM for AP_0051X and MON0065X include Gamma Ray, Density, Compressional Velocity, and Shear Velocity. From the 1D MEMs generated, AP_0051X and MON0065X are interpretated to have similar stress regimes in the Vedder Sands (**Figure 76**). In the overburden through the 1st Vedder Sand, the overburden gradient is maximum principal stress; SHmin and SHMax magnitudes do not exceed overburden. Both AP_0051X and MON0065X have an SHMax that begins to exceed overburden in Vedder 2 and Vedder 4, indicating presence of a strike slip stress regime.

Given the lack of laboratory tests, it is very difficult to assess the "ductility" of the different Vedder sands, i.e., if their behavior under current stress conditions can be classified as "ductile", "brittle" or in a transition state. An empirical correlation between UCS and the brittle-to-ductile transition stress for sedimentary rocks is presented by Davarpanah et al. (2023)

Equation 4.

$$\sigma_{TR}[\text{MPa}] = 1.361\ UCS[\text{MPa}]^{0.947}$$

Based on the uncalibrated UCS values calculated from sonic logs and presented in **Figure 74**, the value of the UCS in the Vedder sands ranges from approx. 1000 to 2500 psi (6.9 to 17.2 MPa), then from the equation above, the transition stress would be in the range of 8.5 to 20.1 MPa (1200 to 2900 psi). Results from the 1D MEMs (**Figure 75**) indicate that the effective mean stress in the Vedder sands is in the range of 1300 to 2200 psi, which means that most of the

Vedder sands are probably in a transitional brittle-to-ductile regime. These results will be confirmed later, once laboratory tests become available and the brittle-to-ductile transition could be observed in the experimental stress vs strain curves.

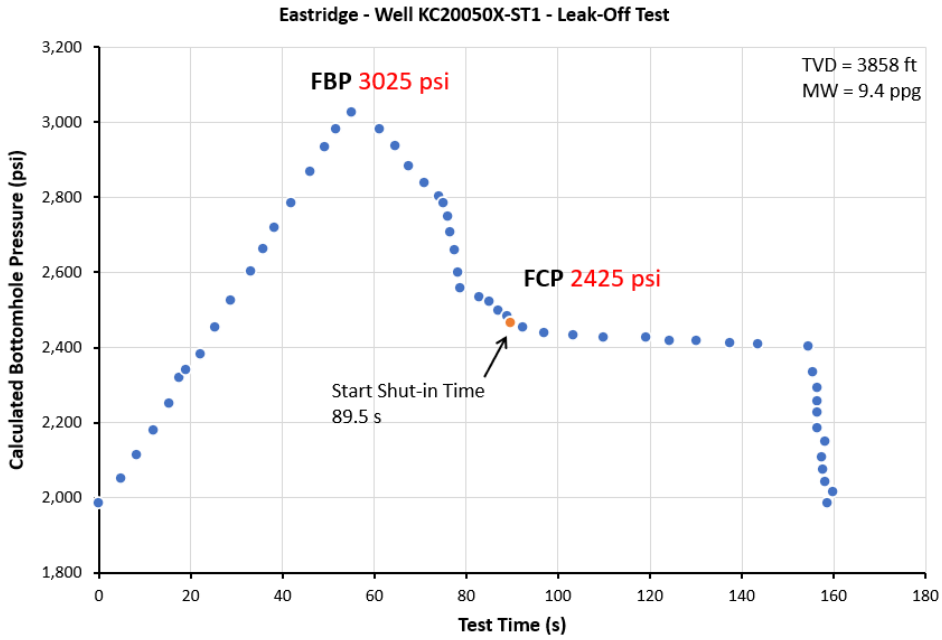

Figure 69. Interpreted LOT data from KC20050X_ST1, highlighting FBP and FCP. FCP is used for calibration of SHmin.

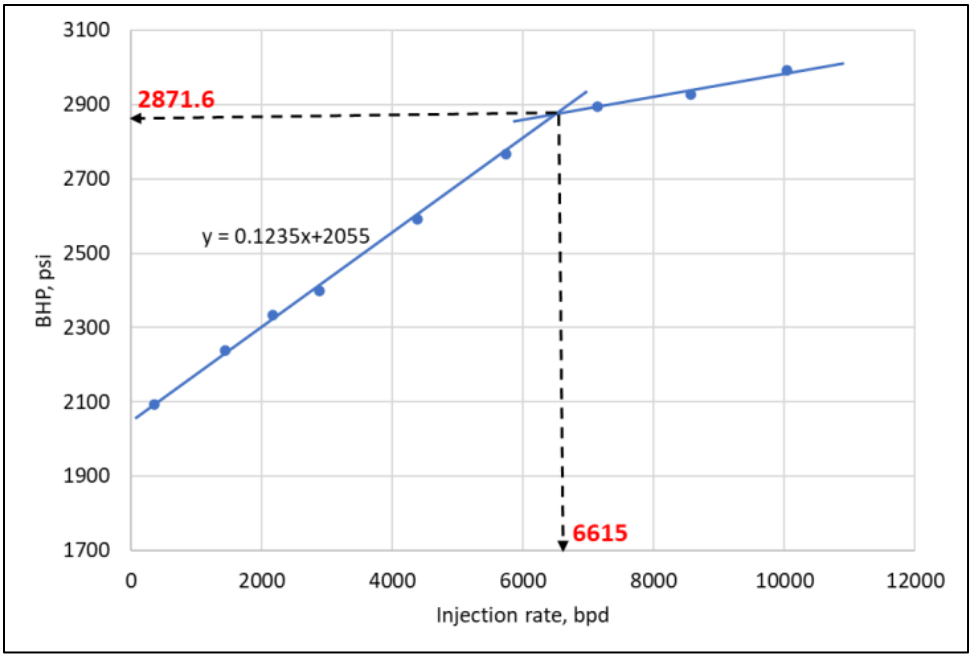

Figure 70. Interpreted Step Rate Test from KC20050X indicating a Fracture Propagation Pressure of 2871.6 psi.

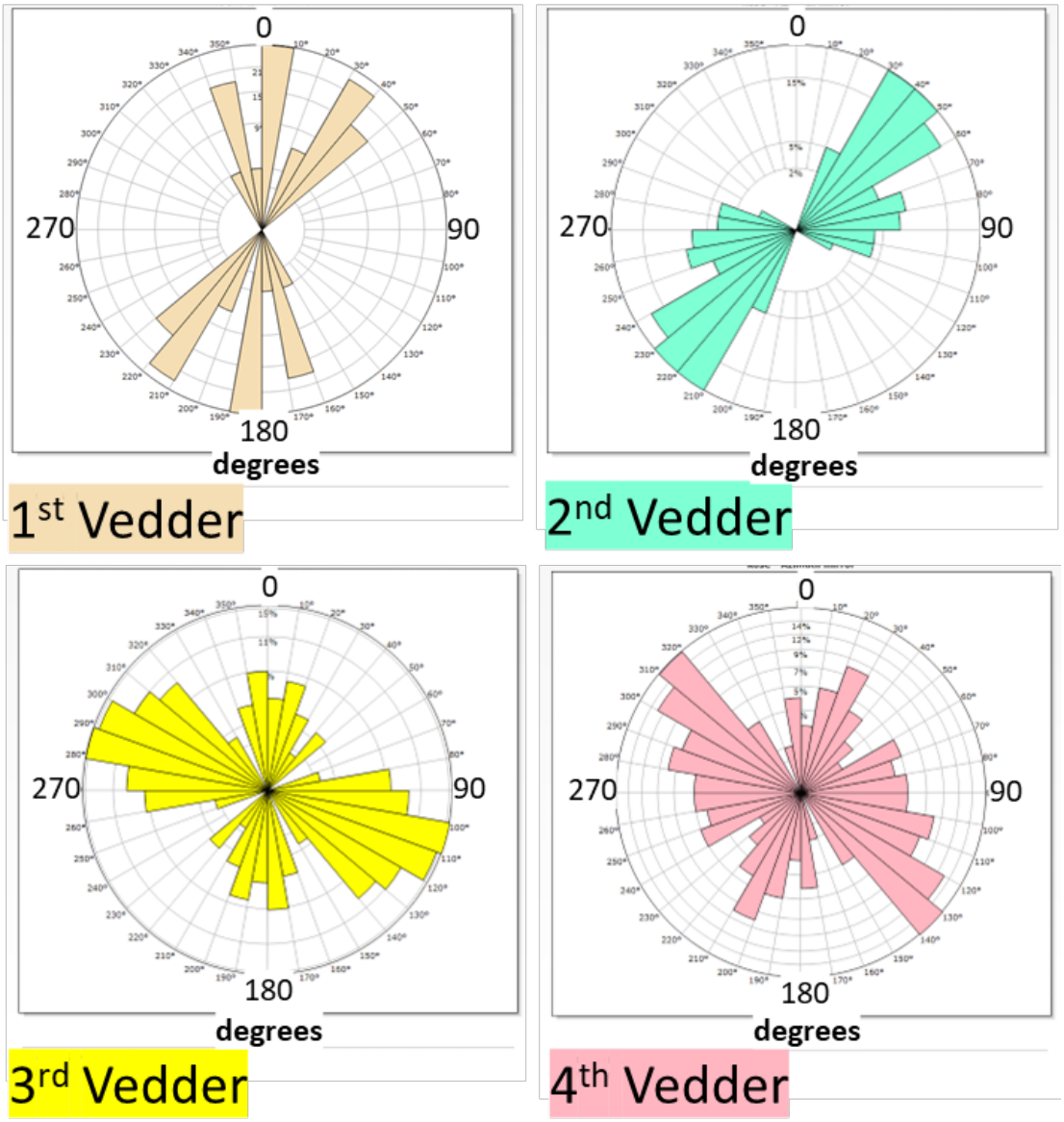

Figure 71. SHmax orientation at KC20050X_ST1 interpreted from sonic-log data.

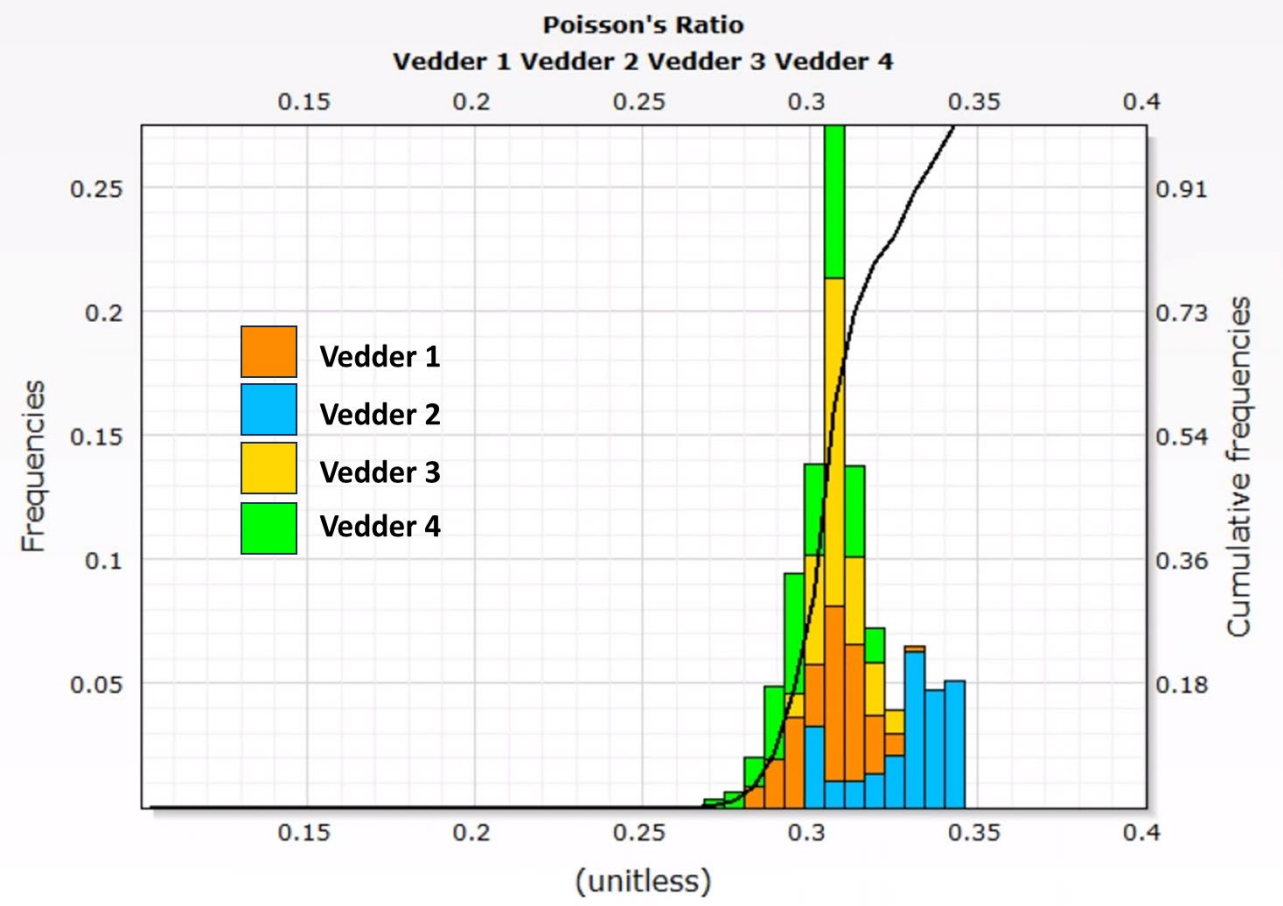

Figure 72. Preliminary model of static Poisson's Ratio for the injection zone.

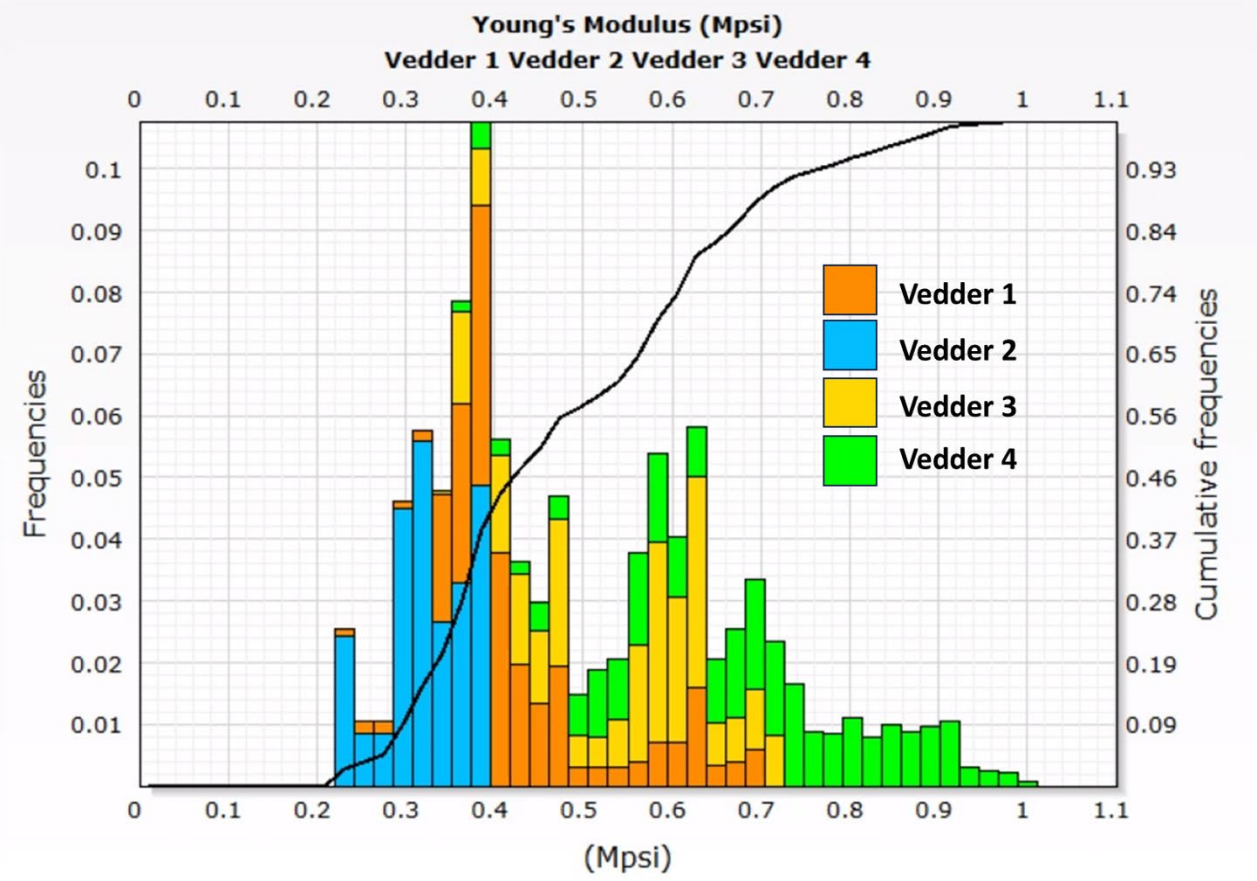

Figure 73. Preliminary model of static Young's Modulus for the injection zone.

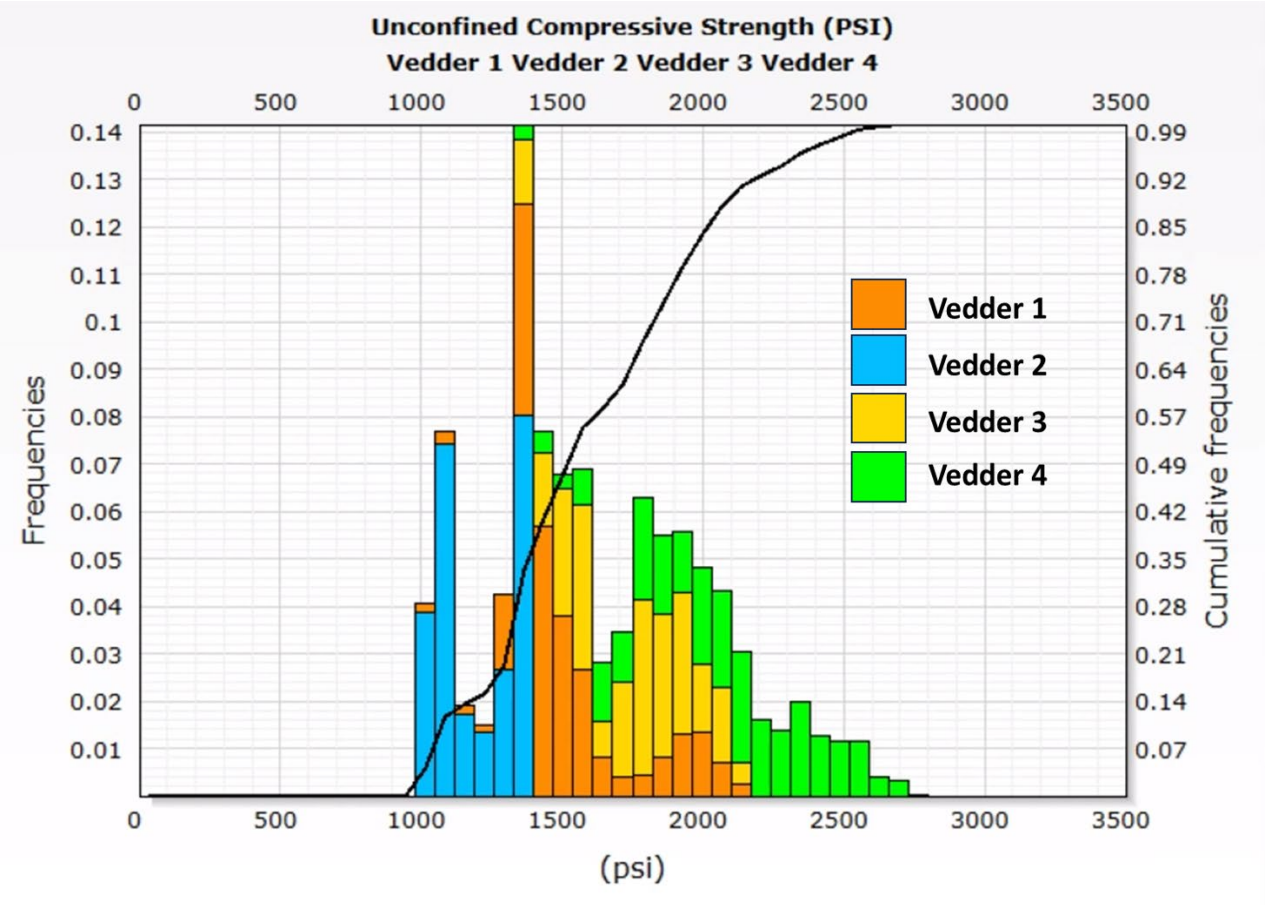

Figure 74. Preliminary model of Unconfined Compressive Strength for the injection zone.

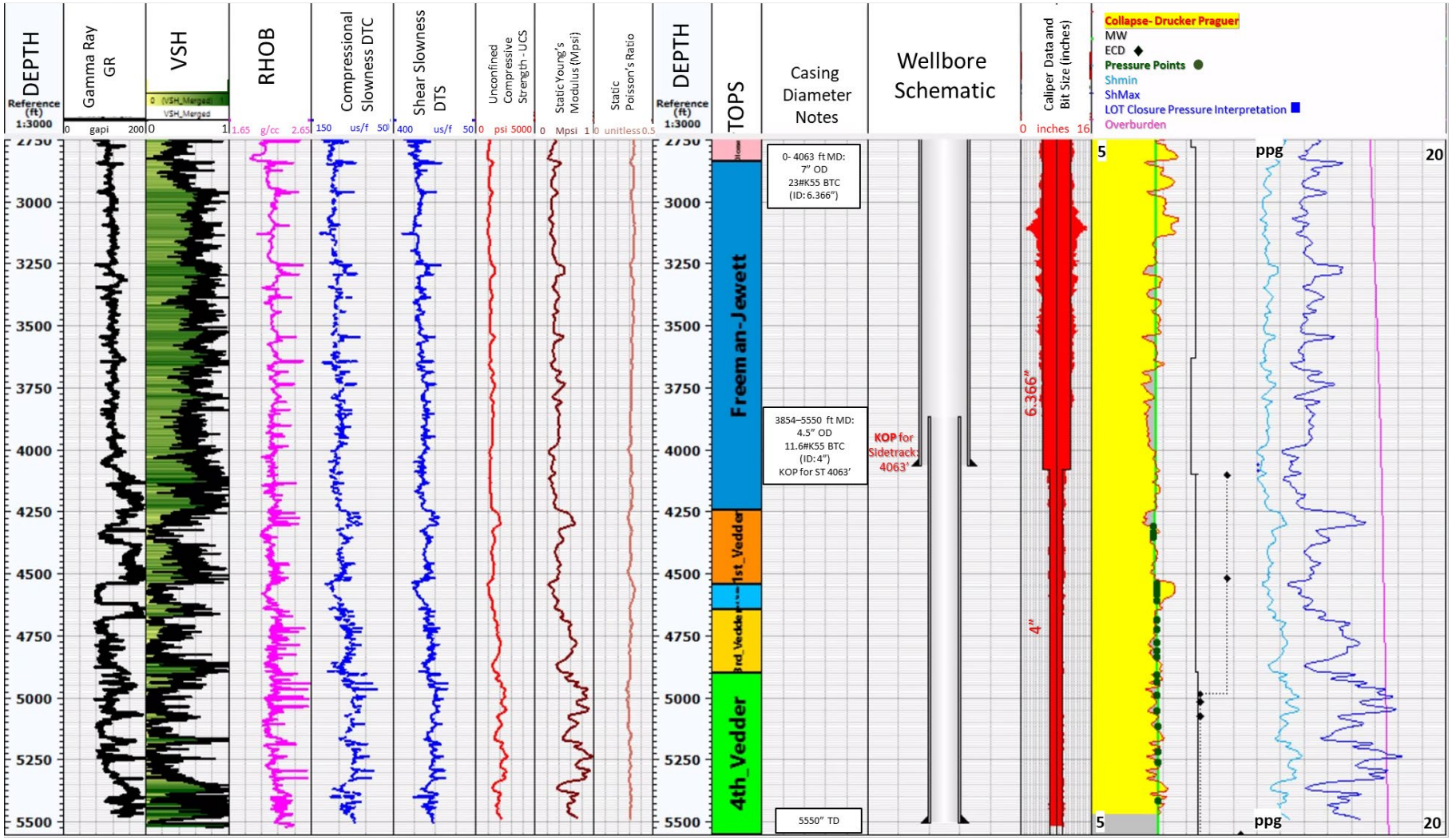

Figure 75. Rock properties and 1D MEM model results for KC20050X_ST1 well.

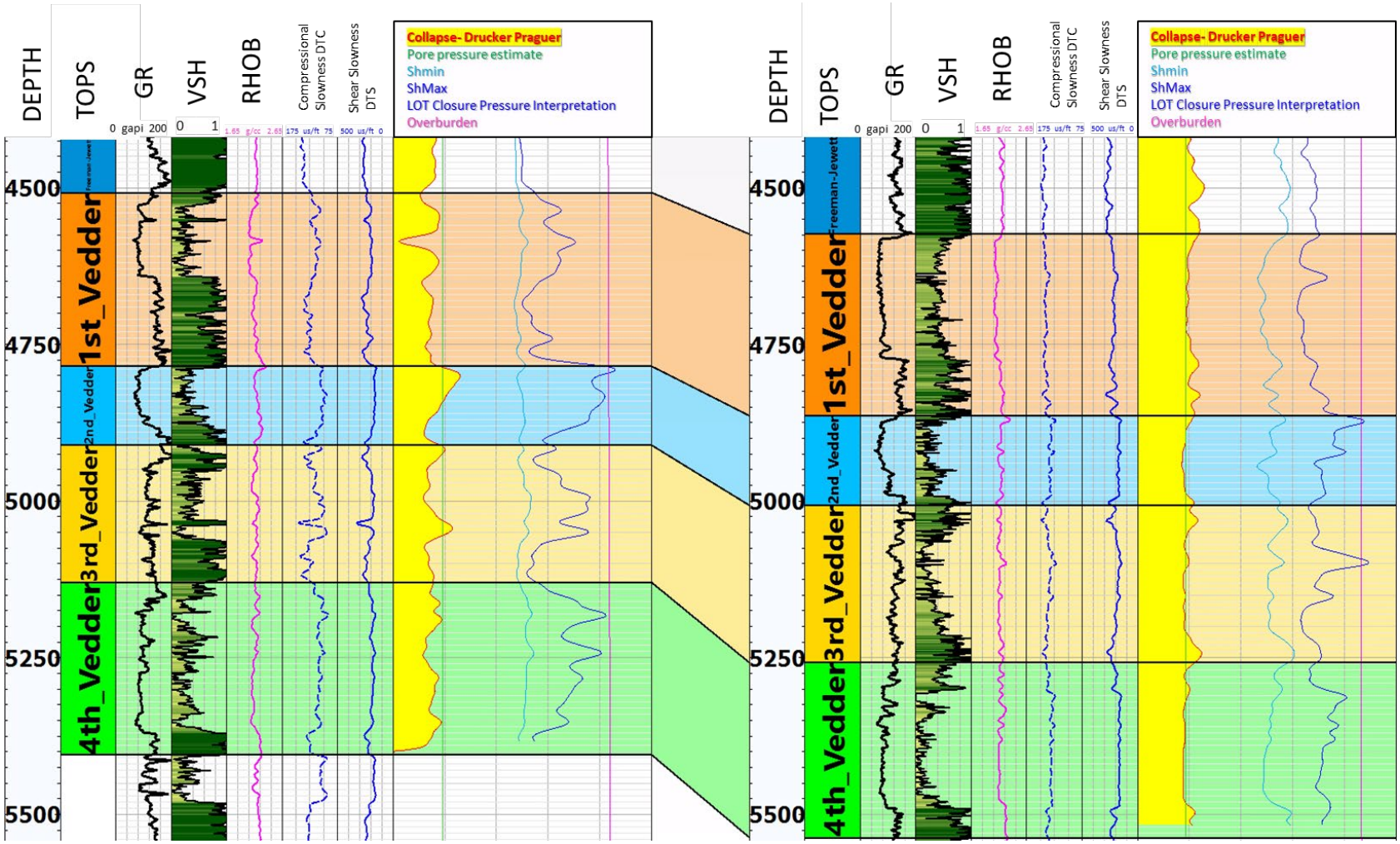

Figure 76. Rock properties and 1D MEM model results for AP_0051X and MON0065X.

Induced Seismicity

A deterministic fault stability analysis was performed on the mapped faults located in the AoI using the stresses computed by the three 1D MEMs (KC20050X_ST1, AP_0051X and MON0065X) (see previous section for more information on the 1D MEMs). The locations of mapped faults and 1D MEMs are indicated in **Figure 66**.

Faults were discretized into triangles having approximately 98 ft (30 m) sides such that each fault is represented by smaller planes instead of a single plane. This approach accounts for local variations in fault orientation along strike and dip so that the stability analysis is done for individual triangular segments. The 1D MEM stresses and pore pressure are projected as gradients onto each of the faults within Vedder subunits Vd1-Vd4.

Given the variability of stress orientation recorded by the sonic dipole log in the Vedder Sand, 1D MEM analyses were done using the dominant modes of stress azimuth by stratigraphic interval. For example, **Figure 77** shows the results obtained for well KC20050X_ST1 in the 1st Vedder Sand (Vd1). Three dominant modes were observed in the interpreted stress azimuth (36°, 120° and 166°). The analysis shows that the 120° azimuth (NW-SE orientation) is the least favorable for fault stability. For this azimuth, the friction coefficient of the faults approaches 0.4. Similar geomechanical analyses performed on other Vedder intervals yielded similar results. A stress orientation of NW-SE would result in at least one of the mapped faults approaching the friction coefficient of 0.4. Refer to **Figure 78**, **Figure 79** and **Figure 80** for the results on the 2nd, 3rd and 4th Vedder sands respectively.

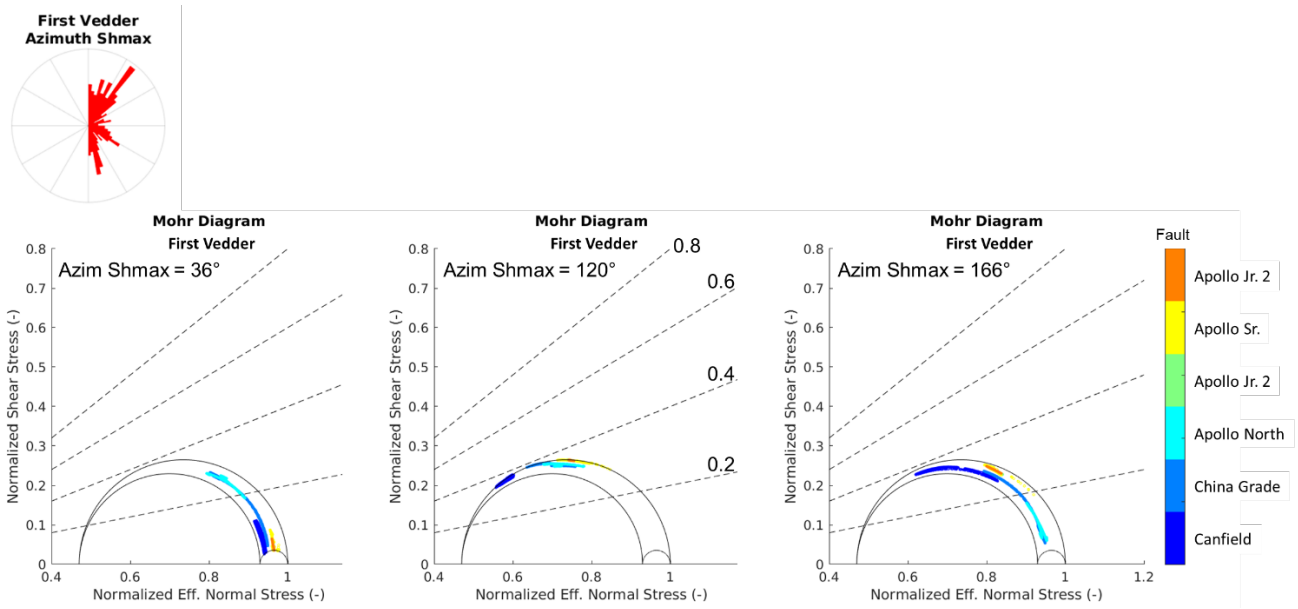

Figure 77. Fault stability results for faults near well KC20050X_ST1 for Vd1. The analysis is for three dominant modes of stress azimuth (36°, 120° and 166°). Stresses are normalized with respect to effective vertical stress.

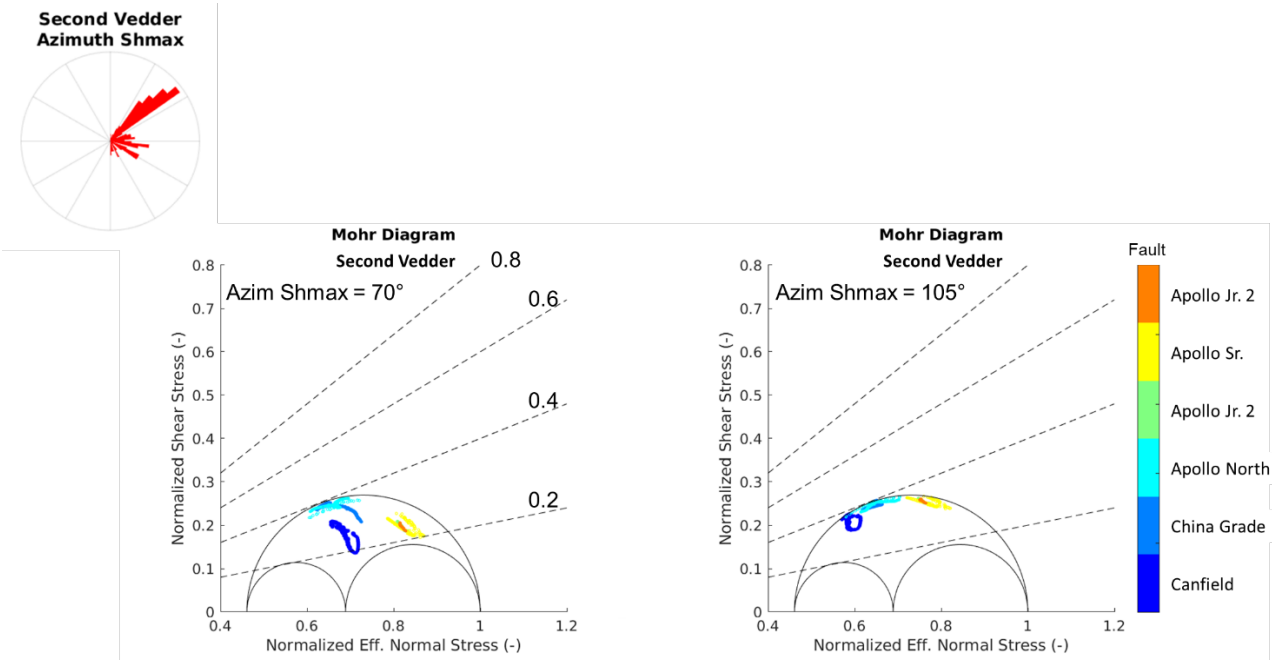

Figure 78. Fault stability results for faults near well KC20050X_ST1 for Vd2. The analysis is done for the two dominant modes of stress azimuth (70° and 105°). Stresses are normalized with respect to effective vertical stress.

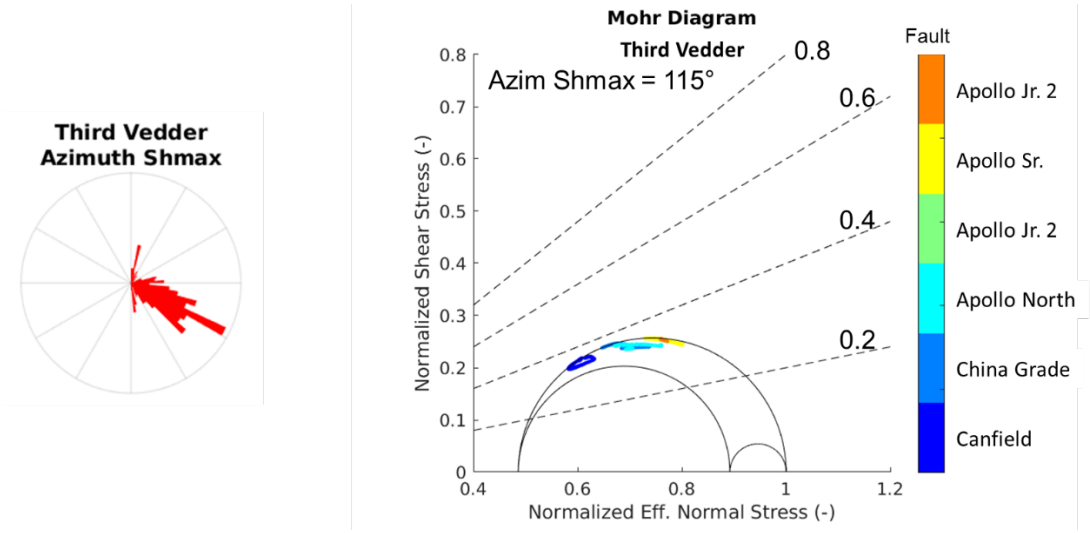

Figure 79. Fault stability results for faults near well KC20050X_ST1 for Vd3. A single stress azimuth of 115° was considered for this analysis. Stresses are normalized with respect to effective vertical stress.

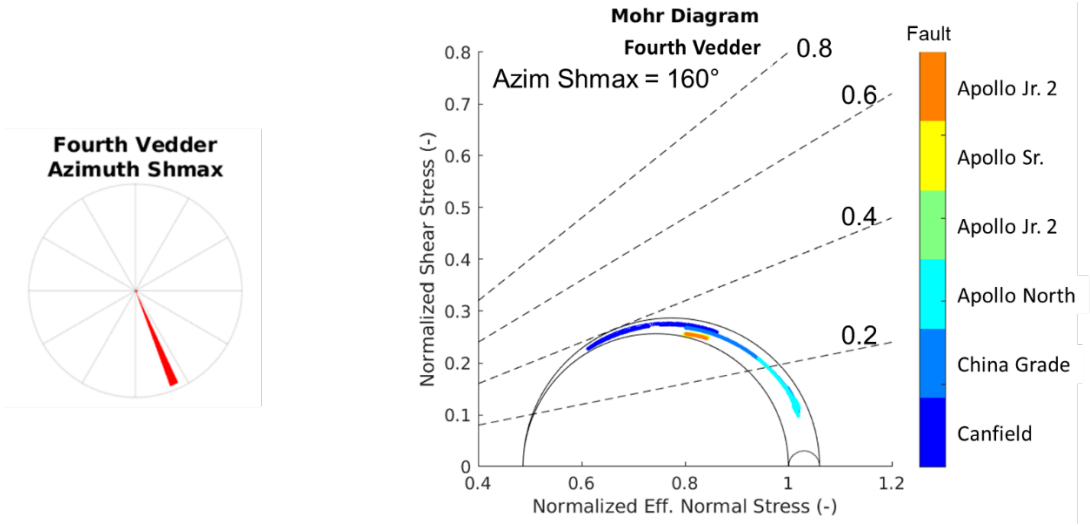

Figure 80. Fault stability results for faults near well KC20050X_ST1 for Vd4. A single stress azimuth of 160° was considered for this analysis. Stresses are normalized with respect to effective vertical stress.

Similar fault stability results were observed using stresses from the AP_0051X and MON0065X 1D MEMs. In general, a stress orientation of NW-SE has the highest friction coefficient. Faults with this orientation have a friction coefficient that approaches 0.4.

Past operational information supports fault stability under injection. For example, Chevron has injected over 50,000,000 barrels of water in the Vedder Sand over the past 40 years with no observed seismic response or pressure build up. Additionally, Chevron plans to include a pressure management water production system that reduces reservoir pressure through the life of the injection. As part of the Testing and Monitoring Plan, Chevron plans to install a seismic monitoring system that includes surface and/or shallow borehole seismometers coupled with downhole distributed acoustic sensing fiber (DAS). For more information regarding inducted seismicity monitoring, please see the “Induced Seismicity Monitoring” section of the Testing and Monitoring Plan.

Petrophysical Information

The initial stratigraphic framework for the Project area was defined using 210 legacy wells that penetrated the Vedder Sand inside and outside of the AoI. The reservoir model was conditioned using seventy (70) wells inside the AoI, including sixty-four (64) legacy wells, 5 legacy sidetracks and 1 sidetrack KC20050X_ST1 that was drilled as a stratigraphic well through the Vedder Sand.

The inventory of legacy wells penetrating the Vedder Sand in the AoI spans from 1908 to 2022. Wells drilled after 1973 in the Project AoI are typically reliable for quantifying log-based porosity, volume of shale, and water saturation due to the types of logs run for these wells. Data from older wells are useful for identifying formation tops, faults, fluid contacts, and other subsurface markers, and typically have quantitative and qualitative core data. Analyses of these legacy wells were conducted using methodologies described below.

Within the AoI, thirty (30) wells drilled after 1973 have reliable electric log data for calculating volume of shale (Vsh), porosity, permeability, and saturation within the Vedder Sand. Additionally, there are seven (7) legacy wells with quantitative whole-core data and logs, yielding a total of 260 individual routine core analysis (RCA) data points to enable robust calibration. KCL20050X_ST1 is a recently drilled well that will provide additional log and core data to supplement the legacy well dataset. Quantitative RCA core analysis consisted mainly of porosity, permeability, and water saturation measurements. Additional legacy core data predominantly comes from percussion sidewall cores. Percussion sidewall coring can induce physical damage to the sample, mostly from disaggregation and fracturing during the sampling process (e.g., Bajsarowicz, 1992), and is interpreted to be less representative of the reservoir properties than the whole core data.

These legacy wells, and associated logs and core comprise a rich source of petrophysical and routine and special core analysis data (RCA and SCAL) to characterize the Vedder Sand and underlying units. The overall quality of borehole geophysical logs varies with vintage and historical development objectives; thus, wells may have distinct types of logs across the AoI. The subsection below summarizes the legacy well evaluation, well logs, and special core analysis that support the geological interpretations and reservoir description of the Vedder Sand in the AoI.

Numerous types of borehole geophysical logs were used to interpret the reservoir framework and reservoir properties **(Table 9, Table 10, Table 11** and **Figure 61)**. Triple-combination (triple combo: neutron porosity, density, and resistivity) log suites are the most common modern log suites used to describe borehole conditions. These logs were supplemented with dielectric, borehole-image, nuclear magnetic resonance (NMR), sonic, and formation-pressure logs.

Table 10. Summary of open-hole wireline logs ranges typically used to characterize reservoir properties and conditions in the Vedder Sand. Principal well-log vendors are Halliburton (HAL) and Schlumberger (SLB), according to California Air Resources Board (CARB) CCS Draft Protocol Section 2.2.3 (p. 39-44).

Log	**Common name**	**Measured property**	**Units and ranges**
Caliper	CALI	Hole diameter	4-14 inches
Gamma Ray	GR	Lithology	0-200 GAPI
Resistivity	DRES SRES	Deep resistivity Shallow resistivity	0.2-200 Ωm
Spontaneous Potential	SP	Lithology & permeability	-160 to +40 mV
Neutron-Density	RHOB	Bulk density	1.65-2.65 g/cm^3
Neutron-Porosity	NPHI	Porosity	0-0.6 V/V
Borehole image log	FMI (SLB) RMI (HAL)	Static resistivity Dynamic resistivity	Ωm, shown as 0-127 (8-bit color scale)
KTIM & CKTIM_F	PERM	Permeability transforms from NMR and core	250-10,000 mD
Pressure	RDT (HAL) pressure	Downhole formation pressure	1700-2700 psia
DT	Delta T	Formation “slowness” (inverse of velocity)	40-240 µs/ft
Vsh	Vshale	Shale volume, calculated log	0-1 V/V
RQI	Rock Quality Index	Permeability & Porosity (Amaefule et al., 1993)	0-8 µm

Table 11. Summary of existing borehole datasets for wells that penetrate the Vedder Sand. Asterisk (*) denotes the recently drilled well KC20050X_ST1.

Well Info		Core & Mineralogy Data				Well Log Data									Derived Logs				
API12	Well Name	Vedder Whole core	Vedder Sidewall	Freeman–Jewett Sidewall	Vedder XRD	SP	SRES	DRES	GR	RHOB	DPHI	NPHI	NMR	FMI	RQI	PHIE	PHIT	VSH	PERM
040292497300	3990001-11					X	X	X								X	X	X	X
040296721700	AP_0051X	X			X		X	X	X	X	X	X			X	X	X	X	X
040294479200	BIS0085					X	X	X		X									
040296771100	CP_0073X		X				X	X	X	X	X	X			X	X	X	X	X
040292631600	F280001					X	X	X											
040292411200	FEC0074					X	X	X											
040296110500	GWA0001WD		X			X	X	X											
040292697300	GWA0145					X	X												
040294934300	JUN0055D		X			X	X	X	X	X	X								
040296990300	KA_0053X		X	X		X	X	X	X	X	X	X			X	X	X	X	X
040290031800	KA_0071X					X	X	X											
040296989800	KC30001X		X	X		X	X	X	X	X	X	X			X	X	X	X	X
040292803800	LUC0154		X			X	X												
040292273800	MS_0113					X	X	X											
040290009800	OM_0044		X			X	X	X											
040296655800	OM_0044X	X	X		X	X	X	X	X	X	X	X			X	X	X	X	X
040292403700	SA_0001					X	X	X											
040295391100	SJ_0001WD		X			X	X	X											
040296110600	SJ_0002WD		X			X	X	X											
040301418200	SJ_0010WD					X	X	X	X	X	X	X	X		X	X	X	X	X
040301621700	SJ_0011WD					X	X	X	X	X	X	X			X	X	X	X	X
040296641100	33_0028X	X	X		X		X	X	X	X	X	X			X	X	X	X	X
040292887200	33_0058X					X	X	X											
040294423200	3990072C					X	X	X											
040296441200	AP_0001WD		X			X	X	X	X	X	X	X			X	X	X	X	X
040298942100	CHP00WD1					X	X	X	X	X									
040295678200	COR0001WD	X				X	X	X											
040306065200	KH_WDV1		X			X	X	X	X	X	X	X	X		X	X	X	X	X
040296758700	MON0065X		X			X	X	X	X	X	X	X			X	X	X	X	X
040306215900	ORLWD2		X	X		X	X	X	X	X	X	X			X	X	X	X	X
040296194100	S4_WDV1		X			X	X	X	X	X	X	X			X	X	X	X	X
040298201900	S4_WDV2	X	X			X	X	X	X	X	X	X			X	X	X	X	X
040305241300	S4_WDV3					X	X	X	X	X	X	X			X	X	X	X	X
040297837600	SOVWD-1	X	X			X	X	X	X	X	X	X			X	X	X	X	X
040297837500	VESWD-1		X					X		X	X	X			X	X	X	X	X
040296905500	BIS0224X					X	X	X	X	X	X	X			X	X	X	X	X

040297107500	BIS0225X					X	X	X	X	X	X	X			X	X	X	X	X
040297559102	KC30068XSTD					X	X	X	X	X	X	X							
040298795500	S3_0919X		X				X	X	X	X	X	X			X	X	X	X	X
040294247600	JUN0054D		X			X	X	X											
040304573400	CP_0094X					X	X	X	X	X	X	X			X	X	X	X	X
040297301700	ELW0100X					X	X	X	X	X	X	X			X	X	X	X	X
040294937400	HF90001D					X	X	X	X	X	X	X			X	X	X	X	X
040296906900	HF90003D					X	X	X											
040297205000	K100002X					X	X	X											
040304874500	KC20050X		X			X	X	X	X	X	X	X		X	X	X	X	X	X
040304874501	*KC20050X_ST1	X			X	X	X	X	X	X	X	X	X	X					
040297396900	KC30067X		X	X		X	X	X	X	X	X	X			X	X	X	X	X
040297396901	KC30067X_ST1					X	X	X	X	X	X	X							
040297393700	RIV0002-10					X	X	X											
040297135800	S3_0719X		X			X	X	X	X	X	X	X			X	X	X	X	X
040297371201	S3_0819XRD1		X			X	X	X	X	X	X	X			X	X	X	X	X
040296721701	AP_0051X_ST1					X	X	X	X	X	X	X							
040290026100	GW_0105-D		X	X		X	X	X											
040292215100	RAS0028																		
040296976200	REV0004X	X				X	X	X	X	X	X	X			X	X	X	X	X
040297371200	S3_0819X		X	X		X	X	X	X	X	X	X			X	X	X	X	X
040292404700	MTC0001					X	X	X											
040294034800	MTC0071X					X	X	X											
040292200100	BOS0001																		
040293200900	CCM0041					X	X												
040292404800	F280003					X	X	X											
040292689700	FOS0001					X	X	X											
040294615600	K120001					X		X											
040297559100	KC30068X		X	X		X	X	X	X	X	X	X			X	X	X	X	X
040297559101	KC30068XST					X	X	X	X	X	X	X							
040291846200	SBB0027					X	X												
040292620100	SEC21-D																		
040292402900	ZAN0001					X	X	X											
040292673800	ZAN0002					X	X												

Three wells in the Project AoI have nuclear magnetic resonance (NMR) logs, which can be used to evaluate permeability in the formation (Timur, 1969). NMR logs measure pore-size distributions of rock by aligning hydrogen atoms in the formation with a strong magnetic field. The aligned hydrogens are then perturbed by use of a radio frequency, which causes the hydrogen atoms to produce a radio signal as they re-align with the applied magnetic field. The resulting signal is measured and correlated to pore size. In porous rocks, the primary means of magnetic realignment is through interaction among atoms or molecules and grain surfaces. The faster the hydrogen atoms realign with the imposed magnetic field, the more surface area exists in the pores, which equates with a smaller pore size that would be indicative of lower permeability rock. In more permeable rock, the signal persists for a longer period of time because statistically hydrogen atoms are less likely to encounter pore walls in rocks having larger pores and thus higher permeability.

Vedder Sand mineralogy data from x-ray diffraction (XRD) measurements two wells within the AoR (AP_0051X, API# 040296721700; 33_0028X, API# 040296641100) and an additional well within the AoI (OM_0044X, API# 040296655800) indicates a mixture of quartz and felspar. Clays occur in distinct layers, as distinct clasts, and in bioturbated intervals, depending on the specific environment of deposition. Nineteen (19) data points from these three wells indicate clay mineral content ranges of 10-45% and consists of illite, which occurs as authigenic, pore-lining cements and as detrital matrix clay.

Core analysis sourced from the Vedder Sand within the AoI (well S4_0002WDV) was analyzed at reservoir temperature and pressure to evaluate CO_2-brine interfacial tension and contact angles of 30.2 mN/m and 35°- 44°, respectively. This information was incorporated into the reservoir model as described in detail in the Model Calibration section of the Area of Review and Corrective Action Plan.

Reservoir properties calculated from borehole geophysical logs and core data include volume of shale (Vshale) and effective porosity (PHIT and PHIE, respectively), total water saturation (Swt), effective shale-corrected water saturation (Swe), and shale volume (Vshale). Permeability transforms are based on regressions among PHIT, PHIE and Vshale.

Total porosity was calculated from neutron and density logs using the methodology described in Coates et al. (1982) and the component values listed in **Table 12**. These results agree with core derived porosity values for the region. This methodology is commonly applied in sandstone reservoirs and is especially well suited to shaly sand intervals within the Vedder Sand.

Table 12. Density and Neutron endpoint values for the Vedder Sand.

Component	Neutron porosity	Density (g/cm^3)
Matrix	0.00	2.68
Shale	0.43	2.23
Fluid	1.00	1.00

Equation 5.

Volume of shale (Vshale) is also computed from neutron and density logs (**Equation 5**)

$$V_{shale} = \frac{\phi_n - \phi_d}{\phi_{n,sh} - \phi_{d,sh}}$$

where, ϕ_n is porosity from the neutron log, ϕ_d is density-porosity given by the density log, $\phi_{n,sh}$, the neutron-porosity of the shale and $\phi_{d,sh}$is the density-porosity of the shale.

Effective porosity is defined herein as the total porosity minus the clay bound water. This is consistent with the approach described in Coates et al. (1982). The volume of clay bound water is proportional to the volume of shale; the proportionality constant is related to the cation exchange capacity (CEC). The parameters given in **Table 12** are sufficient to compute total porosity and shale volume.

Permeability was estimated using a transform of the total porosity (PHIT), effective porosity (PHIE), and volume of shale (Vsh) against permeability calibrated to nuclear magnetic resonance (NMR) logs and core. The permeability of the Vedder sand is controlled by a combination of shale volume and pore size. Whereas shale volume is calculated from neutron and density logs, pore size can only be measured in the subsurface using NMR logs.

Equation 6.

Water Saturation in the Vedder Sand injection zone is calculated using the Archie (1942) equation:

$$S_w = \left(\frac{a}{\emptyset^m} + \frac{R_w}{R_t}\right)^{1/n}$$

where *Sw* is water saturation of the uninvaded zone, *Rw* is formation water resistivity at formation temperature, *Rt* is true resistivity of formation, corrected for invasion, ϕ is porosity, a is a tortuosity factor, m is a cementation exponent, and n is a saturation exponent. For the Vedder Sand, the constants of a = 1.13, m = 1.73, and n = 2 were used to calculate water saturation.

Thirty-one (31) of the (70) wells that penetrate the Vedder Sand have complete log suites to allow petrophysical interpretations of porosity, shale volume, and permeability transform. This left 7 wells with partial log suites of gamma ray, neutron, density, and resistivity log data. Log suites for 29 wells do not have neutron or density curves. Three (3) additional wells had no logs and were not used for modeling petrophysical properties.

Seismic History [40 CFR 146.82(a)(3)(v)]

The Kern River Oil Field has been in nearly continuous production for over 124 years without seismogenic incident, and significant seismicity has not been observed in the shallow subsurface (i.e., through the depth of Cenozoic basin fill).

The U.S. Geological Survey has identified numerous faults surrounding the Project AoI (**Figure 81**); U.S. Geological Survey, 2022). Many of these faults have predominantly northerly and northwesterly strike orientations, with sparse northeasterly fault traces mapped. Northwest-northeast- and east-trending faults have been recognized in the AoI (**Figure 49**) and are denoted as red-dashed lines on **Figure 81**.

The Kern Front fault, which has been identified as a Holocene-active fault by the State of California based on a prominent surface trace mapped along the western border of the Kern River Oil Field (**Figure 81**, see California Geological Survey, 1998). The Kern Front fault is a south-striking, west-dipping normal fault that displaces Quaternary alluvium along the western edge of the Kern River Oil Field (Smith, 1983). The fault is recognized at the ground surface as a low-relief, west-facing scarp that cuts Quaternary alluvium. The Kern Front fault is aseismic and has lengthening in a northerly direction. Vertical ground movement on the order of 3 to 12 mm per year has been documented by a creepmeter installed by the National Oceanographic Survey between 1968 and 1974.

Other large fault zones have been mapped in the region, including the Kern Gorge fault, a range-bounding normal fault approximately 8 miles east of the AoI (U.S. Geological Survey, 2022). Historical earthquake data comes from a catalog maintained by the California Geological Survey (e.g., Toppozada et al., 2000). More than 17 miles south of the AoI is the White Wolf fault, which was the source of the 7.3 Mw Kern County earthquake in 1952. The San Andreas fault zone is approximately 39 miles south of the AoI. The epicenter of the 7.9 Mw Fort Tejon earthquake of 1857 was located on the San Andreas fault zone, near the town of Parkfield, which is more than 45 miles west of the AoI.

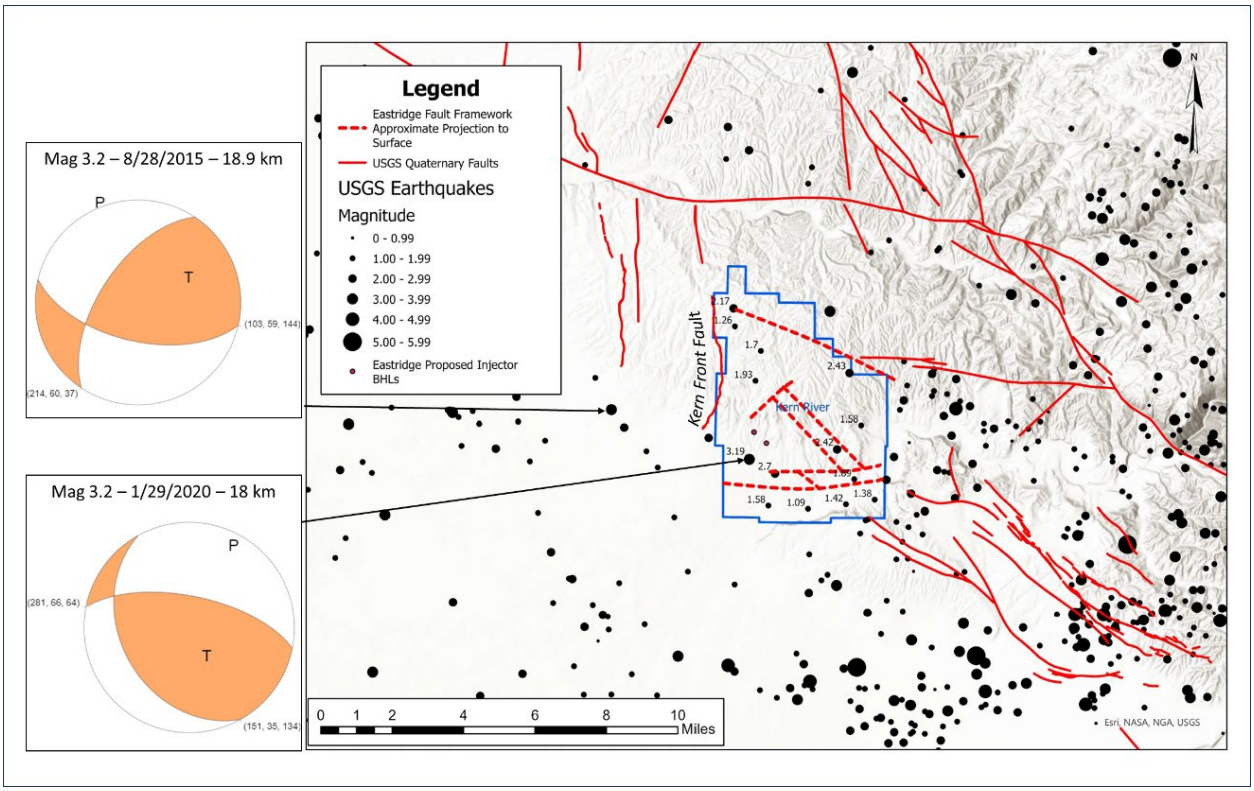

Figure 81. Shaded-relief map showing instrumental seismicity in and around the Project AoI (blue line) and mapped faults (solid red line) with Quaternary movement based on data from the U.S. Geological Survey (U.S. Geological Survey, 2022 and 2023). Dashed red lines denote faults within the AoI that have been projected to the ground surface. Focal mechanisms of two events indicate normal-oblique fault movement (*left*). With the exception of a shallow quarry blast event, hypocenters occur in crystalline basement.

Regional catalogs of instrumental and historical seismicity and focal mechanisms indicate that no major events have been recorded within the Project AoI for over 75 years, which is the duration of instrumental records (**Table 13** and **Figure 81**). Recorded earthquake hypocenters occurred in crystalline basement more than 3 km below the ground surface, at depths far below the base of the Vedder Sand and Walker Formation. Fourteen (14) seismic events have been instrumentally recorded on the Project AoI (**Table 13**). The largest event (Mw=3.19) occurred southwest of the AoI. A 1.93 Mw event occurred on the northern boundary of the AoR. Based on an earthquake catalog of historical events (from 1980 to 2023) within a 6 mile radius of the AoI center and with a moment-magnitude of completeness of approximately 1.6 Mw, the background seismicity rate is calculated to be approximately 0.15 Mw > 0 per year per square kilometer, assuming a Gutenberg-Richter b value of 1. Using a 1-mile radius away from the proposed injection well locations, the yearly probability of a 2.7 Mw event is 0.24 percent. The risk of induced seismicity within the Vedder Sand is lower due to the depth of the injection zone and the planned use of a pressure management system. In general, as supported by historical catalogs, faults at shallow depths are more likely to move through aseismic slip due to velocity strengthening behaviors described by rate-and-state fault friction (e.g., Scholz, 1998).

Table 13. Instrumental seismicity in Project AoI (U.S. Geological Survey, 2023). Earthquake magnitude is reported as Richter local magnitude (ml), magnitude of completeness (mc), and nonstandard magnitude measurement (mh). The asterisk (*) denotes an epicenter location on the northern boundary of the AoR. Earthquake magnitude, magnitude type, date, depth, and event type are from the U.S. Geological Survey Earthquake Catalog maintained by the Earthquake Hazards Program.

Magnitude	Magnitude type	Date (YYYY-MM-DD)	Depth (mile)	Depth (km)	Below basin-fill	Event type
3.19	ml	2020-01-29	11.18	17.99	Yes	Earthquake
2.70	ml	1947-02-25	3.73	6.00	Yes	Earthquake
2.43	mh	1976-02-15	3.73	6.00	Yes	Earthquake
2.42	ml	2009-03-25	12.12	19.51	Yes	Earthquake
2.17	ml	2017-07-24	9.71	15.63	Yes	Earthquake
1.93*	mh	1981-01-30	2.95	4.74	Yes	Earthquake
1.89	ml	2006-08-05	10.25	16.5	Yes	Earthquake
1.70	mh	2001-05-31	12.77	20.55	Yes	Earthquake
1.58	mc	2000-06-12	2.99	4.81	Yes	Earthquake
1.42	ml	2022-09-23	8.40	13.53	Yes	Earthquake
1.38	mc	1995-02-02	12.07	19.43	Yes	Earthquake
1.26	ml	2008-01-20	3.34	5.38	Yes	Earthquake
1.09	mc	1994-09-21	2.99	4.81	Yes	Earthquake
1.58	ml	2012-09-26	-0.44	-0.71	No	Quarry blast

The potential for ground motion from earthquakes is calculated using probabilistic assessments based on data from historic earthquakes, slip rates on major faults and regional deformation (e.g., Peterson et al., 2014). Earthquake shaking potential is calculated as the level of ground motion that has a 2% chance of being exceeded in 50 years, which predicts the level of ground shaking with a 2500-year average recurrence time. Regional assessments of earthquake shaking potential (e.g., Branum et al., 2008) indicate that the AoI will experience relatively low levels of ground acceleration (<0.5 g in basin fill) less frequently (2% exceedance probability in 50 years) than in areas closer to major seismogenic faults, such as the historically active White Wolf and San Andreas fault zones, which are located more than 17 miles south and 39 miles west of the AoI, respectively.

The direct impacts of naturally occurring seismic events on proposed Project operations and subsurface containment are considered low based on low seismicity within the AoI, aseismic movement across faults, and predictions of relatively low ground acceleration during earthquake events.

Hydrologic and Hydrogeologic Information [40 CFR 146.82(a)(3)(vi), 146.82(a)(5)]

Within the AoI, USDWs are, in descending stratigraphic order, perched groundwater within the Kern River Formation overlying the top of the aquifer-exempt Kern River oil-bearing zone, the confined Chanac Formation aquifer, and the Santa Margarita Sandstone, which represents the deepest USDW.

"*Underground source of drinking water* (USDW) means an aquifer or its portion:

(1)

(i) Paragraph tools not available for definition subparagraphs. Which supplies any public water system; or

(ii) Which contains a sufficient quantity of ground water to supply a public water system; and

(A) Currently supplies drinking water for human consumption; or

(B) Contains fewer than 10,000 mg/l total dissolved solids; and

(2) Which is not an exempted aquifer."

eCFR :: 40 CFR Part 146 -- Underground Injection Control Program: Criteria and Standards

The Olcese, which is stratigraphically above the Vedder and below the Santa Margarita, is a non-USDW aquifer. Water sampled from well no. WDV1 (API No. 029-61941) in the Kern River Oil Field shows reservoir fluids in the Olcese contain 25,500 mg/L total dissolved solids (TDS) within the AoI. Since the reservoir fluids contain an excess of 10,000 mg/L TDS, according to Title 40 Code of Federal Regulations §146.3, the aquifer is non-USDW. The detailed analytical results are included in Appendix III of the "Subsurface Water Disposal Project Application, Olcese Formation" submitted by Chevron (June 2014) in consideration for a water disposal project. The application was subsequently approved, and a Project Approval Letter was issued for UIC #34000166 on March 13, 2015.

The Vedder Sand within the AoI is an exempted aquifer (California Department of Conservation & US EPA, 1982 and 2015), and therefore is not a USDW.

Coburn and Gillespie (2002) summarized the hydrogeologic characteristics of the AoI, using hydrological pressure data from (1) open-hole formation pressure tests, (2) nuclear logs combined with temperature surveys, and (3) static fluid levels. The following descriptions summarize Colburn and Gillespie (2002) and others to describe the Hydrologic and Hydrogeologic conditions of the AoI.

Surface hydrology and ground water recharge

Groundwater recharge from precipitation will occur updip of the AoI, at the Kern River Formation outcrop. Currently, the area around the Kern River Field receives on average approximately 6 inches of precipitation annually and has an evapotranspiration rate of approximately 73 inches annually (RWQCB 2005). Therefore, very little recharge will occur by precipitation at the outcrop along the east edge of the AoI. This conclusion agrees with those reached by Dale et al. (1966), which showed that precipitation in the area does not infiltrate below the root zone. Groundwater inflow into the AoI is considered to be negligible because of

the presence of major faults on the west, south, north and northeast boundaries of the AoI. The Kern Front fault provides a seal, preventing fluids in the Etchegoin, Chanac and Kern River Formations west of the AoI from crossing the boundary (Link et al., 1990). As shown in cross sections prepared by Kodl (1990), displacement of air-oil and oil-water contacts across the China Grade fault indicate the fault is sealing in nature and acts as a barrier to flow.

The Kern River waterway is the largest potential source of recharge in the AoI, as it directly flows over the Kern River Formation zones in the eastern and southeastern parts of the AoI; hence, infiltration of surface water would generally be expected to reach groundwater. However, recharge from the river, on a field-scale basis, is low. Low recharge is shown by potentiometric contours that do not dip away from the river (**Figure 82**).

Coburn and Gillespie (2002) presented potentiometric maps using 1992 to 1993 data based on a vadose zone contact derived from neutron logs and water agency water level data **(Figure 82)**. The maps show the potentiometric surface generally following the regional structural dip, indicating water flowing generally downdip (from northeast to southwest), with the surface along the eastern edge of the field dipping west at 10 to 100 feet per mile. The potentiometric surface is shown to be flattening in the western part of the field as the Kern Front Fault is approached. The change in gradient to nearly zero indicates that the downdip flow of fluids is stopped by the Kern Front Fault. Current shallow groundwater conditions include perched groundwater zones separated by unsaturated soils (commonly referred to as "air sands"). Coburn and Gillespie (2002) also presented potentiometric maps of 1992 to 1993 data from the Upper Chanac and the R1 zone in the lower Kern River Formation (**Figure 84** and **Figure 85**). The map illustrates the effect of the Kern Front Fault and the local effect of other faults within the field on fluid flow by interrupting the groundwater gradient and influencing the flow pattern and gradient magnitude.

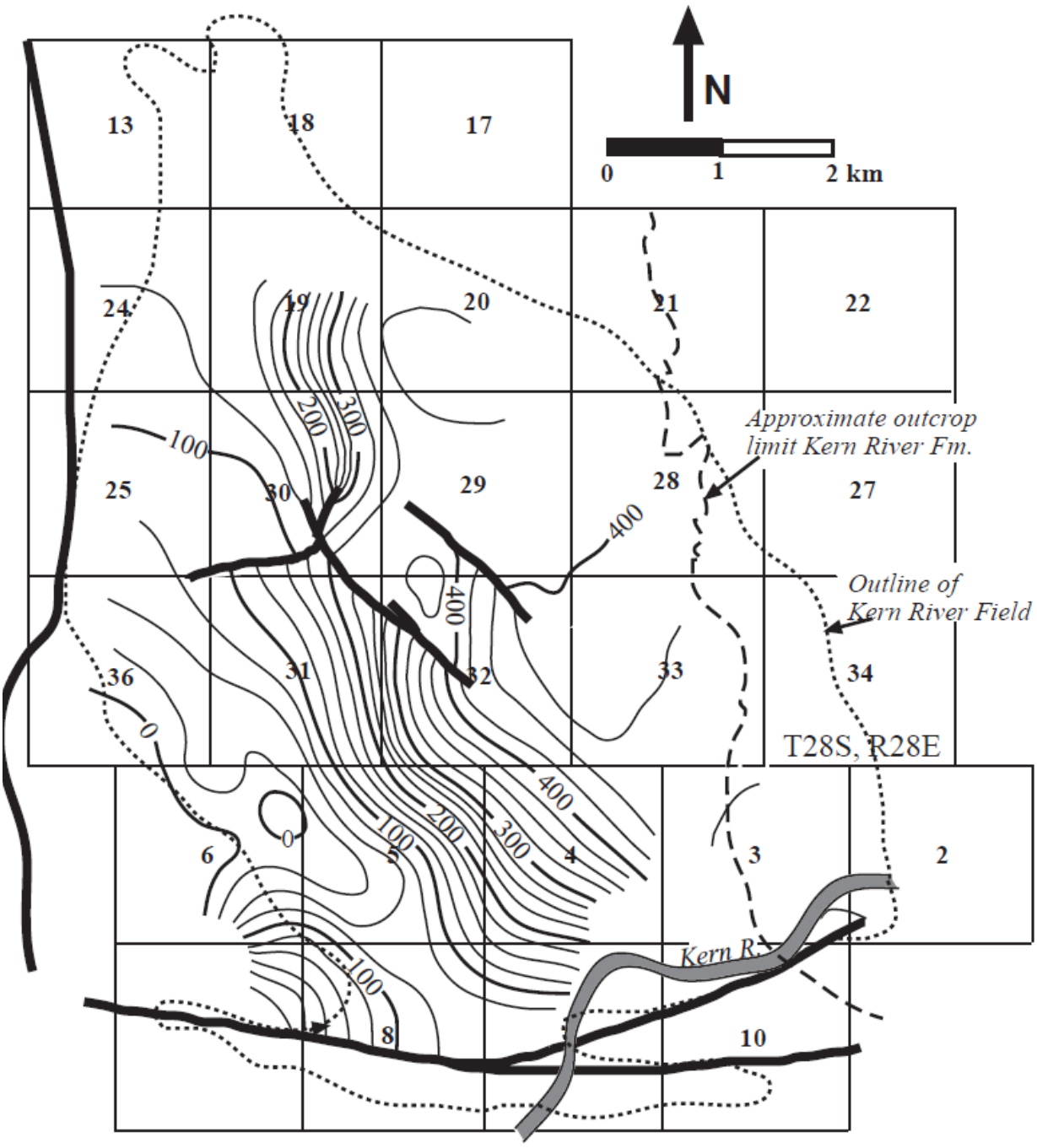

Figure 82. Contour Map of the elevation of the regional groundwater table in 1992-1993, defined by the elevation of the water/oil table in the highest fluid filled zone (Coburn and Gillespe, 2002)

Kern River Formation

The upper Miocene–Pleistocene Kern River Formation is the main oil-producing and associated Class II UIC injection formation in the AoI. Sandstone percentages are generally higher in the southern part of the field and lower in the northern part (Coburn,1996). Sedimentary rocks range from mudstones to pebbly or boulder sandstones. Typical features include crosscutting channels and overbank mudstones and siltstones (Nicholson, 1980). Mudstones act as local aquitards, separating distinct aquifer units. The thickness and lateral extent of the mudstones separating the sand intervals have important ramifications for hydraulic communication between zones (Ginger et al., 1995; Williams et al., 1998).

Perched water in otherwise unsaturated sand have been identified in the overlying sediments above the oil-bearing zone of the Kern River Reservoir. The aquifer below the perched water is an unconfined aquifer (**Figure 83**). This unconfined aquifer consists of the zones in the lower Kern River Formation and the upper zone of the Chanac Formation. Potentiometric mapping of the AoI indicate that regional groundwater flow is to the west (**Figure 84**).

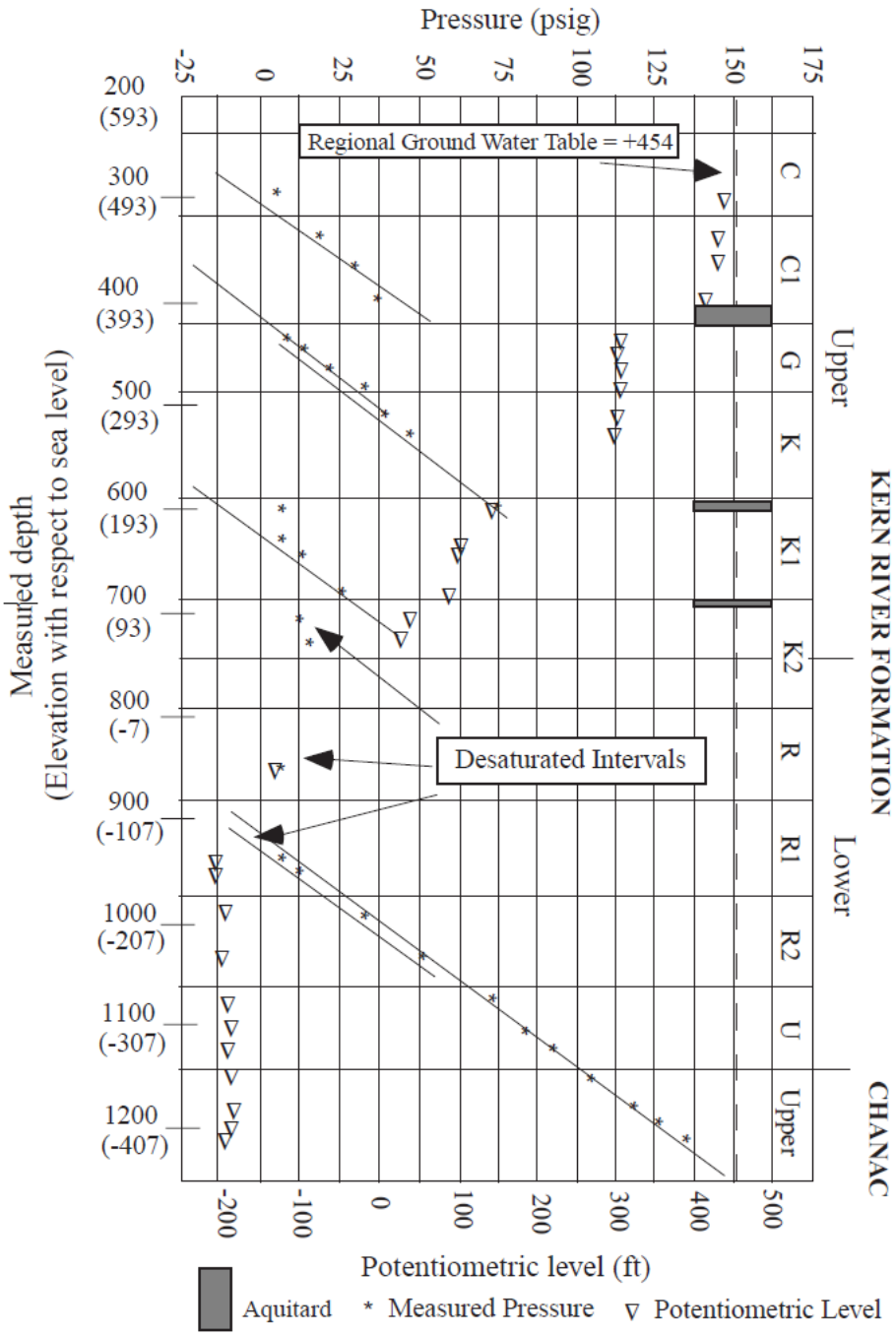

Figure 83. Pressure and potentiometric level plot for the upper Chanac and Kern River Formations. Depths are in feet. (Coburn and Gillespe, 2002)

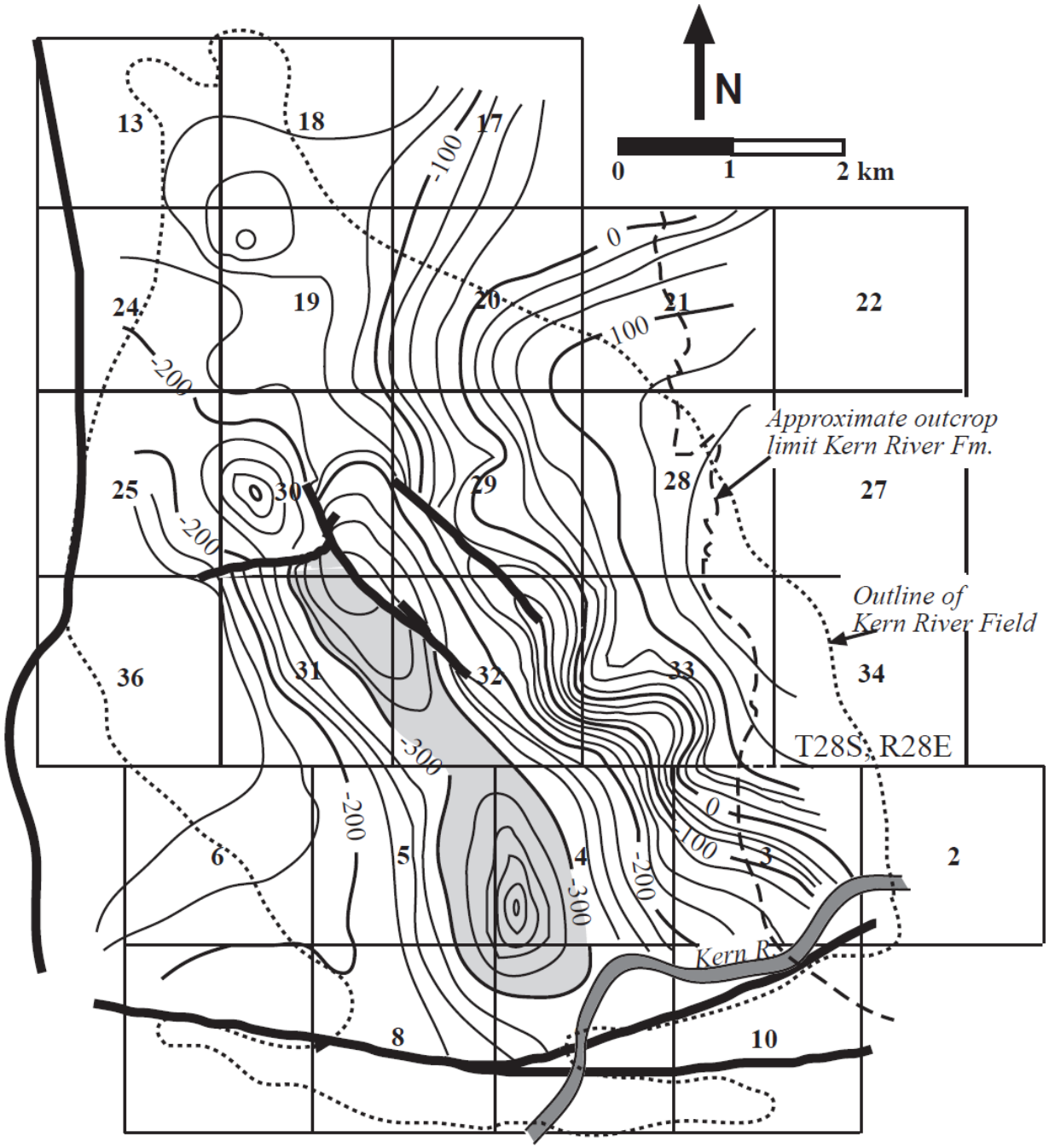

Figure 84. Map of the potentiometric surface in the R1 zone of the lower Kern River Formation. The shaded region indicates a depression in the potentiometric surface. The gradient flattens in the west where fluids moving downdip via gravity drainage are banked against the Kern Front fault. (Coburn and Gillespe, 2002)

Chanac Formation

The Chanac Formation is an upper Miocene nonmarine interval consisting of clayey mudstones to pebbly, very coarse-grained sands (Olsen et al., 1986) deposited in alluvial environments (Kodl et al., 1990; Link et al., 1990). It thins to nearly zero to the east. In the AoI, the Chanac varies in thickness from 0-700', has an average porosity of 31%, and a permeability of 720-5,000 md (Coburn and Gillespie, 2002). It occurs at a depth of 425'-1,335' below ground surface in the AoI, and dips southwest (California Division of Oil and Gas, 1981, Table 2, p. B-5).

The potentiometric surface in the upper zone of the Chanac Formation slopes westward at approximately 225 ft/mi (43 m/km) in the eastern part of the field (**Figure 85**).

Both the lower and middle zones of the Chanac Formation appear to act as separate aquifers (**Figure 86**). In each zone, the elevation of the potentiometric surface lies above the top of the zone, indicating confined conditions.

Within the AoI, the Chanac Formation was historically treated as aquifer exempt (HTAE) and was used for Class II injection (California Division of Oil and Gas, 1981, Table 2, p. B-5). The Chanac Formation was clarified as a non-exempt aquifer as of March 7, 2017, and no injection is currently permitted or operational in that zone in the AoI.

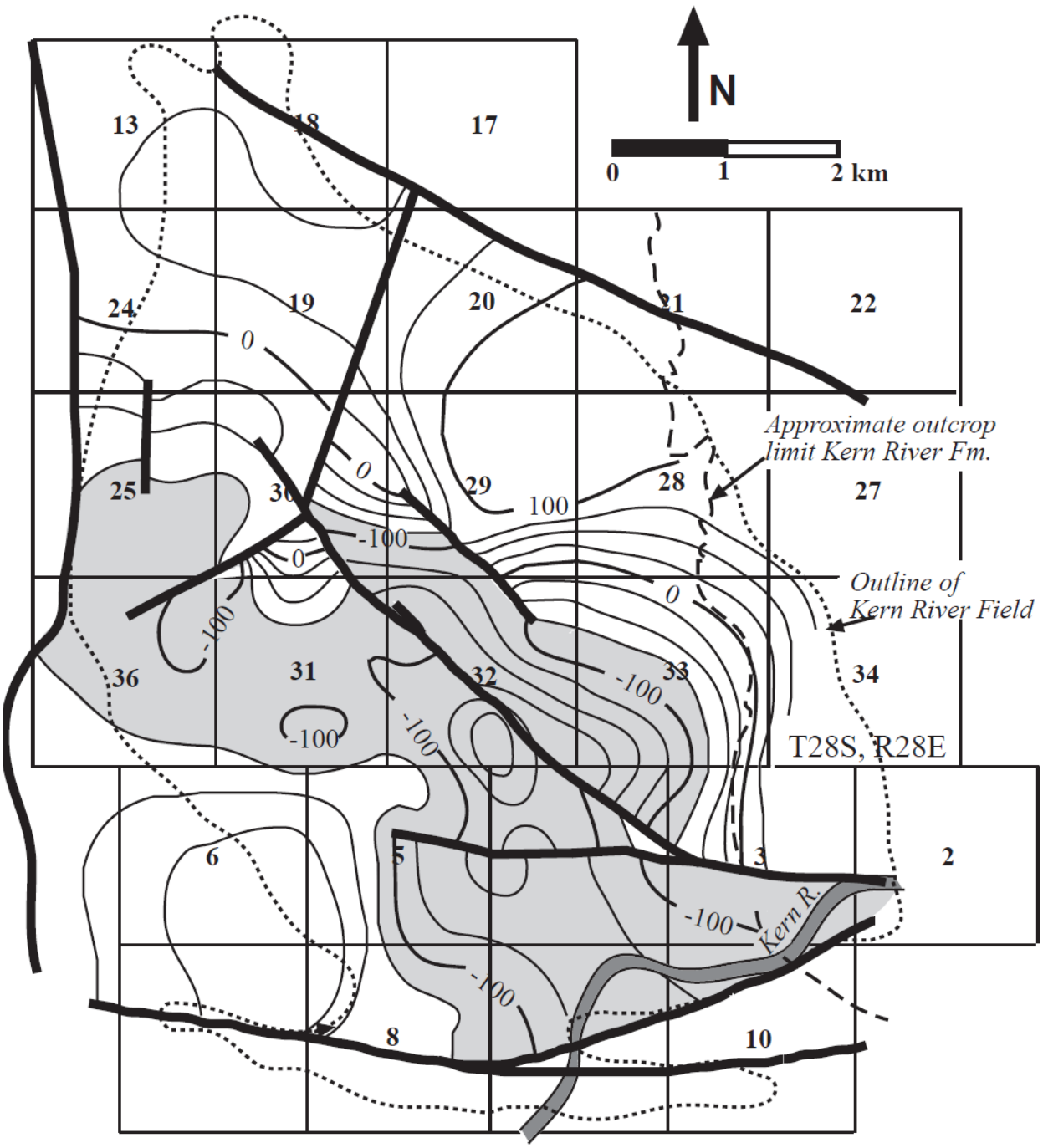

Figure 85. Potentiometric surface map of the upper Chanac Formation. The shaded region indicates a depression in the potentiometric surface.

Santa Margarita Sandstone

The Santa Margarita sandstone conformably overlies the Round Mountain formation and represents the lowermost USDW within the AoI and the AoR. The Santa Margarita Sandstone is an upper Miocene marine interval consisting of gray to white, fine-grained to coarse-grained sandstone that thins eastward (Kodl et al., 1990). The Santa Margarita sandstone consists of a lower main zone and an upper transition zone across most of the AoI and is conformably overlain by the Chanac Formation. In the eastern part of the AoI, the transition zone and the Chanac Formation are progressively eroded, resulting in an unconformable contact between the Santa Margarita and the Chanac or Kern River formations (Kodl et al., 1990). The thickness of the Santa Margarita Sandstone ranges between approximately 125 and 650 ft, the average porosity is 31 percent, and the average permeability is 400 mD (Coburn and Gillespie, 2002). It occurs at a depth of 760'-1,185' below ground surface in the AoI, and dips southwest (California Division of Oil and Gas, 1981, Table 2, p. B-5). A gradient line was determined in the main Santa Margarita sandstone interval with pressure ranging from 575-655 psig (**Figure 86**); Coburn and Gillespie, 2002).

Figure 87 is a potentiometric surface map of the main Santa Margarita interval reflecting a compartmentalization based on pressure data. Coburn and Gillespie (2002) demonstrated that there is no groundwater flow through the Canfield fault based on pressure differences across the fault illustrated on the potentiometric surface map. Coburn and Gillespie (2002) also explained that the high pressure could be caused by historical disposal of produced water contained in the Santa Margarita Sandstone. Historically, within the AoI, the Santa Margarita Sandstone was a historically treated as aquifer exempt (HTAE) and was used for Class II injection (California Division of Oil and Gas, 1981, Table 2, p. B-5). The Santa Margarita Sandstone was clarified as a non-exempt aquifer as of March 7, 2017, and no injection is currently permitted or operational in that zone in the AoI.

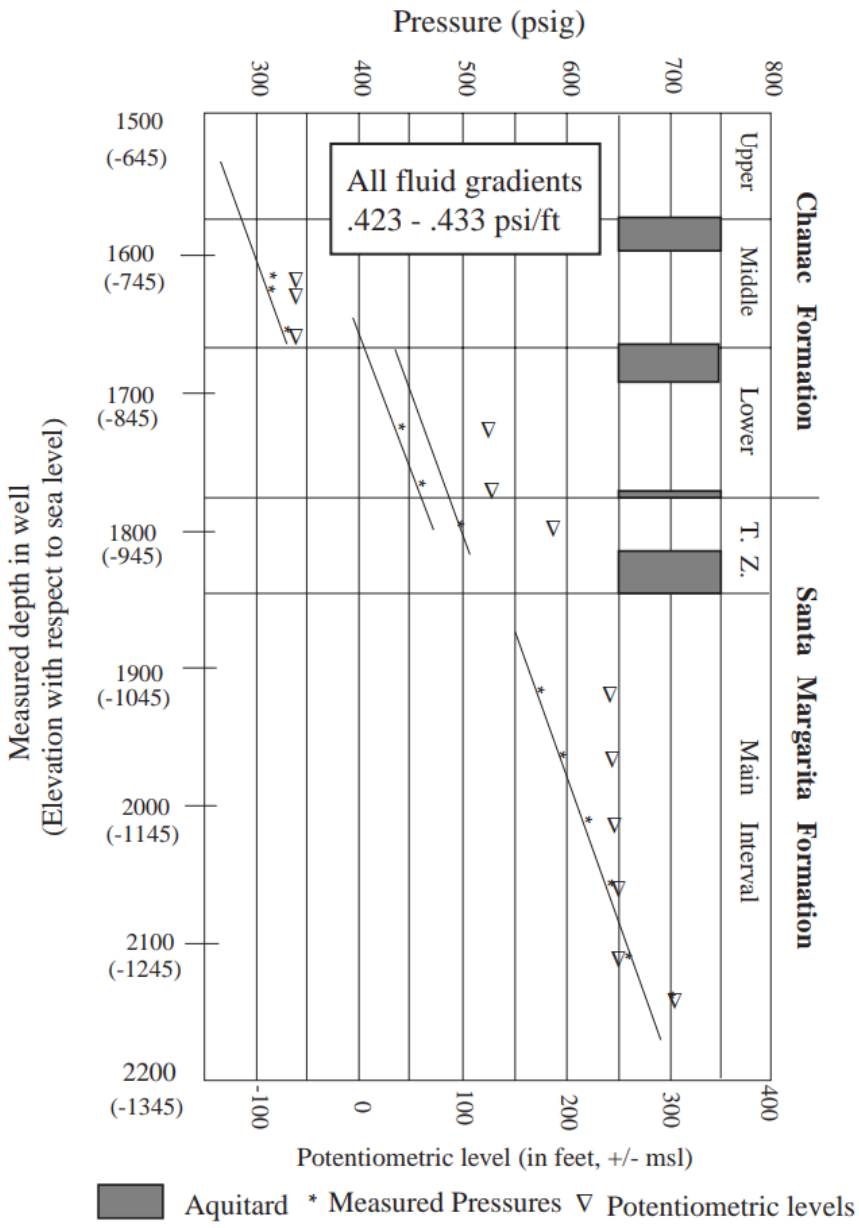

Figure 86. Pressure profile across Chanac Formation and Santa Margarita Sandstone (from Coburn and Gillespie, 2002).

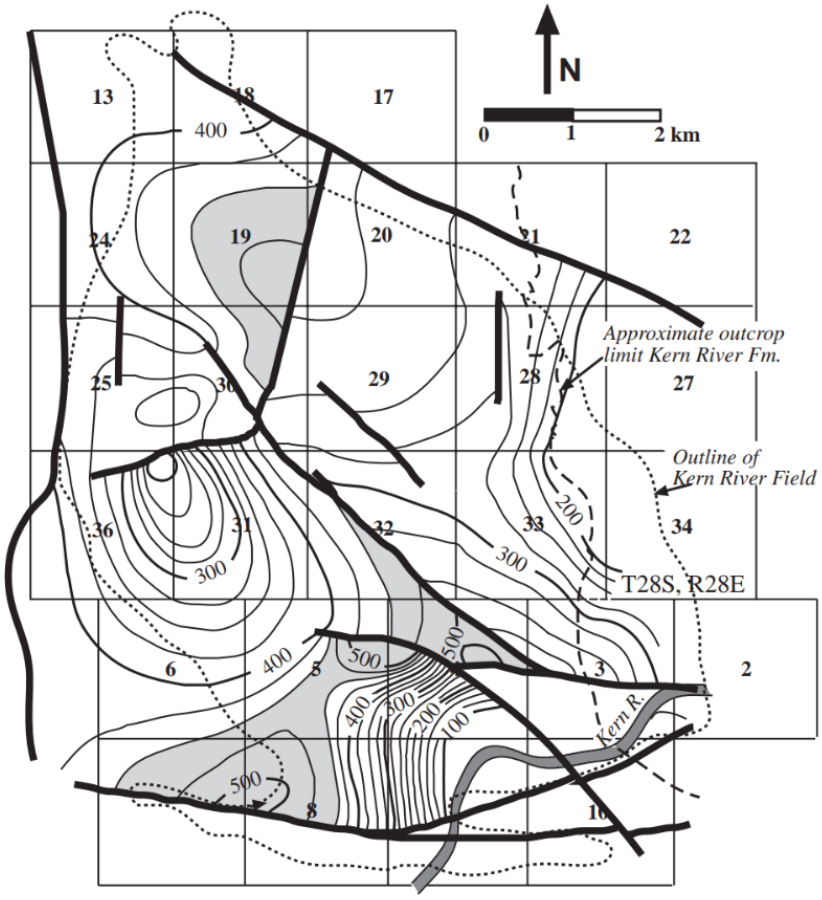

Figure 87. Potentiometric surface map of Santa Margarita. Shaded areas imply areas of higher pressure in this confined aquifer (from Coburn and Gillespie, 2002).

Water Wells

On behalf of Chevron, California Geologic Energy Management (CalGEM) performed a water well search and capture zone analysis and published its findings and conclusions in a memo dated 22 March 2019. The water well search used a combination of Division of Water Resources (DWR) water well completion reports, Kern County Environmental Health (KCEH) water well completion reports, Geotracker GAMA, and field reconnaissance to identify water wells that are located in or near the AoI. Chevron searched the California Water Board Ground Water Ambient Monitoring and Assessment Program (GAMA, 2023) and the California Department of Water Resources Well Completion Reports (California Department of Water Resources, 2023) for new wells drilled since the memorandum dated 22 March 2019 to update the water well list provided by California Geologic Energy Management Division (CalGEM). Where possible, satellite imagery was used to verify the surface locations associated with new wells since the memorandum. Identified active water wells are less than 1200 ft deep, much shallower than the proposed injection zone in the Vedder Sand.

There are no wells of current beneficial use in the project AoR. The nearest active water-supply wells are approximately 2,400 ft southeast of the AoR and have been completed in perched groundwater in the Kern River Formation to depths of less than 1000 ft below ground surface. The nearest water-supply well to the proposed injectors is WW_KR_001 (**Table 14**), which is approximately 3000 ft from the planned injection site **(Figure 88)**. **Figure 88** shows the water-supply wells within 1 mile of the Project AoR. **Figure 89** is a cross section illustrating the difference in depths, objective stratigraphy encountered, and the distance between water-supply wells and the proposed injection targets.

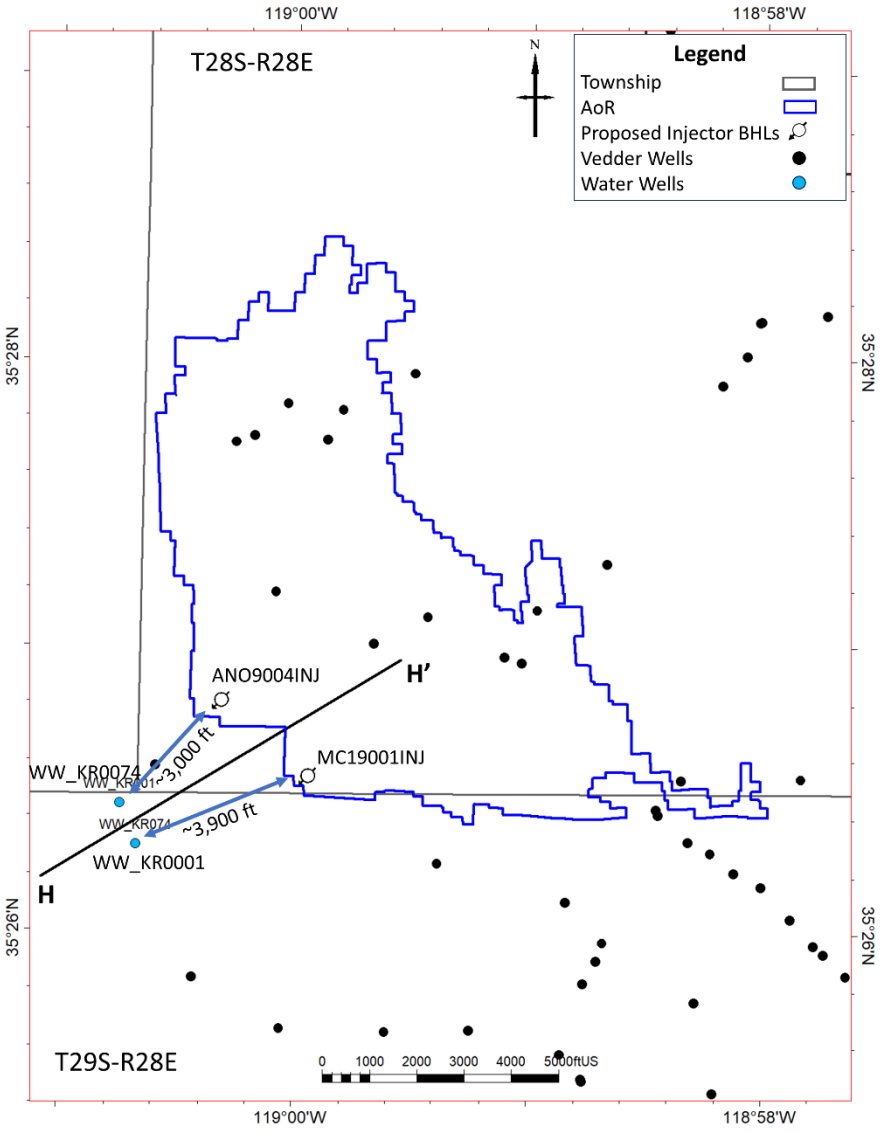

Figure 88. Map showing water-supply wells (blue circles) and wells with Vedder Sand penetrations (black symbols).

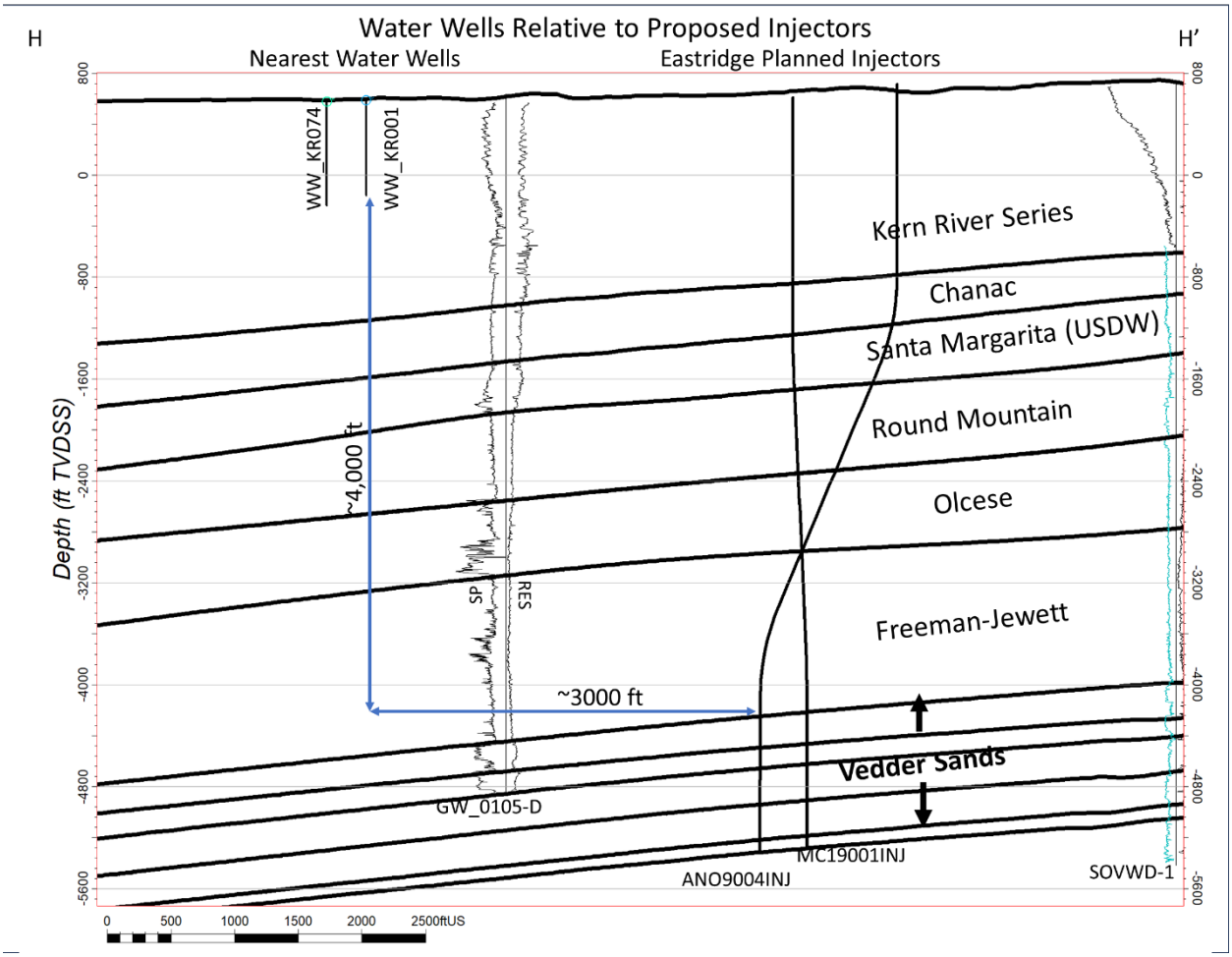

Figure 89. Cross-section showing distances from the proposed CO2 injectors (Class VI injection zone) to the nearest water-supply wells.

Table 14. Summary of nearest water-supply to the Project AoR depicted in **Figure 88** and **Figure 89**.

Well ID	TRS	Latitude	Longitude	Well Type	Elev.	TD	Top Perf	Btm Perf	Screen len
					ft	MD, ft	MD, ft	MD, ft	MD, ft
WW_KR001	T29S R28E S6	35.4407	-119.0133	Domestic	592	750	600	750	150
WW_KR074	T29S R28E S6	35.4383	-119.0121	Industrial	-	780	610	780	170

Geochemistry [40 CFR 146.82(a)(6)]

Site specific Vedder Sand geochemical fluid data was sourced from formation fluid analyses, while solid-phase geochemistry data was sourced from x-ray diffraction (XRD) analysis. **Table 15** summarizes specific data sourcing by well and by sample count. Samples were taken from within the Area of Interest (AoI). Though the specific constituents that were tested for vary slightly from sample to sample, most water samples have been analyzed to identify carbonates, bicarbonates, chlorides, sulfates, sulfides, nitrates, silica, calcium, magnesium, boron, iron, total dissolved solids, pH, conductivity, and resistivity. Analyses are taken as presented by the reporting companies. The data in **Table 15** and **Figure 90** provides a spatially diverse and representative dataset for examining water chemistry and mineralogy throughout the Vedder sands in the AoI.

Table 15. Geochemical data sourcing of the Vedder Sand within Kern River Oil Field.

Well Info		**Data type and sample count**		
API 10	**Well Name**	**Fluid Analysis**	**XRD**	**Well Location**
0402966411	33_0028X	4	4	AoR
0402967217	APV0051X	6	10	AoR
0402966558	OM_0044X		5	AoI
0402969903	KA_0053X	16		AoR
0402953911	SJ_0001WD	1		AoI
0402964412	APV_0001WD	2		AoI
0402967587	MON0065X	3		AoR
0402969762	REV0004X	3		AoI

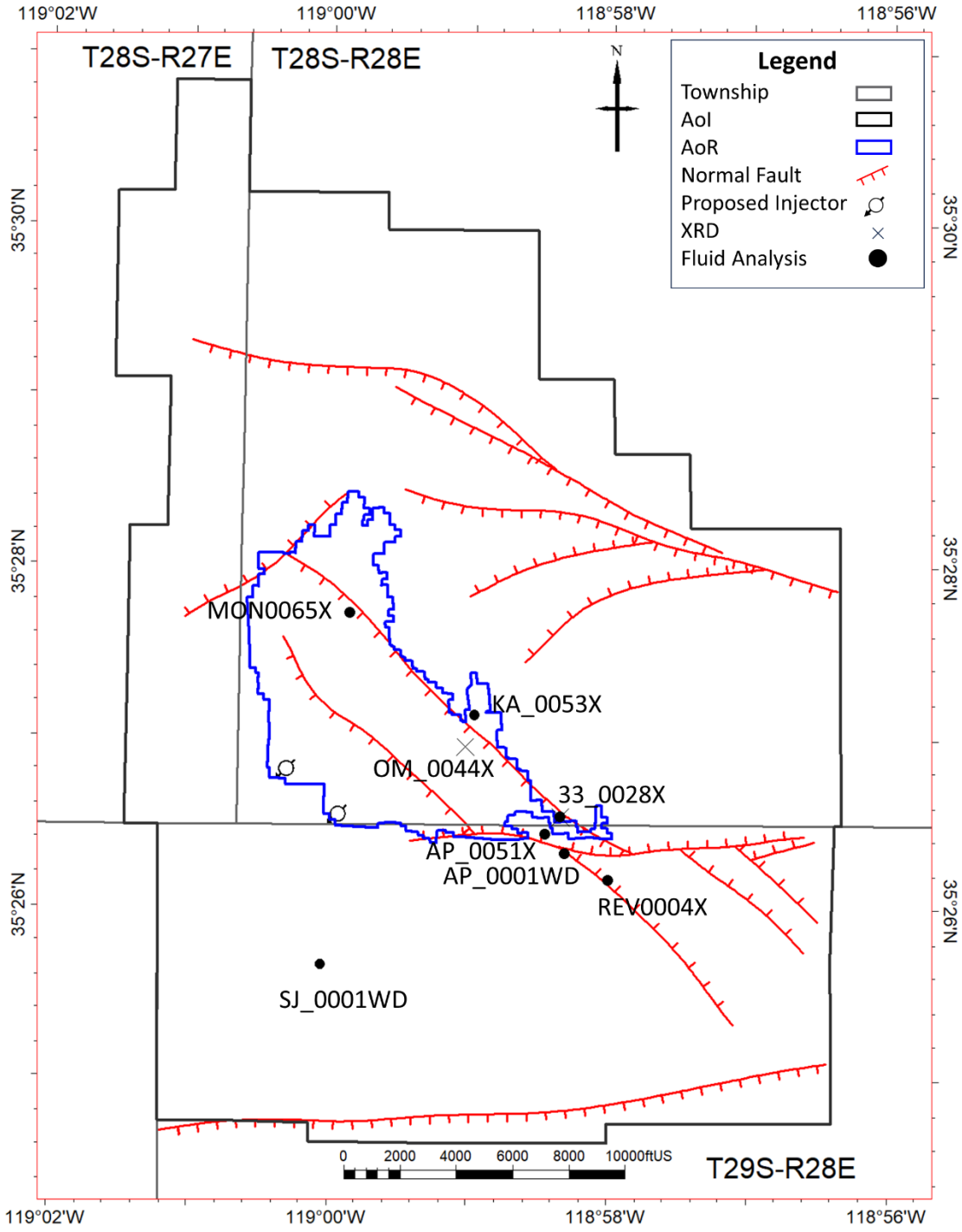

Figure 90. Location of wells with geochemical data, including fluid analyses and XRD data.

XRD analysis has identified calcium rich smectite, feldspar, quartz, and minimal illite and kaolinite within the Vedder sands. Chevron analyzed intra-Vedder mudstone because they represent a reasonable analog for the expected composition of the Freeman–Jewett Silt. Additional data will be collected during construction of the injection wells to analyze the mineralogy of seals within the Freeman–Jewett Silt.

Chevron partnered with Lawrence Berkeley National Laboratory (LBNL) to combine site specific solid and fluid geochemical data with static earth model properties to simulate geochemical reactions and their impact when CO_2 is injected into the reservoir. The simulations were run using the TOUGHREACT simulator, a 3D reactive transport code that handles the non-isothermal, multi-phase/multi-component fluid flow, heat transport, aqueous and gaseous species advection-diffusion, and equilibrium/kinetic water-gas-rock-biological reactions (Sonnenthal et al. 2021; and Xu et al., 2011). The ECO2n V2.0 equation of state module was used in the modeling work done by LBNL. ECO2n V2.0 is based on the work by Spycher and Pruess (2005) and describes the mixture of CO_2 and water in brine aquifers over an extended range of temperatures, pressures, and halite concentrations. In addition, ECO2n V2.0 accounts for the impacts of water on the properties of CO_2 that were overlooked in V1.0 (thermophysical) (Pan et al., 2014), as well as increasing the temperature limit from 105° C to 305° C (along with the saturation pressure). Fluid phases can appear and disappear during the simulation along with the precipitation/dissolution of salt (Sonnenthal et al. 2021). The thermodynamic database used in the course of this work is the Pitzer database with updates for dawsonite data, switched basis species, and gas diffusion coefficients. Thermodynamic database used in the simulations is based on a conversion of the EQ3/6 Pitzer database (after Wolery et al., 2004; and Alai et al., 2005), suitable for ionic strengths up to about 40 molal for some systems and temperatures around 150° C at solution vapor saturation pressures (see Spycher et al., 2021). Kinetic data were derived from a variety of sources, many based originally on Palandri and Kharaka (2004), and many estimated based on similar mineral structures. Because the reactive surface area is a major factor in the effective reaction rates, and can vary by many orders of magnitude, uncertainties in the rate constants are included in the effective reaction rates. Thermodynamic data are generally much more impactful in the system evolution because they control mineral evolution (i.e., whether a mineral has a tendency to dissolve or precipitate). Determining the effective reaction rate is done by calibrating reactive surface areas, and modifications to kinetic parameters and reaction-rate laws, to observed changes in mineral abundances over time and water chemistry, once site-specific field data are available. Many secondary (and primary) minerals are solid solutions that can have several endmembers and potential substituting ions. Thermodynamics of solid solutions can be nonideal and data are uncertain for many of the highly complex minerals such as montmorillonite. The model approach and data used here is similar to many reactive-transport simulations of carbonate dissolution and precipitation in geologic formations (e.g., Addassi et al., 2021; Benjakul et al. 2020; Plampin et al., 2021; Kumar et al., 2020; Zhang et al., 2019; and Aradóttir et al., 2012, 2015).

Data from a representative sample from the Section 33_28X well in the Vedder Sand was used to establish initial geochemical conditions for the model. **Table 16** lists the initial geochemical input data. Some primary species concentrations were set small, either because they were not measured (e.g., Ba and Sr) or they are determined *in-situ* based on reactions with primary minerals (e.g., Al^{+3}).

Table 16. Initial water geochemistry inputs for TOUGHREACT simulations.

TOUGHREACT Water Chemistry Input		
Composition	**ppm**	**Comments**
H_3BO_3	65.20	12 ppm Boron
Ca(2+)	51.00	
Mg(2+)	1.80	
K(+)	18.00	
Na(+)	1500.00	
Li(+)	1.00E-8	molal
HCO_3(-)	135.10	
Cl(-)	2336.40	
SO_4(2-)	5.00	
HS-	1.00E-20	molal
F(-)	3.20	
Fe(2+)	0.96	
Mn(2+)	0.05	
Zn(2+)	0.01	
Al(3+)	1.00E-20	molal
SiO_2(aq)	32	equilibrated with quartz
HPO_4(2-)	0.10	
Ba(2+)	1.00E-10	molal
Sr(2+)	1.00E-10	molal
H_20	1.00	
pH	8.10	

The modeled secondary and gaseous species are shown in **Table 17**. **Table 18** is a list of primary and secondary minerals of the model.

Table 17. List of secondary and gas species in the geochemical model.

Secondary Species						
clo4-	bh4-	alf+2	caco3(aq)	feco3(aq)	feso4+	hsio3-
fe+3	po4-3	alf2+	caoh+	fe(co3)2-2	fe(so4)2-	h2po4-
h2(aq)	oh-	alf3(aq)	caso4(aq)	feoh+	fecl+2	h3po4(aq)
hpo3-2	co3-2	alf4-	cacl+	fe(oh)2(aq)	fecl2+	licl(aq)
o2(aq)	alo2-	b(oh)4-	cacl2(aq)	feoh+2	fef+	mgco3(aq)
mn+3	aloh+2	b3o3(oh)4-	co2(aq)	fe(oh)2+	fef+2	mghco3+
mno4-2	alo+	b4o5(oh)4-2	fecl+	fe(oh)3(aq)	fef2+	mgoh+
so3-2	halo2(aq)	cab(oh)4+	fehco3+	fe(oh)4-	hso4-	mgb(oh)4+

Gas Species
$CO_2(g)$
$O_2(g)$
$H_2S(g)$

Table 18. List of kinetic (kin.) and equilibrium (eq.) reaction minerals and initial volume fractions (logK) in the geochemical model.

Kin.minerals	log(K)
calcite	1.363
siderite	-2.159
Dolomite (ordered)	1.828
anhydrite	-4.705
quartz	-3.345
cristobalite	-2.817
chalcedony	-3.135
silica-amorphous	-2.271
anorthite	17.783
albite-high	2.221
microcline	-1.645
annite	25.184
phlogopite	32.925
clinochlore	48.745
daphnite	37.438
muscovite	6.918
kaolinite	1.171
nontronite-ca	-25.610
nontronite-mg	-25.702
nontronite-na	-25.431
nontronite-k	-25.683
sepiolite	27.670
analcite	5.000
hematite	-15.384
magnetite	-6.358
pyrite	191.317
pyrrhotite	118.378
sphalerite	111.507
apatite-f	-32.295

eq.minerals	log(K)
halite	1.605
barite	-9.590
witherite	1.463
gypsum	-4.685
bloedite	-2.347
glauberite	-5.867

The simulations included the overburden of the Freeman–Jewett Silt and the injection zone of the Vedder sand. Zonal injection of 14 MMSCF per day were injected into a single well in a 2-D radial TOUGHREACT model. The model discretization, porosity and permeability are shown in **Figure 91** The model is 1-km (3280-ft) in length with 61 m of Vedder Sand with 50 m of Freeman–Jewett Silt overburden and approximately 40 m (130 ft) of underlying shale (underburden). The near wellbore region of the model horizontal discretization is 7 ft (2 m)–for nearly 250 ft (76 meters) radially around the wellbore–gradually increasing to328 ft (100 m) at the far boundary (3280 ft [1 km] from the wellbore). The vertical discretization of the model is approximately 3 ft (1 m) throughout the injection zone and Vedder sands for 1 layer into the caprock and basal seal, gradually increasing to nearly 66 ft (20 m) at the top and bottom boundaries. The Vedder sand has a permeability of 5000 mD and a porosity of 30%, whereas the Freeman–Jewett Silt has a permeability of 2.06 mD. Permeability anisotropy (kv/kh) varies from 1.0 to 0.1 in the target zone and overburden, respectively.

Steady-state thermal-hydrological simulations were first performed using a temperature gradient of 28° C/km and a top temperature of 62.5° C and top pressure of 15.427 Mpa. The initial salinity (i.e., ppm NaCl) was assumed uniformly distributed at 3849.6 ppm, with an initial dissolved CO_2 mass fraction of about 1.0 x 10^{-4}. The steady-steady conditions were then used as the initial conditions for the supercritical CO_2 injection, assuming no-flux at top and bottom boundaries and a far-field hydrostatic (infinite) boundary.

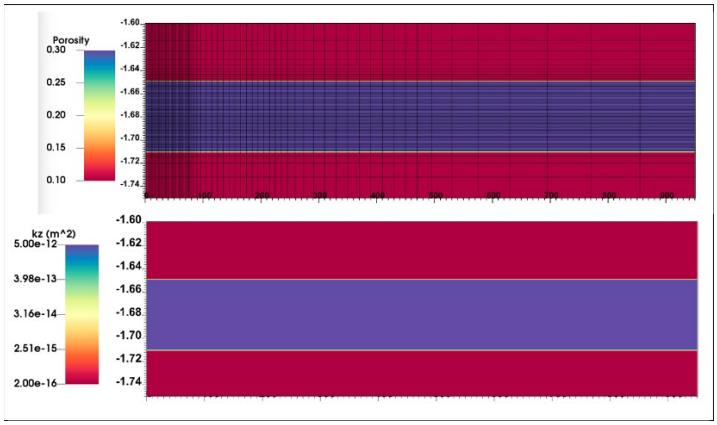

Figure 91. Geometry, porosity, and permeability of the 2D radial model.

The total simulation time for the final supercritical CO_2 injection simulation was 20 years with minimum timestep of 1 second. A similar simulation to 2 years was also performed with a slightly different time-stepping criteria. The simulator uses a backward Euler time discretization scheme and an operator splitting scheme to couple transport and reactions. The timestep starts at 1 second and dynamically adjusts depending on the Courant limit for the maximum gas or liquid velocity, the number of Newton–Raphson iterations, or the maximum number of chemical iterations. For a 2-year simulation, the timestep was around 470 seconds for much of the simulation (Courant criterion=0.5), dropping to less than 0.1 second during chemical convergence time periods. The 20-year simulation was run with a Courant criterion of 1.0, with an improved chemical convergence scheme and had timesteps typically about 1341 seconds.

During early time (4 days), as the CO_2 moves into the formation, pH drops and a small zone of dry out occurs along with an increase in Na+. During this time, bicarbonate increases in the pore water and salt begins to precipitate in very small quantities. On a net basis very close to the wellbore, there is a very small increase in the porosity observed (change of +3.05E-05 pore units). In terms of mineralogical changes, a small amount of albite, K-feldspar, and illite dissolution occurs. Ca-montmorillonite dissolution also occurs near the wellbore with a small amount of precipitation towards the very edge of the CO_2 front.

Over larger time frames (1-2 years) and extended areas of supercritical CO_2 contact with brine, the overburden formation (i.e., Freeman–Jewett Silt), and the injection zone (i.e., Vedder Sand), multiple geochemical reactions occur at different scales. Even though numerous minerals dissolve and precipitate, the net porosity change is small. In the first few meters adjacent to the well, **Figure 92** shows the near wellbore change in porosity where closest to the wellbore, a net decrease of porosity is observed, due to “dryout” adjacent to the well, that rapidly changes to a net increase in porosity 3 meters away from the wellbore.

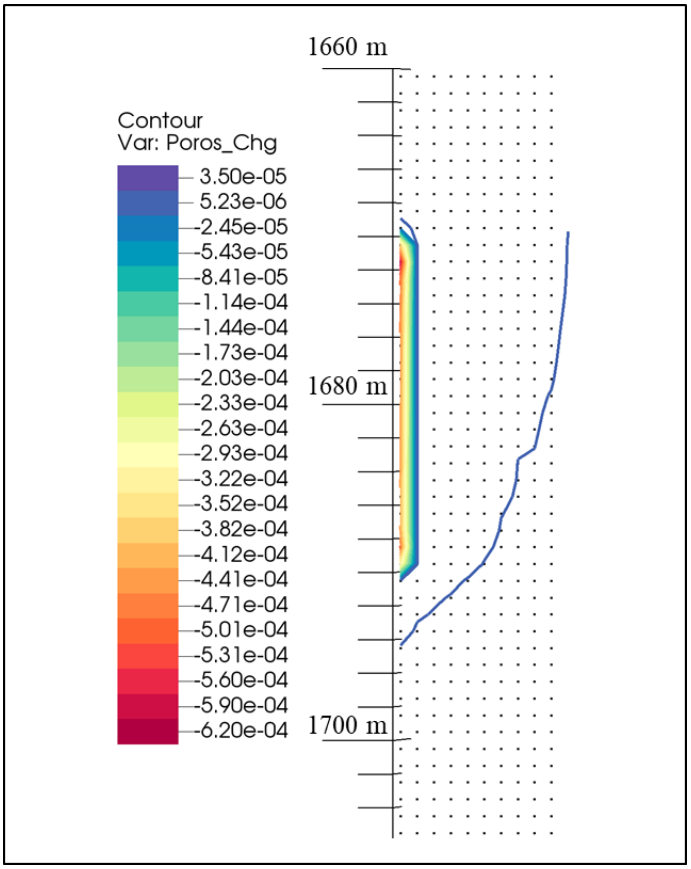

Figure 92. Net porosity changes after 2 years of supercritical CO_2 injection at 14 MMSCF per day. Spatial increments in image are 2 meters between each dot (grid block center) laterally. Image shows minimal change to porosity from -6.20E-04 pore units (volume fraction) closest to the wellbore that rapidly changes to +3.5E-05 pore units at a distance greater than 3-4 meters.

Model Snapshots for feldspar dissolution (K-feldspar and albite), montmorillonite dissolution, kaolinite precipitation, and porosity change are shown in **Figure 93** In these images, a more global change to porosity is observed further into the formation, where the net change is positive (larger porosity). The interpretation of these simulations shows that acid dissolution of the feldspars and montmorillonite overwhelmed the kaolinite precipitation. Even over longer time frames, the changes to porosity are very small in the Vedder Sand or Freeman–Jewett Silt.

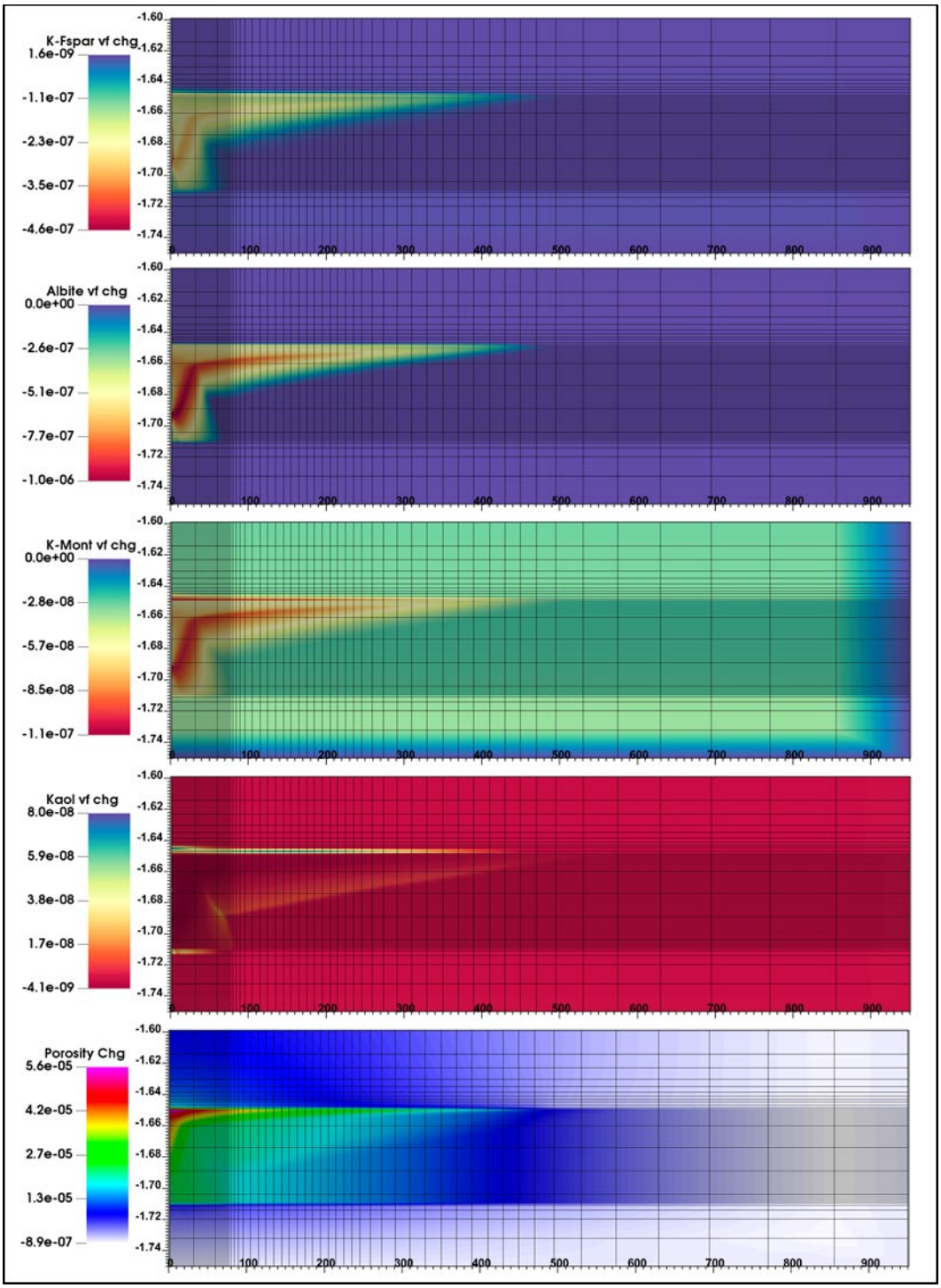

Figure 93. Dissolution of feldspar (K-feldspar and albite) and montmorillonite. Precipitation of kaolinite and the net change to porosity after 1 year of supercritical CO_2 injection at 14 MMSCF per day.

The simulation results indicate a slight increase in reservoir temperature (maximum about 3° C) which is due to gas expansion (Joule-Thomson) and enthalpy of the solution. Due to high permeability and near reservoir pressure and temperature of the gas, the Joule-Thompson effect is small.

The results from this study highlight an expected net positive change to porosity since acid dissolution was found to dissolve more than is being precipitated. The minor amount of precipitation also indicate that geochemical trapping is not expected to play a significant role in trapping CO_2 during the expected project timeframes. Results from the LBNL study show negligible permeability and porosity changes with virtually no expected degradation of injectivity due to geochemical reactions (Sonnenthal et al, 2022.).

Site Suitability [40 CFR 146.83]

The detailed reservoir characterization provided in previous sections of this application demonstrates that Vedder Sand meets the suitability requirements delineated at 40 CFR 146.83. The site suitability section provides supplementary support for the geologic containment, storage capacity, and injectivity of CO2 within the AoR.

The Project, which is located in Kern County, California, will inject and sequester between 265,000 and 455,000 metric tonnes per year in the Vedder Sand within the Kern River Oil Field for a period of 20 years. The cumulative amount of sequestered CO_2 is expected to total 6.82 million tonnes over the life of the Project.

CO_2 will be captured from a variety of emission sources (e.g., direct air capture). The CO_2 will be compressed and transported via pipeline to the injector well locations. The CO_2 will be injected into the Vedder Sand for 20 years and then monitored for a period of 50 years after last CO_2 injection.

The Vedder Sand is ideally situated as a high-quality CO_2 storage complex with favorable reservoir quality and laterally extensive shale zones that form multiple stratigraphic seals within and above the injection interval. Project datasets within the AoR and AoI include 3D seismic, wireline, core data, injection and fracture gradient tests, and pressure transient analysis.

The AoI has been characterized by a rich dataset including 3D seismic, well log, core data, injection and fracture gradient tests, and pressure transient analysis. A high-quality 3D, depth-converted seismic survey covering 20 square miles across the AoI delineates the structural framework (e.g., faults and stratigraphic horizons). Wells penetrating the Vedder within the AoI (n=70) provide a detailed source of petrophysical data including routine and special core analysis (RCA and SCAL) for stratigraphic characterization and reservoir model conditioning.

The Vedder Sand is a gently dipping, exempted aquifer possessing high-porosity and permeability, stable mineralogy, excellent lateral connectivity, and strong vertical heterogeneity. Regional seismicity, formation tests, 1D mechanical earth model (MEM) analysis, and fault slip potential tests indicate a low probability of induced seismicity during project operations.

Key findings from multiple technical studies with data sourcing from within the AoR and AoI demonstrate the Vedder Sand and vertically confining Freeman-Jewett Silt within the AoI to be an ideal location for safe and reliable storage of CO_2.

Geologic containment

- The presence of multiple, thick, and laterally extensive low-permeability zones provides vertical stratigraphic containment and isolation of the Vedder Sand from USDW's.
- Injection near the southwestern parts of the AoI will increase the areal contact of injected CO_2 across the injection zone, which dips 3 to 6 degrees southwest.
- Normal faults are mapped in the AoI that compartmentalize the Vedder reservoir.
- The Freeman–Jewett Silt is the upper confining zone for the Vedder Sand injection zone, has a mean thickness of 1,140 ft within the AoI, and is laterally continuous across the region. Additionally, the Vedder Sand has produced more than 600 MMBO and 200 BCFG in the southeastern San Joaquin Basin (Tye et al., 1993), the Freeman-Jewett Silt is the primary topseal for those hydrocarbon accumulations, corroborating the sealing capacity of the Freeman-Jewett Silt to maintain significant columns of oil and gas. Secondary seals, including the Round Mountain Silt and intraformational Vedder seals, provide additional sealing capacity, and are also regional topseals for hydrocarbon accumulations in the region and in the AoI, respectively.
- Chevron will operate with automated, fail-safe control systems to ensure bottomhole injection pressures are no more than 90 percent of the observed Propagation Pressure in the Vedder Sand. This results in an equivalent maximum injection pressure gradient of 0.578 psi/ft, which is well below the observed 0.63 psi/ft fracture gradient in the Freeman–Jewett Silt.
- Faults provide additional lateral containment. An extensive technical study coupled Allen diagrams and SGR with dynamic simulations and pressure transient analysis to assess lateral sealing capacity and demonstrated geologic containment within the AoR.
- The Vedder Sand is a suitable sequestration reservoir that forms a widespread saline aquifer in the supercritical CO_2 window. The Vedder Sand is 1050 ft in thickness and has excellent reservoir properties with an average porosity of 29% and an average permeability of approximately 2000 mD. Reservoir properties were determined using petrophysical data, whole-core and sidewall-core data.

CO_2 plume simulations

- The Vedder Sand and overlying Freeman–Jewett Silt form a high-quality CO_2 storage complex with favorable reservoir quality and laterally extensive shale zones that form numerous stratigraphic seals. Multiple, independent datasets have been integrated to demonstrate the mechanical integrity of this storage complex, that fluid migration and the extent of pressure elevation are within safe limits, and that USDWs are not endangered.
- A robust set of interpretations using available data was incorporated into a full-field 3D geocellular model to support reservoir simulations. Multiple reservoir simulations using this comprehensive model were used to analyze CO_2 migration, evaluate impacts of multiple CO_2 trapping mechanisms, and to demonstrate geologic containment within the storage complex.
- Numerous plume migration scenarios have been evaluated using dynamic reservoir simulation that support containment of CO_2 within the proposed AoR.
- The AoR includes the area swept by CO_2 and the region of elevated pressure above the site-specific critical pressure threshold. Preliminary reservoir simulations indicate that the inclusion of water-producers into the project design can minimize the elevated pressure region associated with CO_2 injection, reducing the size of the AoR to the maximum extent of CO_2.

AoR and Corrective Action

AoR and Corrective Action GSDT Submissions
GSDT Module: AoR and Corrective Action ***Tab(s):*** All applicable tabs Please use the checkbox(es) to verify the following information was submitted to the GSDT: ☒ Tabulation of all wells within AoR that penetrate confining zone ***[40 CFR 146.82(a)(4)]*** ☒ AoR and Corrective Action Plan ***[40 CFR 146.82(a)(13) and 146.84(b)]*** ☒ Computational modeling details ***[40 CFR 146.84I]***

Chevron's AoR and Corrective Action Document outlines the data, processes, software, and simulation results used to delineate the AoR. The AoR and Corrective Action Document details data sourcing and analysis that was leveraged to generate a representative model that has been used to forecast pressure front and CO_2 plume migration through the life of the project. The document also provides a report on the wide variety of sensitivities that have been analyzed and their corresponding impacts to the AoR. The project AoR is shown in **Figure 1**.

In addition, the AoR and Corrective Action Document provides a tabulation of all wells within the AoR that penetrate the confining zone. Under current operational conditions, there are no integrity concerns for these wells. With proposed CO_2 injection, Chevron plans to conduct work on specific wells to support proactive zonal isolation. This plan is detailed in the AoR and Corrective Action Document.

Financial Responsibility

Financial Responsibility GSDT Submissions
GSDT Module: Financial Responsibility Demonstration ***Tab(s):*** Cost Estimate tab and all applicable financial instrument tabs Please use the checkbox(es) to verify the following information was submitted to the GSDT: ☒ Demonstration of financial responsibility ***[40 CFR 146.82(a)(14) and 146.85]***

Chevron U.S.A. Inc. (Chevron) is providing financial responsibility pursuant to 40 CFR 146.85. Chevron intends to use a corporate guarantee from Chevron Corporation, of which it is a wholly owned subsidiary, to provide financial assurance for the project.

Injection Well Construction

Chevron plans to permit four new CO_2 injection wells into the Vedder Sands in the Kern River Field (MC19001INJ, ANO9004INJ, ANO9005INJ, and MC19002INJ). Once permitted, Chevron plans to construct MC19001INJ and ANO9004INJ. Chevron plans to retain ANO9005INJ and MC19002INJ as undrilled permitted contingent injectors in the unlikely event MC19001INJ or ANO9004INJ must be abandoned prior to planned injection cessation. Chevron has planned the contingent injectors to be within 250ft of MC19001INJ and ANO9004INJ. These wells have been engineered with appropriate materials to meet the structural integrity requirements of 40 CFR 146.86, to meet Chevron's internal standards for well design, and to minimize corrosion throughout the life of the project.

The full well construction details for the CO_2 injectors can be found in the Construction Details Documents.

Proposed Stimulation Program [40 CFR 146.82(a)(9)]

It is anticipated that the target injection zone will require near-wellbore maintenance to dissolve drilling mud, carbonate and other minerals introduced to the near-wellbore region during drilling, completion, and injection operations. The objective of the near-wellbore maintenance program is to increase injectivity by removing skin that is degrading the permeability in the near-wellbore region and returning the near-wellbore region to native conditions. Near-wellbore maintenance does not include hydraulic fracturing.

Exact near-wellbore maintenance program design will depend on final drilling program fluid design, final open hole logs, analysis of the chemical constituents of the injection gas, formation mineral content obtained from wellbore or offset well core studies, and injectivity trends as a function of time.

Full details can be found in the Stimulation Program.

Construction Procedures [40 CFR 146.82(a)(12), 146.86, 146.87]

Conductor casing will be set for drilling the first surface casing hole and cementing the first surface casing.

The first surface casing hole will be drilled as detailed in **Table 19**. Deviation check surveys will be taken while drilling (40 CFR 146.87(a)(1)). Open hole logs including resistivity, spontaneous potential, caliper, and gamma ray will be run prior to running casing (40 CFR 146.87(a)(2)(i)). The first surface casing will be run and cemented to surface. After the casing is set and cemented, a cement bond log, variable density log, and temperature log will be run (40 CFR 146.87(a)(2)(ii)).

The second surface casing hole section will be drilled to the base of the Freeman-Jewett Silt (confining layer). Deviation check surveys will be taken while drilling (40 CFR 146.87(a)(1)). Open hole logs including resistivity, spontaneous potential, caliper, and gamma ray will be run prior to running casing (40 CFR 146.87(a)(2)(i)). The second surface casing will be run and cemented to surface to isolate the USDW zones as required by 40 CFR 146.86(a)(1) and 40 CFR 146.86(b)(2). After the casing is set and cemented, a cement bond log, variable density log, and temperature log will be run (40 CFR 146.87(a)(2)(ii)).

The injection casing hole section will be drilled to the base of the 5th Vedder sand. Deviation check surveys will be taken while drilling (40 CFR 146.87 (1)). Open hole logs including resistivity, spontaneous potential, porosity, caliper, gamma ray, and fracture finder logs will be run prior to running casing (40 CFR 146.87(a)(3)(i)). The injection casing will be run and cemented to surface (40 CFR 146.86(b)(3)). After the casing is set and cemented, a cement bond log, variable density log, and temperature log will be run (40 CFR 146.87(a)(3)(ii)).

The long string casing design will consist of materials compatible with exposure to the injected fluids (40 CFR 146.86(b)(1)). Casing conveyed distributed acoustic sensing (DAS) fiber optics will be run on the long string for testing and monitoring purposes. Refer to the Testing and Monitoring plan and/or QASP for more details. The cement and additives will be compatible with the injection and formation fluids as required by 40 CFR 146.86(b)(5). Casing centralizers will be used to centralize the casing to 70% standoff or greater as per 40 CFR 146.86(b)(3). Well construction materials comply with American Petroleum Institute (API) and American National Standards (ANSI) Recommended Practices, Specifications and Standards.

The injection well will be completed by perforating the authorized injection zones. Completion equipment consisting of packers, monitoring equipment, and tubing will be installed. The flow wetted components of the packer and wellhead will also use material compatible with the injected fluid. Noncorrosive packer fluid treated with corrosion inhibitors and biocide will be circulated in the tubing-by-casing annulus as per 40 CFR 146.88(c).

Table 19 shows the approximate setting depths for the casing strings in the four wells. There may be small adjustments in the setting depths depending on actual formation tops identified while drilling.

Table 19. Proposed casing setting depths.

	Injection Well MC19001INJ	Injection Well ANO9004INJ	Contingent Injection Well MC19002INJ	Contingent Injection Well ANO9005INJ
Conductor (MD ft)	84	84	84	84
First Surface Casing (MD ft)	1,425	1,500	1,425	1,500
Second Surface Casing (MD ft)	4,879	5,174	5,006	5,154
Injection Casing (MD ft)	6,040	6,373	6,169	6,326

Material Selection

The material selected for the flow wetted well construction components including the lower tubing and lower casing is 25 Cr. Modeling results and a literature search confirmed an acceptable corrosion rate for 25 Cr material for the life of the project to meet the well materials compatibility requirement in 40 CFR 146.86(b)(1).

Downhole Monitoring

Downhole monitoring equipment includes a dual transducer pressure/temperature gauge run on tubing above packer and distributed acoustic sensors (DAS) on casing. Oxygen activation logs will be used to conduct the annual external mechanical integrity test as required by 40 CFR 146.90(e), in addition to monitoring the operation of the CCS project.

Safety System for Injection Wells

Well monitoring systems consist of surface sensors for measuring temperature, pressure, and flow. Data from the sensors will be collected and stored in a Supervisory Control and Data Acquisition (SCADA) system. Monitored parameters will have high and low alarms that will be activated when a measured parameter is outside its normal operating range. When a critical parameter such as pressure alarms, the well will be shut in by a fail-safe actuated gate valve that is a component of the injection tree. Operating personnel will be notified that an alarm was activated. The reason for the alarm will be investigated to evaluate what needs to be done to make sure the well is safe. After any needed repairs or maintenance are conducted, the well can be put back into service. A landing nipple profile will be installed near the packer to allow setting a plug or other downhole safety device if required for well maintenance and servicing.

Contingency Plans

Drilling, completion, and workover operations have been deemed low-risk in the Kern River Field due to the low pressure and depleted sands and the low-likelihood of wellbore problems based on the historical records of wells within this field. Chevron has standard operating procedures (SOPs) in place to address contingencies during drilling operations as needed. Some potential drilling problems that Chevron has built contingencies for include:

- Wellbore Placement
- Lost Circulation Management
- Primary Cementing
- Remedial Cementing

Casing and Cementing [40 CFR 146.86(a)(1), (b)]

Casing

The casings and tubing have been designed to withstand all expected loads during the life of the well, including the maximum injection and annulus pressure loads. The materials selected for these items were based on corrosion analysis for compatibility with the injected fluids and reservoir fluids. The tubular design also takes into consideration the expected temperature profile. The upper casing section will be carbon steel with a corrosion resistant alloy (CRA) lower section. The upper tubing section will be carbon steel lined with a glass reinforced epoxy (GRE) for compatibility with the injected and reservoir fluids per 40 CFR 146.86(b)(1). The flow wetted lower part of the injection casing, tubing, and packer will be CRA materials.

Additional details regarding CO_2 injector design can be found in the Construction Details Documents.

Table 20. Casing details and specifications.

Injection Well MC19001INJ	**Setting Depth (ft)**	**Open Hole Diameter (in.)**	**Outside Diameter (in.)**	**Inside Diameter (in.)**	**Weight (ppf)**	**Grade**	**Connection**	**Burst Strength (psi)**	**Collapse Strength (psi)**	**Tensile Strength (lbf)**
Conductor	84	26	20							
First Surface Casing	1,425	17.5	13.375	12.615	54.5	K55	API	2,730	1,130	853,240
Second Surface Casing	4,879	12.25	9.625	8.921	36	K55	API	3,520	2,020	564,000
Injection casing section 1	4,350	8.75	7	6.366	23	L80	Premium (1)	6,340	3,830	532,440
Injection casing section 2	6,040	8.75	7	6.366	23	25Cr80	Premium (1)	6,340	3,830	532,440
Injection Well ANO9004INJ	**Setting Depth (ft)**	**Open Hole Diameter (in.)**	**Outside Diameter (in.)**	**Inside Diameter (in.)**	**Weight (ppf)**	**Grade**	**Connection**	**Burst Strength (psi)**	**Collapse Strength (psi)**	**Tensile Strength (lbf)**
Conductor	84	26	20							
First Surface Casing	1,500	17.5	13.375	12.615	54.5	K55	API	2,730	1,130	853,240
Second Surface Casing	5,174	12.25	9.625	8.921	36	K55	API	3,520	2,020	564,000
Injection casing section 1	4,650	8.75	7	6.366	23	L80	Premium (1)	6,340	3,830	532,440
Injection casing section 2	6,373	8.75	7	6.366	23	25Cr80	Premium (1)	6,340	3,830	532,440

Contingent Injection Well MC19002INJ	Setting Depth (ft)	Open Hole Diameter (in.)	Outside Diameter (in.)	Inside Diameter (in.)	Weight (ppf)	Grade	Connection	Burst Strength (psi)	Collapse Strength (psi)	Tensile Strength (lbf)
Conductor	84	26	20							
First Surface Casing	1,425	17.5	13.375	12.615	54.5	K55	API	2,730	1,130	853,240
Second Surface Casing	5,006	12.25	9.625	8.921	36	K55	API	3,520	2,020	564,000
Injection casing section 1	4,500	8.75	7	6.366	23	L80	Premium (1)	6,340	3,830	532,440
Injection casing section 2	6,169	8.75	7	6.366	23	25Cr80	Premium (1)	6,340	3,830	532,440
Contingent Injection Well ANO9005INJ	**Setting Depth (ft)**	**Open Hole Diameter (in.)**	**Outside Diameter (in.)**	**Inside Diameter (in.)**	**Weight (ppf)**	**Grade**	**Connection**	**Burst Strength (psi)**	**Collapse Strength (psi)**	**Tensile Strength (lbf)**
Conductor	84	26	20							
First Surface Casing	1,500	17.5	13.375	12.615	54.5	K55	API	2,730	1,130	853,240
Second Surface Casing	5,154	12.25	9.625	8.921	36	K55	API	3,520	2,020	564,000
Injection casing section 1	4,600	8.75	7	6.366	23	L80	Premium (1)	6,340	3,830	532,440
Injection casing section 2	6,326	8.75	7	6.366	23	25Cr80	Premium (1)	6,340	3,830	532,440

Notes: (1) Connection with metal-to-metal seals and full pipe body strength.

Cementing

The cementing program will consist of Chevron proprietary blends including a CO_2 resistant blend. The need for fluid loss, retarder, and other additives will be determined as part of the slurry design during initial lab pilot testing by the cement service provider. Choice of the extender and mix water ratio will be considered to minimize free water. Proposed cement jobs will consist of a single slurry that will be preceded by a water or weighted spacer. The cement jobs will consist of light-weight blends and are not currently planned to be staged.

First Surface Casing

The first surface casing cement will be circulated to surface. Top and bottom wiper plugs will be used to minimize contamination.

Casing will be cemented with a 12 ppg surface casing slurry with the top of cement at surface as required by 40 CFR 146.86(b)(2).

Excess slurry volume of 50 – 100% will be pumped to circulate cement to surface. Excess will depend on hole conditions specific to the well.

Second Surface Casing

The casing will be cemented with a 12 ppg surface casing slurry with the top of cement at surface to isolate the USDW zones as required by 40 CFR 146.86(b)(2).

Excess open hole slurry volume of 50 – 100% will be pumped to circulate cement to surface. Excess volume will depend on hole conditions specific to the well.

Injection Casing

The casing will be cemented to surface as required by 40 CFR 146.86(b)(3) with a CO_2 resistant cement blend. The slurry density will be 13 ppg.

Excess slurry volume of 25 – 50% in the open hole section will be used to circulate cement to surface. An open hole caliper log will be used to estimate the annulus volume and the excess volume will ensure cement to surface.

The casing will be centralized (40 CFR 146.86(b)(3)) to provide 70% or greater stand-off.

Casing conveyed DAS fiber optics will be run for testing and monitoring purposes. Refer to the Testing and Monitoring plan and QASP for more details.

Cement Bond, Temperature, and Inspection Logs

After the surface and long-string casings have been cemented, a cement bond and variable density log as well as a temperature log will be run for the CO2 injection wells as required by 40 CFR 146.87(a)(3)(ii) to verify an annular seal. A baseline casing inspection log will also be run.

Tubing and Packer [40 CFR 146.86(b)]

Injection will be through tubing and multiple packers per 40 CFR 146.86(c)(2). Materials for the tubing and packer are shown in **Table 21** and **Table 22** and were selected for compatibility with the injected fluids and reservoir fluids as required by 40 CFR 146.86(c)(1). The packers will be set in the casing opposite the cement.

The tubing size was selected based on the proposed injection rate, composition, reservoir conditions, and monitoring equipment.

Table 21. Tubing Details. Note: (1) Connection with metal-to-metal seals and full pipe body strength.

Well MC19001INJ	**Setting Depth (ft)**	**Outside Diameter (in.)**	**Inside Diameter (in.)**	**Weight (ppf)**	**Grade**	**Connection**	**Burst strength (psi)**	**Collapse strength (psi)**	**Tensile strength (lbf)**
Injection tubing Section 1	4,879	4.5	4.0	11.6	L80 (GRE)	Premium (1)	7,780	6,350	267,040
Injection tubing Section 2	5,849	4.5	4.0	11.6	25Cr80	Premium (1)	7,780	6,350	267,040
Well ANO9004INJ	**Setting Depth (ft)**	**Outside Diameter (in.)**	**Inside Diameter (in.)**	**Weight (ppf)**	**Grade**	**Connection**	**Burst strength (psi)**	**Collapse strength (psi)**	**Tensile strength (lbf)**
Injection tubing Section 1	5,257	4.5	4.0	11.6	L80 (GRE)	Premium (1)	7,780	6,350	267,040
Injection tubing Section 2	6,189	4.5	4.0	11.6	25Cr80	Premium (1)	7,780	6,350	267,040
Well MC19002INJ	**Setting Depth (ft)**	**Outside Diameter (in.)**	**Inside Diameter (in.)**	**Weight (ppf)**	**Grade**	**Connection**	**Burst strength (psi)**	**Collapse strength (psi)**	**Tensile strength (lbf)**
Injection tubing Section 1	5,006	4.5	4.0	11.6	L80 (GRE)	Premium (1)	7,780	6,350	267,040
Injection tubing Section 2	5,976	4.5	4.0	11.6	25Cr80	Premium (1)	7,780	6,350	267,040
Well ANO9005INJ	**Setting Depth (ft)**	**Outside Diameter (in.)**	**Inside Diameter (in.)**	**Weight (ppf)**	**Grade**	**Connection**	**Burst strength (psi)**	**Collapse strength (psi)**	**Tensile strength (lbf)**
Injection tubing Section 1	5,211	4.5	4.0	11.6	L80 (GRE)	Premium (1)	7,780	6,350	267,040
Injection tubing Section 2	6,142	4.5	4.0	11.6	25Cr80	Premium (1)	7,780	6,350	267,040

Table 22. Packer details.

Well	Item	Value
Injection Well MC19001INJ	Packer Setting Depths	4,936 ft, 5,200 ft, 5,474 ft, 5,743 ft
	Packer material	Same CRA material as the tubing and casing or a CRA such as Alloy 718
	Packer element material	HNBR
	Packer type	Hydraulic set retrievable packer
	Maximum casing ID	6.366 in. (nominal ID for 7 in. 23 ppf casing)
	Minimum casing ID	6.241 in. (drift diameter for 7 in. 23 ppf casing)
	Packer / seal assembly ID	4.5 in.
	Packer rating	Differential pressure ±5,000 psi, axial capacity ±125,000 lbf
	Maximum packer to casing forces	95,000 lbf Upward 123,000 lbf Downward
Injection Well ANO9004INJ	Packer Setting Depths	5,257 ft, 5,509 ft, 5,764 ft, 6,068 ft
	Packer material	Same CRA material as the tubing and casing or a CRA such as Alloy 718
	Packer element material	HNBR
	Packer type	Hydraulic set retrievable packer
	Maximum casing ID	6.366 in. (nominal ID for 7 in. 23 ppf casing)
	Minimum casing ID	6.241 in. (drift diameter for 7 in. 23 ppf casing)
	Packer / seal assembly ID	4.5 in.
	Packer rating	Differential pressure ±5,000 psi, axial capacity ±125,000 lbf
	Maximum packer to casing forces	95,000 lbf Upward 124,000 lbf Downward
	Packer Setting Depths	5,061 ft, 5,327 ft, 5,590 ft, 5,870 ft
	Packer material	Same CRA material as the tubing and casing or a CRA such as Alloy 718
	Packer element material	HNBR
	Packer type	Hydraulic set retrievable packer

Well	Item	Value
Contingent Injector Well MC19002INJ	Maximum casing ID	6.366 in. (nominal ID for 7 in. 23 ppf casing)
	Minimum casing ID	6.241 in. (drift diameter for 7 in. 23 ppf casing)
	Packer / seal assembly ID	4.5 in.
	Packer rating	Differential pressure ±5,000 psi, axial capacity ±125,000 lbf
	Maximum packer to casing forces	95,000 lbf Upward 123,000 lbf Downward
Contingent Injector Well ANO9005INJ	Packer Setting Depths	5,211 ft, 5,464 ft, 5,719 ft, 6,021 ft
	Packer material	Same CRA material as the tubing and casing or a CRA such as Alloy 718
	Packer element material	HNBR
	Packer type	Hydraulic set retrievable packer
	Maximum casing ID	6.366 in. (nominal ID for 7 in. 23 ppf casing)
	Minimum casing ID	6.241 in. (drift diameter for 7 in. 23 ppf casing)
	Packer / seal assembly ID	4.5 in.
	Packer rating	Differential pressure ±5,000 psi, axial capacity ±125,000 lbf
	Maximum packer to casing forces	95,000 lbf Upward 124,000 lbf Downward

Pre-Operational Logging and Testing [40 CFR 146.82(a)(8) and 146.87]

Pre-Operational Logging and Testing GSDT Submissions
GSDT Module: Pre-Operational Testing ***Tab(s):*** Welcome tab Please use the checkbox(es) to verify the following information was submitted to the GSDT: ☒ Proposed pre-operational testing program ***[40 CFR 146.82(a)(8) and 146.87]***

Testing Selection Strategy

Chevron U.S.A., Inc. (Chevron) plans to collect data during the pre-injection phase of the project from two (2) CO_2 injection wells, four (4) deep monitoring wells, six (6) shallow monitoring wells, and one (1) stratigraphic well. A summary of the CO_2 injection wells, shallow monitoring wells, and deep monitoring wells is provided in **Table 25.** The specific tests and test intervals were selected to address uncertainties and data gaps discussed in the Site Characterization section of the Project Narrative and the Area of Review (AoR) and Corrective Action Plan. For a list of testing activities see **Table 23**. Chevron plans to collect a robust suite of data including (1) whole core across both the Vedder Sand injection zone and the Freeman-Jewett Silt confining zone, (2) formation pressures (Reservoir Description Tool [RDT]) from the Vedder Sand and the Santa Margarita (i.e., the lowermost Underground Source of Drinking Water [USDW]), (3) fluid samples (modular formation dynamics tool [MDT]) from the Vedder Sand, (4) a wireline stress test (stress test) in the Freeman Jewett Silt, (5) a pressure transient analysis (PTA) in the Vedder Sand, (6) a basic logging suite (e.g., Gamma Ray [GR], Resistivity [RES], Spontaneous Potential [SP], Bulk Density [RHOB], Neutron Density [NPHI], Dielectric, and Caliper), and (7) an advanced logging suite (e.g., Nuclear Magnetic Resonance [NMR], Formation Imaging [FMI], and Dipole Sonic) across all zones of interest. In addition to the tests listed below, all wells will run a cement bond log (CBL) and a variable density log (VDL) to assess mechanical integrity, and the injectors will additionally run a casing inspection log (CIL) to establish a corrosion baseline.

The tests outlined above provide a wide range of information that Chevron plans to use to refine and enhance the site characterization, reservoir modeling, and dynamic simulation of the project. Specifically, the tests can inform the stratigraphic and structural framework (e.g., GR, RES, SP), reservoir properties such as porosity and permeability (e.g., whole core, PTA, NMR, RHOB, NPHI), the presence and analysis of faults and fractures in the injection and confining zone (e.g., whole core, PTA, FMI), geomechanical evaluation (e.g., whole core, stress test, FMI, Dipole Sonic, RHOB, RDT), geophysical evaluation (e.g., Dipole Sonic), and updates to the critical pressure calculation (e.g., RDT, MDT).

Testing Strategy and Design by Well Type

The stratigraphic well data collection strategy was designed (1) to provide information on the Vedder Sand injection zone, (2) to test the fracture gradient of both the Freeman-Jewett Silt confining zone and the Vedder Sand injection zone, and (3) to assess and calibrate the sealing

capacity of faults within the Area of Interest (AoI). The well (KC20050X_ST1) was located outside of the AoR near the Apollo Jr. Fault to limit the number of artificial penetrations in the AoR, to facilitate a whole core through the fault zone, and to be close enough to a fault to measure its properties in a pressure transient analysis. Core analysis includes (1) core description and photographs, (2) routine core analysis (e.g., porosity and permeability plugs), (3) special core analysis (e.g., X-ray diffraction [XRD], thin sections, mercury injection capillary pressure [MICP], scanning electron microscope images [SEM], capillary pressure [air brine porous plate]), (4) relative permeability values in a CO_2/brine system, (5) core nuclear magnetic resonance (NMR), (6) X-ray fluorescence (XRF) across the fault zone, and (7) a full suite of geomechanical analyses in the sandstone, shale, and fault zone intervals. In addition to collecting and analyzing core, Chevron performed a pressure transient analysis (PTA) and step rate test in the Vedder Sand along with an extended leak off test (LOT) in the Freeman-Jewett Silt.

The CO_2 injection well data collection strategy was designed (1) to address uncertainties and data gaps in the Freeman-Jewett Silt, (2) assess local reservoir conditions including reservoir injectivity at the injection wells, and (3) to minimize any damage to the formation or near-wellbore conditions that might affect injectivity. To address uncertainties and data gaps in the Freeman-Jewett Silt, Chevron plans to collect NMR and FMI logs across the Freeman-Jewett Silt in the CO_2 injection wells. Due to CO_2 injector wellbore deviation in the Freeman-Jewett Silt, which significantly complicates coring operations, Chevon plans to collect two Freeman-Jewett Silt cores in the two of the four deep monitoring wells and calibrate the core properties to the CO_2 injection wells using NMR and FMI logs collected in both the CO_2 injection and deep monitoring wells. NMR and FMI logs in conjunction with a standard logging suite will provide information on local reservoir conditions at the CO_2 injection wells. To minimize near-wellbore damage to the formation from drilling fluids designed to improve core recovery, Chevron plans to collect Vedder Sand core in the stratigraphic well instead of in the CO_2 injection wells. This Vedder Core will supplement the other seven (7) legacy cores across the AoI.

The deep monitoring well data collection strategy was designed (1) to address uncertainties and data gaps in the Freeman-Jewett Silt, (2) to provide additional data points across the AoR and AoI, and (3) to reduce uncertainty in the variability in permeability across the AoR and AoI. To address uncertainties and data gaps in the Freeman-Jewett Silt, Chevron plans to collect whole cores and perform wireline stress tests in the Freeman-Jewett Silt in the two of the four deep monitoring wells. These data will be calibrated to properties at the CO_2 injection wells using NMR and FMI logs collected in both the CO_2 injection and deep monitoring wells. A standard logging suite will supplement the 70+ well penetrations from legacy and project wells and NMR logs will provide information on the variability of permeability within the Vedder Sand. The shallow monitoring well data collection strategy was designed to provide the information required to select the perforated intervals for above zone fluid sampling.

Pre-Operation Data Collection Timing and Zonal Coverage

Chevron plans to drill injectors MC19001INJ and ANO9004INJ as well as all monitoring wells at approximately the same time after receiving the authorization to construct the CO_2 injection wells. The stratigraphic well was drilled in late 2022 to provide enough time to complete and incorporate extensive core analysis with the other data collected from the CO_2 injection and monitoring wells during the pre-operational phase of the project. **Figure 94** below shows the

relative locations of the CO_2 injection wells, the deep and shallow monitoring wells, the stratigraphic well, mapped faults within the Vedder Sand, the AoR, and the AoI.

Chevron plans to drill the two (2) CO_2 injection wells and the four (4) deep monitoring wells to the base of the Vedder Sand (i.e., the injection zone). Chevron plans to drill two (2) of the six (6) shallow monitoring wells to the base of the Olcese Sand (i.e., the first permeable zone) and four (4) of the six shallow monitoring wells to the base of the Santa Margarita Sand (i.e., the lowermost USDW). The stratigraphic well was drilled outside of the AoR through the base of the Vedder Sand. Exact depths will depend on logging, drilling conditions and other drilling data. Wireline logs will be run to the total depth (TD) of the well, or as deep as possible.

Testing and Monitoring Baseline Data

Chevron will conduct several baseline tests prior to injection to help determine if there are significant changes after CO_2 injection begins. These baseline tests will help decrease errors in the repeatability of future data. A cement bond log and variable density log will be run after each string of casing is installed to verify cement placement. A casing inspection log will be run after the installation of the injection string of casing on the injection wells to evaluate initial casing conditions and provide a baseline for further corrosion related logs. To calibrate CO_2 plume monitoring techniques, a cased hole pulsed neutron log (PNL) will be run in all project wells (i.e., CO_2 injection wells, deep monitoring wells, and shallow monitoring wells). Distributed acoustic sensing fiber optic (DAS) vertical seismic profiles (VSPs) or equivalent technologies will be performed to establish a baseline survey. An oxygen activation log will generate a baseline for external mechanical integrity. A baseline injectivity and pressure fall-off test will also be performed for each CO_2 injection well prior to injection.

Baseline fluid sampling & analysis will be conducted quarterly on the first permeable zone above the caprock (i.e., Olcese) and the lowermost USDW (i.e., Santa Margarita) for a year prior to injection to assess initial water quality. Additionally, baseline wireline fluid samples will be taken in the Vedder Sand Injection Zone prior to injection. Baseline fluid samples will collect data across a wide range of parameters. For a full list of baseline fluid sample parameters, see the Testing and Monitoring Plan.

Existing Data

Chevron has a robust dataset that complements the pre-operational data collection program that includes seventy (70) wells. In addition to the proposed coring program, there are seven (7) wells with whole-core data in the Vedder Sand, twenty-nine (29) wells with sidewall core data in the Vedder Sand, and seven (7) wells with sidewall core data in the Freeman-Jewett Silt.

Table 23. Summary of pre-operational testing program. All wireline logs, denoted by an "X", will be run as deep as possible in the open hole section of the deepest string. Whole core, formation pressures (RDT), fluid samples (MDT), stress tests, pressure transient analysis (PTA, and injectivity/pressure fall off tests (Inj Test) will be collected for specific zones (SM = Santa Margarita Sandstone, OL = Olcese Sand, FJ = Freeman-Jewett Silt, V = Vedder Sand). For more information on the stratigraphic intervals see the Site Characterization Section of the Project Narrative.

Well Information			Core	Formation Testing					Basic Logging Suite							Advanced Logging Suite		
Well Name	Well Type	Deepest Zone	Whole Core	RDT (Pressure)	MDT (Samples)	Stress Test	PTA	Inj Test	GR	RES	SP	RHOB	NPHI	Dielectric	Caliper	NMR	FMI	Dipole Sonic
KC20050X_ST1	Stratigraphic	Famoso	V	V			V	V	X	X	X	X	X	X	X	X	X	X
ANO9004INJ	CO_2 Injector	Vedder		SM, V	SM, V			V	X	X	X	X	X	X	X	X	X	X
MC19001INJ	CO_2 Injector	Vedder		SM, V	SM, V			V	X	X	X	X	X	X	X	X	X	X
RCA9001OB	Deep Monitoring	Vedder							X	X	X	X	X	X	X			
COR9001OB	Deep Monitoring	Vedder	FJ			FJ			X	X	X	X	X	X	X	X	X	X
HK_9001OB	Deep Monitoring	Vedder	FJ			FJ			X	X	X	X	X	X	X	X	X	X
DDA9001OB	Deep Monitoring	Vedder							X	X	X	X	X	X	X			
ANO9001B	Shallow Monitoring	St. Margarita							X	X	X	X	X	X	X			
ANO9003OB	Shallow Monitoring	Olcese							X	X	X	X	X	X	X			
GW_9001OB	Shallow Monitoring	St. Margarita							X	X	X	X	X	X	X			
GW_9002OB	Shallow Monitoring	Olcese							X	X	X	X	X	X	X			
KER9001OB	Shallow Monitoring	St. Margarita							X	X	X	X	X	X	X			
IR_9001OB	Shallow Monitoring	St. Margarita							X	X	X	X	X	X	X			

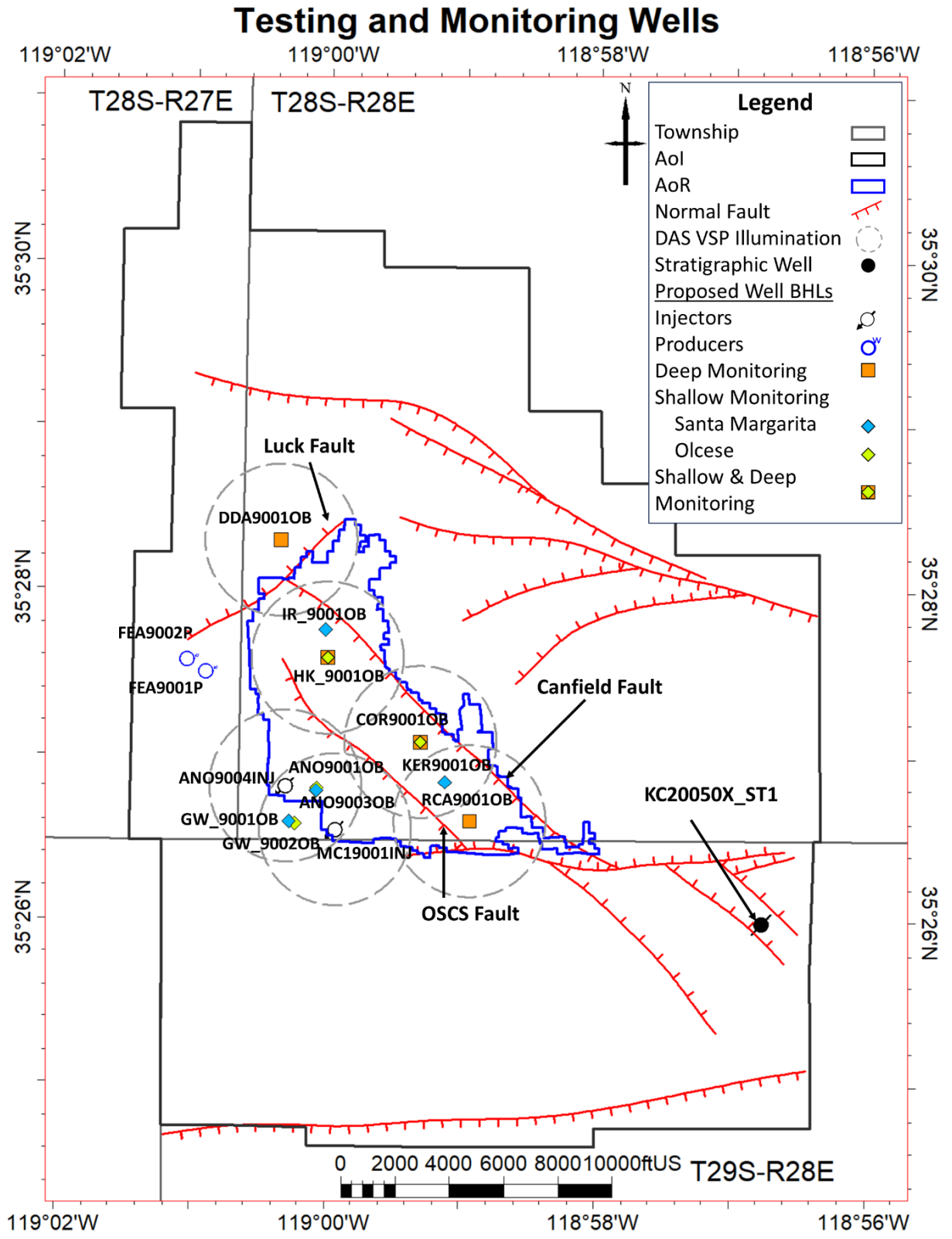

Figure 94. Locations of the CO_2 injection wells, the deep and shallow monitoring wells, the stratigraphic well, mapped faults within the Vedder Sand, the AoR, and the AoI.

Well Operation

Two active CO_2 injectors are planned for this project, with two additional permitted contingent wells permit to be drilled in the event one of the injectors requires replacement during the injection period for the project. Pressure in the injection zones will be managed with water production wells. CO_2 and pressure front migration will be monitored using wells that penetrate the Vedder Sand. Additional monitoring wells will also be utilized to sample shallower formation fluids at periodic intervals.

Total project CO_2 injection is anticipated to be between 265,000 and 455,000 tonnes per year. The cumulative amount of sequestered CO_2 is expected to total 6.82 million tonnes over the life of the Project.

Injection wells will be perforated near the base of the Vedder Sand and constrained by a maximum bottomhole injection pressure set to 90% of the approved fracture gradient.

Operational Procedures [40 CFR 146.82(a)(10), 146.88]

Proposed operational procedures are shown in **Table 24**.

Chevron executed a 2022 step rate test within the Vedder Sand to identify the fracture pressure. The observed fracture pressure gradient, 0.642 psi/ft, with a multiplier of 0.9 (representing 90% of the fracture pressure gradient) is used to determine the maximum downhole injection pressure. The expected operational injection pressures are sufficiently below the identified fracture gradient.

Through the project life, Chevron plans to target individual zones within the Vedder Sand with tubing and packer completions through the life of the Project, starting with the deepest target and recompleting into increasingly shallower Vedder Sand intervals through time as necessary based upon monitoring data. With each recompletion, Chevron plans to update operating constraints based upon any wellbore changes (e.g., additional perforations for a shallower Vedder Sand target resulting in a new maximum allowable bottomhole pressure). Chevron plans to include water producers within each target zone to depressurize the reservoir, which may impact injection pressure through time. The producers have been included in simulation modeling. Additional details regarding fracture pressure, maximum injection pressure, and pressure management are provided in the Area of Review and Corrective Action Document.

Injection rates and total volume are based on forecast CO_2 availability from sources specified in the Proposed Carbon Dioxide Stream section.

Table 24. Proposed operational procedures.

Parameters/ Conditions	**Limited or Permitted Value**				**Unit**
	Injection Well MC19001INJ	**Injection Well ANO9004INJ**	**Contingent Injection Well ANO9005INJ**	**Contingent Injection Well MC19002INJ**	
Maximum Downhole Injection Pressure					
1st Vedder	2829	2891	2892	2826	Psi
2nd Vedder	2982	3037	3038	2979	Psi
3rd Vedder	3140	3184	3185	3131	Psi
4th Vedder	3295	3360	3360	3293	Psi
Average Downhole Injection Pressure					
1st Vedder	1908	1914	1914	1908	Psi
2nd Vedder	2012	2005	2005	2012	Psi
3rd Vedder	2120	2106	2106	2120	Psi
4th Vedder	2261	2256	2256	2261	Psi
Average Injection Rate	363-624	363-624	363-624	363-624	Tonnes CO_2 per day
Maximum Daily Injection Volume	1,248	1,248	1,248	1,248	Tonnes CO_2
Maximum Injection Volume and/or Mass	6,820,000	6,820,000	6,820,000	6,820,000	Tonnes CO_2
Minimum Annulus Pressure/Tubing Differential	100	100	100	100	Psi

Proposed Carbon Dioxide Stream [40 CFR 146.82(a)(7)(iii) and (iv)]

CO_2 will be captured from a variety of emission sources (e.g., direct air capture). Sources may come online at various points throughout the life of the Project. Each CO_2 stream will be analyzed and shared with the EPA prior to any injection.

The injectate composition is predicted to be approximately 95% CO_2 by volume with other minor components including H_2 (maximum 4% by volume), N_2 (maximum 4% by volume), H_20 (maximum 500 ppm), CO (maximum 35 ppm), Ar (maximum 4% by volume), O_2 (maximum 0.001% by volume), SO_2 (maximum 100 ppm), H_2S (maximum 0.01% by volume), CH_4 (maximum 4% by volume), NO_x (maximum 100 ppm), NH_3 (maximum 50 ppm), and C_2H_6 (maximum 1% by volume). The injectate composition will be refined based on specific sources and changes to the composition will be communicated to the EPA. Given the low moisture specification, this stream is not expected to be highly corrosive. The pressure and temperature conditions of the Vedder Sand are such that the CO_2 will remain supercritical in the reservoir for the lifetime of the Project.

The CO_2 temperature at the injector wellhead prior to injection is expected to be 20 – 130˚F. The temperature is expected to be heavily influenced by ambient temperature.

Testing and Monitoring

Testing and Monitoring GSDT Submissions
GSDT Module: Project Plan Submissions ***Tab(s):*** Testing and Monitoring tab Please use the checkbox(es) to verify the following information was submitted to the GSDT: ☒ Testing and Monitoring Plan ***[40 CFR 146.82(a)(15) and 146.90]***

Testing and Monitoring Plan Objectives

Chevron has created a comprehensive monitoring plan designed to assess (1) the location of the CO_2 front, (2) the region where the reservoir pressure is elevated beyond the critical pressure, and (3) the non-endangerment of USDW's. The technologies and techniques for this monitoring plan were selected based on site-specific focus areas as determined by the site characterization, reservoir modeling and simulation, and AoR sensitivity analysis. This plan will cover three main aspects: (1) well integrity, (2) operational parameters, and (3) geologic system changes. The combination of these aspects will provide the ability to assess the protection of groundwater resources.

Testing and Monitoring Plan Focus Areas

Chevron has determined seven (7), site-specific, focus areas for the testing and monitoring plan based on site characterization, reservoir modeling and simulation, and an AoR sensitivity analysis**.**

Site characterization identified the presence of multiple faults within the AoR that penetrate both the injection zone (i.e., reservoir) and the primary confining zone (i.e., top seal). A combination of fault seal analysis and reservoir simulation has determined that these faults are likely to act as sealing mechanisms, either slowing or permanently trapping CO_2. However, because these faults act as a trapping mechanism and extend vertically beyond the primary confining zone, the monitoring plan is designed to assess unexpected CO_2 migration as it pertains to faults, either vertically up the faults or laterally across faults at rates or volumes that are outside the range of simulated CO_2 movement and associated sensitivities. For more information on either the site characterization or CO_2 simulation, please see either the Project Narrative or the AoR and Corrective Action Plan.

Chevron has assessed wells within the AoR that penetrate the injection zone and/or the primary confining zone. Under current operational conditions, there are no integrity concerns for these wells. With proposed CO_2 injection, Chevron plans to conduct work to support proactive zonal isolation for three specific wells within the AoR (FEC0074, API# 040292411200; GWA0145, API# 040292697300; and OM_0044, API# 040290009800). With proposed CO_2 injection, Chevron also plans to abandon KA_0053X (API# 040296990300). Additionally, Chevron has robust drilling and completion procedures to provide vertical containment and isolation for Project wells (i.e., CO_2 injection, monitoring, and pressure management wells). The location of

the CO_2 injection wells and other well penetrations informed the monitoring well locations. For more information on AoR well penetrations, please see the AoR and Corrective Action Plan

Chevron utilized reservoir simulation coupled with a sensitivity analysis to determine a range of outcomes for the location of the CO_2 front and the region where the reservoir pressure is elevated beyond the critical pressure. The sensitivity analysis included varying the (1) permeability, (2) porosity, (3) relative permeability, (4) injection strategy, (5) fault threshold pressure, and (6) fault transmissibility. While this sensitivity study provides a range of potential outcomes for the movement of CO_2 and region of elevated pressure, the possibility still exists that CO_2 could migrate at a rate or in a direction not predicted by the model, or in such a way as to produce a thin plume that is below seismic resolution (i.e., seismic detectability). Chevron has designed a monitoring well network and selected monitoring technologies to evaluate these possibilities.

As part of the site characterization for the Project, Chevron assessed the potential for induced seismicity related to injection from the Project. Results from this study, in general, conclude that southeast striking faults have a friction coefficient that approaches 0.4. Past operational information supports fault stability under injection. Chevron has injected over 50,000,000 barrels of water in the Vedder Sand over the past forty (40) years with no observed seismic response or pressure build up. To reduce the potential pressure build-up within the Vedder Sand related to CO_2 injection, Chevron plans to include a pressure management water production system that reduces reservoir pressure through the life of the injection. In addition to this pressure management system, Chevron plans to install a seismic monitoring system.

Overview of Monitoring Technologies and Techniques

Chevron plans to utilize a combination of monitoring techniques deployed on deep, injection zone monitoring wells (deep monitoring wells); shallow, groundwater monitoring wells (shallow monitoring wells); and the CO_2 injection wells. **Table 25** summarizes the different well types and the Monitoring Zones/Geologic Formations. **Figure 95** provides a schematic diagram of Chevron's monitoring plan, and **Table 26** provides a list of monitoring techniques and their frequency during the different stages of the project.

Table 25. Summary of monitoring wells.

Well Types	Well Name	Monitoring Zone	Formation	Top Zone Depth (ft TVDSS)	Quantity
Shallow Observation	IR_9001OB KER9001OB ANO9003OB GW_9001OB	Lowermost USDW	Santa Margarita	-810 to -1350	4
	ANO9001OB GW_9002OB	1st Permeable Zone	Olcese	-1840 to -2420	2

Well Types	Well Name	Monitoring Zone	Formation	Top Zone Depth (ft TVDSS)	Quantity
Deep Observation	HK_9001OB COR9001OB	1st Permeable & Injection Zone	Olcese & Vedder	-1840 to -2420 -3690 to -4230	2
	RCA9001OB DDA9001OB	Injection Zone	Vedder	-3690 to -4230	2
CO_2 Injection	ANO9004INJ MC19001INJ	Injection Zone	Vedder	-3690 to -4230	2

The deep monitoring wells are designed to monitor the location of the CO_2 front and the region where the reservoir pressure is elevated beyond the critical pressure using both direct and indirect methods. The wells will use a combination of direct cased hole pulsed neutron logs (PNLs) and indirect casing-conveyed distributed acoustic sensing fiber optics (DAS) vertical seismic profiles (VSPs) or equivalent technologies to monitor the location and thickness of the CO_2 plume. The deep monitoring wells will directly measure reservoir pressure in the injection zone via a casing-conveyed pressure sensor array or equivalent technology.

The shallow monitoring wells are designed to monitor the first permeable zone above the caprock (i.e., Olcese) for early detection of loss of containment and to monitor the lowermost USDW (i.e., Santa Margarita) to establish the non-endangerment of USDWs. The wells will be utilized to sample the groundwater using a U-tube tubing-conveyed sampling system or via a fluid sampling tool deployed on coil tubing or wireline or an equivalent technology while maintaining reservoir pressure of the sample. Chevron plans to have four (4) sampling locations for the Santa Margarita and four (4) sampling locations for the Olcese (**Figure 96**). For each zone, one well is located downdip of the CO_2 injection wells, one well is located updip of the CO_2 injection wells, and two wells are located within the AoR near faults and well penetrations. All four (4) Santa Margita sampling locations will be in dedicated shallow monitoring wells (IR_9001OB, KER9001OB, ANO9003OB, and GW_9001OB). Two (2) Olcese sampling locations will be in dedicated shallow monitoring wells (ANO9001OB and GW_9002OB), and two (2) sampling locations will be in two (2) of the deep monitoring wells (HK_9001OB and COR9001OB). The deep monitoring wells will be cased through the injection zone (i.e., there will be no perforations across the injection zone), and the shallow perforated intervals will be isolated via packers. All wells will use the same sampling technologies as described above.

The CO_2 injection well monitoring equipment is designed to measure operational parameters (e.g., injection rate, volume, and pressure), monitor potential corrosion, verify external and internal mechanical integrity, and to monitor the location of the CO_2 front. Chevron plans to install and use continuous recording devices to monitor injection pressure, rate, and volume; the pressure on the annulus between the tubing and the long string casing; and the temperature of the CO_2 stream. To assess potential corrosion, Chevron plans to use corrosion loops or an equivalent technology. A pressure fall-off test is planned no less than every five (5) years on each operational CO_2 injection well. Oxygen activation logs will monitor external mechanical integrity.

In addition to the well-based monitoring technologies summarized above, Chevron plans to deploy and maintain a seismic monitoring system to determine the presence or absence of any induced micro-seismic activity associated with project injection. The seismic monitoring system will consist of surface and/or shallow borehole seismometers coupled with DAS fiber or equivalent technologies.

Chevron plans to monitor the CO_2 stream via an online analyzer, continuous emissions monitoring system (CEMS), or similar device.

The monitoring technologies and monitoring and reporting frequencies provided in this permit may change, pursuant to Environmental Protection Agency (EPA) approval, based on monitoring data and/or regulatory changes.

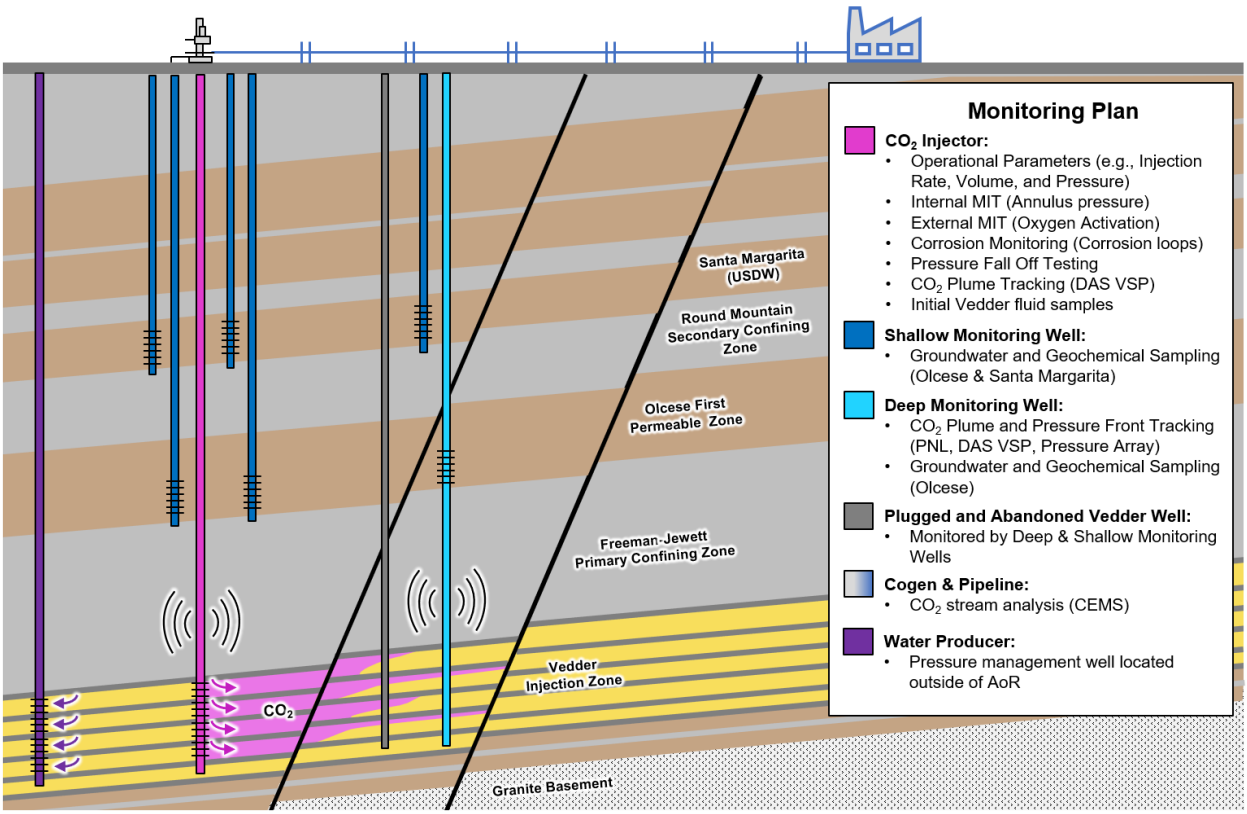

Figure 95. Schematic diagram of Chevron's monitoring plan.

Table 26. Monitoring methodologies and monitoring frequencies for baseline, injection, and post-injection phases

Monitoring Category	Monitoring Method		Baseline Frequency (1 year)	Injection Phase Frequency (20 years)*	Post-Injection Frequency (50 years)*
Monitoring Plan Update	Reviewed every 5 years. Updated as required		N/A	As required	As required
CO_2 Injection Stream Analysis	Continuous monitoring of injection stream composition		N/A	Continuous	N/A
CO_2 Injection Process Monitoring	Continuous monitoring of injection process (e.g., injection rate, pressure, and temperature; annulus pressure)		N/A	Continuous	N/A
Hydrogeologic Testing	Injection well pressure fall-off testing		1 Prior to injection	1 per every 5 years	N/A
Injection Well Mechanical Integrity Testing	*Internal*	Continuous annulus pressure monitoring of pressurized annulus	1 after well completion *(injectors*)	Continuous *(injectors*)	1 prior to abandonment
	External	Oxygen activation log	1 after well completion *(injectors)*	Annual *(injectors)*	1 prior to abandonment *(injectors)*
Corrosion Monitoring	Corrosion loop (well and pipeline materials)		N/A	Quarterly	N/A
Groundwater Quality and Geochemistry Monitoring (Above-Zone)	Above-zone & shallow groundwater fluid sampling		Quarterly, 1 yr. prior to injection	Quarterly	Annual
Direct Pressure Monitoring	Pressure array sensors in deep monitoring wells		1 yr. prior to injection	Monthly	1 per every 5 years
Direct & Indirect Plume Monitoring Techniques	*Wireline*	PNL	1 prior to injection	Annual	1 per every 5 years
	Seismic	Timelapse 3D DAS-VSP surveys	1 prior to injection	1 per every 5 years	10, 30, & 50 years post injection

*Monitoring technologies and monitoring and reporting frequencies provided in this permit may change, pursuant to EPA approval, based on monitoring data and/or regulatory changes.

Monitoring Network Design and Strategy

Chevron integrated the site-specific focus areas into both the technology selection for the monitoring plan **(Figure 95, Table 96)** and the location of the monitoring wells **(Figure 96)**. Deep monitoring well locations were determined using approximate illumination based on ray tracing of a modeled DAS VSP seismic shoot. The location of the deep monitoring wells and CO_2 injection wells with their associated illumination provides seismic imaging across the major faults within the AoR (e.g., Canfield, Omar Sterling Cortez South, Luck **[Figure 96]**) and well penetrations within the AoR. The wells are positioned to provide overlapping seismic imaging across the AoR with an additional well placed to the northwest of the Luck Fault. This arrangement of wells provides broad coverage inside and outside of the AoR to address the possibility that CO_2 could migrate at a rate or in a direction not predicted by the model. To address the possibility that the CO_2 plume could develop in such a way as to produce a thin plume that is below seismic resolution (i.e., seismic detectability), Chevron has added pulsed neutron logs to assess the location and thickness of the CO_2 plume. This method has a vertical resolution of less than one foot. To monitor potential induced seismicity associated with CO_2 injection, Chevron will deploy and maintain a seismic monitoring system, which consists of surface and/or shallow borehole seismometers coupled with DAS fiber on the deep monitoring wells and the CO_2 injection wells. The deep monitoring wells are positioned near faults that computation models indicate may interact with the CO_2 plume and the surface and/or shallow borehole seismometers will be positioned in such a way to triangulate the position of potential seismic events. Additionally, Chevron plans to use between 1 and 4 pressure management wells located outside of the AoR to manage any potential increase in pressure due to CO_2 injection. Simulation, described in detail in the AoR and Corrective Action Plan, indicates that these pressure management wells prevent pressure build up and therefore reduce the potential for induced seismicity. The locations of monitoring wells may change based on updated data or analysis, including data collected during the construction phase of the project. For more information on Chevron's data collection strategy see the Pre-Operational Logging and Testing Plan. Additionally, Chevron has surface estate and/or physical access rights at the proposed monitoring well locations.

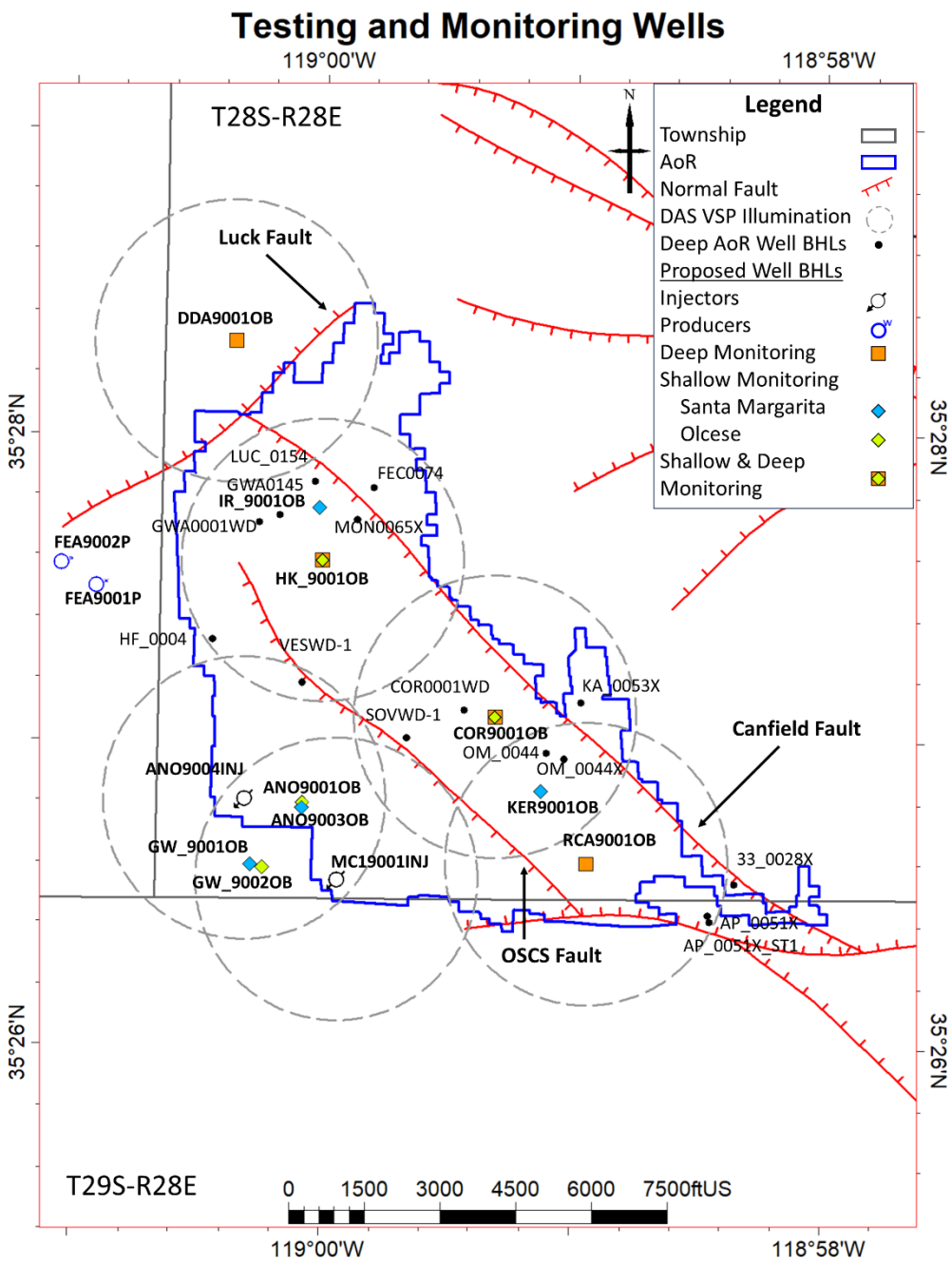

Figure 96. Location of the project wells including CO_2 injection wells (2), deep monitoring wells (4), shallow monitoring wells (4), and pressure management water production wells (2). Deep monitoring wells are located to provide overlapping seismic illumination from DAS VSPs of the AoR. The AoR for this project was calculated as the intersection of the CO_2 plume and the region where the reservoir pressure is elevated beyond the critical pressure. However, due to the use of pressure management wells, reservoir simulations indicate that there is no increase in pressure increase from to CO_2 injection. Therefore, the resulting AoR boundary is a function of the extent of the CO_2 plume.

Injection Well Plugging

Injection Well Plugging GSDT Submissions
GSDT Module: Project Plan Submissions ***Tab(s):*** Injection Well Plugging tab Please use the checkbox(es) to verify the following information was submitted to the GSDT: ☒ Injection Well Plugging Plan ***[40 CFR 146.82(a)(16) and 146.92(b)]***

A comprehensive Injection Well Plugging Plan pursuant to 40 CFR 146.82(a)(16) and 146.92(b) describing the process, materials, and methodology for injection well plugging is included in Injection Well Plugging Plan Document.

Prior to plugging and abandoning any injection wells, external mechanical tests will be conducted and taken into consideration during plugging operations. Once wells have reached the end of their life they will be plugged and abandoned in accordance with, federal, state, and local regulatory standards. CO_2 injection and freshwater zones will be isolated. Once barriers have been placed within the wellbore to isolate CO_2 and USDW zones, a cement plug will be set to ground surface. The casing will then be cut below grade, wellhead will be removed and a steel cap will be welded over the well. The remaining casing stump will be backfilled, and the location will be restored to its original condition prior to well construction.

Post-Injection Site Care (PISC) and Site Closure

PISC and Site Closure GSDT Submissions
GSDT Module: Project Plan Submissions ***Tab(s):*** PISC and Site Closure tab Please use the checkbox(es) to verify the following information was submitted to the GSDT: ☒ PISC and Site Closure Plan ***[40 CFR 146.82(a)(17) and 146.93(a)]***
GSDT Module: Alternative PISC Timeframe Demonstration ***Tab(s):*** All tabs (only if an alternative PISC timeframe is requested) Please use the checkbox(es) to verify the following information was submitted to the GSDT: ☐ Alternative PISC timeframe demonstration ***[40 CFR 146.82(a)(18) and 146.93(c)]***

The Post-Injection Site Care and Site Closure (PISC) Document describes the activities that Chevron will perform to meet the requirements of 40 Code of Federal Regulations 146.93. Following the cessation of injection, Chevron will continue to monitor ground water quality and track the position of the carbon dioxide plume and pressure front for fifty (50) years or until the Underground Injection Control (UIC) Program Director approves an alternative duration based upon a demonstration by Chevron that the geologic sequestration project poses no endangerment to Underground Sources of Drinking Water (USDWs). Additionally, the PISC overviews the criteria for USDW non-endangerment demonstration, monitoring well plugging procedures, and site closure reporting details. Please refer to The Post-Injection Site Care and Site Closure Document for more information.

Emergency and Remedial Response

Emergency and Remedial Response GSDT Submissions
GSDT Module: Project Plan Submissions ***Tab(s):*** Emergency and Remedial Response tab Please use the checkbox(es) to verify the following information was submitted to the GSDT: ☒ Emergency and Remedial Response Plan ***[40 CFR 146.82(a)(19) and 146.94(a)]***

A comprehensive Emergency and Remedial Response Plan is attached, pursuant to 40 CFR 146.82(a)(19) and 146.94(a) describing the process, materials, and methodology for emergency response and remediation relating to:

- Injection, water production, or monitoring well integrity failure;
- Injection well monitoring equipment failure (e.g., shut-off valve or pressure gauge);
- Fluid (e.g., formation water) or CO_2 leakage to a USDW or to the surface;
- A natural disaster (e.g., large earthquake, lightning strike); or
- Induced or natural seismic event.

For additional details, please refer to the Emergency and Remedial Response Plan.

Optional Additional Project Information [40 CFR 144.4]

As described above, Chevron has submitted a CUP to the Kern County Planning and Natural Resources Department, and as such this project will be subject to CEQA. As such, a comprehensive environmental evaluation is expected for the project which may involve coordination with a variety of federal, state and/or local agencies.

Other Information

References (published or publicly available)

Addassi, M., Omar, A., Ghorayeb, K., Hoteit, H., 2021,Comparison of various reactive transport simulators for geological carbon sequestration: International Journal of Greenhouse Gas Control, v.110.

Addicott, W., 1970, Miocene gastropods and biostratigraphy of the Kern River area, California: U.S. Geological Survey Professional Paper 642, 174 p., 21 pl.

Alai, M., M. Sutton, and S. Carroll, 2005, Evaporative evolution of a Na–Cl–NO3–K–Ca–SO4–Mg–Si brine at 95 °C: Experiments and modeling relevant to Yucca Mountain, Nevada, Geochemical Transactions, v. 6, n. 2, p. 31-45.

Allan, U.S., 1989, Model for hydrocarbon migration and entrapment within faulted structures: AAPG Bulletin, v. 73, n. 7, p. 803–811.

Amaefule, J.O., Altunbay, M., Tiab, D., Kernsey, D.G., and Keelan, D.K., 1993, Enhance reservoir description: using core and log data to identify hydraulic (flow) units and predict permeability in uncored intervals/wells: Society of Petroleum Engineers Journal SPE26436, p. 205-220.

Aradóttir, E.S.P., E.L. Sonnenthal, G. Björnsson, and H. Jónsson, 2012. Multidimensional reactive transport modeling of CO_2 mineral sequestration in basalts at the Hellisheidi geothermal field, Iceland: International Journal of Greenhouse Gas Control, v. 9, p.24-40.

Aradóttir, E.S.P., Gunnarsson, I., Sigfússon, B., Gunnarsson, G., Júliusson, B.M., Gunnlaugsson, E., Sigurdardóttir, H., Arnarson, M.T., Sonnenthal, E., 2015, Toward cleaner geothermal energy utilization: Capturing and Sequestering CO_2 and H2S Emissions from Geothermal Power Plants. Transport in Porous Media v. 108, p. 61-84.

Archie, G.E., 1942, The electrical resistivity log as an aid in determining some reservoir characteristics: Petroleum Technology, v. 5, p. 54-62.

Bajsarowicz, C.J., 1992, Core alteration and preservation: part 3, well site methods, *in* Morton-Thompson, D., and Woods, A.M., eds., American Association of Petroleum Geologists, Methods in Exploration v. 10, Development Geology Reference Manual, p. 127-130.

Baker, S.E., Joshuah K. Stolaroff, George Peridas, Simon H. Pang, Hannah M. Goldstein, Felicia R. Lucci, Wenqin Li, Eric W. Slessarev, Jennifer Pett-Ridge, Frederick J. Ryerson, Jeff L. Wagoner, Whitney Kirkendall, Roger D. Aines, Daniel L. Sanchez, Bodie Cabiyo, Joffre Baker, Sean McCoy, Sam Uden, Ron Runnebaum, Jennifer Wilcox, Peter C. Psarras, Hélène Pilorgé, Noah McQueen, Daniel Maynard, Colin McCormick, 2020, Getting to Neutral: Options for Negative Carbon Emissions in California, January 2020, Lawrence Livermore National Laboratory, LLNL-TR-796100. https://www-gs.llnl.gov/content/assets/docs/energy/Getting_to_Neutral.pdf

Baron, D., Negrini, R. M., Golob, E. M., Miller, D., Sarna-Wojcicki, A, Fleck, R. J., Hacker, B., Erendi, A., 2008, Geochemical correlation and $^{40}Ar/^{39}Ar$ dating of the Kern River ash bed and related tephra layers: Implications for the stratigraphy of petroleum-bearing formations in the San Joaquin Valley, California: Quaternary International, v. 178, p. 246-260.

Bartow, J. A. and Pittman, G. M., 1983, The Kern River Formation, Southeastern San Joaquin Valley, California, U.S. Geological Survey Bulletin 1529-D, 17 p.

Bartow, J. A., 1991, The Cenozoic evolution of the San Joaquin Valley, California: United States Geological Survey, Professional paper 1501, 40 p.

Bartow, J.A., 1984, Geologic map and cross sections of the San Joaquin Valley, California: United States Geological Survey Miscellaneous Investigations Series Map I-1496, scale 1:150,000, 3 plates, doi.org/10.3133/i1496.

Bartow, J.A., and McDougall, K.A., 1984, Tertiary stratigraphy of the southeastern San Joaquin Valley, California: U.S. Geological Survey Bulletin 1529-J, 41 p.

Bartow, J.A., and Nilsen, T., 1990, Review of the Great Valley sequence, eastern Diablo Range and northern San Joaquin Valley, central California, *in* Kuespert, J.G., and Reid, S.A., eds., Structure, Stratigraphy and Hydrocarbon Occurrences of the San Joaquin Basin, California, Pacific Section American Association of Petroleum Geologists, p. 253-265.

Bedrossian, T.L., Hayhurst, C.A., Lancaster, J., 2014, Surficial geologic mapping and associated GIS databases for identification of alluvial fans: Environmental and Engineering Geoscience, v. 20, n. 4, p. 335-348, doi.org/10.2113/gseegeosci.20.4.335

Beeson, D., Hoffman, K., Larue, D., McNaboe, J., and Singer, J., 2014, Creation and utility of a large fit-for-purpose earth model in a giant mature field: Kern River field, California: American Association of Petroleum Geologists Bulletin, v. 98, n. 7, p. 1305-1324.

Benjakul, R., Hollis, C., Robertson, H.A., Sonnenthal, E.L., Whitaker, F.F., 2020. Understanding controls on hydrotherm187olomitizationion: insights from 3D reactive transport modelling of geothermal convection: Solid Earth, v. 11, p. 2439-2461.

Bent, J.V., 1985, Provenance of upper Oligocene-middle Miocene sandstones of the San Joaquin Basin, California, *in* Graham, S.A., ed., Geology of the Temblor Formation, western San Joaquin Basin, California: Los Angeles, Pacific Section, Society of Economic Paleontologists and Mineralogists, v. 44, p. 97-120.

Branum, D., Harmsen, S., Kalkan, E., Petersen, M.D., and Wills, C. J., 2008, Earthquake Shaking Potential for California: California Geological Survey Mapsheet 48 (Revised 2008), Southern California Earthquake Consortium (SCEC) Contribution Number 7919.

Bretan, P., Yielding, G., and Jones, H., 2003, Using calibrated shale gouge ratio to estimate hydrocarbon column heights: American Association of Petroleum Geologists Bulletin, v. 87. p. 397-413.

Caers, J., and Zhang, T., 2004, Multiple-point statistics: a quantitative vehicle for integrating geologic analogs into multiple reservoir models, *in* Grammer, M., Harris, P.M., and Eberli, G.P., eds., Integration of outcrop and modern analogs in reservoir modeling: American Association of Petroleum Geologists, Memoir 80, Chapter 18, p. 383-394

California Department of Conservation & EPA, 1982 & 2015, Underground Injection Control Program, Memorandum of Agreement between California Division of Oil and Gas and the United States Environmental Protection Agency, Region 9: Important Note Regarding the Memoranda of Agreement on Primacy and Exempted Aquifers (February 6, 2015) and Document 1: Memorandum of Agreement dated September 29, 1982, as originally posted to Department of Conservation FTP Site, 59 p. www.conservation.ca.gov/calgem/for_operators/Documents/MOU-MOA/MOA_EPA_UIC_1982.pdf

California Department of Conservation, 1998, California oil & gas fields, volume 1 – central California: California Department of Conservation, 499 p.

California Department of Water Resources, 2020, California's groundwater, update: California Department of Water Resources, Bulletin 118, https://data.cnra.ca.gov/dataset/3f87088d-a2f9-4a46-a979-1120069db2c6/resource/d2b45d3c-52c0-45ba-b92a-fb3c90c1d4be/download/calgw2020_full_report.pdf.

California Department of Water Resources, 2003, California's Groundwater, 2003 Basin descriptions, 5-22.14: California Department of Water Resources, Bulletin 118, San Joaquin Valley Groundwater Basin Eastern San Joaquín Subbasin (ca.gov)

California Division of Oil and Gas, 1973, California oil and gas fields, volume 1, north and east central California: California Division of Oil and Gas, Sacramento, California, 668 p.

California Division of Oil and Gas, 1981, Application for primacy in the regulation of class II injection wells under Section 1425 of the Safe Drinking Water Act: State of California Resources Agency, Department of Conservation, Division of Oil and Gas, 129 p., https://www.conservation.ca.gov/calgem/general_information/Documents/Application%20for%20Primacy.pdf [accessed August 22, 2022].

California Division of Oil, Gas and Geothermal Resources, 1998, California Oil and Gas Fields, Volume–I - Central California: California Department of Conservation.

California Geologic Energy Management Division (CalGEM), 2019, Water well capture radius analysis update, Kern River Aquifer Exemption: California Geologic Energy Management Division (CalGEM) Memorandum, dated 22 March 2019.

California Geological Survey, 1998, Maps of known active fault near-source sones in California and adjacent portions of Nevada: California Geological Survey (CGS) in cooperation with the Structural Engineers Association of California's (SEAOC) Seismology Committee, published by the International Conference of Building Officials, https://www.conservation.ca.gov/cgs/Pages/Earthquakes/near_source_zones.aspx

California Geological Survey, 2006, An overview of geologic carbon sequestration potential in California: CGS Special Report 183, PIER Collaboration Report, prepared for California Energy Commission and U.S. Department of Energy (CEC-500-2006-088), 64 p.

Chang, C., Zoback, M.D., and Khaksar, A., 2006, Empirical relations between rock strength and physical properties in sedimentary rocks: Journal of Petroleum Science and Engineering, v. 51, n. 3-4, p. 223-237, doi.org/10.1016/j.petrol.2006.01.003

Childs, C., Manzocchi, T., Walsh, J. J., Bonson, C., Nicol, A., and Schöpfer, M., 2009, A geometric model of fault zone and fault rock thickness variations: Journal of Structural Geology, v. 31, p. 117-127.

Coates, Schulze, and Throop, 1982, Volan – an advanced computational log analysis: SPWLA 23rd Annual Logging Symposium, Paper A

Coburn, M.G., and J.M. Gillespie, 2002 A hydrogeologic study to optimize stream flood performance in a giant oilfield: Kern River Field, California: American Association of Petroleum Geologists Bulletin, v. 86, n. 8, p. 1489-1505.

Condon, M.W., 1986, Review of Vedder pool development, Kern River field, Kern County, California [abstract]: Conference Proceedings, American Association of Petroleum Geologists, Bulletin, v. 7, n. 7, p. 3-4, www.osti.gov/biblio/5187116

Dale, R. H., J. J. French, and G. V. Gordon, 1966. Ground water geology and hydrology of the Kern River alluvial fan area, California: U.S. Geological Survey Open File Report 66-21,92 p.

Davarpanah, S.M., Sharghi, M., Narimani, S., Torok, A. and Vasarhelyi.B., 2023, Brittle-ductile transition stress of different rock types and its relationship with uniaxial compressive strength and Hoek-Brown material constant (mi). Sci. Rep. v. 13, p. 1186.

Davis, G.H., Green, J.H., Olmstead, F.H., and Brown, D.W., 1959, Ground-water conditions and storage capacity in the San Joaquin Valley, California: U.S. Geological Survey Water Supply Paper 1468.

Dibblee, T. W., Jr. and Chesterman, C.W., 1953, Geology of the Breckenridge Mountain Quadrangle California: California Division of Mines, Bulletin No. 168, 56 p.

Dodds, W.S., Stutzman, L.F., and Sollami, B.J., 1956, Carbon dioxide solubility in water: *Ind. Eng. Chem. Chem. Eng. Data Series*, v. 1., n. 1, p. 92-95.

Doughty, P.T., 2003, Clay smear seals and fault sealing potential of an exhumed growth fault, Rio Grande rift, New Mexico: American Association of Petroleum Geologists Bulletin, v. 87, n. 3, p. 427-444, doi.org/10.1306/10010201130

Edwards, E.C., 1941, Kern Front oil field, Kern County, California, *in* Levorsen, A.I., Bass, N.W., Heaton, R.L., Kew, W.S.W., Olcott, D.P., and Wasson, T., eds, American Association of Petroleum Geologists, Special Paper 11: Stratigraphic Type Oil Fields, p. 9-18.

Enick, R.M., Klara, S.M., 1990, CO_2 solubility in water and brine under reservoir conditions: Chemical Engineering Communications, v. 90, n. 1, p. 23-33, doi.org/10.1080/00986449008940574.

Evans, B.L., 2012, The Vedder lease, Section 9, Mt. Poso Field, California: Society of Petroleum Engineers SPE153940, 8 p.

Freeman, B., Yielding, G., Needham, D.T. and Badley, M.E., 1998. Fault seal prediction: the gouge ratio method: Geological Society, London, Special Publications, v. 127, n. 1, p. 19-25.

Gillespie, J., Kong, D., and Anderson, S.D., 2017, Groundwater salinity in the southern San Joaquin Valley: American Association of Petroleum Geologists, Bulletin, v. 101, n. 8, p. 1239-1261.

Ginger, E.P., Almon, W.R., Longacre, S.A., and Huggins, C.A., 1995, The impact of geological reservoir characterization on the flow unit modeling at the Kern River Field, California, USA, *in* Stoudt, E.L., and Harris, P.M., eds., Hydrocarbon reservoir characterization – geologic framework and flow unit modeling: Society for Sedimentary Geology (SEPM), Short Course No. 34, p. 317-357.

GitHub, 2023, dmlc/xgboost, scalable, portable and distributed gradient boosting (GBDT, GBRT or GBM) library, for Python, R, Java, Scala, C++ and more, accessed on August 17, 2023, https://github.com/dmlc/xgboost/

Goodman, E. D., and Malin, P. E., 1992, Evolution of the southern San Joaquin Basin and mid-Tertiary "transitional" tectonics, central California: Tectonics, v. 11, n. 3, p. 478-498, doi:10.1029/91TC02871.

Graham, S.A., Carroll, A.R., and Miller, G.E., 1988, Kern River Formation as a recorder of uplift and glaciation of the southern Sierra Nevada, *in* Graham, S.A., ed., Studies of the Geology of the San Joaquin Basin: Society for Sedimentary Geology (SEPM), p. 319-331.

Heidbach, O., M. Rajabi, X. Cui, K. Fuchs, B. Müller, J. Reinecker, K. Reiter, M. Tingay, F. Wenzel, F. Xie, M. O. Ziegler, M.-L. Zoback, and M. D. Zoback. 2018, The World Stress Map database release 2016: Crustal stress pattern across scales. Tectonophysics, v. 744, p. 484-498. doi.org/10.1016/j.tecto.2018.07.007

Hewlett, J.S., Phillips, S., and Bazeley, W.J.M., 2014, Middle Tertiary sequence stratigraphy, southern San Joaquin Basin, California: Pacific Section, American Association of Petroleum Geologists, Book Miscellaneous Publication No. 51, 73 p.

Hosford Scheirer, A., and Magoon, L.B., 2007, Age, distribution, and stratigraphic relationship of rock units in the San Joaquin Basin Province, California, *in* Hosford Scheirer, ed., Petroleum Systems and Geologist Assessment of Oil and Gas in the San Joaquin Basin Province, California: U.S. Geological Survey Professional Paper 1713, 107 p.

Hosford Scheirer, A.H., ed., 2007, Petroleum Systems and Geologist Assessment of Oil and Gas in the San Joaquin Basin Province, California: U.S. Geological Survey Professional Paper 1713.

Jennings, C.W., Gutierrez, C., Bryant, W., Saucedo, G., and Wills, C., 2010, Geologic map of California: California Geological Survey, Geologic Data Map 2, scale 1:750,000.

Johnson, C.L. and Graham, S.A., 2007, Middle Tertiary stratigraphic sequences of the San Joaquin basin, California: Petroleum systems and geologic assessment of oil and gas in the San Joaquin Basin Province, California: US Geological Survey Professional Paper 1268, p. 1-18.

Journel, A.G., 1974, Geostatistics for conditional simulation of ore bodies: Economic Geology, v. 69, n. 5, p. 673-687, doi.org/10.2113/gsecongeo.69.5.673

Journel, A.G., Alabert, F.G., 1990, New method for reservoir mapping: Journal of Petroleum Technology, *v.* 42, p. 212-218, doi.org/10.2118/18324-PA

Karolytė, R., Johnson, G., Yielding, G., and Gilfillan, S.M., 2020, Fault seal modelling–the influence of fluid properties on fault sealing capacity in hydrocarbon and CO_2 systems: Petroleum Geoscience, v. 26, n. 3, p. 481-497.

Kennedy/Jenks Consultants, 2020, Data in support of the aquifer exemption boundary expansion application for the Kern River reservoir including the Kern River Formation and upper Chanac Formation, Kern River Field, Kern County, California: Kennedy/Jenks Consultants, dated September 28, 2020.

Knipe, R.J., 1993, The Influence of Fault Zone Processes and Diagenesis on Fluid Flow, *in* Horbury, A.D., and Robinson, A.G., eds., Diagenesis and basin development: American Association of Petroleum Geologists, Studies Geology 36, Chapter 10, p. 135-148, doi.org/10/1306/St36574

Kodl, E.J., Eacmen, J.C., and Coburn, M.G., 1990, A geologic update of the emplacement mechanism within the Kern River Formation at the Kern River Field, *in* Kuespert, J.G., and Reid, S.A., eds., Structure, stratigraphy and hydrocarbon occurrences of the San Joaquin Basin, California: Pacific Section SEPM/AAPG Guidebook 65, p. 59-71.

Kuespert, J.G., and Sanford, S.J., 1990, Kern River Field history, in Kuespert, J.G., and Reid, S.A., eds., Structure, stratigraphy and hydrocarbon occurrences of the San Joaquin Basin, California: Pacific Section SEPM/AAPG Guidebook No. 65, p. 55-57.

Kumar, R., Campbell, S., Sonnenthal, E., Cunningham, J., 2020,. Effect of brine salinity on the geological sequestration of CO_2 in a deep saline carbonate formation: Greenhouse Gases Sci. Technol., v.10, p. 296-312.

Link, M.H., Helmold, K.P., Long, W.T. 1990. Depositional Environments and Reservoir Characteristics of the Upper Miocene Etchegoin and Chanac Formations, Kern Front Oil Field, California, *in* Kuespert, J.G., Reid., S.A., eds., Structure, Stratigraphy, and Hydrocarbon Occurrences of the San Joaquin Basin, California. Pacific Section SEPM Special Publication 64, p. 93-96.

Loomis, K.B., 1990, Depositional environments and sedimentary history of the Etchegoin Group, west-central San Joaquin Valley, California, *in* Kuespert, J.G., and Reid, S.A., eds., Structure, Stratigraphy and Hydrocarbon Occurrences of the San Joaquin Basin, California, Pacific Section American Association of Petroleum Geologists, p. 231-246.

Lundstern, J.E., Zoback, M.D., 2020, Multiscale variations of the crustal stress field throughout North America: Nature Communications, v. 11, 1951, doi.org/10.1038/s41467-020-15841-5.

Magara, K., 1986, Geological models of petroleum entrapment: London, Elsevier Applied Science Publishers, ISBN 0-85334-439-6, 342 p.

Manzocchi, T., Walsh, J.J., Nell, P., and Yielding, G., 1999, Fault transmissibility multipliers for flow simulation models: Petroleum Geoscience, v. 5, p. 53-63.

Miller, R.H., and Bloom, C.V., 1937, Mountain View oil field, *in* Summary of operations, California oil fields: San Francisco, Annual Report of the State Oil and Gas Supervisor, v. 22, n. 4, p. 5-36.

NRCS, 2007, Soil survey of Kern County, northeastern part, and southeastern part of Tulare County, California: United States Department of Agriculture, Natural Resources Conservation Service. Accessible online at http://soils.usda.gov/survey/printed_surveys/.

Olson, H.C., Miller, G.E. and Bartow, J.A., 1986, Stratigraphy, Paleoenvironment and Depositional Setting of Tertiary Sediments, Southeastern San Joaquin Basin, *in* Bell, P., ed., Southeast San Joaquin Valley Field Trip, Kern County, California Part II: Structure and Stratigraphy, Pacific Section American Association of Petroleum Geologists, p. 18-46. 1986_Bell.pdf (sanjoaquingeologicalsociety.org)

Palandri, J., & Kharaka, Y., 2004, A compilation of rate parameters of water–mineral interaction kinetics for Application to geochemical modeling: U.S. Geological Survey, Open-File Report 2004-1068.

Pan, L., Spycher, N., Doughty, C., and Pruess, K.., 2014, ECO2N V. 2.0: A new TOUGH2 fluid property module for mixtures of water, NaCl, and CO_2: United States:doi:10.2172/1170605.

Petersen, M.D., Moschetti, M.P., Powers, P.M., Mueller, C.S., Haller, K.M., Frankel, A.D., Zeng, Y., Rezaeian, S., Harmsen, S.C., Boyd, O.S., Field, N., Chen, R., Rukstales, K.S., Luco, N., Wheeler, R.L., Williams, R.S. and Olsen, A.H., 2014, Documentation for the 2014 Update of the United States National Seismic Hazard Maps, USGS Open-File Report 2014-1091, 243 p. http://dx.doi.org/10.3133/ofr20141091/

Plampin, M.R., Blondes, M.S., Sonnenthal, E.L., and Craddock, W.H., 2021, Potential Pb2+ mobilization, transport, and sequestration in shallow aquifers impacted by multiphase CO_2 leakage: a natural analogue study from the Virgin River Basin in SW Utah: Petroleum Geoscience, v.27.

Pyrcz, M.J., and Deutsch, C.V., 2014, Geostatistical reservoir modeling: Oxford University Press, Second Edition, ISBN978-0199731442, 448 p.

Rawling, G.C. and Goodwin, L.B., 2003, Cataclasis and particulate flow in faulted, poorly lithified sediments: Journal of Structural Geology, v. 25, n. 3, p. 317-331, doi.org/10.1016/S0191-8141(02)00041-X

Ren, B., Bryant, S.L. and Lake, L.W., 2015, November. Fast Modeling of local capillary trapping during CO_2 injection into a saline aquifer: Carbon Management Technology Conference.

Richardson, E.E., 1966, Structure contours on top of the Vedder sand, southeastern San Joaquin Valley, California: U.S. Geological Survey, Open-File Report, 15 p.

Saleeby, J., and Saleeby, Z., 2019, Late Cenozoic structure and tectonics of the southern Sierra Nevada–San Joaquin Basin transition, California: Geosphere, v. 15, n. 4, p. 1164–1205, doi.org/10.1130/GES02052.1

Saleeby, J., Saleeby, Z., and Le Pourhiet, L., 2013, Epeirogenic transients related to mantle lithosphere removal in the southern Sierra Nevada region: Part II. Implications of rock uplift and basin subsidence relations: Geosphere, doi:10.1130/GES00816.1.

Saleeby, J., Saleeby, Z., and Le Pourhiet, L., 2013a, Epeirogenic transients related to mantle lithosphere removal in the southern Sierra Nevada region, California, Part II: Implications of rock uplift and basin subsidence relations: Geosphere, v. 9, n. 3, p. 394–425, doi.org/10.1130/GES00816.1

Saleeby, J., Saleeby, Z., and Sousa, F., 2013b, From deep to modern time along the western Sierra Nevada Foothills of California, San Joaquin to Kern River drainages, *in* Putirka, K., ed., Geologic Excursions from Fresno, California, and the Central Valley: Geological Society of America Field Guide 32, p. 37–62, doi.org/10.1130/2013.0032(03)

Scholz, C.H., 1998, Earthquakes and friction laws: Nature, v. 391, p. 37-42, https://doi.org/10.1038/34097.

Sheehan, J.R., 1986, Tectonic evolution of the Bakersfield Arch, Kern County, California, *in* Bell, P., ed., Southeast San Joaquin Valley Field Trip, Kern County, California Part II: Structure and Stratigraphy, Pacific Section American Association of Petroleum Geologists, p. 10-17.

SLB, 2023, Petrel subsurface software: Schlumberger, accessed August 14, 2023, www.software.slb.com/products/petrel/

Smith, T.C., 1983, Kern Front, New Hope, and Premier faults, Kern County: California Division of Mines and Geology, Fault evaluation report FER-143, 15 p.

Sonnenthal, E., N. Spycher, T. Xu, and L. Zheng, 2021, TOUGHREACT V4.12-OMP and TReactMech V1.0 Geochemical and Reactive-Transport User Guide: Lawrence Livermore National Laboratory, LBNL Report 2001410. https://tough.lbl.gov/software/toughreact.

Spycher, N. and Pruess, K., 2005, CO_2-H2O Mixtures in the Geological Sequestration of CO_2. II. Partitioning in Chloride Brines at 12–100 ˚C and up to 600 bar: Geochim. Cosmochim. Acta, v.69, n.13, p. 3309-3320, doi:10.1016/j.gca.2005.01.015.

Spycher, N., Zhang, G., Sonnenthal, E., 2021, TOUGHREACT-Brine: Supplement to TOUGHREACT-V4.0-OMP User's Guide for Modeling Concentrated Solutions and Osmosis Using the Pitzer Ion-Interaction Model: Lawrence Livermore National Laboratory, LBNL-2001-387.

State of California, 2010, Field boundaries map, district 4: State of California Department of Conservation, Division of Oil, Gas, and Geothermal Resources.

Thakur, G., 2012, Moving toward 70% recovery factor: multiple disciplines, different methods, one goal: Journal of Petroleum Technology, v. 64, p. 14-15.

Timur, A., 1969, Pulsed nuclear magnetic resonance studies of porosity, movable fluid, and permeability of sandstones: Journal of Petroleum Technology, p. 775-786.

Toppozada, T., Branum, D., Petersen, M., Hallstrome, C., Cramer, C., and Reichle, M., 2000, Epicenters of and areas damaged by M≥5.0 California earthquakes, 1800-1999: California Division of Mines and Geology, Map Sheet 49.

Tye, R.S., Hewlett, J.S., Thompson, P.R., and Goodman, D.K., 1993, Integrated stratigraphic and depositional-facies analysis of parasequences in a transgressive systems tract, San Joaquin Basin, California: AAPG Memoir 58, Siliciclastic sequence stratigraphy: recent developments and applications, Chapter 5, p. 99-133.

U.S. Geological Survey, 2022, Interactive U.S. fault map: United States Geological Survey, Quaternary fault and fold database, https://www.usgs.gov/tools/interactive-us-fault-map [accessed August 27, 2023].

U.S. Geological Survey, 2023, Earthquake Catalogue, Earthquake Hazards Program. https://earthquake.usgs.gov/earthquakes [accessed August 1, 2023].

United States Code of Federal Regulations, Title 40, Chapter I, Subchapter D, Part 146, Subpart A, Section 146.6.

Verly, G. W., 1993, Sequential Gaussian Cosimulation: a simulation method integrating several types of information, *in* Soares, A., ed., Geostatistics Tróia '92. Quantitative Geology and Geostatistics, Volume 5: Netherlands, Springer Dordrecht, p. 543-554, doi.org/10.1007/978-94-011-1739-5_42

Wagoner, Jeffrey, 2009, 3D Geologic Modeling of the Southern San Joaquin Basin for the Westcarb Kimberlina Demonstration Project - A Status Report: Lawrence Livermore National Laboratory, LLNL-TR-410813, 27 p.

Walsh, F.R. III, and Zoback, M.D., 2016, Probabilistic assessment of potential fault slip related to injection-induced earthquakes: application to north-central Oklahoma, USA: Geology, doi:10.1130/G38275.1

Walsh, R. III, Zoback, M.D., Lele, S.P., Pais, D., Weingarten, M., and Tyrrell, T., 2017, FSP 2.0: a program for probabilistic estimation of fault slip potential resulting from fluid injection: Stanford University, modified November 2018, https://scits.stanford.edu/fault-slip-potential-fsp.

Watts, N.L., 1987, Theoretical aspects of cap-rock and fault seals for single- and two-phase hydrocarbon columns, Marine and Petroleum Geology, Volume 4, Issue 4, 1987, Pages 274-307, ISSN 0264-8172, https://doi.org/10.1016/0264-8172(87)90008-0.

Wolery T., Jove-Colon C., Rard., J., and A. Wijesinghe., 2004, Pitzer Database Development: Description of the Pitzer Geochemical Thermodynamic Database data0.ypf. Appendix I in In- Drift Precipitates/Salts Model (P. Mariner) Report ANL-EBS-MD-000045 REV 02. Las Vegas, Nevada: Bechtel SAIC Company.

Xu, T., N. Spycher, E. Sonnenthal, G. Zhang, L. Zheng, and K. Pruess, 2011. TOUGHREACT Version 2.0: A simulator for subsurface reactive transport under non-isothermal multiphase flow conditions: Computers & Geosciences, v.37, p.763-774.

Xu, T., Sonnenthal, E., Spycher, N., Pruess, K., 2018, TOUGHREACT-a simulation program for non-isothermal multiphase reactive geochemical transport in variability saturation geologic media: applications to geothermal injectivity and CO_2 geological sequestration: Computers & Geosciences, v. 32, n. 2, p. 145-165.

Yielding, G., Freeman, B., and Needham, D.T., 1997, Quantitative fault seal prediction: American Association of Petroleum Geologists Bulletin, v. 81, n. 6, p. 897-917.

Zhang, G., Lu, P., Luo, P., Sonnenthal, E., Huang, Y., Zhu, C., 2019, Effects of natural gas acidic components on local porosity generation in a carbonate reservoir: Insights from reactive transport modeling: American Association of Petroleum Geologists Bulletin, v. 103, p.2975-3001.

Glossary of Terms

Appendix. List of acronyms and abbreviations used in this report.

Acronym or Abbreviation	Name and Comment
ΔSh	Horizontal stress
Δz	Thickness
°	Degree
°C	Degree, Celsius
°F	Degree, Fahrenheit
µm	micron (micrometer)
1D	One-dimensional
2D	Two-dimensional
3D	Three-dimensional
4D	Four-dimensional (spatial and time)
AJ1	Apollo Jr. 1 fault splay
ANSI	American National Standards Institute
AoI	Area of Investigation
AoR	Area of Review
API	American Petroleum Institute
atm	Atmospheric unit
BCFG	Billion cubic feet of gas
bbl	barrel
bgs	Below ground surface
BHA	Bottomhole assembly
btm	bottom
CAL or CALI	Caliper (hole diameter) log
CalGEM	California Geologic Energy Management Division
CARB	California Air Resources Board
CCS	Carbon Capture and Sequestration
CEC	cation exchange capacity
CEMS	Continuous Emission Monitoring Systems
CEQA	California Environmental Quality Act

Acronym or Abbreviation	Name and Comment
CFR	Code of Federal Regulations
CGFZ	China Grade fault zone
CGS	California Geological Survey
CKTIM_F	
CI	Contour interval
CO_2	Carbon dioxide
Cogen	Cogeneration facility
coSGS	Co-simulated SGS
CPP	Chevron Pipeline & Power
CPR	California Public Resources Code
CUP	Conditional Use Permit
D/L	Fault displacement/length ratio
D/L	Fault Displacement to Length
DAS	Distributed acoustical sensing
DECT	Dual energy computed tomography
DEM	Digital Elevation Model
DOC	California Department of Conservation
DOE	U.S. Department of Energy
DOG	California Division of Oil and Gas
DOGGR	California Division of Oil, Gas, and Geothermal Resources
DPHI	Density-porosity log
DRES	Deep resistivity log
DT	Delta T
DWR	California Department of Water Resources
ECD	Equivalent Circulating Density
EIR	Environmental Impact Report
EMW	Equivalent mud weight
EOD	Environment of Deposition
EPA	United States Environmental Protection Agency
ERRP	Emergency and Remedial Response Plan

Acronym or Abbreviation	Name and Comment
ESA	Endangered Species Act
ESD	Equivalent static density
FBP	Formation breakdown pressure
FCP	Fracture closure pressure
FJ	Freeman–Jewett Silt
Fm	Geological Formation
FMI	Formation micro-resistivity log (image log)
FPM	Facies Proportion Map
FPP	Fracture propagation pressure (psi)
ft	foot or feet
g	Gravitational acceleration (9.8 m^2/s)
g/cm^3	Grams per cubic centimeter
GAMA	Groundwater Ambient Monitoring and Assessment Program
GR	Natural gamma ray log
GSDT	Geologic Sequestration Data Tool
HAL	Halliburton, Inc.
HR	Hydrologic Region
HRSG	Heat Recovery System Generator
ILD	Resistivity, long-normal (Ωm)
KCEH	Kern County Environmental Health
km	kilometer
KRF	Kern River Oil Field
KTIM	Permeability
kr	Radial permeability (relative to borehole)
kv	Vertical permeability
kh	Horizontal permeability
LCFS	California Lower Carbon Fuel Standards
LCM	Lost circulation material
LLBL	Lawrence Berkeley National Laboratory
LLNL	Lawrence Livermore National Laboratory

Acronym or Abbreviation	Name and Comment
LOP	Leak-off point
LOT	Leak-off test
LKO	Lowest known oil
LWD / MWD	Logging While Drilling / Measurement While Drilling
m.y.	Million years
Ma	Million years
MD	Measured depth
mD	Millidarcy
MEM	Mechanical Earth Model
Mg/l	Milligrams per liter
MICP	Mercury Injection Capillary Pressure
MIT	Mechanical Integrity Test
ML	Machine Learning
MMBO	Million barrels of oil
MMSCF	Million standard cubic feet
MM mt	million metric tonnes
MM mt/yr	million metric tonnes per year
mm/yr	millimeters per year
mmhos/cm	millimhos per centimeter
MOA	Memorandum of Agreement
MPa	MegaPascal
MPS	Multi-Point Statistics
MUA	Memorandum of Understanding
Mw	Moment Magnitude (earthquake)
MW	Mud weight
MW[e]	Megawatts of electricity
NMR	nuclear magnetic resonance
NPHI	Neutron-Porosity log
NtG	Net-to-gross

Acronym or Abbreviation	Name and Comment
OOIP	Original Oil in Place
OSCS	Omar-Sterling-Cortez South fault zone
OWC	Oil-water contact
PERM	Permeability log (derived)
PHIE	Effective porosity (v/v)
PHIT	Total porosity (v/v)
PISC	Post-Injection Site Care
ppf	Pounds per foot
ppg	Pounds per gallon
ppm	Parts per million
ppm	Parts per million
PSHA	Probabilistic Seismic Hazard Analysis
psi	Pound per square inch
psi/ft	Pressure per square inch per foot
psia	Pound per square inch, absolute
psig	Pound per square inch at gage
PSTM	Post-stack time migration
PTA	Pressure-transient analysis
QA	Quality assurance
QC	Quality control
RCA	Routine Core Analysis
RDT	Halliburton downhole formation pressure log
RES	Resistivity log
RHOB	Bulk density log
RQI	Rock-quality index
SAF	San Andreas fault zone
SCAL	Special Core Analysis
SCEC	Southern California Earthquake Center
SEM	Scanning electron microscope
SGMA	California Sustainable Groundwater Management Act

Acronym or Abbreviation	Name and Comment
SGR	Shale-gouge ratio
SGS	Sequential Gaussian Simulation
SHmax	Maximum horizontal stress
SHmin	Minimum horizontal stress
SJV	San Joaquin Valley
SLB	Schlumberger, Inc.
SP	Spontaneous Potential log
SPEDS	Spontaneous Potential, edited
SRES	Shallow resistivity log
SWC	side-wall core
Swe	Effective water saturation (v/v)
SWRCB	California State Water Resources Control Board
TD	Total depth
TDS	Total Dissolved Solids, in mg/l or ppm
TI	Training image
TOC	Total organic carbon (%)
Triple combo	Triple combination logs: neutron porosity, density, and resistivity
TVD	True vertical depth
TVDss	Vertical depth below mean sea level
TVT	True vertical thickness
UCS	Unconfined compressive strength
UIC	Underground Injection Control
USDW	Underground Source of Drinking Water
USGS	United States Geological Survey
v/v	Volume per volume [0-1 or percentage]
VBM	Volume-based modeling
Vcl	Clay volume log
VE	Vertical exaggeration (dimensionless)
VPC	Vertical Proportion Curve
Vsh or VSH	Shale volume

Acronym or Abbreviation	Name and Comment
VSP	Vertical Seismic Profile
WH	Wellhead
WM1-5	Wilmar fault zone, segments
WMA1-2	Wilmar fault zone, antithetic fault splays
WMF	Wilmar fault zone
Wt%	Percent weight
WUT	Well Utility Team
XGBoost	Gradient boosting machine-learning algorithm
XMRI	HAL Extended Range Micro-Imager log (image log)
XPT	Schlumberger Downhole formation pressure log
XRD	x-ray diffraction
XRF	x-ray fluorescence
ϕ_d	Porosity from density-porosity log
$\phi_{d,sh}$	Shale porosity from density-porosity log
ϕ_n	Porosity from neutron-density log
$\phi_{n,sh}$	Shale porosity from neutron-density log
Ωm	Ohm·m, measure of electrical resistivity

Appendix A. List of wells that penetrate the Vedder Sand in the Project AoI used for subsurface characterization. Surface locations in California State Plane V (NAD27, in feet). Well type and status from California Geologic Energy Management Division (CalGEM) databases.

Well Name	API12	Well Type	Status	Northing (ft)	Easting (ft)
KC20050X_ST1	040304874501	Oil & Gas	Idle	703,973	1,718,020
OM_0044X	040296655800	Cyclic Steam	Active	710,739	1,706,946
KA_0071X	040290031800	Cyclic Steam	Active	712,825	1,708,761
MS_0113	040292273800	Cyclic Steam	Active	716,879	1,704,699
KC30067X	040297396900	Cyclic Steam	Idle	703,482	1,713,687
KC30067X_ST1	040297396901	Cyclic Steam	Idle	703,482	1,713,687
KC20050X	040304874500	Cyclic Steam	Idle	703,973	1,718,020
33_0058X	040292887200	Cyclic Steam	Idle	708,262	1,712,852
BIS0085	040294479200	Cyclic Steam	Idle	716,605	1,711,221
CCM0041	040293200900	Dry Hole	Plugged	697,023	1,714,257
MTC0001	040292404700	Dry Hole	Plugged	716,755	1,717,945
MTC0071X	040294034800	Dry Hole	Plugged	718,109	1,719,279
SBB0027	040291846200	Dry Hole	Plugged	719,258	1,716,027
SA_0001	040292403700	Dry Hole	Plugged	726,163	1,702,192
FOS0001	040292689700	Dry Hole	Plugged	727,536	1,708,246
K120001	040294615600	Dry Hole	Plugged	729,426	1,696,963
JUN0054D	040294247600	Injection Well	Plugged	700,937	1,707,717
SJ_0001WD	040295391100	Injection Well	Plugged	703,021	1,701,791
SJ_0002WD	040296110600	Injection Well	Plugged	706,498	1,705,145
K100002X	040297205000	Multiple	Idle	702,074	1,715,369

OM_0044	040290009800	Multiple	Plugged	710,863	1,706,589
MON0065X	040296758700	Multiple	Plugged	715,488	1,702,852
3990072C	040294423200	Oil & Gas	Active	701,619	1,710,967
S3_0919X	040298795500	Oil & Gas	Active	704,263	1,715,173
S4_WDV1	040296194100	Oil & Gas	Active	704,830	1,708,620
S3_0819X	040297371200	Oil & Gas	Idle	704,642	1,713,072
3990001-11	040292497300	Oil & Gas	Plugged	697,997	1,706,890
RIV0002-10	040297393700	Oil & Gas	Plugged	701,161	1,716,192
RAS0028	040292215100	Oil & Gas	Plugged	703,540	1,710,583
GWA0145	040292697300	Oil & Gas	Plugged	715,584	1,701,312
FEC0074	040292411200	Oil & Gas	Plugged	716,118	1,703,180
LUC0154	040292803800	Oil & Gas	Plugged	716,253	1,702,016
BIS0225X	040297107500	Oil & Gas	Plugged	717,228	1,711,736
F280003	040292404800	Oil & Gas	Plugged	717,840	1,714,679
BIS0224X	040296905500	Oil & Gas	Plugged	717,948	1,712,058
F280001	040292631600	Oil & Gas	Plugged	718,075	1,713,436
SEC21-D	040292620100	Oil & Gas	Plugged	719,660	1,713,746
BOS0001	040292200100	Oil & Gas	Plugged	721,564	1,709,553
ZAN0001	040292402900	Oil & Gas	Plugged	724,670	1,706,758
ZAN0002	040292673800	Oil & Gas	Plugged	727,316	1,706,386
KC30068XSTD	040297559102	Water Disposal	Active	703,172	1,714,430
KC30068X	040297559100	Water Disposal	Active	703,172	1,714,430
KC30068XST	040297559101	Water Disposal	Active	703,172	1,714,430

KC30001X	040296989800	Water Disposal	Active	703,451	1,714,097
ELW0100X	040297301700	Water Disposal	Active	703,463	1,714,630
S4_WDV3	040305241300	Water Disposal	Active	703,943	1,708,228
ORLWD2	040306215900	Water Disposal	Active	704,115	1,699,952
S4_WDV2	040298201900	Water Disposal	Active	704,428	1,708,503
S3_0719X	040297135800	Water Disposal	Active	704,555	1,713,325
S3_0819XRD1	040297371201	Water Disposal	Active	704,642	1,713,072
KH_WDV1	040306065200	Water Disposal	Active	705,667	1,707,864
CP_0094X	040304573400	Water Disposal	Active	706,033	1,711,236
AP_0001WD	040296441200	Water Disposal	Active	706,941	1,710,463
AP_0051X	040296721700	Water Disposal	Active	707,627	1,709,786
AP_0051X_ST1	040296721701	Water Disposal	Active	707,627	1,709,786
33_0028X	040296641100	Water Disposal	Active	708,244	1,710,314
HF90003D	040296906900	Water Disposal	Idle	701,888	1,708,198
SJ_0010WD	040301418200	Water Disposal	Idle	702,933	1,704,024
CP_0073X	040296771100	Water Disposal	Idle	706,696	1,710,928
KA_0053X	040296990300	Water Disposal	Idle	711,855	1,707,279
GWA0001WD	040296110500	Water Disposal	Idle	715,450	1,700,912
CHP00WD1	040298942100	Water Disposal	Idle	727,937	1,700,058
HF90001D	040294937400	Water Disposal	Plugged	701,922	1,708,185
JUN0055D	040294934300	Water Disposal	Plugged	702,451	1,707,734
SJ_0011WD	040301621700	Water Disposal	Plugged	702,960	1,705,810
REV0004X	040296976200	Water Disposal	Plugged	705,978	1,712,007

GW_0105-D	040290026100	Water Disposal	Plugged	708,603	1,699,185
SOVWD-1	040297837600	Water Disposal	Plugged	711,164	1,703,820
COR0001WD	040295678200	Water Disposal	Plugged	711,719	1,704,965
VESWD-1	040297837500	Water Disposal	Plugged	712,270	1,701,751

Appendix B. Compilation of available sidewall core data from wells penetrating the Vedder in the AoI.

Sidewall Core Data				
Well	Depth (ft md)	Permeability (mD)	Porosity (%)	SW (%)
33_0028X	4765.01	6	0.29	--
	4794.01	31	0.21	--
	4904.01	55	0.32	--
	4906.01	110	0.28	--
	4911.01	46	0.25	--
	4924.01	19	0.25	--
	4934.01	38	0.24	--
	4941.01	61	0.19	--
	4948.01	45	0.23	--
	4965.01	49	0.19	--
	4984.01	90	0.26	--
	4993.01	160	0.24	--
	5023.01	110	0.23	--
	5039.01	190	0.24	--
	5065.01	380	0.23	--
	5078.01	59	0.31	--
	5123.01	16	0.27	--
	5200.01	9	0.27	--
	5218.01	140	0.20	--
	5270.011	6	0.30	--
	5316.011	43	0.28	--
	5340.011	21	0.25	--
	5355.011	73	0.29	--
	5371.011	56	0.31	--
	5419.011	9	0.28	--
	5470.011	43	0.27	--
	5639.011	76	0.27	--
	5668.011	58	0.27	--
	5695.011	14	0.25	--
	5723.011	31	0.21	--
	5730.011	62	0.23	--
	5738.012	4	0.22	--
	5795.012	49	0.27	--
	5813.012	83	0.27	--
	5894.012	12	0.25	--
	5926.012	31	0.22	--
AP_0001WD	4501	39	--	0.96
	4511	35	--	0.93
	4522	37	--	0.99

Sidewall Core Data				
Well	Depth (ft md)	Permeability (mD)	Porosity (%)	SW (%)
	4527	110	--	0.82
	4533	249	--	--
	4613	364	--	--
	4665	15	--	--
	4703	80	--	--
	4746	3	--	--
	4756	139	--	0.76
	4769	480	--	0.77
	4786	112	--	--
	4810	168	--	--
	4822	62	--	--
	4836	32	--	--
	4886	254	--	--
	4892	378	--	--
	4906	3	--	--
	4919	65	--	--
	4921	25	--	--
	4931	104	--	--
	4945	42	--	--
	4988	1897	--	--
	5002	174	--	--
	5018	860	--	--
	5050	1495	--	--
	5079	130	--	--
	5105	196	--	--
	5179	139	--	--
	5208	410	--	--
	5318	290	--	--
	5435	193	--	--
	5610	382	--	--
	5665	6	--	--
	5710	3591	--	--
	5765	36	--	--
AP_0051X	4510	41	0.28	0.68
	4620	240	0.31	0.91
	4787	120	0.23	0.60
	4830	530	0.27	0.84
	4845	72	0.27	0.63
	4884.1	31	0.26	0.67
	4913	85	0.31	0.73
	4916	56	0.29	0.58
	4918	29	0.28	0.77

Sidewall Core Data				
Well	Depth (ft md)	Permeability (mD)	Porosity (%)	SW (%)
	4922	51	0.31	0.87
	4935	17	0.31	0.85
	4940	40	0.28	0.81
	4956	120	0.33	0.88
	4958	190	0.34	0.88
	5000	82	0.34	0.91
	5006	690	0.24	0.80
	5016	310	0.28	0.59
	5041	880	0.24	0.72
	5052	2160	0.25	0.76
	5057	1070	0.26	0.71
	5098	26	0.27	0.77
	5134	60	0.34	0.65
	5137	18	0.29	0.88
	5152	170	0.27	0.84
	5152.5	110	0.38	0.74
	5303	170	0.31	0.86
	5347	440	0.30	0.89
	5384	28	0.33	0.83
	5407	160	0.22	0.71
	5417.001	390	0.30	0.84
CP_0073X	4460	17	0.29	0.81
	4464	12	0.30	0.85
	4473	45	0.32	0.79
	4483	29	0.30	0.83
	4486	12	0.24	0.89
	4491	130	0.28	0.60
	4719	1	0.26	0.78
	4720	7	0.25	0.81
	4722	0	0.22	0.91
	4731	76	0.29	0.75
	4733	110	0.32	0.63
	4738	93	0.34	0.66
	4741	136	0.31	0.63
	4748	270	0.33	0.64
	4756	310	0.36	0.59
	4773	730	0.18	0.84
	4779	560	0.31	0.88
	4798	620	0.32	0.86
	4819	13	0.26	0.83
	4825	28	0.30	0.75
	4869	19	0.32	0.74
	4875	42	0.33	0.70

Sidewall Core Data				
Well	Depth (ft md)	Permeability (mD)	Porosity (%)	SW (%)
	4890	15	0.30	0.85
	4898	39	0.32	0.58
	4901	18	0.27	0.90
	4904	42	0.31	0.74
	4907	20	0.30	0.87
	4915	59	0.40	0.74
	4919	73	0.34	0.63
	4923	38	0.34	0.89
	4933	46	0.32	0.87
ELW0100X	104	1730	0.34	0.45
	164	1510	0.30	0.47
	261	1070	0.32	0.54
	294	2370	0.33	0.40
	364	670	0.32	0.56
	394	1750	0.35	0.40
	424	1280	0.31	0.46
	563	--	0.31	0.47
	542	610	0.24	0.65
	574	530	0.30	0.61
	608	690	0.17	0.80
	646	--	0.15	0.43
	664	410	0.29	0.83
	797	--	0.19	0.39
	949	--	0.21	0.82
	997	690	0.31	0.77
	1086	57	0.26	0.88
	1136	1230	0.27	0.92
	1183	750	0.31	0.83
	1211	370	0.29	0.93
	1245	430	0.31	0.92
	1300	810	0.31	0.88
	1305	260	0.30	0.84
	4269	7	0.30	0.63
	4275	2	0.33	0.82
	4279	90	0.34	0.85
	4285	130	0.33	0.88
	4379	4	0.30	0.68
	4395	180	0.30	0.84
	4458	39	0.29	0.93
	4466	78	0.33	0.86
	4483	83	0.30	0.77
	4639	5	0.26	0.76

Sidewall Core Data				
Well	Depth (ft md)	Permeability (mD)	Porosity (%)	SW (%)
	4643	4	0.25	0.84
	4646	2	0.30	0.83
	4650	35	0.26	0.81
	4655	590	0.29	0.61
	4665	270	0.27	0.74
	4675	320	0.18	0.74
	4681	82	0.23	0.78
	4693	160	0.28	0.76
	4705	150	0.25	0.70
	4723	40	0.30	0.78
	4755	10	0.28	0.87
	4758	1	0.26	0.86
	4760	2	0.31	0.85
	4762	2	0.34	0.83
	4773	7	0.31	0.69
	4777	5	0.25	0.77
	4783	7	0.20	0.73
	4787	380	0.27	0.58
	4794	100	0.27	0.92
	4800	40	0.29	0.93
	4807	85	0.32	0.92
	4812	150	0.28	0.88
	4815	140	0.27	0.69
	4858	110	0.31	0.67
	4869	850	0.27	0.65
	4891	610	0.28	0.74
	4916	100	0.31	0.78
	4923	92	0.32	0.76
	4958	97	0.29	0.81
	5017	32	0.24	0.81
	5020	160	0.26	0.65
	5051	30	0.30	0.87
GW_0105-D	746	920	--	0.81
	842	5010	--	0.46
	872	3600	--	0.47
	893	3700	--	0.47
	933	4310	--	0.39
	985	7	--	0.89
	1026	1885	--	0.49
	1086	1100	--	0.40
	1116	4490	--	0.41
	1169	1310	--	0.57

Sidewall Core Data				
Well	Depth (ft md)	Permeability (mD)	Porosity (%)	SW (%)
	1208	2350	--	0.74
	1224	3520	--	0.44
	3198	261	--	0.66
	3568	51	--	--
	3706	77	--	--
	3759	35	--	--
	4289	336	--	--
	4409	157	--	--
	5102	18	--	--
	5185	865	--	--
	5235	2460	--	--
	5347	1245	--	--
	5390	835	--	--
	5450	1520	--	--
HF90001D	1528	2280	0.32	71.00
	1756	1370	0.31	87.00
	1810	1510	0.29	87.00
	1870	590	0.36	92.00
	2042	87	0.43	87.00
	2071	240	0.34	93.00
	3145	68	0.31	79.00
	4860	210	0.31	78.00
	5100	785	0.35	63.00
	5156	695	0.26	91.00
	5273	22	0.31	88.00
	5400	310	0.33	91.00
	5535	770	0.32	87.00
	5629	385	0.29	65.00
	5674	460	0.30	93.00
JUN0054D	4952	188	0.32	--
	4974	104	0.34	--
	4998	24	0.32	--
	5024	13	0.31	--
	5043	1110	0.33	--
	5056	27	0.29	--
	5187	14	0.25	--
	5233	135	0.21	--
	5260	197	0.27	--
	5272	683	0.30	--
	5288	515	0.27	--
	5309	1240	0.30	--
	5369	16	0.33	--
	5410	70	0.30	--
	5428	144	0.32	--

Sidewall Core Data				
Well	Depth (ft md)	Permeability (mD)	Porosity (%)	SW (%)
	5462	224	0.33	--
	5505	158	0.33	--
	5533	32	0.26	--
	5660	25	0.30	--
	5676	46	0.28	--
	5691	122	0.22	--
	5716	70	0.31	--
	5737	26	0.31	--
	5777	161	0.29	--
	5797	945	0.30	--
	5806	820	0.33	--
JUN0055D	5863	1180	--	--
	5897	305	--	--
	6015	870	--	--
	6053	505	--	--
	6137	1290	--	--
	6183	1180	--	--
	6190	1390	--	--
KA_0053X	4507	5	0.32	0.77
	4552	47	0.32	0.91
	4853	21	0.32	0.85
	4968	15	0.32	0.96
	4988	23	0.30	0.93
	4998	9	0.34	0.89
	5007	37	0.34	0.92
	5018	49	0.32	0.93
	5023	73	0.33	0.95
	5028	19	0.32	0.92
	5055	36	0.36	0.99
	5060	21	0.35	0.93
	5066	46	0.36	0.87
	5072	17	0.36	0.96
	5087	43	0.37	0.97
	5125	21	0.30	0.85
KC20050X	4528	5	0.27	0.85
	4539	300	0.35	0.82
	4550	100	0.33	0.80
	4563	200	0.30	0.75
	4580	300	0.31	0.84
	4623	5	0.27	0.90
	4627	25	0.33	0.71
	4632	25	0.31	0.65
	4646	5	0.28	0.87

Sidewall Core Data				
Well	Depth (ft md)	Permeability (mD)	Porosity (%)	SW (%)
	4654	300	0.32	0.63
	4658	400	0.29	0.53
	4662	500	0.26	0.58
	4664	400	0.29	0.47
	4667	400	0.31	0.46
	4670	500	0.29	0.55
	4672	300	0.29	0.43
	4674	400	0.33	0.52
	4676	300	0.26	0.79
	4679	300	0.25	0.82
	4681	300	0.25	0.74
	4685	200	0.32	0.82
	4690	200	0.31	0.84
	4700	150	0.31	0.91
KC30001X	4226	58	0.35	0.60
	4231	50	0.34	0.69
	4234	68	0.35	0.70
	4333	44	0.33	0.75
	4345	37	0.28	0.85
	4370	66	0.34	0.83
	4402	32	0.33	0.89
	4445	40	0.33	0.85
	4607	310	0.29	0.61
	4608	270	0.29	0.79
	4613	810	0.32	0.67
	4630	560	0.30	0.83
	4657	2160	0.28	0.82
	4683	1730	0.29	0.79
	4725	8	0.29	0.82
	4756	11	0.31	0.58
	4758	10	0.34	0.58
	4763	13	0.31	0.83
	4775	7	0.33	0.89
	4797	210	0.30	0.90
	4803	180	0.28	0.90
	4807	190	0.33	0.86
	4813	230	0.32	0.84
	4837	48	0.35	0.90
	4883	640	0.28	0.62
	4921	620	0.29	0.66
	4975	280	0.30	0.79
	5045	1401	0.29	0.72

Sidewall Core Data				
Well	Depth (ft md)	Permeability (mD)	Porosity (%)	SW (%)
	5076	2010	0.28	0.82
	5147	1850	0.27	0.83
	5181	1780	0.31	0.59
	5251	370	0.31	0.81
	5307	4	0.25	0.58
	5330	1200	0.21	0.85
	5365	1140	0.23	0.65
	5425	18	0.20	0.26
	5505	24	0.23	0.68
	5543	1880	0.25	0.85
	5564	9	0.19	0.66
	5651	670	0.20	0.71
	5709	720	0.20	0.45
	5750	200	0.27	0.52
	5802	1420	0.24	0.76
	5857	1280	0.29	0.67
KC30067X	2536	50	0.38	0.81
	2546	70	0.35	0.73
	2559	70	0.41	0.77
	2567	60	0.40	0.90
	2574	110	0.39	0.88
	2580	120	0.37	0.82
	2585	140	0.41	0.88
	2590	250	0.41	0.87
	2600	380	0.39	0.88
	3397	0	0.22	0.81
	4126	1	0.31	0.81
	4301	90	0.31	0.70
	4304	85	0.35	0.63
	4310	100	0.37	0.56
	4314	80	0.35	0.70
	4319	95	0.32	0.72
	4419	55	0.35	0.60
	4422	40	0.33	0.66
	4429	35	0.31	0.51
	4437	45	0.29	0.57
	4443	50	0.31	0.61
	4446	50	0.32	0.61
	4509	75	0.28	0.59
	4533	170	0.36	0.63
	4550	35	0.30	0.84
	4554	30	0.32	0.70

Sidewall Core Data				
Well	Depth (ft md)	Permeability (mD)	Porosity (%)	SW (%)
	4558	33	0.32	0.76
	4571	20	0.31	0.77
	4590	15	0.37	0.79
	4605	18	0.33	0.83
	4615	22	0.33	0.64
	4625	25	0.33	0.78
	4646	12	0.28	0.91
	4673	14	0.30	0.82
	4705	9	0.28	0.84
	4735	2	0.29	0.81
	4737	2	0.30	0.79
	4739	13	0.23	0.83
	4741	4	0.34	0.75
	4743	130	0.31	0.59
	4747	200	0.31	0.60
	4749	230	0.30	0.67
	4751	220	0.29	0.57
	4753	100	0.32	0.61
	4755	610	0.28	0.44
	4757	400	0.30	0.50
	4759	740	0.30	0.55
	4761	130	0.37	0.68
	4763	95	0.30	0.51
	4765	140	0.31	0.62
	4767	1200	0.29	0.35
	4769	950	0.31	0.32
	4771	1100	0.30	0.53
	4773	1400	0.31	0.47
	4775	380	0.26	0.40
	4777	550	0.25	0.30
	4780	260	0.28	0.32
	4805	65	0.25	0.46
	4823	210	0.32	0.56
	4853	50	0.32	0.58
	4886	5	0.24	0.81
	4905	2	0.30	0.92
	4907	12	0.28	0.64
	4909	15	0.29	0.59
	4913	2	0.30	0.78
	4926	5	0.26	0.81
	4946	9	0.27	0.79
	4950	280	0.25	0.75

Sidewall Core Data				
Well	Depth (ft md)	Permeability (mD)	Porosity (%)	SW (%)
	4954	110	0.28	0.80
	4958	130	0.28	0.68
	4964	80	0.27	0.80
	4967	100	0.29	0.71
	4972	1250	0.26	0.59
	4976	16	0.27	0.88
	4985	--	--	--
	5043	180	0.27	0.85
	5063	630	0.28	0.80
	5087	320	0.30	0.67
	5120	10	0.27	0.73
	5141	55	0.30	0.67
	5153	40	0.33	0.66
	5188	0	0.40	0.90
	5197	2	0.32	0.91
	5211	120	0.23	0.79
	5217	95	0.25	0.87
	5239	25	0.24	0.80
	5257	140	0.26	0.53
	5265	500	0.23	0.68
	5293	3	0.28	0.57
	5335	4	0.27	0.67
	5352	850	0.25	0.67
	5385	30	0.28	0.75
KC30068X	2351	1300	0.32	0.33
	2358	3000	0.29	0.82
	2386	80	0.39	0.94
	2550	1950	0.37	0.58
	2593	120	0.39	0.97
	2868	5	0.33	0.89
	2920	200	0.33	0.93
	2940	75	0.32	0.94
	3024	25	0.30	0.90
	3034	260	0.33	0.86
	3080	1	0.35	0.96
	3119	18	0.30	0.85
	3130	20	0.30	0.81
	3146	65	0.33	0.87
	3550	22	0.28	0.81
	3765	50	0.29	0.89
	4017	40	0.29	0.88
	4045	20	0.30	0.87

Sidewall Core Data				
Well	Depth (ft md)	Permeability (mD)	Porosity (%)	SW (%)
	4104	25	0.35	0.71
	4112	14	0.32	0.85
	4126	450	0.32	0.87
	4132	60	0.31	0.77
	4150	24	0.28	0.83
	4155	75	0.29	0.85
	4207	5	0.29	0.66
	4211	50	0.30	0.79
	4217	--	--	--
	4220	400	0.34	0.80
	4221	320	0.35	0.80
	4223	300	0.38	0.79
	4225	310	0.33	0.74
	4227	350	0.34	0.71
	4233	300	0.33	0.89
	4235	270	0.35	0.90
	4237	330	0.34	0.89
	4239	2	0.36	0.73
	4246	0	0.25	0.73
	4252	3	0.32	0.72
	4258	140	0.34	0.86
	4269	12	0.30	0.73
	4276	1	0.28	0.76
	4282	150	0.31	0.85
	4286	3	0.38	0.80
	4301	1	0.27	0.81
	4315	20	0.29	0.83
	4325	18	0.32	0.84
	4327	60	0.32	0.60
	4330	55	0.32	0.76
	4334	100	0.34	0.68
	4338	50	0.32	0.88
	4345	70	0.31	0.90
	4348	85	0.30	0.93
	4351	120	0.35	0.91
	4356	105	0.32	0.85
	4360	90	0.30	0.92
	4367	60	0.32	0.91
	4370	65	0.30	0.92
	4372	80	0.29	0.92
	4376	60	0.29	0.88
	4384	40	0.30	0.93

Sidewall Core Data				
Well	Depth (ft md)	Permeability (mD)	Porosity (%)	SW (%)
	4386	70	0.33	0.92
	4397	35	0.32	0.93
	4400	60	0.30	0.94
	4407	20	0.15	0.73
	4413	2000	0.34	0.82
	4415	2020	0.33	0.81
	4417	1980	0.30	0.93
	4419	2050	0.31	0.88
	4422	40	0.30	0.81
	4425	2040	0.35	0.78
	4428	210	0.31	0.83
	4433	360	0.31	0.80
	4437	110	0.29	0.88
	4443	80	0.31	0.86
	4449	35	0.29	0.92
	4458	50	0.31	0.82
	4463	40	0.31	0.82
	4468	38	0.31	0.87
	4472	75	0.35	0.88
	4476	45	0.33	0.88
	4485	42	0.31	0.86
	4494	60	0.33	0.93
	4498	100	0.35	0.89
	4504	55	0.33	0.91
	4507	85	0.33	0.83
KH_WDV1	2306	6	0.47	0.94
	2484	2	0.58	0.98
	2500	2	0.56	0.98
	2535	365	0.48	1.00
	2614	45	0.33	0.80
	2700	5	0.11	0.73
	2825	4	0.33	0.73
	2833	18	0.35	0.91
	2876	42	0.34	0.93
	2906	3	0.33	0.93
	2958	9	0.41	0.99
	3016	49	0.35	0.99
	3056	79	0.38	0.77
	3100	20	0.34	0.89
	3232	42	0.34	0.95
	3290	53	0.35	0.96
	3860	1	0.30	0.99
	4591	50	0.31	0.98

Sidewall Core Data				
Well	Depth (ft md)	Permeability (mD)	Porosity (%)	SW (%)
	4664	39	0.32	0.92
	4756	50	0.22	0.80
	4940	1836	0.29	0.68
	4988	57	0.26	0.78
	5085	21	0.33	0.98
	5193	4	0.32	0.99
	5270	172	0.25	0.83
	5336	4	0.27	0.74
	5412	100	0.30	0.82
	5558	209	0.33	0.85
	5812	706	0.26	0.81
	5844	5	0.25	0.84
	5892	105	0.23	0.81
	5912	167	0.28	0.85
	5946	2	0.20	0.77
	5964	1	0.23	0.82
	5985	1	0.24	0.78
OM_0044X	430	1096	0.29	55.00
	473	448	0.28	54.00
	482	464	0.30	54.00
	492	740	0.32	48.00
	505	491	0.29	55.00
	510	820	0.11	52.00
	520	1357	0.32	75.00
	530	312	0.30	54.00
	549	1114	0.31	55.00
	562	847	0.33	65.00
	610	86	0.28	67.00
	631	204	0.32	66.00
	642	79	0.32	63.00
	656	329	0.28	81.00
	665	105	0.31	71.00
	702	878	0.31	68.00
	741	910	0.27	52.00
	839	2133	0.28	46.00
	863.9999	2011	0.30	62.00
	869	2065	0.29	50.00
	882	1100	0.25	49.00
	913	470	0.28	62.00
	931.0001	500	0.30	57.00
	992.9999	900	0.18	61.00
	2421	5	0.56	93.00
	2449	5	0.47	75.00

Sidewall Core Data				
Well	Depth (ft md)	Permeability (mD)	Porosity (%)	SW (%)
	2834	128	0.41	95.00
	4591	218	0.33	93.00
	4768	20	0.28	98.00
	4772	48	0.27	88.00
	4783	103	0.33	85.00
	4786	77	0.32	76.00
	4801	24	0.31	95.00
	4816	84	0.31	90.00
	4914	33	0.29	81.00
	4933	98	0.31	95.00
	4967	52	0.28	91.00
	4969	84	0.33	81.00
	4975	47	0.33	72.00
	5000	63	0.32	93.00
	5007	174	0.29	91.00
	5019	58	0.31	88.00
	5027	43	0.30	90.00
	5049	23	0.29	85.00
	5070	113	0.33	87.00
	5092	240	0.33	79.00
	5125	130	0.27	86.00
	5127	91	0.29	85.00
	5252	2552	0.30	58.00
	5253	119	0.32	85.00
	5274	1041	0.31	66.00
	5324	55	0.28	86.00
	5373	201	0.33	81.00
	5419	180	0.32	91.00
	5439	177	0.33	96.00
	5623	99	0.26	81.00
	5643	747	0.27	78.00
	5656	1386	0.27	71.00
	5668	1221	0.27	87.00
	5670	3030	0.31	58.00
	5679	680	0.14	68.00
	5716	1311	0.29	64.00
	5778	1340	0.21	73.00
	5858	80	0.29	71.00
	5944	199	0.28	71.00
ORLWD2	3215	5	0.41	0.91
	3318	5	0.44	0.90
	3390	553	0.31	0.79

Sidewall Core Data				
Well	Depth (ft md)	Permeability (mD)	Porosity (%)	SW (%)
	3512	7	0.33	0.99
	3678	15	0.39	0.81
	3702	5	0.42	1.00
	3725	38	0.34	0.95
	3773	108	0.36	0.96
	3785	60	0.35	0.94
	3845	31	0.35	0.93
	3895	18	0.34	0.93
	3965	15	0.33	0.96
	3995	19	0.34	0.96
	4025	37	0.33	0.95
	4215	0	0.28	0.94
	4310	0	0.30	0.99
	4408	15	0.33	0.99
	4718	1	0.37	1.00
	4815	32	0.33	0.99
	4950	288	0.36	1.00
	5188	5	0.34	0.97
	5278	5	0.38	0.98
	5305	27	0.30	0.99
	5335	18	0.33	0.89
	5385	466	0.36	0.77
	5409	219	0.31	0.80
	5453	7	0.32	0.96
	5502	161	0.37	0.97
	5545	616	0.32	0.77
	5575	1054	0.32	0.64
	5615	185	0.30	0.81
	5675	169	0.32	0.81
	5778	5	0.47	1.00
	5815	24	0.31	0.88
	5835	52	0.33	0.75
	5875	84	0.34	0.81
	5895	125	0.35	0.76
	5942	122	0.41	0.99
	5960	33	0.32	0.74
	5980	58	0.34	0.73
	6040	43	0.34	0.91
	6080	63	0.33	0.87
	6103	130	0.33	0.91
	6125	123	0.34	0.92
	6178	324	0.39	0.99
	6277	1	0.31	0.96
	6365	74	0.31	1.00
	6392	174	0.26	0.54

Sidewall Core Data				
Well	Depth (ft md)	Permeability (mD)	Porosity (%)	SW (%)
	6411	677	0.26	0.83
	6463	1259	0.28	0.76
	6510	800	0.22	0.66
	6545	974	0.27	0.69
	6563	1179	0.32	0.72
	6595	78	0.25	0.76
	6610	110	0.31	0.73
	6690	15	0.28	0.99
REV0004X	2023	4	0.64	0.90
	2205	4	0.63	0.93
	4478	16	0.32	0.79
	4498	74	0.36	0.65
	4576	1050	0.33	0.76
	4604	25	0.31	0.77
	4612	23	0.32	0.64
	4691	388	0.32	0.58
	4694	3090	0.30	0.44
	4700	1830	0.33	0.46
	4704	411	0.29	0.44
	4709	186	0.28	0.56
	4713	1000	0.30	0.63
	4717	743	0.04	0.55
	4725	837	0.33	0.65
	4728	167	0.30	0.68
	4733	561	0.29	0.85
	4739	138	0.31	0.81
	4746	48	0.28	0.88
	4782	26	0.26	0.92
	4800	33	0.26	0.89
	4809	23	0.28	0.88
	4821	30	0.32	0.68
	4842	10	0.26	0.86
	4866	181	0.30	0.64
	4872	68	0.31	0.72
	4905	192	0.39	0.68
	4959	146	0.28	0.78
S3_0719X	2199	260	0.35	0.89
	4435	17	0.30	0.84
	4467	25	0.30	0.68
	4470.5	340	0.36	0.68
	4487	78	0.36	0.70
	4539	3	0.28	0.82
	4566	4	0.33	0.89

Sidewall Core Data				
Well	Depth (ft md)	Permeability (mD)	Porosity (%)	SW (%)
	4642	30	0.25	0.77
	4650	2300	0.26	0.46
	4657	700	0.31	0.60
	4665	2020	0.21	0.21
	4667	1030	0.33	0.57
	4673	1180	0.29	0.65
	4676	1370	0.32	0.61
	4680	1240	0.31	0.70
	4687	1120	0.35	0.65
	4697	910	0.32	0.67
	4710	640	0.25	0.79
	4724	360	0.30	0.87
	4735	280	0.31	0.86
	4757	18	0.28	0.68
	4792	24	0.29	0.61
	4796	16	0.32	0.72
	4811	28	0.32	0.78
	4824	12	0.27	0.84
	4832	210	0.33	0.52
	4850	31	0.31	0.91
	4868	150	0.35	0.94
	4923	770	0.25	0.79
	4935	330	0.34	0.91
	4966	450	0.28	0.86
	4987	440	0.28	0.90
	5026	380	0.32	0.74
	5066	50	0.18	0.76
S3_0819X	196	187	0.31	0.71
	228	547	0.35	0.77
	257	169	0.30	0.61
	277	228	0.28	0.60
	302	357	0.34	0.70
	330	518	0.31	0.63
	357	39	0.35	0.82
	398	685	0.31	0.55
	425	387	0.34	0.65
	452	213	0.30	0.59
	507	1270	0.33	0.57
	520	1820	0.32	0.73
	553	185	0.33	0.62
	575	433	0.30	0.62
	610	292	0.33	0.62
	654	983	0.28	0.69

Sidewall Core Data				
Well	Depth (ft md)	Permeability (mD)	Porosity (%)	SW (%)
	667	136	0.27	0.75
	692	91	0.26	0.75
	718	47	0.23	0.83
	729	75	0.23	0.70
	763	152	0.27	0.77
	781	434	0.29	0.78
	869	684	0.33	0.95
	4476	190	0.30	0.71
	4488	130	0.28	0.93
	4502	170	0.25	0.81
	4510	310	0.31	0.92
	4519	34	0.32	0.94
	4540	30	0.36	0.92
	4552	28	0.36	0.89
	4558	53	0.30	0.89
	4568	40	0.26	0.87
	4580	33	0.33	0.89
	4592	190	0.34	0.88
	4622	160	0.34	0.94
	4638	18	0.39	0.92
	4644	72	0.31	0.94
	4653	13	0.33	0.85
	4665	9	0.34	0.89
	4708	1400	0.31	0.64
	4712	680	0.31	0.66
	4723	210	0.26	0.79
	4732	1530	0.31	0.63
	4746	360	0.30	0.88
	4755	300	0.27	0.86
	4768	190	0.29	0.80
	4777	28	0.25	0.81
	4786	14	0.27	0.78
	4804	18	0.30	0.79
	4841	4	0.30	0.89
	4844	3	0.30	0.86
	4847	10	0.31	0.83
	4849	57	0.34	0.68
	4860	180	0.34	0.71
	4872	170	0.32	0.76
	4875	260	0.32	0.65
	4881	390	0.36	0.75
	4886	130	0.29	0.90

Sidewall Core Data				
Well	Depth (ft md)	Permeability (mD)	Porosity (%)	SW (%)
	4900	280	0.36	0.95
	4906	39	0.36	0.87
	4916	490	0.26	0.80
	4923	120	0.40	0.73
S3_0819XRD1	4890	--	0.29	0.62
	4895	100	0.31	0.52
	4895.001	100	0.31	0.52
	4900	300	0.31	0.71
	4905	300	0.35	0.55
	4910	400	0.31	0.57
	4915	100	0.30	0.71
	4920	300	0.31	0.68
	4930	200	0.32	0.64
	4940	100	0.32	0.72
	4960	--	0.30	0.87
	5055	--	0.30	0.70
	5060	--	0.32	0.73
	5065	--	0.32	0.68
	5080	--	0.31	0.77
	5090	--	0.31	0.76
	5100	--	0.34	0.62
	5125	--	0.31	0.76
	5140	--	0.35	0.69
	5150	--	0.33	0.78
	5175	--	0.32	0.92
	5223	200	0.31	0.89
	5414	100	0.30	0.92
S4_WDV1	4665	35	0.28	92.00
	4919	1340	0.27	93.00
	4954	460	0.17	77.00
	5060	3	0.34	91.00
	5070	18	0.29	87.00
	5235	580	0.25	85.00
	5330	3	0.41	91.00
	5432	290	0.29	93.00
	5479	680	0.27	88.00
	5565	110	0.29	94.00
	5710	200	0.29	89.00
	5915	840	0.23	79.00
	6000	98	0.21	83.00
S4_WDV2	2590	26	0.31	0.66
	2614	29	0.33	0.87
	2660	26	0.42	0.88

Sidewall Core Data				
Well	Depth (ft md)	Permeability (mD)	Porosity (%)	SW (%)
	2954	25	0.43	0.89
	3155	57	0.48	0.93
	3313	52	0.34	0.83
	4690	43	0.34	0.85
	4730	16	0.33	0.77
	4750	162	0.36	0.79
	4870	27	0.31	0.90
	4936	1748	0.30	0.62
	4950	933	0.30	0.88
	4960	426	0.29	0.74
	4980	1758	0.27	0.28
	5000	351	0.30	0.79
	5130	1030	0.28	0.67
	5170	19	0.29	0.70
	5189	17	0.29	0.78
	5230	21	0.28	0.78
	5450	682	0.30	0.52
	5680	1022	0.28	0.60
	5860	42	0.27	0.70
	5870	43	0.22	0.89
	5910	1510	0.28	0.77
	5930	1176	0.29	0.70
	5956	885	0.30	0.68
	5970	7	0.26	0.68
SOVWD-1	1438	178	0.25	0.99
	1458	369	0.28	0.98
	1473	601	0.29	1.00
	1496	121	0.27	0.83
	1764	1209	0.28	1.00
	1958	1129	0.28	1.00
	2030	282	0.28	1.00
	2830	1181	0.38	1.00
	4760	1717	0.30	1.00
	4804	2772	0.36	1.00
	4852	1305	0.35	1.00
	4990	1678	0.32	1.00
	5055	615	0.31	1.00
	5095	465	0.35	1.00
	5201	169	0.30	1.00
	5258	48	0.31	0.99
	5320	134	0.35	1.00
	5460	67	0.29	1.00
	5530	121	0.34	1.00

Sidewall Core Data				
Well	Depth (ft md)	Permeability (mD)	Porosity (%)	SW (%)
	5613	1020	0.35	1.00
	5788	57	0.28	1.00
	5920	23	0.26	1.00
	5970	650	0.26	1.00
	6027	154	0.34	1.00
	6058	921	0.33	1.00
	6103	17	0.25	1.00
	6140	56	0.26	1.00
VESWD-1	1310	21	0.36	0.99
	1338	2950	0.31	0.43
	1350	34	0.31	0.98
	1356	1384	0.26	0.33
	1367	998	0.28	0.72
	1376	1139	0.27	0.67
	1384	284	0.25	0.80
	1395	6966	0.32	0.95
	1402	620	0.26	0.76
	1454	177	0.31	0.92
	1480	462	0.27	0.84
	1492	660	0.29	0.88
	1868	247	0.26	0.80
	2940	414	0.32	0.80
	2984	251	0.35	0.99
	3369	43	0.33	0.99
	4828	942	0.29	0.88
	4874	1770	0.31	0.90
	4998	29	0.33	0.85
	5013	25	0.31	0.97
	5025	36	0.31	0.85
	5066	1530	0.32	0.86
	5080	2647	0.31	0.75
	5104	630	0.31	0.88
	5212	33	0.32	0.91
	5265	56	0.31	0.92
	5280	975	0.33	0.86
	5322	64	0.33	0.95
	5410	42	0.34	0.76
	5515	665	0.36	0.76
	5885	318	0.25	0.87
	5918	1072	0.28	0.87
	5960	1063	0.26	0.61
	6001	470	0.26	0.84

Appendix C. Compilation of available whole core data from wells penetrating the Vedder in the AoI.

Whole Core Data				
Well	Depth (ft md)	Permeability (mD)	Porosity (%)	SW (%)
33_0028X	4528.10	163.00	0.28	0.74
	4530.10	185.00	0.28	0.78
	4532.10	157.00	0.29	0.77
	4544.09	2053.00	0.28	0.75
	4681.00	18.00	0.31	0.79
	4687.09	23.00	0.17	0.71
	4689.12	17.00	0.20	0.86
	4802.75	5087.00	0.34	0.74
	4804.78	3976.00	0.33	0.87
	4806.81	4719.00	0.32	0.75
	4815.94	5549.00	0.33	0.86
	4820.00	316.00	0.24	0.95
	4824.00	1992.00	0.36	0.90
	4828.00	1033.00	0.34	0.92
	4832.00	1263.00	0.34	0.86
	4834.00	3.70	0.14	0.79
AP_0051X	4856.40	9.00	0.21	0.73
	4858.50	22.00	0.26	0.79
	4861.07	427.00	0.26	0.56
	4862.76	5.10	0.19	0.89
	4875.43	26.00	0.31	0.83
	4878.86	8.30	0.28	0.84
	4881.40	6.80	0.20	0.73
	4883.93	6.90	0.22	0.80
	4886.46	3.10	0.25	0.69
	4891.52	2.70	0.25	0.85
	4894.05	2.00	0.26	0.92
	4896.58	3.50	0.30	0.91
	4899.12	3.20	0.28	0.65
	4901.65	2.50	0.26	0.65
	4903.81	9.90	0.29	0.61
	4905.93	9.90	0.30	0.59
	4909.11	4.90	0.26	0.76
	4911.23	7.20	0.21	0.64
	4913.35	8.00	0.33	0.70
	4915.47	7.10	0.24	0.74
	4917.59	3.70	0.23	0.85
	4919.71	7.40	0.26	0.89
	4921.83	7.20	0.26	0.92
	4923.95	1.30	0.28	0.87
	4926.03	4.90	0.30	0.63

Whole Core Data				
Well	Depth (ft md)	Permeability (mD)	Porosity (%)	SW (%)
	4932.89	10.00	0.30	0.83
	4933.86	5.70	0.25	0.89
	4936.19	21.00	0.27	0.89
	4938.54	28.00	0.30	0.93
	4940.90	124.00	0.32	0.78
	4943.25	184.00	0.31	0.74
	4945.61	302.00	0.25	0.73
	4947.97	4.70	0.26	0.81
	4949.14	12.00	0.24	0.78
	4951.50	624.00	0.25	0.65
	4953.06	905.00	0.31	0.76
	4953.84	602.00	0.33	0.67
	4955.40	74.00	0.31	0.75
	4956.96	140.00	0.28	0.72
	4958.52	329.00	0.26	0.75
	4960.07	617.00	0.32	0.77
	4961.56	32.00	0.33	0.80
	4963.05	506.00	0.26	0.69
	4964.54	358.00	0.24	0.56
	4966.25	17.00	0.35	0.85
	4968.67	212.00	0.27	0.81
	4973.56	15.00	0.32	0.79
	4976.01	45.00	0.31	0.79
	4978.46	9.30	0.27	0.74
	4980.50	29.00	0.29	0.71
	4982.50	38.00	0.29	0.61
	4984.50	2309.00	0.28	0.75
	4985.50	3904.00	0.29	0.80
	4986.50	4918.00	0.28	0.73
	4990.50	32.00	0.33	0.74
COR0001WD	4646.00	1375.00	0.36	--
	4647.00	1861.00	0.36	--
	4648.00	1021.00	0.37	--
	4649.00	471.00	0.36	--
	4650.00	1023.00	0.36	--
	4651.00	1732.00	0.36	--
	4652.00	2157.00	0.36	--
	4653.00	973.00	0.35	--
	4654.00	1226.00	0.35	--
	4655.00	959.00	0.36	--
	4656.00	1429.00	0.36	--
	4657.00	64.00	0.32	--

Whole Core Data				
Well	Depth (ft md)	Permeability (mD)	Porosity (%)	SW (%)
	4658.00	2990.00	0.35	--
	4659.00	3639.00	0.34	--
	4660.00	3529.00	0.34	--
	4661.00	3321.00	0.34	--
	4662.00	3123.00	0.33	--
	4663.00	3342.00	0.34	--
	4664.00	0.01	0.04	--
	5301.00	7764.00	0.28	--
	5302.00	8029.00	0.28	--
	5303.00	2576.00	0.29	--
	5304.00	1071.00	0.30	--
	5305.00	1656.00	0.28	--
	5306.00	658.00	0.32	--
	5307.00	341.00	0.32	--
	5308.00	788.00	0.31	--
	5309.00	475.00	0.30	--
	5310.00	412.00	0.32	--
	5311.00	215.00	0.31	--
	5312.00	131.00	0.30	--
	5313.00	349.00	0.32	--
	5314.00	391.00	0.33	--
	5315.00	1579.00	0.29	--
	5316.00	3749.00	0.29	--
	5817.00	2215.00	0.30	--
	5818.00	4947.00	0.29	--
	5819.00	6344.00	0.30	--
	5820.00	5032.00	0.30	--
	5821.00	6359.00	0.31	--
	5822.00	3435.00	0.28	--
	5823.00	3418.00	0.29	--
	5824.00	2991.00	0.29	--
	5825.00	3623.00	0.31	--
	5826.00	4630.00	0.30	--
	5827.00	4874.00	0.29	--
	5828.00	1775.00	0.32	--
	5829.00	1889.00	0.33	--
	5830.00	1126.00	0.32	--
	5831.00	2466.00	0.32	--
	5832.00	4039.00	0.30	--
	5833.00	3045.00	0.29	--
	5834.00	1535.00	0.29	--
	5835.00	1567.00	0.29	--

Whole Core Data				
Well	Depth (ft md)	Permeability (mD)	Porosity (%)	SW (%)
MON0065X	5719.54	1.90	0.16	0.98
	5720.54	0.00	0.17	0.98
	5721.54	1.30	0.17	0.93
	5722.54	0.00	0.18	0.95
	5723.54	0.00	0.12	0.97
	5724.54	0.00	0.16	0.96
	5725.54	1.70	0.18	0.98
	5726.54	0.00	0.17	0.93
	5727.54	0.00	0.18	0.95
	5728.54	0.27	0.17	0.92
	5729.54	0.00	0.16	0.98
	5730.54	5.30	0.15	0.97
	5731.54	0.00	0.16	0.99
	5732.54	5374.00	0.30	0.96
	5733.54	3593.00	0.32	0.93
	5734.54	2538.00	0.32	0.98
	5735.54	4766.00	0.31	0.85
	5736.06	3406.00	0.33	0.91
	5736.58	5001.00	0.33	0.85
	5737.52	4654.00	0.32	0.80
	5738.46	5308.00	0.33	0.84
	5739.40	4815.00	0.33	0.84
	5740.34	2150.00	0.30	0.73
	5741.29	4050.00	0.32	0.91
	5742.23	5197.00	0.31	0.88
	5743.17	6719.00	0.31	0.74
	5744.11	4987.00	0.32	0.79
	5745.05	5035.00	0.31	0.86
	5745.99	1411.00	0.29	0.91
	5746.93	4814.00	0.31	0.95
	5747.88	5815.00	0.29	0.90
	5748.82	5815.00	0.30	0.89
	5749.76	3814.00	0.31	0.93
	5750.70	5002.00	0.32	0.94
	5751.64	4537.00	0.29	0.95
	5752.58	5576.00	0.26	0.93
	5753.52	6977.00	0.27	0.88
	5754.47	5499.00	0.26	0.78
	5755.41	4340.00	0.28	0.78
	5756.35	3623.00	0.28	0.82
	5757.29	4295.00	0.27	0.86
OM_0044X	5011.00	36.00	0.31	0.88

Whole Core Data				
Well	Depth (ft md)	Permeability (mD)	Porosity (%)	SW (%)
	5015.00	44.00	0.33	0.89
	5017.00	23.00	0.32	0.85
	5019.00	58.00	0.32	0.86
	5021.00	56.00	0.33	0.87
	5023.00	150.00	0.31	0.81
	5025.00	80.00	0.29	0.95
	5027.00	48.00	0.28	0.88
	5029.00	33.00	0.30	0.82
REV0004X	4724.00	1210.00	0.29	0.50
	4725.00	2820.00	0.30	0.50
	4726.00	2620.00	0.29	0.62
	4727.00	462.00	0.29	0.57
	4728.00	1510.00	0.29	0.66
	4729.00	2390.00	0.29	0.48
	4730.00	2120.00	0.30	0.61
	4731.00	663.00	0.28	0.53
	4732.00	4980.00	0.32	0.48
	4733.00	4510.00	0.41	0.61
	4734.00	1410.00	0.31	0.55
	4735.00	3820.00	0.38	0.64
	4736.00	1680.00	0.38	0.64
	4737.00	6.90	0.08	0.91
	4753.00	2560.00	0.36	0.77
	4754.00	6000.00	0.41	0.67
	4755.00	5110.00	0.42	0.71
	4756.00	3210.00	0.42	0.80
	4757.00	2810.00	0.36	0.83
	4758.00	1370.00	0.38	0.89
	4759.00	3030.00	0.42	0.78
	4760.00	111.00	0.32	0.94
	4761.00	65.00	0.30	0.94
	4762.00	1700.00	0.35	0.85
	4840.00	188.00	0.30	0.99
	4841.00	772.00	0.33	0.99
	4842.00	997.00	0.38	0.99
	4843.00	789.00	0.38	1.00
	4844.00	5.40	0.25	0.94
	4845.00	14.00	0.27	0.89
	4846.00	19.00	0.28	0.88
	4847.00	47.00	0.29	0.76
	4848.00	30.00	0.28	0.90
	4849.00	110.00	0.31	0.64
	4850.00	367.00	0.29	0.79
	4851.00	266.00	0.26	0.82

Whole Core Data				
Well	Depth (ft md)	Permeability (mD)	Porosity (%)	SW (%)
	4852.00	811.00	0.25	0.72
	4853.00	1280.00	0.25	0.63
	4854.00	2170.00	0.25	0.53
	4855.00	29.00	0.28	0.86
	4856.00	57.00	0.30	0.84
	4857.00	30.00	0.25	0.84
	4858.00	35.00	0.28	0.83
	4859.00	242.00	0.28	0.73
	4860.35	48.00	0.28	0.81
	4861.65	278.00	0.30	0.58
	4862.30	210.00	0.29	0.68
	4863.25	444.00	0.28	0.50
	4864.90	183.00	0.30	0.68
	4865.45	261.00	0.30	0.73
	4866.80	42.00	0.28	0.79
	4867.90	86.00	0.30	0.80
	4868.90	128.00	0.29	0.74
	4869.90	149.00	0.03	0.73
	4870.95	34.00	0.26	0.83
	4871.65	93.00	0.28	0.76
	4872.30	48.00	0.27	0.82
	4873.30	29.00	0.23	0.80
	4874.95	58.00	0.27	0.75
	4875.85	80.00	0.28	0.78
	4876.60	892.00	0.30	0.64
	4877.75	351.00	0.25	0.57
	4878.45	480.00	0.24	0.65
	4879.50	622.00	0.28	0.83
	4880.35	261.00	0.28	0.82
	4881.95	500.00	0.29	0.86
	4882.35	588.00	0.28	0.80
	4883.60	223.00	0.31	0.67
	4884.65	318.00	0.32	0.74
	4885.30	123.00	0.30	0.85
	4886.90	70.00	0.24	0.79
	4887.35	399.00	0.31	0.71
	4888.65	302.00	0.29	0.77
	4889.90	62.00	0.29	0.91
	4890.35	517.00	0.33	0.89
	4891.45	141.00	0.29	0.80
	4892.75	149.00	0.30	0.75
	4893.25	293.00	0.32	0.76
	4894.70	481.00	0.33	0.71
	4895.90	2420.00	0.29	0.52
	4896.75	273.00	0.30	0.86

Whole Core Data				
Well	Depth (ft md)	Permeability (mD)	Porosity (%)	SW (%)
	4897.45	271.00	0.35	0.89
	4898.45	180.00	0.30	0.90
	4899.80	931.00	0.37	0.83
	4900.60	862.00	0.35	0.79
	4901.65	179.00	0.36	0.91
	4902.45	1190.00	0.37	0.65
	4903.90	1050.00	0.36	0.79
	4904.65	732.00	0.34	0.82
	4905.30	689.00	0.33	0.84
	4906.25	1230.00	0.36	0.83
	4907.60	929.00	0.36	0.86
	4908.10	642.00	0.34	0.86
	4909.45	38.00	0.33	0.93
	4910.60	55.00	0.34	0.90
	4911.30	122.00	0.34	0.92
	4912.55	10.00	0.17	0.89
	4913.60	75.00	0.34	0.88
	4914.30	82.00	0.33	0.90
	4915.60	28.00	0.24	0.89
	4916.40	96.00	0.32	0.92
	4916.40	96.00	0.32	0.92
S4_WDV2	4905.50	1.50	34.10	0.68
	4906.50	5.90	33.00	0.92
	4907.50	0.90	18.30	0.78
	4908.50	2.10	25.80	0.74
	4909.50	3.60	25.90	0.64
	4910.50	17.80	29.40	0.79
	4911.50	13.00	30.50	0.81
	4912.50	1.20	25.10	0.80
	4913.50	18.40	26.50	0.84
	4914.50	38.90	29.30	0.83
	4915.50	28.10	26.90	0.71
	4916.50	28.70	29.20	0.84
	4917.50	33.30	29.00	0.85
	4918.50	18.10	27.10	0.81
	4919.50	39.10	26.70	0.76
	4920.50	2.40	6.70	0.69
	4921.50	1.00	17.70	0.73
	4922.50	1.60	19.00	0.72
	4923.50	2.10	20.20	0.67
	4924.70	2.20	12.20	0.47
	4925.50	8.60	11.20	0.62
	4926.50	4.60	9.30	0.58

Whole Core Data				
Well	Depth (ft md)	Permeability (mD)	Porosity (%)	SW (%)
	4927.50	1129.00	25.90	0.69
	4928.50	2817.00	28.70	0.66
	4929.50	1.40	14.10	0.90
	4930.30	0.20	4.90	0.65
	4932.50	1.40	12.10	0.64
	4933.60	2581.00	32.30	0.78
	4934.50	5553.00	32.10	0.60
	4935.50	2941.00	32.10	0.88
	4936.60	2773.00	32.50	0.81
	4937.50	2248.00	36.10	0.68
	4938.50	3289.00	30.40	0.51
	4939.50	9003.00	30.40	0.48
	4940.40	3423.00	34.70	0.86
	4941.70	1838.00	37.10	0.56
	4942.50	639.00	30.50	0.88
	4943.40	807.00	28.90	0.76
	4944.50	4839.00	32.10	0.68
	4945.60	4756.00	28.40	0.48
	4946.50	6037.00	29.70	0.59
	4947.90	4423.00	32.20	0.53
	4948.50	9434.00	31.60	0.48
	4949.50	5245.00	34.90	0.53
	4950.50	3522.00	34.20	0.44
	4951.60	357.00	31.10	0.53
	4952.70	6808.00	34.10	0.65
	4953.50	2922.00	21.70	0.54
	4954.50	1550.00	32.40	0.56
	4955.50	7724.00	32.80	0.53
	4956.50	4620.00	27.10	0.68
	4957.50	5967.00	23.60	0.47
	4958.50	7421.00	31.60	0.53
	4959.50	4676.00	28.40	0.52
	4960.50	7704.00	31.80	0.40
	4961.50	6741.00	32.80	0.56
	4962.50	6349.00	33.00	0.59
	5844.60	0.00	2.90	0.50
	5845.50	0.00	3.20	0.65
	5846.50	2097.00	23.70	0.83
	5847.50	5831.00	26.60	0.70
	5848.50	1342.00	27.10	0.79
	5849.70	5319.00	26.40	0.70
	5850.50	5284.00	25.20	0.82

Whole Core Data				
Well	Depth (ft md)	Permeability (mD)	Porosity (%)	SW (%)
	5851.50	4960.00	29.50	0.76
	5852.50	9256.00	28.00	0.78
	5853.50	2362.00	25.30	0.76
	5854.40	5252.00	25.80	0.71
	5855.60	2643.00	26.90	0.88
	5856.60	1136.00	24.20	0.85
	5857.60	2890.00	24.10	0.88
	5858.60	3454.00	27.60	0.83
	5859.60	1.30	20.10	0.74
	5860.50	2.50	17.30	0.87
	5861.50	1.10	19.00	0.85
	5862.50	29.90	21.60	0.70
SOVWD-1	1360.50	6063.40	0.35	0.75
	1361.50	6820.50	0.35	0.84
	1362.50	8276.50	0.28	0.92
	1363.50	7733.60	0.34	0.86
	1364.30	964.10	0.34	0.95
	1370.50	4241.10	0.35	0.87
	1371.50	5428.30	0.37	0.65
	1372.50	7253.30	0.37	0.64
	1373.50	4703.20	0.36	0.76
	1374.50	4329.90	0.35	0.61
	1375.50	4319.10	0.36	0.68
	1376.50	4060.50	0.34	0.65
	1380.50	5406.10	0.38	0.55
	1381.50	2656.60	0.34	0.57
	1382.50	5143.50	0.36	0.58
	1383.50	4052.90	0.34	0.60
	1384.50	6920.20	0.34	0.61
	1385.50	2424.10	0.32	0.75
	1386.50	3253.20	0.33	0.81
	1387.50	4972.10	0.34	0.83
	1388.50	10655.20	0.38	0.76
	1390.50	6631.50	0.42	0.74
	1391.50	13282.40	0.40	0.74
	1392.50	3892.70	0.33	0.74
	1393.50	1443.70	0.32	0.80
	1394.50	2281.60	0.33	0.78
	1395.50	2992.40	0.31	0.87
	1396.50	3677.70	0.32	0.87
	1397.50	1261.00	0.30	0.91
	1398.50	1268.80	0.31	0.81

Whole Core Data				
Well	Depth (ft md)	Permeability (mD)	Porosity (%)	SW (%)
	1401.50	1516.80	0.27	0.86
	1402.50	2421.90	0.31	0.85
	1403.50	195.70	0.35	0.92
	1404.50	256.30	0.35	0.94
	1405.50	350.50	0.36	0.99
	1416.50	192.70	0.39	0.92
	1418.50	103.90	0.34	1.00
	1420.50	120.20	0.26	0.93
	1422.50	113.80	0.34	0.95
	1423.50	300.60	0.30	0.73
	1424.50	98.40	0.31	0.99
	1425.50	256.70	0.31	0.95
	1426.50	1252.60	0.32	0.76
	1427.50	640.20	0.30	0.63
	1540.50	658.10	0.30	0.93
	1542.50	572.20	0.30	0.94
	1544.50	1316.70	0.30	0.92
	1546.50	1394.70	0.29	0.96
	1548.50	976.00	0.30	0.94
	1550.50	634.50	0.33	0.92
	1552.50	759.20	0.32	0.93
	1555.50	1579.20	0.30	0.89
	1557.50	1562.40	0.30	0.86
	1559.50	1584.00	0.31	0.92
	1561.50	1094.20	0.29	0.96
	1563.50	1165.50	0.30	0.90
	1565.50	1350.10	0.31	0.86
	1567.50	1155.40	0.29	0.86
	1569.50	1549.40	0.30	0.88
	1571.50	834.20	0.31	0.96
	1573.50	1353.50	0.30	0.91
	1575.50	1003.00	0.30	0.95
	1577.50	2473.10	0.31	0.96
	1579.50	1827.10	0.31	0.98
	1581.50	1234.60	0.28	0.93
	1583.50	1728.50	0.30	0.99
	1585.50	1318.90	0.30	0.97
	1587.50	1654.30	0.30	0.92
	1589.50	1383.90	0.30	0.93
	1795.50	3109.60	0.30	0.98
	1797.50	983.80	0.29	0.97
	1799.70	1046.80	0.29	0.94

Whole Core Data				
Well	Depth (ft md)	Permeability (mD)	Porosity (%)	SW (%)
	1801.50	1653.70	0.28	0.91
	1803.50	582.30	0.27	0.94
	1805.30	340.10	0.34	0.97
	1807.50	338.60	0.32	0.99
	1809.50	440.90	0.29	0.96
	1811.50	108.10	0.35	0.95
	1813.50	1022.10	0.44	0.99
	1815.50	302.60	0.33	0.98
	1817.50	325.80	0.27	0.83
	1819.50	270.00	0.26	0.72
	1821.50	285.00	0.38	0.97
	1823.50	56.90	0.32	0.97
	1825.50	112.50	0.28	0.88
	1827.50	35.00	0.30	0.92
	1830.50	183.80	0.38	0.94
	1832.50	90.10	0.32	0.94
	1834.50	1098.40	0.29	0.82
	1836.50	8938.30	0.32	0.57
	1838.50	14157.50	0.32	0.62
	1840.50	10877.20	0.33	0.71
	1842.50	565.20	0.33	0.96
	1844.50	371.90	0.30	0.92
	1846.50	26.50	0.29	0.96
	1848.50	443.40	0.35	0.99
	1850.50	82.70	0.29	0.91
	1852.50	505.00	0.30	0.83
	1854.50	9556.30	0.34	0.53
	1856.50	2915.10	0.33	0.72
	1858.50	3455.70	0.26	0.74
	1860.50	6016.50	0.30	0.72
	1862.50	10594.00	0.30	0.66
	1864.50	7568.80	0.29	0.72
	1866.50	5080.90	0.28	0.80
	1868.50	182.70	0.31	0.87
	4910.00	13.40	0.22	0.98
	4945.00	10.20	0.07	0.82
	4946.00	36.50	0.22	0.90
	4961.00	3.50	0.20	0.75
	4962.00	32.60	0.20	0.79
	5740.00	30.90	0.26	0.70
	5742.00	10.50	0.14	0.88
	5744.00	10.30	0.24	0.63

Whole Core Data				
Well	Depth (ft md)	Permeability (mD)	Porosity (%)	SW (%)
	5760.00	18.20	0.14	0.85
	5762.00	22.50	0.14	1.00
	5764.00	48.70	0.14	0.94
	5766.00	11.00	0.18	0.97
	5768.00	8.50	0.13	0.84
	5770.00	15.80	0.12	0.98
	5772.00	12.70	0.12	0.99
	5774.00	8.40	0.15	1.00
	5776.00	3.30	0.12	0.98
	5778.00	3.70	0.15	0.71
	5780.00	124.80	0.13	0.97
	5784.00	3.10	0.03	0.68
	5786.50	3093.30	0.36	0.55
	5788.00	392.50	0.26	0.68
	5789.00	187.30	0.28	0.81
	5790.00	3096.70	0.31	0.54
	5791.00	114.20	0.27	0.84
	5792.00	1265.50	0.29	0.47
	5793.00	5515.70	0.30	0.38
	5795.00	2568.80	0.31	0.69
	5797.00	1.50	0.07	0.67
	5799.00	3692.70	0.32	0.55
	5801.00	3699.40	0.32	0.64
	5803.00	1328.10	0.31	0.69
	5803.50	27.00	0.13	0.30
	5804.50	3264.00	0.35	0.64
	5806.50	940.00	0.32	0.83
	5808.50	13112.00	0.35	0.46
	5810.50	12656.00	0.34	0.51
	5812.50	11661.00	0.33	0.45
	5814.50	13909.00	0.32	0.56
	5816.50	8011.00	0.30	0.52
	5818.50	12122.00	0.32	0.60
	5820.50	14835.00	0.34	0.49
	5822.50	5680.00	0.37	0.46
	5824.50	11745.00	0.31	0.61
	5826.50	15407.00	0.33	0.59